

A STUDY OF TOP OF THE LINE CORROSION UNDER DROPWISE  
CONDENSATION

A dissertation presented to  
the faculty of  
the Russ College of Engineering and Technology of Ohio University

In partial fulfillment  
of the requirements for the degree  
Doctor of Philosophy

Ziru Zhang

March 2008

This dissertation titled  
A STUDY OF TOP OF THE LINE CORROSION UNDER DROPWISE  
CONDENSATION

by

ZIRU ZHANG

has been approved for  
the Department of Chemical and Biomolecular Engineering  
and the Russ College of Engineering and Technology by

---

Srdjan Nesic

Professor of Chemical and Biomolecular Engineering

---

Dennis Irwin

Dean, Russ College of Engineering and Technology

**ABSTRACT**

ZHANG, ZIRU, Ph.D., March 2008, Chemical Engineering

A STUDY OF TOP OF THE LINE CORROSION UNDER DROPWISE

CONDENSATION (228 pp.)

Director of Dissertation: Srdjan Nestic

Top of the Line Corrosion (TLC) is a phenomenon encountered in wet gas transportation when problems of corrosion appear inside the pipe due to the condensation of water containing dissolved corrosive gases at the top of the line. Theoretically, TLC can be seen as consisting of three major processes: condensation, chemical reactions in the condensed water, and corrosion at the steel surface. In this study, the theories behind dropwise condensation, corrosion, and droplet transport are investigated. Based on the mechanisms, mathematic models are developed to predict the condensation rate, the corrosion rate, and the possibility of effective droplet transport.

In the dropwise condensation model, the heat and mass conservation equations are established to account for the effect of all important heat and mass transfer resistances. A numerical method is proposed to solve the non-linear equation system and predict the condensation rate. Meanwhile, through force analysis on a single droplet, the maximum droplet size and the condensation regime can be determined. With the inputs of the condensation rate and the droplet growth scenario from the dropwise condensation model, an electrochemical mechanism from Nestic et al. (1996) is adapted to model the corrosion process at the top of the line. The breakdown of species concentrations in the droplet is established through the main thermodynamic and chemical equilibria. The

general corrosion rate is predicted using the kinetics of the electrochemical reactions at the steel surface and by taking into account the mass transfer and chemical reactions occurring inside the droplet. In order to verify the mechanistic model, long term experiments are conducted in large scale flow loops equipped with an *in situ* camera. In comparison with the experimental results, the model was able to predict reasonably well the condensation rate, the corrosion rate, and the condensation regime.

Being a standard method for corrosion control in the oil and gas industry, corrosion inhibitors are not useful for TLC prevention since traditional inhibitors are liquid and flow at the bottom of the line and cannot easily reach the top of the line where the aggressive condensed water is formed. However, it is believed that under certain circumstances inhibitors may be transported to the top of the line as entrained droplets are deposited there. In order to theoretically describe how and when a droplet is entrained from the liquid at the bottom and then deposited at the top of the line, several inception and transition criteria have been defined. Firstly, two mechanisms (undercutting and tearing) are determined for the onset of droplet formation. Secondly, according to the wave-mixing and entrainment-deposition mechanism, two criteria for the transition from stratified to non-stratified flow are established, respectively. Finally, an effective zone with well defined boundaries is introduced to provide operational guidance for the utilizing of corrosion inhibitors in TLC prevention.

Approved: \_\_\_\_\_

Srdjan Nestic

Professor of Chemical and Biomolecular Engineering

## ACKNOWLEDGMENTS

I would like to express my sincere appreciation to my advisor Dr. Srdjan Nesic for his patient guidance, enlightening advice, and apparently endless encouragement during the course of my PhD study. Whenever I have had difficulties, he always offered me constructive suggestions and continuous support. I am now much more confident and ready to face the many new challenges awaiting me in the future and part of that is due to the thorough training I received under Dr. Nesic's supervision at Institute for Corrosion and Multiphase Technology.

I am indebted to Mr. Marc Singer for his assistance in the technical work and his leadership with the TLC JIP teamwork. I would like to extend my thanks to all staff members and fellow graduate students at the institute for their help and companionship. I would also like to acknowledge Dr. Valerie Young for her warm help on academic issues for my PhD study. And thanks also go to Dr. Dusan Sormaz for his valuable suggestions on my research project.

The financial support and technical directions from sponsor companies (BP, ConocoPhillips, ENI, and Total) are appreciated.

Finally, I would like to express my gratefulness to my parents and Ms. Zhengzheng Fei for their love, care, and support.

## TABLE OF CONTENTS

	Page
Abstract.....	3
Acknowledgments.....	5
List of Tables .....	10
List of Figures .....	11
Chapter 1: Introduction.....	17
Chapter 2: Literature review .....	22
2.1    Condensation at the top of the line .....	22
2.1.1    Filmwise condensation.....	23
2.1.2    Dropwise condensation.....	25
2.2    Thermodynamics/chemistry in the droplets.....	30
2.3    Corrosion process at the top of the line .....	30
2.3.1    Experimental and case studies of top of the line corrosion .....	31
2.3.2    Modeling of top of the line corrosion .....	35
2.3.3    Mechanistic models for bottom of the line corrosion .....	40
2.4    Droplet transport in gas-liquid two-phase flow .....	41
2.4.1    Hydrodynamics in droplet transport .....	41
2.4.2    Onset of droplet entrainment .....	46
2.4.3    Transition to non-stratified flow .....	55
2.5    Objectives .....	57
2.6    Summary.....	59

Chapter 3: Experimental study of top of the line corrosion in a large scale flow loop ....	60
3.1 Introduction.....	60
3.2 Experimental procedures .....	61
3.2.1 Experimental setup.....	61
3.2.2 Test matrix .....	68
3.2.3 Materials and methods .....	64
3.3 Results and discussions.....	71
3.3.1 Baseline test .....	71
3.3.2 Effect of gas temperature .....	88
3.3.3 Effect of gas velocity .....	90
3.3.4 Effect of CO <sub>2</sub> partial pressure .....	97
3.3.5 Effect of condensation rate .....	100
3.3.6 Effect of acetic acid concentration.....	102
3.4 Summary .....	105
Chapter 4: A mechanistic model of dropwise condensation at the top of the line.....	107
4.1 Introduction.....	107
4.2 Model development .....	108
4.2.1 Droplet-size distribution function .....	109
4.2.2 Heat flux in dropwise condensation.....	110
4.2.3 Heat balance .....	111
4.2.4 Mass balance .....	117
4.2.5 Determination of minimum and maximum radii of droplets .....	119

4.2.6	Numerical method.....	125
4.3	Verification of the condensation model.....	126
4.3.1	Condensation rate and heat flux.....	126
4.3.2	Maximum droplet size and the dropwise condensation regimes	128
4.4	Parametric study.....	132
4.4.1	Parametric study of the condensation model .....	132
4.4.2	Maximum droplet and condensation regimes .....	137
4.5	Summary.....	143
Chapter 5: A mechanistic model of top of the line corrosion .....		145
5.1	Introduction.....	145
5.2	Model development .....	147
5.2.1	Chemical reactions.....	150
5.2.2	Transport processes (Nesic, 1996).....	151
5.2.3	Scale growth.....	153
5.2.4	Initial and boundary conditions .....	155
5.2.5	Numerical method.....	157
5.3	Verification of the corrosion model.....	159
5.4	Prediction software package (TOPCORP).....	172
5.5	Summary .....	173
Chapter 6: Droplet transport in gas-liquid two-phase concurrent flow .....		175
6.1	Introduction.....	175
6.2	Model development .....	177

6.2.1	Momentum balance in stratified flow .....	177
6.2.2	Onset of atomization .....	181
6.2.3	Transition to non-stratified flow .....	187
6.2.4	Numerical method.....	196
6.3	Model prediction.....	197
6.3.1	Onset of atomization .....	197
6.3.2	Transition to non-stratified flow .....	200
6.3.3	“Effective zone” .....	202
6.4	Summary .....	203
Chapter 7: Conclusions and recommendations for future development.....		205
References.....		209
Appendix I: Chemical reactions and their reaction/equilibrium constants.....		218
Appendix II: Calculation of gas properties in nonideal gas mixtures.....		220
Appendix III: Interface of TOPCORP .....		225

**LIST OF TABLES**

	Page
Table 3-1: Chemical analysis of the carbon steels used in the experiments.....	65
Table 3-2: Composition of Clarke's solution.....	66
Table 3-3: Baseline conditions in large scale loop .....	70
Table 3-4: Ranges of test conditions in large scale loop .....	70
Table 3-5: Evolution of pH and the ferrous ion concentration in baseline test.....	72
Table 4-1: Test conditions on condensation in large scale loop .....	127
Table 5-1: Test conditions on corrosion in large scale loop .....	160
Table I-1: Chemical reactions accounted for in the model and their equilibrium constants (Adapted from Nordsveen et al., 2003 ) .....	218
Table I-2: Equilibrium ( $K$ ), forward ( $k_f$ ), and backward ( $k_b$ ) reaction rate coefficients (Note: $K = k_f/k_b$ ) (Adapted from Nordsveen, 2003).....	219
Table II-1: Constants in the calculation of heat capacity.....	224

## LIST OF FIGURES

	Page
Figure 2-1: Stepwise computation of condensation rate in Vitse's model .....	25
Figure 2-2: Dropwise condensation – Nucleation: Droplets are initiated on the surface .	26
Figure 2-3: Dropwise condensation – Growth: Droplets grow up through direct condensation on the gas-liquid interface.....	26
Figure 2-4: Dropwise condensation – Coalescence: Small droplets can join together and form a much bigger droplet.....	26
Figure 2-5: Dropwise condensation – Removal: A droplet (b) is swept by another droplet (a) coming from the upstream.....	27
Figure 2-6: Experimental setup in Pots and Hendriksen's work (2002).....	33
Figure 2-7: Schematic of the flow loop in Vitse's work.....	34
Figure 2-8: Comparison between experiments and de Waard's model (Adapted from Pots and Hendriksen, 2000).....	36
Figure 2-9: Mass transfer of ferrous ion in Vitse's model.....	39
Figure 2-10: Evidence of dropwise condensation at the top of the line seen through a side window (left) and on an exposed weight loss coupon (right).....	40
Figure 2-11: Stratified flow without atomization (ID = 9.53cm, $U_{SG}$ =6.4 m/s, and $U_{SL}$ =0.076 m/s) .....	44
Figure 2-12: Stratified flow with the deposited droplets at the top (ID = 9.53cm, $U_{SG}$ =16 m/s, and $U_{SL}$ =0.076 m/s).....	44
Figure 2-13: Stratified flow with water rivulets formed by the deposited droplets (ID = 9.53cm, $U_{SG}$ =21 m/s, and $U_{SL}$ =0.076 m/s).....	45
Figure 2-14: Annular flow (ID = 9.53cm, $U_{SG}$ =31 m/s, and $U_{SL}$ =0.076 m/s) .....	45
Figure 2-15: Atomization mechanisms.....	49
Figure 2-16: Linear extrapolation in Steen's data interpretation .....	50

	12
Figure 3-1: Schematic of large scale flow loop with modifications .....	62
Figure 3-2: Schematic of the test section with a copper coil cooling system .....	63
Figure 3-3: Gas flow meter .....	63
Figure 3-4: Weight loss coupons with a Teflon coating and their mounting to the test section .....	66
Figure 3-5: Normalized corrosion rate at the top and the bottom of the line in the baseline test ( $T_g = 70\text{ }^\circ\text{C}$ , $P_T = 3\text{ bar}$ , $pCO_2 = 2\text{ bar}$ , $WCR = 0.25\text{ mL/m}^2/\text{s}$ , $U_{SG} = 5\text{ m/s}$ , $Free\ HAC = 0\text{ ppm}$ ) .....	74
Figure 3-6: Baseline – Top of the line Weight loss coupons before the removal of the corrosion product layer .....	77
Figure 3-7: Baseline – Top of the line – Test duration: 2 days SEM and EDS analysis of the corrosion product layer on the coupon surface .....	78
Figure 3-8: Baseline – Top of the line – Test duration: 7 days SEM and EDS analysis of the corrosion product layer on the coupon surface .....	79
Figure 3-9: Baseline – Top of the line – Test duration: 14 days SEM and EDS analysis of the corrosion product layer on the coupon surface .....	80
Figure 3-10: Baseline – Top of the line – Test duration: 21 days SEM and EDS analysis of the corrosion product layer on the coupon surface .....	81
Figure 3-11: Baseline – Top of the line – Test duration: 21 days Surface profile of the coupon after the removal of the corrosion product layer .....	82
Figure 3-12: Baseline – Bottom of the line Weight loss coupons before the removal of the corrosion product layer .....	83
Figure 3-13: Baseline – Bottom of the line – Test duration: 2 days SEM and EDS analysis of the corrosion product layer on the coupon surface .....	84
Figure 3-14: Baseline – Bottom of the line – Test duration: 7 days SEM and EDS analysis of the corrosion product layer on the coupon surface .....	85
Figure 3-15: Baseline – Bottom of the line – Test duration: 14 days SEM and EDS analysis of the corrosion product layer on the coupon surface .....	86

- Figure 3-16: Baseline – Bottom of the line – Test duration: 21 days SEM and EDS analysis of the corrosion product layer on the coupon surface..... 87
- Figure 3-17: Effect of gas temperature on the general corrosion rate at the top of the line ( $P_T = 3$  bar,  $pCO_2 = 2$  bar,  $WCR = 0.25$  mL/m<sup>2</sup>/s,  $U_{SG} = 5$  m/s,  $Free\ HAc = 0$  ppm)..... 89
- Figure 3-18: Effect of gas temperature on the general corrosion rate at the bottom of the line ( $P_T = 3$  bar,  $pCO_2 = 2$  bar,  $WCR = 0.25$  mL/m<sup>2</sup>/s,  $U_{SG} = 5$  m/s,  $Free\ HAc = 0$  ppm). 90
- Figure 3-19: Surface analysis on a coupon at high gas velocity (15m/s) by SEM and EDS ( $T_g = 70$  °C,  $P_T = 3$  bar,  $pCO_2 = 2$  bar,  $WCR = 0.25$  mL/m<sup>2</sup>/s,  $Free\ HAc = 0$  ppm)..... 92
- Figure 3-20: Effect of gas velocity on the general corrosion rate at the top of the line (The corrected corrosion rates and space average corrosion rates are represented by dashed lines and solid lines respectively. The definitions of these two corrosion rates can be found in the text.) ( $T_g = 70$  °C,  $P_T = 3$  bar,  $pCO_2 = 2$  bar,  $WCR = 0.25$  mL/m<sup>2</sup>/s,  $Free\ HAc = 0$  ppm)..... 95
- Figure 3-21: Effect of gas velocity on the general corrosion rate at the bottom of the line (The corrected corrosion rates and space average corrosion rates are represented by dashed lines and solid lines respectively. The definitions of these two corrosion rates can be found in the text.) ( $T_g = 70$  °C,  $P_T = 3$  bar,  $pCO_2 = 2$  bar,  $WCR = 0.25$  mL/m<sup>2</sup>/s,  $Free\ HAc = 0$  ppm)..... 97
- Figure 3-22: Effect of CO<sub>2</sub> partial pressure on the general corrosion rate at the top of the line ( $T_g = 70$  °C,  $WCR = 0.25$  mL/m<sup>2</sup>/s,  $U_{SG} = 5$  m/s,  $Free\ HAc = 0$  ppm)..... 98
- Figure 3-23: Effect of CO<sub>2</sub> partial pressure on the general corrosion rate at the bottom of the line ( $T_g = 70$  °C,  $WCR = 0.25$  mL/m<sup>2</sup>/s,  $U_{SG} = 5$  m/s,  $Free\ HAc = 0$  ppm)..... 99
- Figure 3-24: Effect of the condensation rate on the general corrosion rate at the top of the line ( $T_g = 70$  °C,  $P_T = 3$  bar,  $pCO_2 = 2$  bar,  $U_{SG} = 5$  m/s,  $Free\ HAc = 0$  ppm)..... 101
- Figure 3-25: Effect of the condensation rate on the general corrosion rate at the bottom of the line ( $T_g = 70$  °C,  $P_T = 3$  bar,  $pCO_2 = 2$  bar,  $U_{SG} = 5$  m/s,  $Free\ HAc = 0$  ppm)..... 102
- Figure 3-26: Effect of HAc concentration on the general corrosion rate at the top of the line ( $T_g = 70$  °C,  $P_T = 3$  bar,  $pCO_2 = 2$  bar,  $WCR = 0.25$  mL/m<sup>2</sup>/s,  $U_{SG} = 5$  m/s)..... 103
- Figure 3-27: Test with 1000 ppm free HAc – Top of the line – Test duration: 21 days Surface profile of the coupon after the removal of the corrosion product layer..... 104
- Figure 3-28: Effect of HAc concentration on the general corrosion rate at the bottom of the line ( $T_g = 70$  °C,  $P_T = 3$  bar,  $pCO_2 = 2$  bar,  $WCR = 0.25$  mL/m<sup>2</sup>/s,  $U_{SG} = 5$  m/s)..... 105

Figure 4-1: Temperature gradient in a single droplet where the bulk temperature can be assumed to be constant for a very short distance in flow direction. ....	111
Figure 4-2: Force analysis on a single droplet.....	122
Figure 4-3: Flow chart for the numerical calculation in the condensation model .....	126
Figure 4-4: Comparison of the measured and predicted condensation rate.....	128
Figure 4-5: Experimental setup of a transparent flow loop .....	129
Figure 4-6: Comparison between experimental results and the model prediction on the maximum droplet and condensation regimes in transparent flow loop ( $T_g = 25\text{ }^\circ\text{C}$ , $P_T = 1\text{ bar}$ ) .....	130
Figure 4-7: Comparison between experimental results and the model prediction on the maximum droplet size and condensation regimes in stainless flow loop at low pressure ( $P_T = 3\text{ bar}$ $T = 75 \pm 5\text{ }^\circ\text{C}$ ).....	131
Figure 4-8: Comparison between experimental results and the model prediction on the maximum droplet size and condensation regimes in stainless flow loop at high pressure ( $P_T = 7\text{ bar}$ , $T = 70 \pm 5\text{ }^\circ\text{C}$ ).....	132
Figure 4-9: Effect of gas temperature on the condensation rate .....	134
Figure 4-10: Effect of total pressure on the condensation rate .....	135
Figure 4-11: Effect of gas velocity on the condensation rate .....	136
Figure 4-12: Effect of subcooling temperature on the condensation rate.....	137
Figure 4-13: Effect of gas pressure on the maximum droplet size and condensation regimes ( $T_g = 70\text{ }^\circ\text{C}$ ) .....	139
Figure 4-14: Effect of gas temperature on the maximum droplet size and condensation regimes ( $P_T = 8\text{ bar}$ ).....	140
Figure 4-15: Condensation regimes at the top of the line.....	142
Figure 4-16: Condensation regime map.....	143
Figure 5-1: The simplification from a three-dimension problem to a one dimensional problem .....	149

Figure 5-2: Flow chart for the calculation of corrosion rate.....	159
Figure 5-3: Comparison between a long term test and model prediction on the corrosion rate ( $T=70\text{ }^{\circ}\text{C}$ , $P_T=3\text{ bar}$ , $pCO_2=2\text{ bar}$ , $WCR=0.25\text{ mL/m}^2/\text{s}$ , $U_{SG}=5\text{ m/s}$ , $Free\ HAc=0\text{ ppm}$ ).....	161
Figure 5-4 <sup>3,4</sup> : Comparison between a long term test and model prediction on the corrosion rate ( $T=40\text{ }^{\circ}\text{C}$ , $P_T=3\text{ bar}$ , $pCO_2=2\text{ bar}$ , $WCR=0.25\text{ mL/m}^2/\text{s}$ , $U_{SG}=5\text{ m/s}$ , $Free\ HAc=0\text{ ppm}$ ).....	163
Figure 5-5 <sup>3,4</sup> : Comparison between a long term test and model prediction on the corrosion rate ( $T=85\text{ }^{\circ}\text{C}$ , $P_T=3\text{ bar}$ , $pCO_2=2\text{ bar}$ , $WCR=0.25\text{ mL/m}^2/\text{s}$ , $U_{SG}=5\text{ m/s}$ , $Free\ HAc=0\text{ ppm}$ ).....	164
Figure 5-6 <sup>3,4</sup> : Comparison between a long term test and model prediction on the corrosion rate ( $T=70\text{ }^{\circ}\text{C}$ , $P_T=3\text{ bar}$ , $pCO_2=0.13\text{ bar}$ , $WCR=0.25\text{ mL/m}^2/\text{s}$ , $U_{SG}=5\text{ m/s}$ , $Free\ HAc=0\text{ ppm}$ ).....	165
Figure 5-7 <sup>3,4</sup> : Comparison between a long term test and model prediction on the corrosion rate ( $T=70\text{ }^{\circ}\text{C}$ , $P_T=8\text{ bar}$ , $pCO_2=7\text{ bar}$ , $WCR=0.25\text{ mL/m}^2/\text{s}$ , $U_{SG}=5\text{ m/s}$ , $Free\ HAc=0\text{ ppm}$ ).....	166
Figure 5-8 <sup>3,4</sup> : Comparison between a long term test and model prediction on the corrosion rate ( $T=70\text{ }^{\circ}\text{C}$ , $P_T=3\text{ bar}$ , $pCO_2=2\text{ bar}$ , $WCR=0.25\text{ mL/m}^2/\text{s}$ , $U_{SG}=10\text{ m/s}$ , $Free\ HAc=0\text{ ppm}$ ).....	167
Figure 5-9 <sup>3,4</sup> : Comparison between a long term test and model prediction on the corrosion rate ( $T=70\text{ }^{\circ}\text{C}$ , $P_T=3\text{ bar}$ , $pCO_2=2\text{ bar}$ , $WCR=0.25\text{ mL/m}^2/\text{s}$ , $U_{SG}=15\text{ m/s}$ , $Free\ HAc=0\text{ ppm}$ ).....	168
Figure 5-10 <sup>3,4</sup> : Comparison between a long term test and model prediction on the corrosion rate ( $T=70\text{ }^{\circ}\text{C}$ , $P_T=3\text{ bar}$ , $pCO_2=2\text{ bar}$ , $WCR=0.05\text{ mL/m}^2/\text{s}$ , $U_{SG}=5\text{ m/s}$ , $Free\ HAc=0\text{ ppm}$ ).....	169
Figure 5-11 <sup>3,4</sup> : Comparison between a long term test and model prediction on the corrosion rate ( $T=70\text{ }^{\circ}\text{C}$ , $P_T=3\text{ bar}$ , $pCO_2=2\text{ bar}$ , $WCR=1\text{ mL/m}^2/\text{s}$ , $U_{SG}=5\text{ m/s}$ , $Free\ HAc=0\text{ ppm}$ ).....	170
Figure 5-12 <sup>3,4</sup> : Comparison between a long term test and model prediction on the corrosion rate ( $T=70\text{ }^{\circ}\text{C}$ , $P_T=3\text{ bar}$ , $pCO_2=2\text{ bar}$ , $WCR=0.25\text{ mL/m}^2/\text{s}$ , $U_{SG}=5\text{ m/s}$ , $Free\ HAc=100\text{ ppm}$ ).....	171

Figure 5-13 <sup>3, 4</sup> : Comparison between a long term test and model prediction on the corrosion rate ( $T = 70\text{ }^{\circ}\text{C}$ , $P_T = 3\text{ bar}$ , $p\text{CO}_2 = 2\text{ bar}$ , $\text{WCR} = 0.25\text{ mL/m}^2/\text{s}$ , $U_{SG} = 5\text{ m/s}$ , $\text{Free HAc} = 1000\text{ ppm}$ ) .....	172
Figure 5-14: Main window of TOPCORP: Outputs including the condensation rate, the chemistry in droplets, and the corrosion rate can be calculated by different modules with provided case conditions, which are specified in global inputs.....	173
Figure 6-1: Schematic of the cross section of a pipe in gas-liquid two-phase flow .....	178
Figure 6-2: Flow chart for the numerical calculation in the determination of the “effective zone” ( $U_{SG}/U_{SL}$ : superficial gas/liquid velocity, $h_L$ : liquid holdup).....	197
Figure 6-3: Comparison between an experiment and model prediction on the onset of atomization at such conditions $T = 25\text{ }^{\circ}\text{C}$ , $P_T = 1\text{ bar}$ , $D = 0.1\text{ m}$ , $M_{Gas}$ (Molecular weight) = $0.029\text{ kg/mol}$ (Experimental data from Lin and Hanratty, 1987).....	198
Figure 6-4: Onset of atomization at different pressures .....	199
Figure 6-5: Onset of the atomization at different internal diameters.....	200
Figure 6-6: Transitions from stratified to non-stratified flow predicted by the wave-mixing and entrainment-deposition mechanism, and measured by Lin and Hanratty (1987) at such conditions as $T = 25\text{ }^{\circ}\text{C}$ , $P_T = 1\text{ bar}$ , $M_{Gas} = 0.029\text{ kg/mol}$ , and $D = 0.095\text{ m}$ .....	201
Figure 6-7: Transitions from stratified to non-stratified flow predicted by the wave-mixing and entrainment-deposition mechanism, and measured by Jepson and Taylor (1993) at such conditions as $T = 25\text{ }^{\circ}\text{C}$ , $P_T = 1\text{ bar}$ , $M_{Gas} = 0.029\text{ kg/mol}$ , and $D = 0.3\text{ m}$ .....	202
Figure 6-8: A flow map with an indicated “effective zone” in which inhibitors can be effectively transported to the top side of the pipeline though the deposition of entrained droplets ( $T = 25\text{ }^{\circ}\text{C}$ , $P_T = 10\text{ bar}$ , $D = 0.3\text{ m}$ ).....	203

## CHAPTER 1: INTRODUCTION

As Jones (1996) described in his book, *corrosion* is a gradual process disintegrating the essential properties of materials under the attack of aggressive species in the surrounding environment. Typically, the enormous risk of corrosion is overlooked until a major failure occurs due to the cumulative effect of corrosion. Dozens of examples of disasters related to corrosion failures can be easily given in recent human history. The most recent one was the very costly pipeline failure in Alaska which interrupted oil flow and caused a major upset in the US oil and gas market in 2006 (CNN, 2006). With corrosion failures come personnel casualties, financial loss, and environmental contamination. The direct and indirect cost caused by corrosion to the whole economy is tremendous. A study (Koch, 2002) showed that the direct corrosion cost in the United States is about \$276 billions a year, which is approximately 3.1% of the United States Gross Domestic Product (GDP) in 1998.

In that study it was argued that corrosion affects twenty-six major industrial sectors. Among them the oil and gas industry is one of the big contributors to the huge corrosion cost. Although for each barrel of produced crude oil 0.20 to 0.40 dollars have been spent on corrosion prevention in oil and gas exploration and production, internal corrosion in field facilities still causes 30% of the failures (Ruschau and Al-Anezi). Since the recent failure of the oil pipeline in Alaska (CNN, 2006), corrosion has become a more visible concern for the oil companies as well as governments who regulate them, as they suddenly wake up to the fact that the mechanisms in many corrosion cases are not well

understood and therefore they cannot be explained suggesting that new failures cannot be predicted.

Top of the Line Corrosion (TLC) is one of unclear mechanisms which has beset the industry for several decades. Stratified flow regime in wet gas transportation system is the prerequisite to have TLC problems. When the pipeline is exposed to the environment of even partially buried or insulated, a temperature difference between hot gas inside and the cold environment exists. As a consequence, the water vapor in the gas phase condenses on the cooler metal surface at the top of the line and the sides. The aggressive condensed water which contains various corrosive species, such as carbon dioxide ( $\text{CO}_2$ ), hydrogen sulfide ( $\text{H}_2\text{S}$ ), and acetic acid (HAc), attacks the metal wall and causes a severe corrosion problem. The top of the line is the most critical location since severe problems of localized corrosion are found there.

In industry, corrosion inhibitors are generally used to protect pipelines, which can effectively retard the internal corrosion through forming a “protective film” on the metal surface. The “protective film” formed by the organic components in corrosion inhibitors can prevent the direct contact between water (the carrier of corrosive species) and the pipe wall; therefore, slowing down the corrosion process dramatically. However, a corrosion inhibitor is useless for TLC prevention because traditional non-volatile liquid inhibitors remain at the bottom of the line and cannot reach the condensed water at the top of the line. Therefore, TLC is one of the most difficult corrosion problems facing the oil and gas industry without any effective solutions on the horizon. Clearly there is a need

of a better understanding of TLC that will pave the way for designing of more effective corrosion-mitigation strategies.

It is well known that one prerequisite for TLC is that the liquid at the top of the line should exclusively come from the condensation process. The condensed water is fresh and very aggressive since the pH is very low in the presence of CO<sub>2</sub> and/or HAc. In contrast, the liquid solution at the bottom of the line contains a lot of dissolved ions (from the ground reservoir) as well as various injected chemicals: typically corrosion and hydrate inhibitors. If the liquid at the bottom of the line is somehow transported to the top of the line, the mechanism of TLC could be completely changed. This can be easily happen when either annular flow or intermittent (slug) flow is achieved. However, the relatively high gas/liquid velocity needed for annular/intermittent flow is not common for most wet gas field cases facing TLC problems. Since liquid entrainment in stratified flow followed by droplet deposition at the top of the line can happen at lower gas velocity, it is important to establish criteria for an effective droplet transport in which inhibitors can reach the top of the line. The study of the droplet transport might lead to a practical solution for effective application of corrosion inhibitors in TLC prevention.

In order to combat the TLC issue, it is necessary to understand the mechanisms behind the phenomenon. A mechanistic model based on the theory of TLC is an ideal tool to predict the corrosion rate at the top of the line. In the last several decades, TLC has been extensively studied by many researchers. However, most of the studies discussed the TLC histories of field cases (Estavoyer, 1960; Gunaltun et al., 1999) and some basic empirical and semi-empirical models can be found (Olsen and Dugstad, 1991; Pots and

Hendriksen, 2000; Vitse, 2002) based on experimental data from oversimplified experimental setups. Until now, very few studies have been published on the general mechanism of TLC and there is a lack of reliable and consistent data necessary to build an accurate model.

At the Institute for Corrosion and Multiphase Technology (Athens, OH) a TLC Joint Industry Project (JIP) was initiated in 2003 and sponsored by four major oil companies (BP, ConocoPhillips, ENI, and Total). Several large scale flow loops have been built to mimic real wet gas pipelines with TLC issues. Various advanced techniques have been developed and implemented to analyze the experimental data. For example, a unique *in situ* camera system has been developed for condensation/corrosion study. The goals of the project were to identify the main parameters involved in TLC, to develop an understanding of their influence, and to provide reliable and consistent data for model development. In the Phase I of TLC JIP, short term experiments, six important parameters including gas temperature, gas velocity, condensation rate, CO<sub>2</sub> partial pressure, H<sub>2</sub>S partial pressure, and HAc concentration have been investigated (Singer et al., 2004 and Mendez et al., 2005). However, the corrosion rates in short term tests were still not stable and the results of localized corrosion were not conclusive after several days of testing. Therefore, long term corrosion experiments (at least 21 days) became the focus of the Phase II, which is also one of the objectives for this dissertation.

As the primary objective for this dissertation, a mechanistic model, which covers dropwise condensation, chemistry in the water droplets, and resulting corrosion is developed to describe the TLC phenomena observed in our experiments (particularly in

the long term experiments) and in some field cases. In this model, the force analysis on a single droplet is incorporated to predict the transition between various condensation regimes. In addition, a so-called “effective zone” of droplet transport in TLC prevention is defined based on the mechanisms of atomization, entrainment, and deposition. Finally, a software package with a user friendly interface conveying the mechanistic models and lab experimental experience is designed and built to predict TLC risks.

It should be stated that the results and the descriptions of the dropwise and corrosion model presented in the following chapters have already been included in a published journal paper: Zhang, Z., Hinkson, D. C., Singer, M., Wang, H., Nescic, S., A Mechanistic Model of Top of the Line Corrosion, Corrosion, 2007, 63: 1051-1062. The experimental procedure and many of results used in this dissertation have been documented in our internal reports: Singer M., Zhang, Z., Hinkson, D., Camacho, A., Nescic, S., TLC JIP Advisory Board Meeting Report, Institute for Corrosion and Multiphase Technology, Ohio University, Athens, OH, 2004-2007

## CHAPTER 2: LITERATURE REVIEW

Top of the Line Corrosion (TLC) occurs exclusively in wet gas transportation and then only in a stratified flow regime. Condensation happens when the environment outside the pipeline is cooler than the gas carrying a saturated vapor flowing inside the pipe. Water vapor in the gas phase condenses on the pipe wall in two different ways:

- on the side walls of the pipe the condensed liquid forms and then rapidly slides to the bottom of the line due to gravity forces;
- at the top of the pipe droplets of liquid form and remain attached at the metal surface for a longer time.

The dissolution of corrosive gases, such as carbon dioxide ( $\text{CO}_2$ ) and hydrogen sulfide ( $\text{H}_2\text{S}$ ) as well as condensation of acidic vapors such as acetic acid ( $\text{HAc}$ ) in the droplet can cause serious corrosion problems at the metal surface. TLC involves three simultaneously occurring phenomena: condensation, chemical reactions in droplets, and corrosion. In addition, atomization and deposition of droplets in stratified flow might have an effect on TLC. In this chapter, the previous studies available from the open literature covering these four major problem areas are reviewed separately.

### 2.1 Condensation at the top of the line

For better modeling of TLC it is necessary to have an accurate prediction of the condensation rate and condensation regime. In the past some researchers developed models to predict the condensation rate by using the filmwise condensation theory

(Minkowycz and Sparrow, 1970; Vitse, 2002). However, this theory is not valid when trying to predict the condensation rate at the top of the line where dropwise condensation happens. The key differences between the two condensation regimes are discussed below.

### 2.1.1 Filmwise condensation

Filmwise condensation happens when the surface is completely wetted by the condensate. For a laminar film with stagnant vapor, Nusselt in 1916 developed the well known *Nusselt film condensation theory* to calculate the rate of heat transfer. As the first try for modeling of filmwise condensation, Nusselt made several assumptions (such as linear temperature profile in the liquid film) to simplify the theoretical challenges which might be very significant in the 1910's. According to *Nusselt film condensation theory*, the heat transfer coefficient and film thickness can be calculated. However, it is limited to pure water vapor condensation, which is not common in reality.

Chato (1962) extended *Nusselt film condensation theory* to the filmwise condensation with a turbulent film (Reynolds number can be as high as 35,000) in a pipeline system. Starting from the momentum and energy balance equations, Chato derived a correlation for the mean heat transfer coefficient. However, when a non-condensable gas is present, *Nusselt theory* and all its derivatives will over-predict condensation rates due to lack of inclusion of the non-condensable gas effect.

In order to include this effect as well as the effect of gas velocity, Minkowycz and Sparrow (Minkowycz and Sparrow, 1966) proposed that there was another boundary layer in the side of gas phase at the gas/liquid interface beside the boundary layer in the

liquid side. In their heat and mass balance analysis, the double boundary layers of gas and liquid phase acted as major heat and mass transfer resistances. In addition, interfacial resistance, superheating of the vapor phase, and diffusion of water vapor in the gas phase had been incorporated into the model. In their study, it was found that the heat transfer flux was reduced dramatically when a trace amount of non-condensable gas was introduced to the system. Through model simulation, the control process in filmwise condensation in the presence of non-condensable gas was determined to be mass transfer through the gas boundary layer.

Slegers and Seban (1970) carried out experimental study on the effect of non-condensable gas on condensation process. In their experiments, the temperature drop across the gas boundary layer accounted for as high as 90% of the overall temperature difference between the bulk gas and the metal surface. These results confirmed Minkowycz and Sparrow's argument on the control process obtained from their model simulation. However, the model needs some modifications before it can be applied to the configuration of a pipeline system.

In the light of Minkowycz and Sparrow's ideas (1966), Vitse (2002) discretized the whole pipeline into small segments (Figure 2-1). The double boundary layer theory was applied to each segment and the condensation rate was predicted after a stepwise integration of heat flux along the axis of the pipeline. In addition, a mass balance equation was established on the liquid film to calculate the thickness of the film, which was a function of the location but was independent of time.

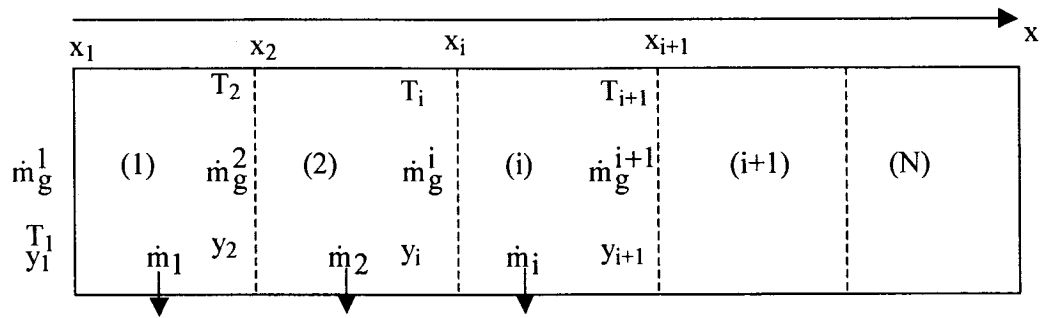


Figure 2-1: Stepwise computation of condensation rate in Vitse's model

(Vitse, 2002)

### 2.1.2 Dropwise condensation

Dropwise condensation will happen if the metal surface cannot be completely wetted by the condensed water. Rather than a continuous liquid film, droplets cover the surface. Based on their experimental study, many researchers (Rose and Glicksman; 1973) had pointed out that dropwise condensation is a random process, which was confirmed by our direct observations using a unique *in-situ* camera developed in our laboratory (Figure 2-2, Figure 2-3, Figure 2-4, and Figure 2-5)<sup>1</sup>.

<sup>1</sup> The pictures of the surface at the top of the line were taken by an *in-situ* camera, which was inserted into the bottom of the line. More detail can be found in our internal report (Singer et al. 2004-2007).

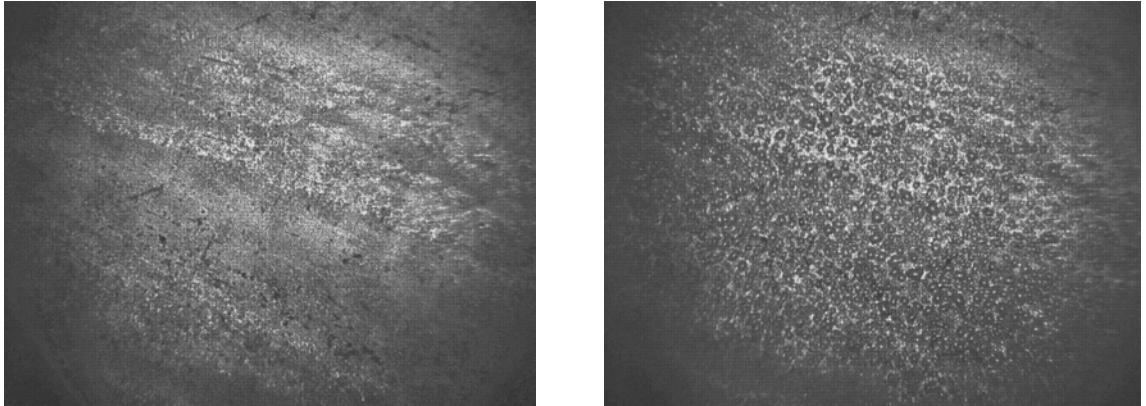


Figure 2-2: Dropwise condensation – Nucleation: Droplets are initiated on the surface

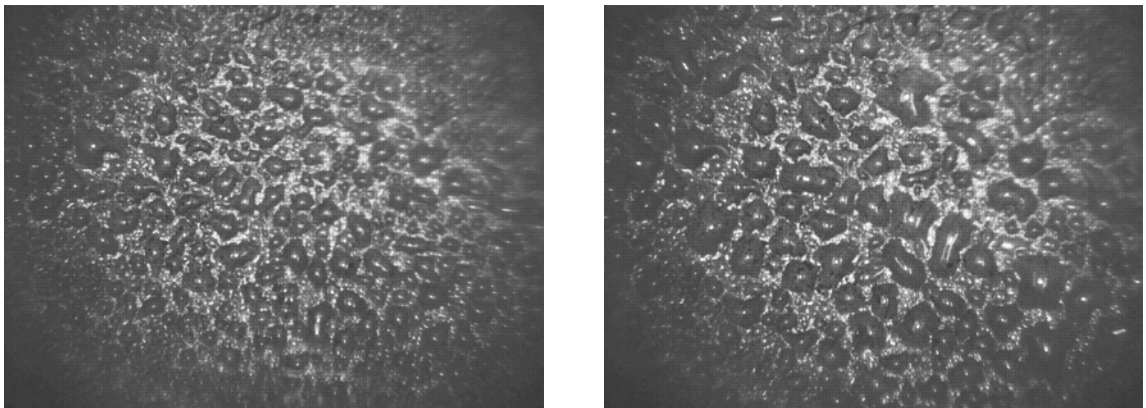


Figure 2-3: Dropwise condensation – Growth: Droplets grow up through direct condensation on the gas-liquid interface

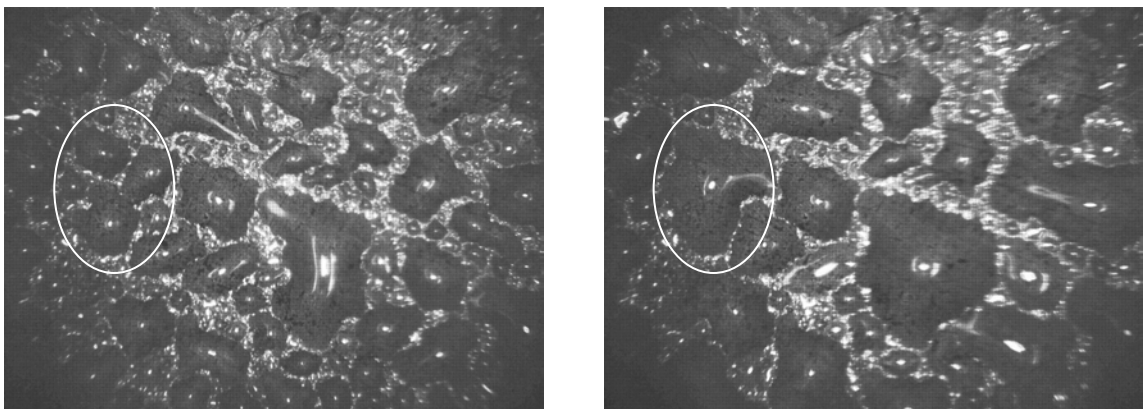


Figure 2-4: Dropwise condensation – Coalescence: Small droplets can join together and form a much bigger droplet

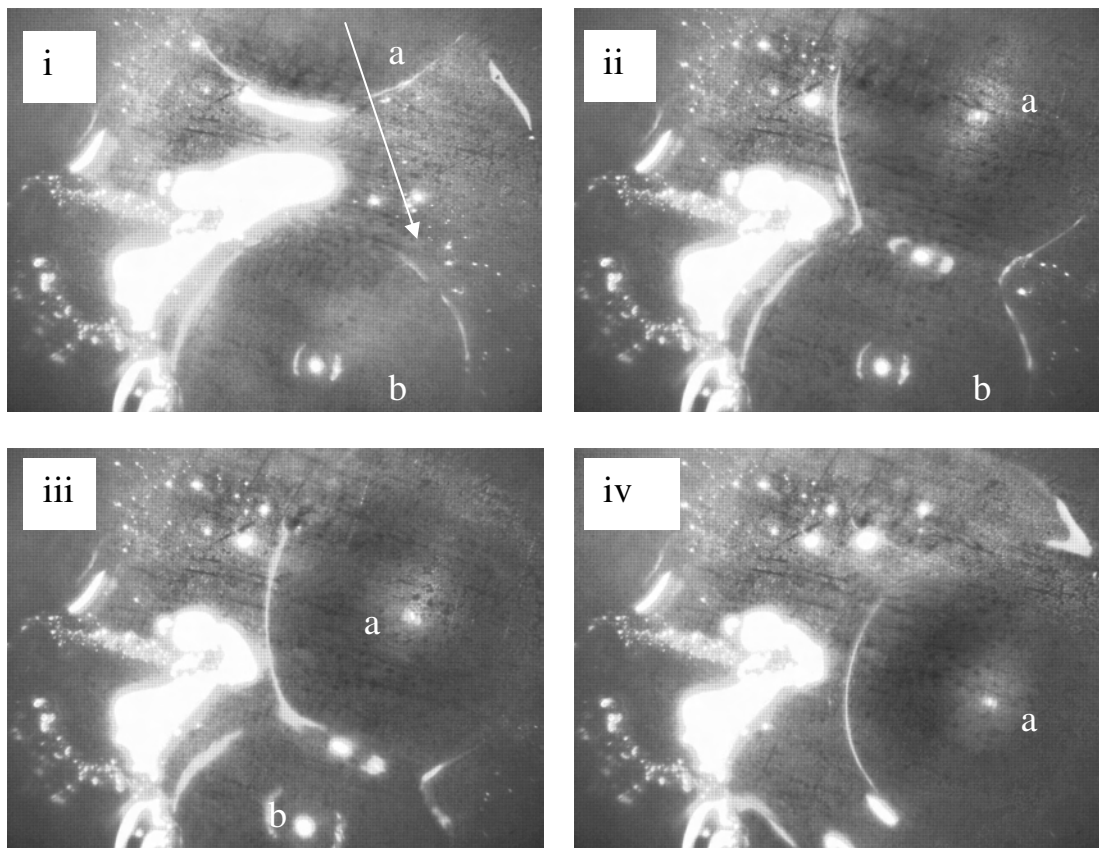


Figure 2-5: Dropwise condensation – Removal: A droplet (b) is swept by another droplet (a) coming from the upstream

The dropwise condensation process at the top of the line in wet gas conditions is one type of heterogeneous condensation in which liquid embryos first nucleate at the interface between a metastable saturated vapor and another solid phase (Figure 2-2). The size of the droplet will continuously increase as the vapor continuously condenses on the gas-liquid interface (Figure 2-3). Coalescence happens when adjacent droplets contact each other due to the continuous increase in droplet size (Figure 2-4). Therefore, the size of the water droplet would increase by means of either direct condensation of vapor or coalescence among adjacent droplets. When the gas velocity increases, the condensate

droplet might move along in the gas flow direction as a result of drag forces from the motion of the surrounding gas, continuously sweeping other droplets on its way forward (Figure 2-5). When a single droplet reaches its maximum size, it flows down along the inner surface of the pipe as a result of gravity. The surface area swept by the falling or moving droplets is now “clean” and new liquid embryos will form on those locations. This cycle of nucleation, growth, moving, and falling repeat itself in dropwise condensation at the top of the line.

Dropwise condensation in a pure and stagnant vapor system has already been well documented by many researchers since the 1970’s. Using a statistical analysis, Rose and Glicksman (1973) proposed that the distribution of all droplets was independent of time and site density and developed a time-averaged distribution equation for all droplets.

$$N(r)dr = \frac{n}{\pi r^2 r_{max}} \left( \frac{r}{r_{max}} \right)^{n-1} dr \quad (2-1)$$

where:

$N(r)dr$ : number of droplets at radius,  $r$ , over  $1 \text{ m}^2$  surface area,  $\text{m}^{-2}$

$n$ : exponent constant, typically as 1/3

$r_{max}$ : the maximum droplet radius, m

In Wu and Maa’s work (1976), a model of heat resistance through a single droplet was proposed including the resistances caused by the curvature of a droplet, interfacial resistance, and resistance of the liquid. Based on Wu and Maa’s work, Abu-Orabi (1998) calculated the heat flux in dropwise condensation through the integration of the heat transfer of each droplet (considering a minimum and maximum droplet radius). In

comparison with the experimental data, the results predicted by these models showed good agreement. But they were limited to pure and stagnant vapor systems.

Tanner et al. (1965) analyzed the influence of major parameters such as gas velocity and the presence of non-condensable gas in dropwise condensation. It was found that the existence of non-condensable gas in the gas phase had a huge effect on the heat transfer and mass transfer in the dropwise condensation process. Even a trace amount of non-condensable gas could dramatically decrease the heat transfer rate (Gener and Tien, 1990; Wang and Tu, 1988; Wang and Utaka, 2004). For example, it has been reported that 10% of non-condensable gas reduced the heat transfer rate by ~60% and 500 ppm of nitrogen gas in the vapor-ethanol mixture could reduce the heat flux by ~50%. However, the mechanism for the huge effect of non-condensable gas on dropwise condensation has not been reported. Moreover, as the gas velocity increases, the distribution of droplets and condensation pattern resulting from the enhanced droplet motion might be changed. Few reports in this area have been found.

Specific to wet gas pipelines, the dropwise condensation process is much more complicated than those previous cases since the water vapor fraction is very small when compared to the large amount of non-condensable and condensable hydrocarbons in the natural gas. Furthermore, the condensation pattern related to the droplet motion is particularly important due to the involvement of hydrodynamics in multiphase flow in these pipelines. As one of objectives for this dissertation, a mechanistic model of dropwise condensation will be developed to take into account these effects in a pipeline system.

## **2.2 Thermodynamics/chemistry in the droplets**

The condensed droplets are separated from the bulk liquid flow at the bottom of the line by the gas phase in the center of the pipeline. Both liquid droplet and bulk liquid flow are in equilibrium with the gas phase. Therefore, all volatile species, such as carbon dioxide, acetic acid, and hydrogen sulfide dissolve in the water and their concentrations can be calculated through Henry's law. After their dissolution in the droplets, volatile species further produce new components through dissociation or hydration.

Nordsveen et al. (2003) did a thorough survey on all possible chemical reactions which can happen in the oil and gas transportation pipelines. In order to incorporate these reactions into their mathematical model, the equations for the calculation of the reaction and chemical equilibrium constants had been either adapted from the open literature or estimated. Those chemical reactions and their constants can be found in Appendix I.

As a subproject of TLC JIP, a study of the chemistry and corrosivity of the condensate was done by Hinkson et al. (2008). The main goal of this study is to model the water chemistry in droplets at the top of the line according to the thermodynamic experiments. Particularly, the behavior of acetic acid in the gas/liquid equilibrium has been evaluated. It confirmed that the free acetic acid concentration in the liquid phase at both the bottom and top of the line depends on the pH.

## **2.3 Corrosion process at the top of the line**

TLC has caused dozens of failures in the last several decades. The first TLC case was identified in the Lacq sour gas field in France by Estavoyer in 1960. In his

observation, Estavoyer (1960) found that TLC only happened at stratified and stratified-wavy flow regimes. The proposed reason was that the injected inhibitor could not reach the top of the line in these flow regimes. Since then, a lot of studies have been done on identifying the TLC mechanism experimentally and theoretically.

### **2.3.1 Experimental and case studies of top of the line corrosion**

Olsen and Dugstad (1991) carried out a series of experiments to evaluate the effect of various important parameters in an autoclave and a flow loop. Among these parameters, temperature was thought to be the most important one because it determined if the formed film in the corrosion process was protective or not. In their experiments it was found that the iron carbonate film was very protective when temperature was greater than 70°C and the condensation rate was very low. Olsen and Dugstad (1991) believed that the condensation rate was not high enough to remove the produced iron ion quickly to avoid supersaturation in the condensed water. They proposed a critical condensation rate below which iron carbonate could precipitate due to high supersaturation. In their study, Olsen and Dugstad (1991) also investigated the influence of the gas velocity on TLC. It seemed that the gas velocity increased the corrosion rate and condensation rate as well. However, Olsen and Dugstad (1991) did not propose any correlation between corrosion rate and the parameters they studied. Furthermore, their experimental results in the flow loop were questionable since the condensation pattern could be totally different in their small scale loop (Internal Diameter = 16 mm) when compared to the condensation pattern in the real lines (typically 300 – 1000 mm ID).

Based on a case study, Gunaltun et al. (1999) pointed out the whole inner surface of the pipeline could be divided into three zones: 1) at the bottom of the line corrosion rate is very low due to the protection of inhibitors; 2) between 1 o'clock and 11 o'clock severe pitting corrosion is detected and iron carbonate film is present; and 3) at the sides of the wall (between 9 o'clock and 11 o'clock and between 1 o'clock and 3 o'clock) corrosion is very high and uniform. The author proposed that the continuous condensation on the existing droplets at the top of the line dilutes the iron concentration in the droplets. Due to the failure of applied empirical models in corrosion predictions of field cases, Gunaltun et al. (1999) realized that prediction of the critical condensation rate rather than the corrosion could be more important. However, Gunaltun et al. (1999) did not suggest how to determine this critical condensation rate.

Pots and Hendriksen (2000) designed a special experimental setup (shown in Figure 2-6) for their study on TLC. Their test matrix included all major well-known parameters such as gas temperature, condensation rate, and gas velocity. The main goal for this study was to provide experimental data for the development of a so-called iron supersaturation model (discussed in the next section of modeling). Although the work was remarkable for its new insights (a small scale experimental setup to mimic TLC in laboratories), many doubts remain. From the point view of dropwise condensation and associated hydrodynamics, it is highly questionable if the condensation and flow patterns on the coupon in their experimental setup did indeed reproduce real field conditions seen in the wet gas lines.

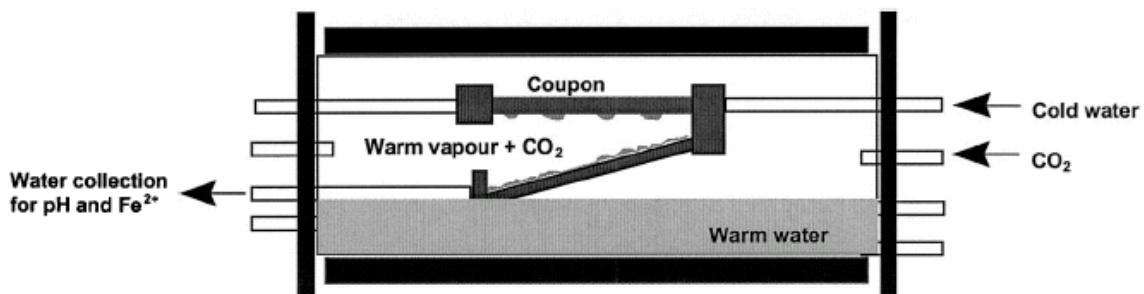


Figure 2-6: Experimental setup in Pots and Hendriksen's work (2002)

(Reproduced with permission from NACE International)

Vitse (2002) built a large scale flow loop (shown in Figure 2-7) to mimic the field pipelines with TLC issues. Through a double pipe heat exchanger, the condensation rate at the top of the line was adjustable. The effect of temperature, CO<sub>2</sub> partial pressure, condensation rate, and gas velocity was studied in short term experiments (up to 3 days). Experimental results "confirmed" the beneficial effect of the surface scale at high temperature and the existence of a *critical condensation rate*. However, the significance of the iron carbonate film was not clarified due to the limitation associated with the short exposure time. Furthermore, the test matrix in Vitse's study (2002) was limited in scope with only two levels of cooling studies (high cooling and very low cooling). Naturally, his justification for the existence of the so-called critical condensation rate is therefore doubtful.

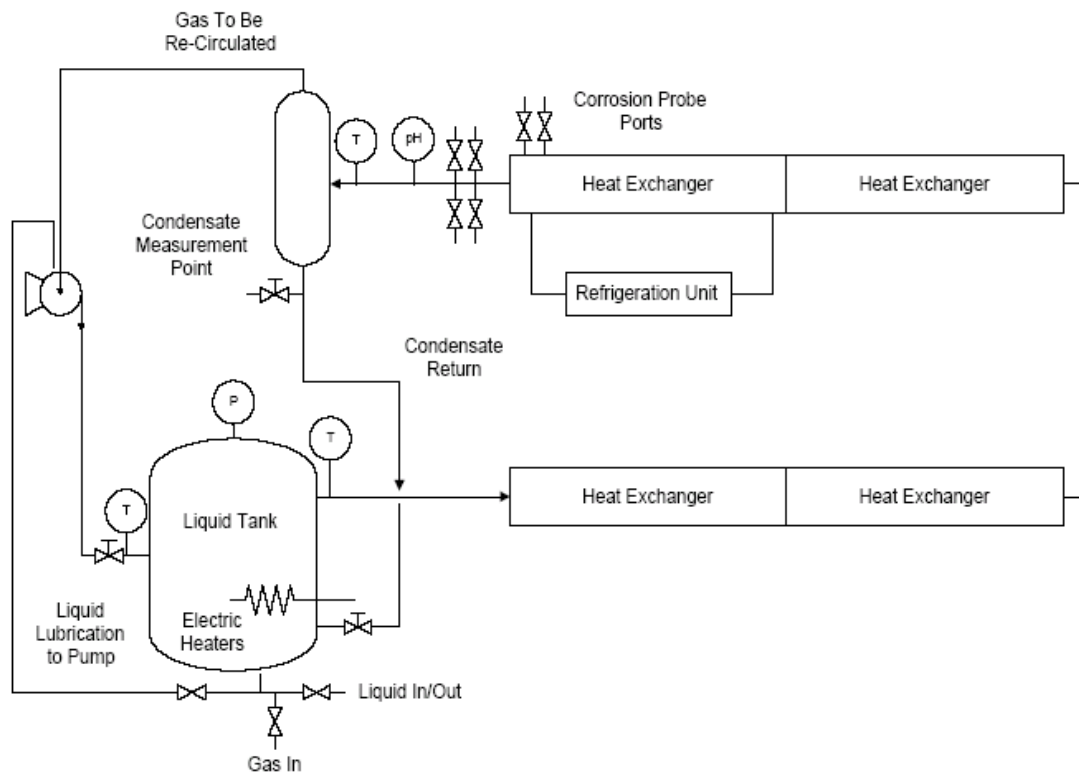


Figure 2-7: Schematic of the flow loop in Vitse's work

(Vitse, 2002)

Based on the preliminary results from Vitse (2002), a joint industry project (JIP) was initiated in 2003 to continue the study of TLC in large scale flow loop. Singer et al. (2004) and Mendez et al. (2005) completed some experiments in large scale flow loop (shown in Figure 2-7) to investigate the effect of acetic acid and the performance of a traditional inhibitor (mono-ethylene glycol) in TLC, which was included in Phase I of TLC JIP. However, the corrosion rates were not stable and the results of localized corrosion were not conclusive after several days of testing in their short term experiments. Therefore, Phase II was started to study the effects of all important parameters (identified in Phase I) in long term experiments. As a sub-project of Phase II,

the present study focuses on the effects of these parameters in sweet conditions (without H<sub>2</sub>S). The H<sub>2</sub>S corrosion is covered by another concurrent sub-project (Camacho, 2006).

### 2.3.2 Modeling of top of the line corrosion

In 1993 de Waard and Lotz (1993) developed an empirical correlation between corrosion rate and CO<sub>2</sub> partial pressure based on their experimental results at normal conditions. Correction factors were introduced to account for the effect of other factors, such as the corrosion product film, pH, fugacity, inhibitor, crude oil, flow velocity, and TLC. The correction factor  $F_c$  for TLC was suggested by de Waard and Lotz (1993) to be 0.1 when the condensation rate is lower than 0.25 mL/m<sup>2</sup>/s. Thus, the corrosion rate at the top of the line can be calculated through:

$$\log(CR) = \log(F_c) \times 5.8 - \frac{1710}{273 + T} + 0.67 \times \log(P_{CO_2}) \quad (2-2)$$

where:

$CR$ : corrosion rate at the top of the line, mm/yr

$T$ : temperature, °C

$P_{CO_2}$ : partial pressure of CO<sub>2</sub>, bar

Since the constant correction factor was used for all cases, it is not surprising that the predicted corrosion rate by de Waard's model (1993) dramatically deviated from the actual corrosion rate (Figure 2-8).

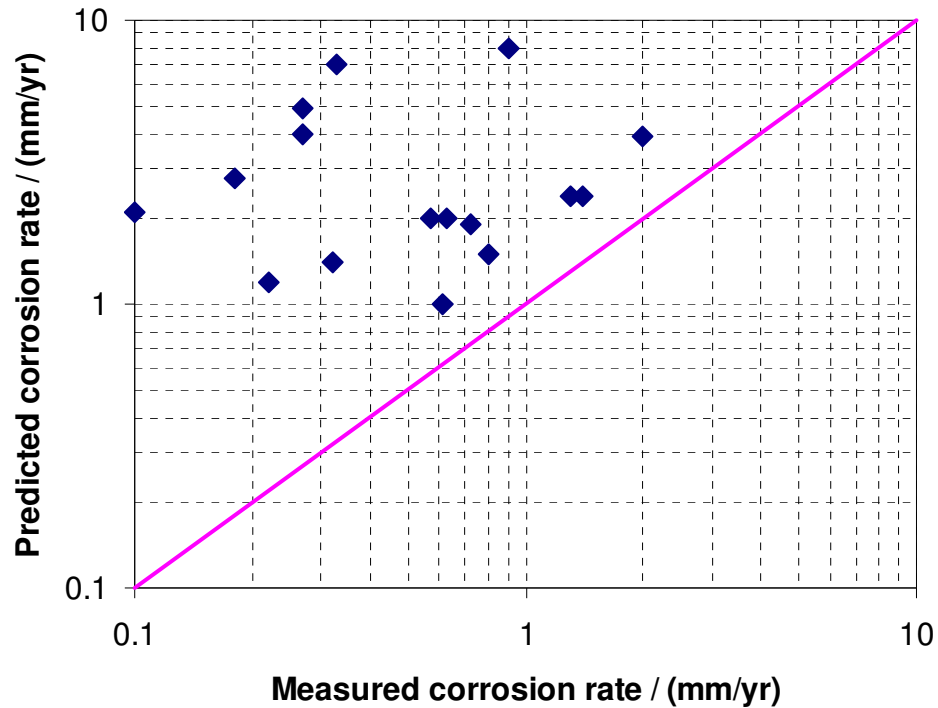


Figure 2-8: Comparison between experiments and de Waard's model (Adapted from Pots and Hendriksen, 2000)

Based on the iron discharge through the supersaturated condensed water, an iron supersaturation model was developed by Pots and Hendriksen (2000). In this model, corrosion rate was a function of the condensation rate and the iron concentration which was determined by supersaturation level:

$$CR = 2.26 \times 10^8 \times [Fe^{2+}]_{supersaturation} \times \frac{WCR}{\rho_w} \quad (2-3)$$

where:

$[Fe^{2+}]_{supersaturation}$ : iron concentration in the condensed water, ppm(w/w)

$WCR$ : condensation rate, mL/m<sup>2</sup>/s

$\rho_w$ : water density, kg/ml

The equation from Van Hunnik et al. (1996) for the precipitation rate ( $PR$ ) of the carbonate film was adopted to calculate the iron concentration in this study:

$$PR = \frac{A}{V} \times A_p \times \exp\left(\frac{-E_{activation}}{RT}\right) \times K_{sp} \times (s-1)\left(1 - \frac{1}{s}\right) \quad (2-4)$$

where:

$A_p$ : a constant

$E_{activation}$ : activation energy, kJ/mol

$R$ : gas constant, J/K mol

$A/V$ : ratio of surface to volume, 1/m

$K_{sp}$ : iron carbonate solubility constant,  $M^2$

$s$ : supersaturation ( $s = \frac{[Fe^{2+}][CO_3^{2-}]}{K_{sp}}$ )

$[Fe^{2+}]$ : ferrous ion concentration in the condensed water, mol/L

$[CO_3^{2-}]$ : carbonate concentration in the condensed water, mol/L

Although they paid a great deal of attention to the condensation process, Pots and Hendriksen (2000) did not provide an explicit procedure for accurate calculation of condensation rate. Without the reliable input of the condensation rate, the precise prediction of corrosion using their model is impossible.

Starting from his filmwise condensation model, Vitse (2002) also developed a quasi-mechanistic model for TLC. According to the mechanism of the filmwise condensation, a Nusselt film was thought to cover the whole metal surface. The thickness profile of the liquid film was stable and independent of time. The condensed water was

drained from the top by the flow along the circumference of the pipeline. Thus, the iron dissolved from metal surface was discharged only through the convection flow of condensed water along the circumference. After discretizing the whole film into control volumes, the mass balance equation below was applied to get the concentration profile in the film.

$$\frac{d(V \times C_{Fe^{2+}})}{dt} = CR \times A_{corr} - PR \times A_{precip} - WCR \times A_{cond} \times C_{Fe^{2+}} \quad (2-5)$$

where:

$t$ : time, s;

$C_{Fe^{2+}}$ : iron concentration, mol/L;

$A_{corr}$ : corroded area, m<sup>2</sup>;

$A_{precip}$ : precipitation area, m<sup>2</sup>;

$A_{cond}$ : condensation area, m<sup>2</sup>;

However, the corrosion rate predicted by Vitse's (2002) model was more than 10 times higher than the experimental result. In the model development, Vitse (2002) treated the precipitation only as a sink of iron ions (Figure 2-9). In fact, the protection effect of the scale formed on the metal surface is more important than the consumption of iron ions in the precipitation process. According to Nestic's paper (Nestic et al., 1996), a very protective film on metal surface could reduce the corrosion rate by one order of magnitude.

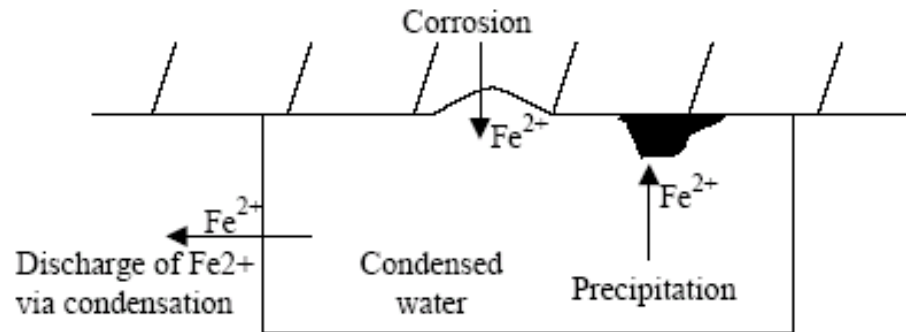


Figure 2-9: Mass transfer of ferrous ion in Vitse's model

(Vitse, 2002)

For all these models, condensation was assumed to be filmwise, which has been confirmed not to be commonly the case. In the reported field cases (Gunaltun et al., 1999), the morphology of the corroded steel surface at the top of the line indicated that dropwise condensation is more likely than filmwise condensation. Our own experimentation including in-situ visual observation (Figure 2-2 to Figure 2-5) and the coupon analysis (Figure 2-10) showed clear evidence of dropwise condensation. Finally it is known that the transition from dropwise to filmwise condensation occurs at much higher heat fluxes than are typical for TLC (Utaka and Saito, 1988). Therefore, a mechanistic corrosion model based on the dropwise condensation theory is required, and its development is one of the main goals of the present work.

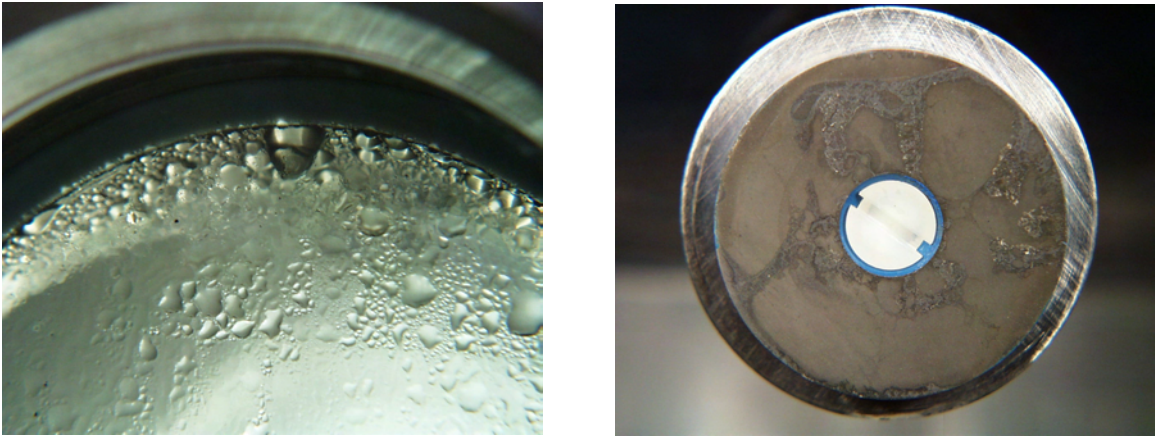


Figure 2-10: Evidence of dropwise condensation at the top of the line seen through a side window (left) and on an exposed weight loss coupon (right).

### 2.3.3 Mechanistic models for bottom of the line corrosion

On the other hand, the corrosion mechanism at the bottom of the line is well understood (at least in sweet environments) and readily modeled as described in a series of papers from Netic and his coworkers (Netic et al., 1996; Nordsveen et al., 2003; Netic et al., 2003; Netic and Lee, 2003). Based on their work, a mechanistic model including the electrochemistry, mass transfer in the solution, and film formation could precisely predict the corrosion rate at the bottom of the line.

In the present dissertation, a mechanistic model based on the dropwise condensation theory will be established. The chemistry in the droplets will be determined by gas-liquid equilibrium. Finally, the mechanistic model of corrosion from Netic's work (1996) can be adapted to consider the TLC scenario. The model will be verified through the comparison with experimental data collected in large scale loops over the last several

years. In addition, the model will be used to evaluate the effects of all important factors through simulations and parametric studies.

## **2.4 Droplet transport in gas-liquid two-phase flow**

Droplet transport is a major concern in various industries as it plays a very important role in heat and mass transfer, particularly in gas-liquid two-phase flow. In order to meet the specific needs in different applications, several parameters on liquid atomization, the droplet distribution, and deposition of the entrained droplets have been adopted to describe the behavior of droplet transport. However, all these phenomena heavily depend on characteristic conditions of multiphase flow. Two good examples are: 1) liquid atomization is linked to the dynamics of turbulent roll waves; and 2) deposition of droplets at the top of the line might result in the transition from stratified to annular flow. In fact, the study of droplet transport cannot be accomplished without the detailed understanding of hydrodynamics in multiphase flow.

### **2.4.1 Hydrodynamics in droplet transport**

In gas-liquid two-phase flow there are three major flow regimes. Their characteristics with corresponding flow conditions are described below respectively:

- **Stratified flow:** At low gas and liquid flow rates, the flow is stratified with gas at the upper level and the liquid at the lower level. At low velocities in stratified flow, the gas-liquid interface is smooth. With increased liquid velocity waves will be initiated at the gas-liquid interface.

- **Intermittent flow:** At higher liquid velocity, the crests of the waves can reach the top of the pipe, and intermittent flow ensues with liquid slugs connecting the top and the bottom of the line.
- **Annular flow:** When gas velocity increases but liquid velocity is kept low, the flow is annular. In annular flow, the liquid forms a film covering the whole pipe wall and the gas stays in the core.

These three flow regimes and their transition criteria have been extensively investigated. Transition criteria between major flow regimes were developed through both experimental and theoretical means. Among them, the transition from stratified to annular flow is of particular importance in the droplet transport. One of widely accepted mechanisms for this transition was developed by Milne-Thomson (1960) through an analysis of the hydrodynamic characteristics of the gas-liquid interface in the presence of instable waves. According to Milne-Thomson's analysis, transition from stratified flow to intermittent/annular flow will happen when waves can grow:

$$U_G > \left[ \frac{g(\rho_L - \rho_G)h_G}{\rho_G} \right]^{1/2} \quad (2-6)$$

where:

$U_G$ : gas velocity, m/s

$g$ : gravity, m/s<sup>2</sup>

$\rho_G$ : density of the gas, kg/m<sup>3</sup>

$\rho_L$ : density of the liquid, kg/m<sup>3</sup>

$h_G$ : gas height, m

Specifically, when the liquid at the bottom of the line is not able to form a liquid slug between the top and the bottom of the pipeline, the liquid in the wave will be pushed by the flowing gas to form a liquid layer around the pipeline and annular flow will ensue.

In 1987 Lin and Hanratty conducted a thorough study on the transition between stratified and annular flow in two flow pipelines (their internal diameters are equal to 2.54 cm and 9.53 cm respectively). In their study, stratified flow gradually transitioned to annular flow with increased gas velocity.

- At low gas velocity ( $U_{SG} = 6.4$  m/s), a stratified flow with two-dimensional roll waves ensued. No droplets were observed and the top wall of the pipeline was not wetted (Figure 2-11).
- At increased velocity ( $U_{SG} = 16$  m/s), although in stratified flow, some droplets were created through atomization. The direct evidence was that some droplets impinging on the top wall of the transparent pipeline were observed (Figure 2-12).
- As the gas velocity was further increased ( $U_{SG} = 21$  m/s), more droplets were deposited at the top of the line and water rivulets were formed through coalescence of deposited droplets (Figure 2-13).
- At highest gas velocity ( $U_{SG} = 31$  m/s), more water rivulets were created and joined a continuous liquid film, which covered the whole inner surface of the pipe. Eventually, annular flow was formed (Figure 2-14).

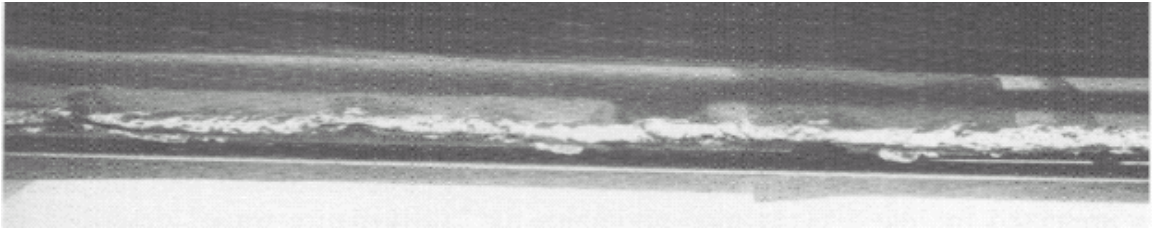


Figure 2-11: Stratified flow without atomization

( $ID = 9.53\text{cm}$ ,  $U_{SG} = 6.4\text{ m/s}$ , and  $U_{SL} = 0.076\text{ m/s}$ )

(Reproduced from Lin and Hanratty, 1987, with permission from Elsevier Limited )



Figure 2-12: Stratified flow with the deposited droplets at the top

( $ID = 9.53\text{cm}$ ,  $U_{SG} = 16\text{ m/s}$ , and  $U_{SL} = 0.076\text{ m/s}$ )

(Reproduced from Lin and Hanratty, 1987, with permission from Elsevier Limited )

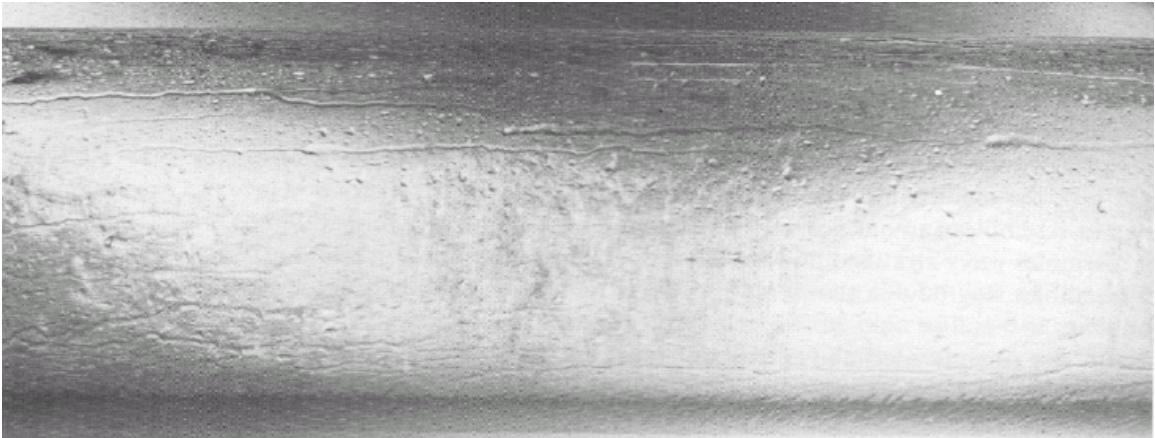


Figure 2-13: Stratified flow with water rivulets formed by the deposited droplets

( $ID = 9.53\text{cm}$ ,  $U_{SG} = 21\text{ m/s}$ , and  $U_{SL} = 0.076\text{ m/s}$ )

(Reproduced from Lin and Hanratty, 1987, with permission from Elsevier Limited )



Figure 2-14: Annular flow ( $ID = 9.53\text{cm}$ ,  $U_{SG} = 31\text{ m/s}$ , and  $U_{SL} = 0.076\text{ m/s}$ )

(Reproduced from Lin and Hanratty, 1987, with permission from Elsevier Limited )

Based on their experimental results, Lin and Hanratty (1987) proposed an alternative mechanism, entrainment-deposition, for the transition from stratified to annular flow.

They further pointed out that the dominance of either of these two mechanisms depends on flow conditions and pipeline diameter. When the pipeline diameter is large or liquid flow rate is less than 0.015 m/s in small pipelines, the entrainment-deposition mechanism is dominant. Unfortunately, they did not offer a criterion for their entrainment-deposition mechanism.

From the study of the flow regimes, droplet formation seems to be associated with the dynamics of waves at the gas-liquid interface. Hanratty and his coworkers (Andratos and Hanratty, 1987a; Andratos and Hanratty, 1987b; Hanratty, 1987 and Lin and Hanratty, 1987) extensively studied waves in gas-liquid two-phase flow. In their experiments various patterns from smooth surface, two-dimensional waves, three-dimensional waves, and roll waves to atomization were observed in sequence with increasing gas velocity. The initiation of droplets results from the combined effect of turbulent liquid and gas flows at the interface.

## **2.4.2 Onset of droplet entrainment**

### **2.4.2.1 Mechanisms of liquid atomization**

As discussed above, waves are formed at high gas velocity and become more turbulent as gas velocity increases further. At the gas-liquid interface, the interaction between the phases is so intense that the gravity and the surface tension are not able to keep the whole body of water in the waves in a continuous phase and parts of the liquid are torn from the liquid film by the high shear gas flow into droplets. Since the formation of droplets is very complicated, there is no unified mechanism which could explain all

phenomena found at different conditions. However, it is very clear that the turbulent force and surface tension control the process of droplet formation. As a physical property, surface tension, which is a weak function of temperature, gas composition etc., is almost constant at different flow conditions. By contrast, the turbulent force, heavily depending on hydrodynamics, is changed dramatically. The wave dimension and flow pattern around the wave decided by gas velocity, liquid velocity, etc. are key factors in mechanism determination.

Based on direct visual observations, four different mechanisms were proposed for droplet formation in liquid entrainment, which are described in detail (Hewitt and Hall-Taylor, 1974; Ishii and Grolmes, 1975):

- i) **Mechanism of bubble burst** (Newitt, 1954) (Figure 2-15i): When a bubble reaches the gas-liquid interface, the very thin liquid wall at the top of the bubble separating the bubble from the gas phase will be broken up by the striking of the moving bubble. Some fine droplets are formed from the liquid fragments. At the same time, a crater is left on the interface due to the disappearance of the bubble in the bulk gas. The liquid around the crater moves to the center of the crater and tries to fill the vacancy. Different liquid streams flowing from the edges of the crater collide in the center and consequently some droplets are produced. These droplets are thought to be the major source of liquid entrainment since their diameter can be as large as the order of 1 mm. Hewitt and Taylor (1974) further suggested that gas bubbles in the liquid phase could come from: 1) nucleation of

dissolved and/or produced gas in boiling process; 2) bubble occlusion in high liquid flow rate.

- ii) **Mechanism of tearing** (Figure 2-15ii): Roll waves formed in high turbulent flows look like hills on a flat base with a growing amplitude. When the height of these waves reaches a certain value, the drag force from the high shear gas flow is great enough to overcome the retaining force from the surface tension. Part of the liquid is torn off from the crest of the waves and entrained into the gas phase.
- iii) **Mechanism of undercutting** (Figure 2-15iii): Opposite to the second mechanism, the gas flow has a much greater effect on the base of waves rather than on the crest of waves in the undercutting mechanism. When the base is very thin, the connection between the wave and the bulk liquid is cut off by the flowing gas. The droplets formed from the wave fragments are thrown away in radial direction. The mechanism is strongly supported by live pictures from Lane's work (1951), in which an axial photographic camera was applied in a tube to record the whole process of droplet formation.
- iv) **Mechanism of impingement** (Figure 2-15iv): Roll waves are dynamic rather than static in two-phase flow. At its first half life, a wave grows up continuously toward the axis of the pipe with increasing amplitude. Either the second or the third mechanism is dominant. When waves reach the maximum height, the front part of waves will turn around and move back toward the bulk liquid. The impingement of waves on the bulk liquid could form small droplets, which are sent to the gas phase with the momentum from the collision.

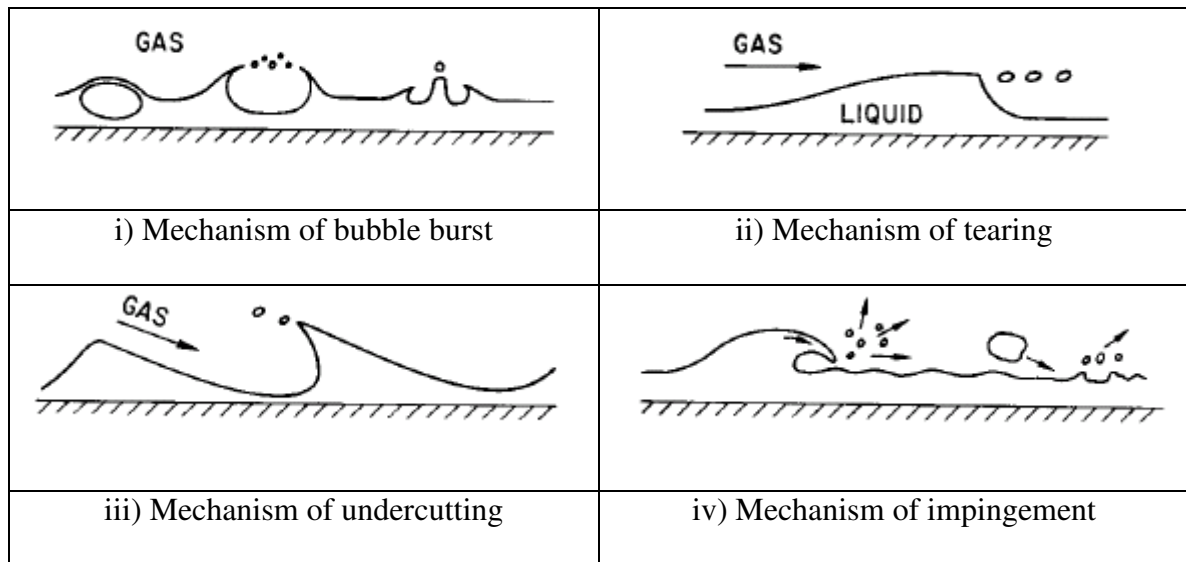


Figure 2-15: Atomization mechanisms

(Reproduced from Ishii and Grolmes, 1975 with permission from John Wiley & Sons)

Under given conditions, one or the other mechanisms is dominant. It is possible to switch from one dominant mechanism to another when condition is changed. Through the analysis of the turbulence, one can determine the transitions between different mechanisms.

#### 2.4.2.2 Experimental studies and empirical models

The first but significant piece of work on droplet entrainment was experimentally conducted by van Rossum in 1959. In his experiments, it was observed that atomization occurred at higher gas velocity than the gas needed to initiate a wave on the gas-liquid interface. When the liquid film was relatively thin, the critical gas velocity decreased with increased film thickness.

Steen (1964) investigated the effect of several important parameters: tube diameter, pressure, and surface tension in the atomization process. In his experiments, it was found that the tube diameter had limited effect on the critical gas velocity while the critical gas velocity was greatly decreased at higher pressure or lower surface tension. However, Steen used a problematic method to extrapolate his data, in which the measured velocity for the inception point was much greater than the actual value (Figure 2-16).

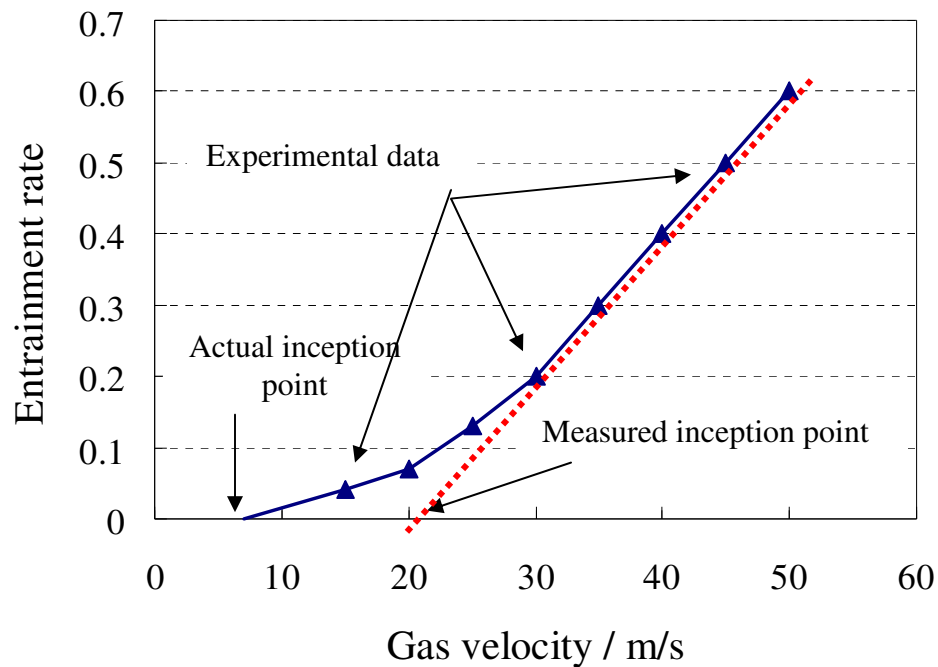


Figure 2-16: Linear extrapolation in Steen's data interpretation

Zhivaikin (1962) observed the onset of entrainment was changed at different flow orientations (concurrent flow, countercurrent flow, and inclined flow) in his experiments. Meanwhile, the author pointed out the turbulence of liquid flow at different liquid velocities was the key on the mechanism determination.

Before the mechanistic model was established, studies of liquid atomization were mainly conducted through the experimental approaches. A large range of experimental conditions had been covered in various experimental and analytical setups. In order to interpret the data, several different empirical models were concurrently proposed. In the review of all these empirical models for the onset of entrainment, huge discrepancies were found among them. One possible reason pointed out by Hewitt and Hall-Taylor (1974) was that the methods used for the determination of the droplet formation were different or even wrong. For instance, the linear extrapolation in Steen's experiments is erroneous. Furthermore, all these empirical equations can only be applied in the same range of experimental database. In order to solve these problems, a unified model from the mechanism of atomization is desired.

#### **2.4.2.3 Mechanistic models**

As mentioned above, four different mechanisms were proposed for the droplet formation. However, both bubble burst and impingement mechanisms are not applicable in a pipeline with TLC issues. Firstly, the bubble source in the liquid phase does not exist since condensation rather than boiling happens in wet natural gas pipelines and the rate of liquid flow (mainly from direct condensation) is very small when compared to the high production rate of natural gas. Secondly, the impingement is often a supporting role to other dominant mechanisms in droplet entrainment. Therefore, only mechanisms of tearing and undercutting are operative in our cases. Their relative importance depends on the flow conditions such as liquid flow rate and gas flow rate.

Some researchers (Hanratty and Engen, 1957; Hanratty and Hershman, 1961; and Brodkey, 1967) observed that roll waves with a large-amplitude in vertical downward flow vanished when the liquid Reynolds number was very low. Obviously, the potential supporting the growth of a roll wave was damaged by the undercutting of gas flow. A range of the liquid Reynolds number from 2 to 5 was suggested for the transition in vertical downward flow. Van Rossum (1959) and Zhivaikin (1962) found the similar phenomenon in horizontal and vertical upward flow when the liquid Reynolds number is around 160. After having studied all available experimental data, Ishii and Grolmes (1975) pointed out that the mechanism of undercutting was dominant when the liquid Reynolds number was less than a critical value (160 for horizontal and vertical upward flow; 2 for vertical downward flow) while the mechanism tearing controls the droplet formation at high Reynolds number ( $>160$  or 2). With this guidance, two different transition criteria and their application ranges were then developed for the onset of entrainment respectively.

### 1) Tearing model

Based on the mechanism of tearing, Zuber (1962) introduced a criterion to determine if a droplet can be torn off from the liquid:

$$F_{drag} \geq F_{\sigma} \quad (2-10)$$

where:

$F_{drag}$ : drag force from the gas flow, N

$F_{\sigma}$ : force from surface tension, N

When the correlations of these two forces, which depended on the gas and liquid flow rate, were substituted into the equations above, the onset of atomization could be predicted (Ishii and Grolmes,1975).

## 2) Undercutting model

Droplet formation by undercutting is very similar to the splitting of a droplet. In both scenarios, part of the liquid is separated from the bulk of the liquid by the flowing gas. Therefore, the mechanism of the droplet splitting can be applied to the droplet formation.

Hinze (1955) provided several basic types of deformation and flow pattern for the splitting of a droplet in the dispersion process. A large variety of mechanisms were derived from the combination of different deformation types and flow patterns. Of course all mechanisms could be analyzed through the investigation of the forces acting on an isolated droplet. For all cases involving the splitting of droplets, there should be a critical Weber number ( $We$ ), beyond which the external force is large enough to overcome the counter force from surface tension and a droplet with this size breaks up. The critical Weber number ( $We_c$ ) is a function of flow conditions as well as properties of the dispersed phase, which can be written as:

$$We_c = C[1 + \varphi(N_{visc})] \quad (2-14)$$

where:

$$C: \quad We_c \text{ at } N_{visc} \rightarrow 0$$

$\phi$ : a function to account for the effect of viscosity ( $\phi \rightarrow 0$  at  $N_{visc} \rightarrow 0$ )

In his study another dimensionless number, viscosity group ( $N_{visc}$ ), was defined to account for the effect of the viscosity of the dispersed phase.

$$N_{visc} = \frac{\mu_L}{\sqrt{\rho_L \sigma d_d}} \quad (2-15)$$

where:

$d_d$ : droplet diameter, m

$\sigma$ : surface tension, N/m

$\mu_L$ : liquid viscosity, Pa s

The constant C and the function  $\phi$ , which depend on flow patterns, can be determined only by specific experiments. Hinze (1955) gave three examples to get these critical Weber numbers. Among them “Breakup of a drop in an air stream” is particularly interesting, which could lead to a mathematical model for the mechanism of undercutting in the onset of atomization. In this situation, a criterion with a modified definition of Weber number could be established as:

$$We = \frac{\rho_G U_G^2 h_L}{\sigma} > We_c \quad (2-16)$$

where:

$h_L$ : liquid holdup, m

Meanwhile, van Rossum (1959) developed a simple correlation to calculate the film thickness. In order to calculate the liquid holdup an empirical equation was developed in his study. Ishii and Grolmes (1975) used another correlation established by Hewitt and Hall-Taylor (1974) and Hughmark (1973), which is:

$$\frac{h_L \rho_L}{\mu_L} \sqrt{\frac{\tau_i}{\rho_L}} = (0.5 \text{Re}_L)^{1/2} \quad (2-17)$$

where:

$\tau_i$ : interfacial shear stress, N/m

$\text{Re}_L$ : liquid Reynolds number

But it is still an empirical correlation, which has been abandoned for a long time since Taitel and Dukler (1976) developed a mechanistic model for the calculation of the liquid height. The improvement of the model's performance is expected if the latest result on hydrodynamics is incorporated.

### 2.4.3 Transition to non-stratified flow

About the transition from stratified to annular flow, two mechanisms were proposed by Taitel and Dukler (1976) and Lin and Hanratty (1987), respectively. In both mechanisms, waves are formed at high gas velocity and the atomization will start from turbulent waves when the gas velocity is further increased. Either waves (the wave-mixing mechanism) or deposited droplets (the entrainment-deposition mechanism) could wet the top of the pipeline to achieve annular flow.

The mechanism for the transition caused by instable waves is well documented and a mathematic model has been developed by Taitel and Dukler (1976). The detailed review of this work can be found in a previous section. By contrast, there was not a simple correlation, not to mention a well developed model for the entrainment-deposition mechanism. Most of the previous work focused on the entrainment rate in a stable annular flow and neglected the importance of the initiation of a film from the deposition

of entrained droplets at the top of the line. A few preliminary studies experimentally/theoretically (Lin and Hanratty, 1987; Baik and Hanratty, 2003) investigated the transition associated with a stable film at the top of the line. Although these can not directly result in mathematical models, their efforts (mentioned below and more detail in Chapter 5) are valuable for the development of such models.

Basically, droplet entrainment and deposition depend on the dynamic process of droplets as well as film characteristics. Various parameters such as the droplet size distribution, local droplet concentrations, and local droplet fluxes are very important to characterize the droplet dynamics. Among them, local droplet concentrations with a mean droplet diameter are particularly useful. Karabelas (1977) developed a mechanistic model to predict the droplet concentration profile based on the diffusion theory. Paras and Karabelas (1991) continued to work on that and offered a simplified equation:

$$\varepsilon \frac{dC}{dy} + u_T C = a \quad (2-19)$$

where:

$\varepsilon$ : eddy diffusivity, m<sup>2</sup>/s;

$u_T$ : terminal velocity, m/s

$a$ : a sink or source of droplets, kg/m<sup>2</sup> s.

When a variety of constants were carefully adjusted, the concentration profile predicted by the model could fit the experimental data very well. Pan and Hanratty (2002) pointed out that Paras and Karabelas' model (1991) could be further simplified if the constant  $a$  in the equation above could be neglected. Baik and Hanratty (2003) tried to correlate the film thickness and the deposition rate from the momentum balance on the film. They also

suggested a critical film thickness at the top of the line, beyond which annular flow ensues. However, their efforts on the theoretical approach did not provide a predictive criterion for the transition from stratified to annular flow.

A great deal of work has been done on the transition to stable annular flow. It is possible to predict the transition with reasonable precision through either the wave-mixing mechanism or the entrainment-deposition mechanism. However, the wetting of the top of the line happens at much smaller gas velocity than is needed for the achievement of stable annular flow. On the other hand, the models about the onset of atomization always under-predicts the critical velocity for droplet deposition. Furthermore, some correlations in the previous studies are either empirical or oversimplified. In this study, an “effective zone” with well defined boundaries by the updated mechanistic models for the onset of atomization and the transition from stratified to annular flow is established to predict if the droplet can be entrained and deposited at the top of the line.

## **2.5 Objectives**

Since the first TLC case was observed in an oil field, a number of studies have been accomplished in this area through case analysis, laboratory experiments, and modeling. All important parameters have been identified and their influences on TLC have been extensively investigated through various experiments for a large range of conditions. Some empirical and semi-empirical models have been developed to correlate the experimental data. However, all these studies could only provide a partial or even

inaccurate understanding for the mechanisms of TLC due to their limitations in either experimental methodologies or fundamental theories. For example, the condensation pattern in the experimental setups (autoclave, small scale loop, etc.) used in these studies is totally different from that in real gas lines. The corrosion rates were not stable and the results of localized corrosion were not conclusive in previous studies since most experiments lasted a maximum of 3 days. Neglecting the huge difference between different condensation regimes, the filmwise condensation theory was applied to model the condensation process at the top of the line, which has been proven by many direct or indirect evidences to be dropwise mode. In summary, TLC is still not predictable based on the currently available knowledge. Therefore it is impossible to effectively prevent TLC and related failures in the oil and gas industry.

In order to fully understand the mechanism and develop a prediction model for TLC, a joint industry project (JIP) was initiated at Institute for Corrosion and Multiphase Technology in 2003. As an important part of the project, the present dissertation will:

- investigate the influences of all important parameters (identified in short term experiments) and the surface films on TLC through long term experiments in large scale flow loop;
- model the dropwise condensation process through the heat and mass transfer theories and predict the condensation rate in wet natural gas pipelines by taking into account the effects of gas velocity, gas temperature, total pressure, and subcooling temperature;

- determine the condensation regimes through a force analysis on an isolated droplet and define the transitions of different condensation regimes in a condensation regime map;
- develop a mechanistic model for TLC by adapting the existing model for bottom of the line corrosion in a dropwise condensation scenario at the top of the line;
- design and build a TLC prediction software package with a user friendly interface including the numerical models for dropwise condensation, water chemistry, and corrosion at the top of the line to predict TLC risks in wet gas pipelines;
- examine the influence of droplet transport on TLC and determine if droplets can be entrained and then deposited at the top of the line by introducing an “effective zone” in a flow regime map.

## **2.6 Summary**

A thorough literature survey has been done to evaluate the strong and weak points of previous studies of TLC and droplet transport. It was found that there is a lack of fully understood mechanism for TLC and the possibility of effective droplet transport has not been examined. Therefore, an approach covering long term experiments, mechanistic models for condensation, chemistry, and corrosion, and droplet transport is needed, which was proposed in the present dissertation.

## **CHAPTER 3: EXPERIMENTAL STUDY OF TOP OF THE LINE CORROSION IN A LARGE SCALE FLOW LOOP**

### **3.1 Introduction**

In industry, the pipelines for oil and gas transportation are always large scale. In order to benchmark those corrosion cases in laboratories, various approaches have been attempted. Olsen and Dugstad (1991) conducted their experiments in an autoclave and small scale flow loop (Internal Diameter = 16mm). Pots and Hendriksen (2000) designed a special experimental setup (Figure 2-6) for TLC tests, in which the condensation was forced to happen at the outer wall surface of a pipe (the diameter of the pipe was not indicated in their work). However, the condensation pattern, which depends on surface orientation and flow conditions (discussed in Chapter 4), on either the inner surface of a small pipe or on the outer surface of any pipeline is totally different from the real one in field cases. In order to reproduce the conditions observed in the field cases, large scale flow loop (Internal diameter = 101.6 mm) was designed and built at Institute for Corrosion and Multiphase Technology (Vitse, 2002). In the Phase I of the TLC JIP, short term experiments (Singer, 2004 and Mendez, 2005) were carried out to evaluate the effect of various parameters. In the analysis of the experimental results, it was found that the corrosion rates were still not stable and the results of localized corrosion were not conclusive after several days of exposure in flow loops. Therefore, long term experiments were necessary and addressed in the Phase II of the TLC JIP. Furthermore, new analytic

methods were introduced to characterize the corrosion coupon for a better understanding of the corrosion behavior at the top of the line.

## **3.2 Experimental procedures**

### **3.2.1 Experimental setup**

The flow loop used in Phase I has been proven to be successfully mimicking the TLC conditions seen in field cases. The loop which was constructed in 2000 has been improved by numerous modifications. Some of major modifications include: the gas/liquid separator, the cooling system on the test section, the secondary test section, and the gas flow meter (Figure 3-1).

1. A gas/liquid separator was added between the tank and the test section to eliminate the entrained liquid droplets in the flowing gas, which are believed to interfere with the condensation process in the test section if they are deposited at the top of the line.
2. The cooling system for the test section was redesigned to achieve more uniform outer wall temperature distribution along the whole test section (Figure 3-2).
3. In order to obtain more experimental data in a long term experiment, another test section with eight ports for corrosion coupons was added to flow loop (Figure 3-2).
4. A gas flow meter was implemented to precisely measure the instantaneous gas velocity (Figure 3-3).

The main idea for the flow loop is that the produced water vapor with the gas mixture (carbon dioxide, nitrogen, acetic acid etc.) is pushed by the blower to flow along the test section, in which the condensation rate and pattern are set through by a cooling system to mimic real field conditions. The weight loss coupons, which are made of the same steel of the real pipelines, are installed in the test section to study the corrosion behavior at the top of the line.

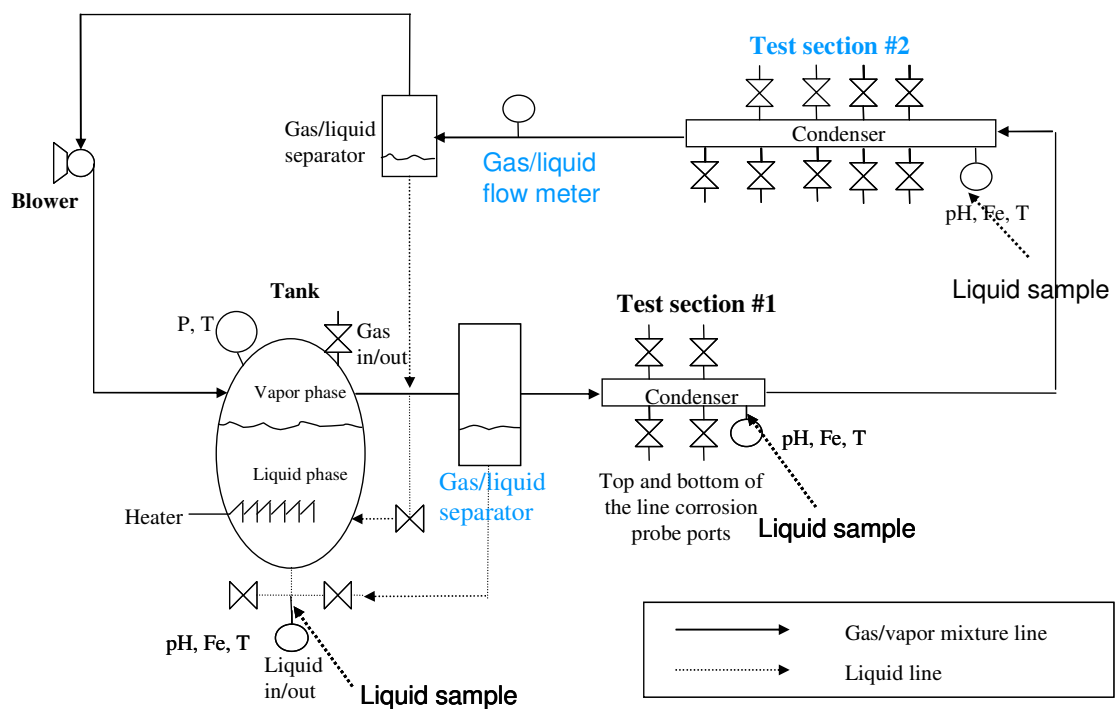


Figure 3-1: Schematic of large scale flow loop with modifications

(Credit M. Singer, Institute for Corrosion and Multiphase Flow, Athens, OH)

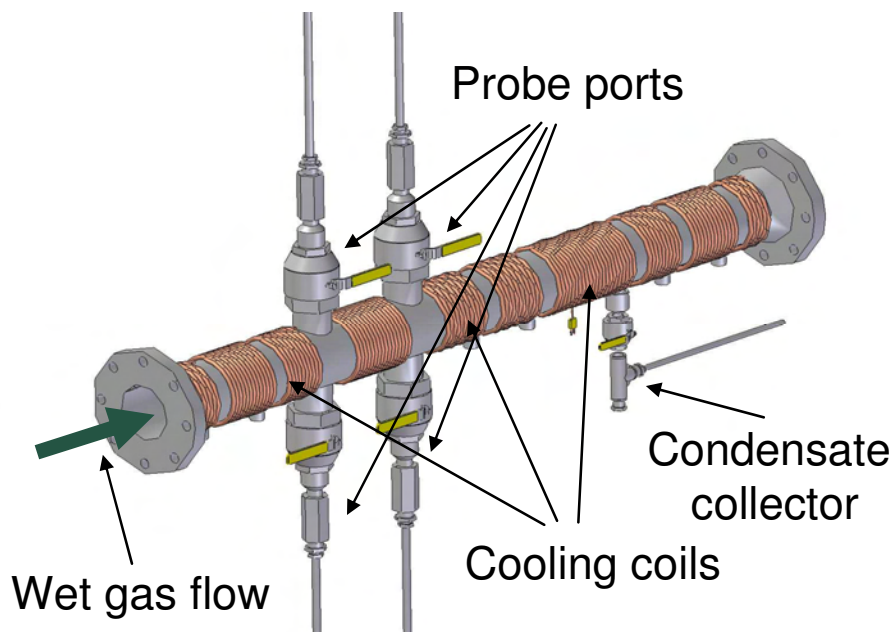


Figure 3-2: Schematic of the test section with a copper coil cooling system

(Credit J. Addis, Institute for Corrosion and Multiphase Flow, Athens, OH)

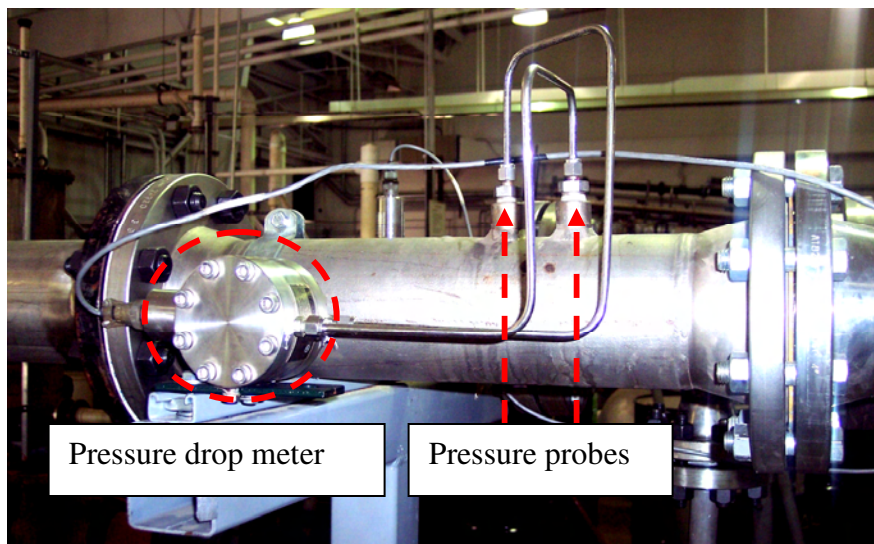


Figure 3-3: Gas flow meter

(Pressure drop along the pipe is measured to determine the gas velocity)

### 3.2.3 Materials and methods

**Weight loss coupon and corrosion measurement:** Carbon steels X65 and 1020 (their compositions are shown in Table 3-1) are the steels used to make the weight loss coupons in the experiments. All surfaces except one facing to the wet gas flow are coated with liquid Teflon (Figure 3-4) to avoid the interference of galvanic coupling between the coupon and the whole pipeline system (which is made of stainless steel). The corrosion coupons are polished by a series of sand papers with different roughness (150, 400, and 600 microns in sequence) before they are mounted to the ports in the test section with specially designed coupon holders (Figure 3-4). After having been removed from the test section, the corrosion coupons are washed using an alcohol (2-propanol) to prevent the oxygen contamination in the exposure to air. In order to dissolve and remove the corrosion product (iron carbonate) precipitated on the coupon surface, Clarke's solution (Table 3-2) is used in the post-processing before the coupons are weighed in a balance. Finally, the corrosion rate can be obtained through the equation below:

$$CR = \frac{m_b - m_a}{S_c \rho_{Fe}} \frac{1}{t_e} \times 365 \times 24 \times 3600 \quad (3-1)$$

where:

- $CR$ : corrosion rate, mm/year
- $m_b$ : mass of corrosion coupon before mounting to the test section, kg
- $m_a$ : mass of corrosion coupon after the treatment of Clarke's solution, kg
- $S_c$ : surface area of the corrosion coupon,  $m^2$
- $\rho_{Fe}$ : iron density,  $kg/m^3$
- $t_e$ : exposure time, s

Table 3-1: Chemical compositions of the carbon steels used in the experiments

Element	1020 Composition (%)	X65 Composition (%)	API 5L X65 Standard (%)	AISI 1020 Standard (%)
Al	0.003	0.032		
As	0.007	0.008		
B	0.0003	0.001		
C	0.19	0.13	< 0.26	0.13-0.23
Ca	0.001	0.002		
Co	0.008	0.007		
Cr	0.1	0.14		
Cu	0.13	0.131		
Mn	0.8	1.16	<1.40	0.30-0.60
Mo	0.035	0.16		
Nb	0.003	0.017		
Ni	0.13	0.36		
P	0.01	0.009	< 0.03	< 0.04
Pb	0.019	<0.001		
S	0.023	0.009	< 0.03	< 0.05
Sb	0.009	0.009		
Si	0.24	0.26		
Sn	0.023	0.007		
Ta	0.005	<0.001		
Ti	<0.001	<0.001		
V	0.06	0.047		
Zr	0.002	<0.001		
<b>Sum</b>	1.7983	2.358		

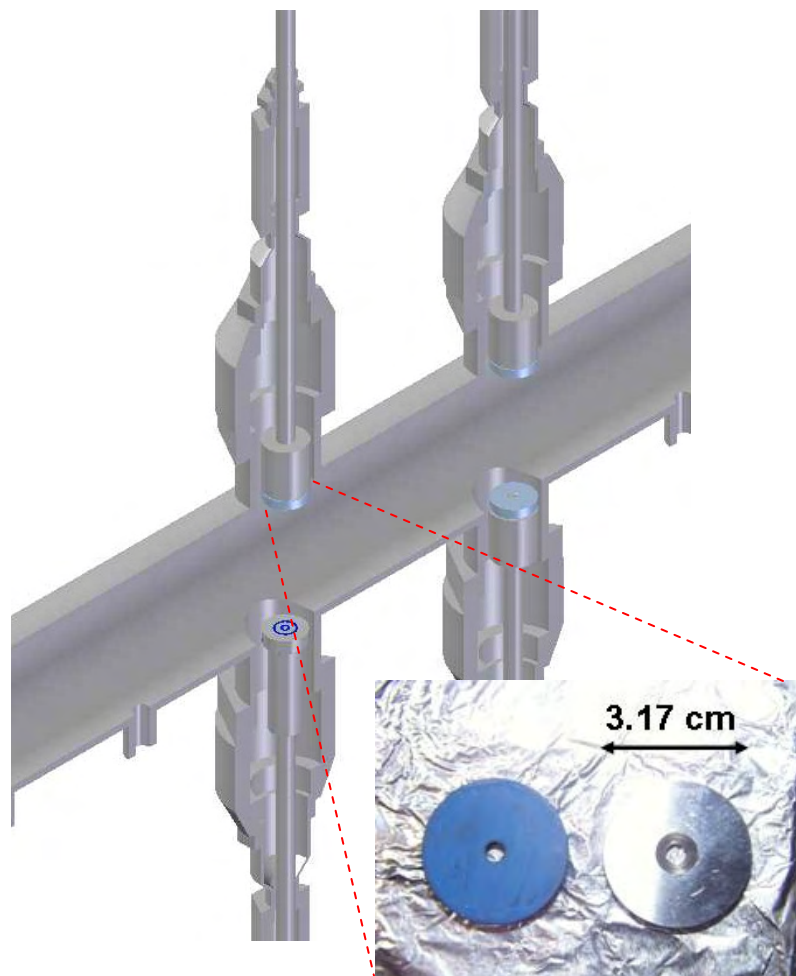


Figure 3-4: Weight loss coupons with a Teflon coating and their mounting to the test section

(Credit J. Addis, Institute for Corrosion and Multiphase Flow, Athens, OH)

Table 3-2: Composition of Clarke's solution

Component	Amount
Hydrochloric acid (HCl, sp gr 1.19)	1 litre
Antimony trioxide (Sb <sub>2</sub> O <sub>3</sub> )	20 g
Stannous chloride (SnCl <sub>2</sub> )	50 g

**Flow loop test:** De-ionized water is heated to the desired temperature and used as the vapor source for the system. Before starting the experiments, the whole system is de-oxygenated by bubbling CO<sub>2</sub> gas at the bottom of the tank. In order to achieve the desired condensation rate at the test section, cooling water flow in the copper coil around the test section is adjusted. A condensate collector is used to determine the volume of condensate produced in the test section. The condensation rate can then be calculated through:

$$WCR = \frac{V_0 - V_f}{S_t} \frac{1}{t_c}$$

where:

$WCR$ : condensation rate, mL/m<sup>2</sup>/s

$V_0$ : volume of liquid before the measurement, mL

$V_f$ : volume of liquid after the measurement, mL

$S_t$ : inner surface area of the test section, m<sup>2</sup>

$t_c$ : counted time, s

Four weight loss coupons are introduced in the test sections (2 at the bottom and 2 at the top). All these four are removed and replaced by new coupons after 2 days. After 2 weeks, one coupon from the top and one from the bottom are replaced. Therefore, there is indication about the evolution of corrosion rate and the corrosion product layer after 2 days, 1 week, 2 weeks, and 3 weeks. In order to have more repeated results in one test, another test section (Test section #2) with 8 ports was added to flow loop after Phase II of TLC project started. Therefore, in some experiments there are three repeated corrosion coupon weight loss measurements for one data point.

The pH in the tank was difficult to maintain as it always drifted up due to the accumulation of  $\text{Fe}^{2+}$  ion from the corrosion process in the solution. Dilute HCl solution was periodically injected to the liquid phase in the tank in order to stabilize the pH at 4.5. For monitoring purpose, the pH and  $\text{Fe}^{2+}$  concentration of the liquid samples collected from the tank and the test section (indicated in Figure 3-1) are measured when new coupons are inserted into flow loop.

**Coupon surface analysis:** Before the removal of the corrosion production layer, all coupons are analyzed by SEM (Scanning Electronic Microscope), EDS (Energy Dispersive Spectrometry), and IFM (Infinite Focus Microscope). From the SEM (JEOL JSM-6390 and Philips XL-30 ESEM) pictures the corroded surface of the coupons can be characterized and the pattern of the corrosion production layer on the surface can be visualized. As a conjunction device with the SEM, EDS (EDAX Genesis) is further applied to identify the composition of the corrosion product on the surface. In order to evaluate the localized corrosion behavior, the three-dimensional structure of the thin layer on the metal surface can be analyzed by IFM (Alicona).

### 3.2.2 Test matrix

In the previous studies in short term experiments (covered in Phase I of TLC JIP), six important parameters in TLC have been determined and well investigated:

- Gas velocity ( $U_{SG}$ )
- $\text{H}_2\text{S}$  partial pressure ( $p_{\text{H}_2\text{S}}$ )

- Un-dissociated acetic acid concentration (free HAc)
- Condensation rate ( $WCR$ )
- $CO_2$  partial pressure ( $pCO_2$ )
- Gas temperature ( $T_g$ )

Based on our understanding gained in short term experiments, a test with *baseline* conditions (Table 3-3), which represents the most common case in field (except total pressure) is done first. Then every other factor is tested through changing the conditions of this factor at three levels. The ranges of these factors are listed in Table 3-3, which cover most field pipelines' conditions (except gas pressure). Finally, the combined effect of two different factors is addressed through changing the conditions of these two factors simultaneously:

- Un-dissociated acetic acid concentration /  $H_2S$  partial pressure
- Condensation rate / Gas velocity
- Condensation rate / Acetic acid

The effect of  $H_2S$  was reported by Camacho (2006) and those tests for the combined effects were reported by Singer et al. (2007), otherwise all other effects by various factors are covered in the present dissertation. It should be stated that the experiments reported in the present dissertation were accomplished with equal contribution by the author and all other TLC team members (M. Singer and D. Hinkson). With some modifications, most of the following part is taken directly from a compilation report (Singer et al., 2007).

This dissertation presents the main findings obtained through the long term tests and provides important information about the influence of the main parameters on the general corrosion and the risk of localized corrosion at the top of the line.

Table 3-3: Baseline conditions in large scale loop

Variables	Value
Absolute pressure (bara)	3
CO <sub>2</sub> partial pressure (bara)	2
Gas temperature (°C)	70
Condensation rate (mL/m <sup>2</sup> /s)	0.25
Gas velocity (m/s)	5
Free HAc concentration in the tank (ppm)	0

Table 3-4: Ranges of test conditions in large scale loop

Variables	Range	
	Minimum	Maximum
Absolute pressure (bara)	3	8
CO <sub>2</sub> partial pressure (bara)	2	7
Gas temperature (°C)	40	85
Condensation rate (mL/m <sup>2</sup> /s)	0.05	1
Gas velocity (m/s)	3	8
Free HAc concentration in the tank (ppm)	0	1000

### **3.3 Results and discussions**

Different results are displayed for each experiment: corrosion rates (from the weight loss coupons), surface analysis (from SEM and IFM), and composition analysis (from EDS). The complete compilation of all SEM, EDS, and IFM results can be found in our internal reports (Singer et al., 2004-2007). For clarity reasons, only the corrosion rates obtained in all experiments are discussed in this dissertation. As an example, the baseline test is explained in detail using the surface and composition analysis.

#### **3.3.1 Baseline test**

##### **3.3.1.1 pH evolution in the tank and the test section**

In order to confirm that the pH in the tank has no effect on TLC in the test section, the pH and  $\text{Fe}^{2+}$  concentration in the tank and the test section are monitored and shown in Table 3-5. While the value of the  $\text{Fe}^{2+}$  concentration in the tank logically increases over time, the behavior of the  $\text{Fe}^{2+}$  concentration at the test section needs also to be explained. In the test section, liquid samples are taken downstream of the corrosion ports and it is believed that the liquid (which is supposed to be pure condensed liquid) is “polluted” by the iron released by the weight loss coupons. Therefore, it is almost logical to observe that  $\text{Fe}^{2+}$  concentration at the test section remains almost constant over time at a value of 11 ppm (as the corrosion rate at the bottom of the line is almost constant too). However, once the corrosion probes are removed from the test section at the end of the test, the  $\text{Fe}^{2+}$  concentration drops back to 3.3 ppm (compared to the 79 ppm in the tank). It shows that there is very little carry-over from the tank and that the pH of the liquid

phase at the test section does not depend on the pH in the tank. It should be emphasized that the water at the top of the line exclusively comes from the condensation process, which is separated completely from the bulk liquid at the bottom of the line. Therefore, the value of the pH in the tank should have no effect on TLC.

Table 3-5: Evolution of pH and the ferrous ion concentration in baseline test

Duration	pH (tank)	Fe <sup>2+</sup> in the tank (ppm)	Fe <sup>2+</sup> at the test section (ppm)
At start	3.94 <sup>a</sup>	0 <sup>b</sup>	0 <sup>b</sup>
After 2 days	4.6	18.7	0.43
After 9 days	4.9	35.8	8.36
After 16 days	4.6	33.7	11.38
After 23 days	4.8	79	11.16
After the removal of the probes	4.8	79	3.3

<sup>a</sup> the pH in the tank can be calculated through the equilibrium of water and 2 bar CO<sub>2</sub>;

<sup>b</sup> the concentration of ferrous ion in de-ionized water should be zero before the weight loss coupons are installed in the test sections

### 3.3.1.2 Corrosion rate results

Figure 3-5 presents the evolution of the general corrosion rates with time, both at the top and the bottom of the line. It should be mentioned that all the corrosion rates shown there have been normalized by the same arbitrary factor to protect the confidentiality of the raw data. The corrosion rates were measured using weight loss coupons made of API X65. At the top of the line, the average corrosion rate decreases

with time. It starts with at 0.6 and decreases gradually to reach 0.24 after 3 weeks. At the bottom of the line, the general corrosion rate seems to stay almost constant at around 3.5. The behavior of the corrosion rate with time is usually closely related to the type of corrosion product film formed on the coupon surface. For example, at the top of the line an iron carbonate film ( $\text{FeCO}_3$ ) formed from precipitation, which is proven to be very protective in previous studies, can slow down the corrosion process. It is highly possible for the formation of this type film at the top of the line where droplets of condensed liquid remain attached for a quit while, inducing super saturation of  $\text{FeCO}_3$  in the droplets. On the contrary, at the bottom of the line where a liquid stream is flowing, constantly renewing the liquid on the metal surface and preventing the solution from achieving super saturation of  $\text{FeCO}_3$ . An iron carbide film ( $\text{Fe}_3\text{C}$ ) made up of the inherent carbon structure of the corroded carbon steel may be detected on the surface. Since  $\text{Fe}_3\text{C}$  film is non-protective, the high corrosion rate will stay constant with time. The presence of different films and their protectiveness should be clarified, which are addressed in the surface and composition analysis through SEM, IFM, and EDS.

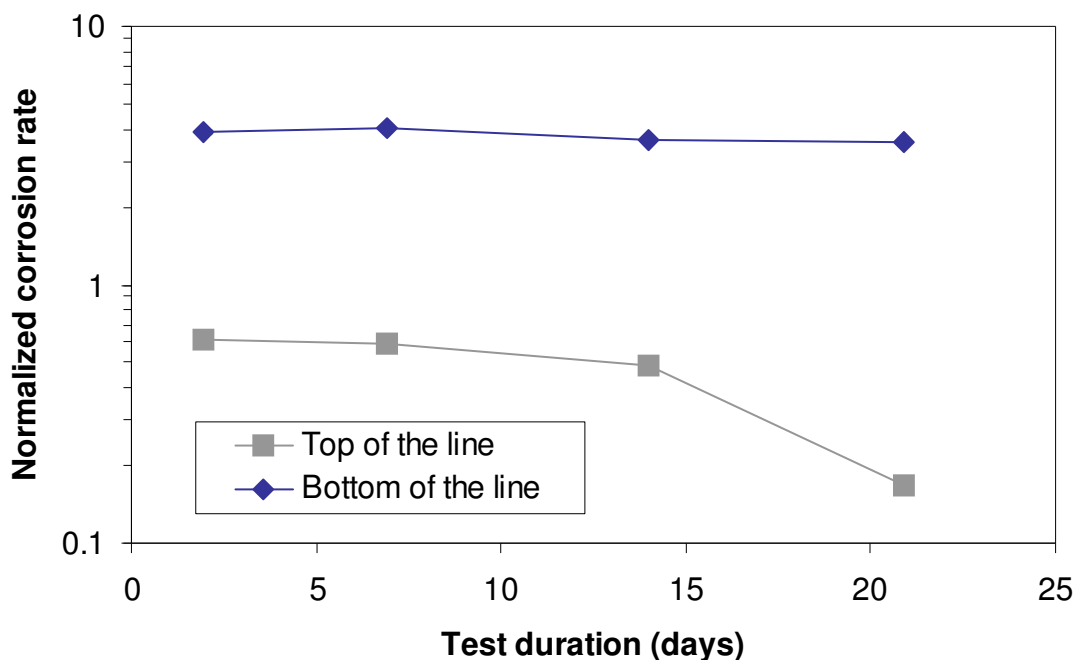


Figure 3-5: Normalized corrosion rate at the top and the bottom of the line in the baseline test ( $T_g = 70\text{ }^\circ\text{C}$ ,  $P_T = 3\text{ bar}$ ,  $pCO_2 = 2\text{ bar}$ ,  $WCR = 0.25\text{ mL/m}^2/\text{s}$ ,  $U_{SG} = 5\text{ m/s}$ ,  $Free\ HAc = 0\text{ ppm}$ )

### 3.3.1.3 Surface and composition analysis<sup>2</sup>

**Top of the line:** All the weight loss coupons were exposed to the corrosive flow in the flow loop for 2, 7, 14, and 21 days respectively. After they were removed from the loop (shown in Figure 3-6) digital pictures were taken immediately. It can be seen that the corrosion product layer is present on the steel surface and appears in all coupons as a grey layer. Some rounded shapes visible on the surface of the steel imply the presence of droplets of condensed liquid attached to the metal surface for a long amount of time. This

<sup>2</sup> The figures related to the surface analysis are presented at the end of this section for clarity reasons.

observation is typical for top of the line experiments. As shown in Figure 3-6, this unique characteristic in TLC is more evident with the increased testing time, which is probably caused by the pattern of the corrosion process under dropwise condensation. In dropwise condensation the formed droplets stay at the original places for a long period of time (when the renewal frequency is low). Corrosion product can continuously accumulate under the droplets due to the high level of supersaturation in the stagnant droplets, which then leads to the modification of the surface characteristics (color, structure, surface roughness etc.). Since some control parameters such as surface tension, which are responsible for the motion of droplets, heavily depend on the surface conditions, the presence of corrosion product film can further change the residence time of droplets on the metal surface and the droplet renewal pattern (location of the formation of a new droplet once an old one detached due to gravity forces). It also suggests that the residence time of a droplet at a specific location at the top may be very long, probably even weeks if the test duration and condensation rate allow it.

The SEM analysis is presented coupon by coupon from Figure 3-7 to Figure 3-10. Crystals can be found on the metal surface of all coupons, which are identified by EDS to be  $\text{FeCO}_3$ <sup>3</sup>. In relative low gas velocity (5m/s), droplet can attach to the metal surface for enough time to achieve the preference conditions of forming a  $\text{FeCO}_3$  film under the droplets. With testing time, the  $\text{FeCO}_3$  film becomes more and more uniform and dense macroscopically. Droplet-shape features are also observed in the SEM pictures and the corrosion product layer seems to be denser at the center of the features than on the side

---

<sup>3</sup> The corrosion product is identified to be  $\text{FeCO}_3$  according to its elemental composition provided by EDS. In a typical EDS spectrum of  $\text{FeCO}_3$ , only those peaks corresponding to three elements (carbon, oxygen, and iron) are present

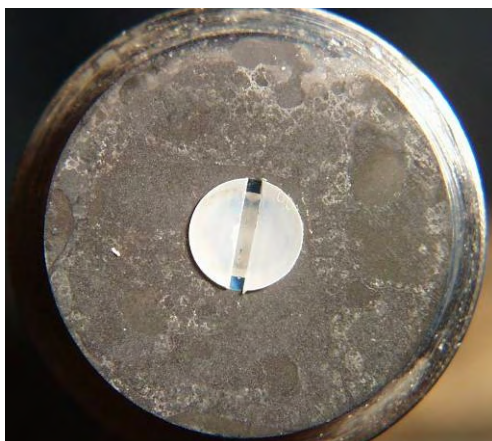
(Figure 3-7a). When testing time is short (less than 7 days), localized corrosion is not evident. However, localized corrosion is pronounced with increased testing time. As shown in Figure 3-9 and Figure 3-10, a number of pits (a common type of localized corrosion in TLC) were observed on the coupon surface in long term experiments (14 and 21 days respectively). After the removal of the corrosion product layer, the pits and their depth could be determined in coupon surface profile (Figure 3-11). It is observed that localized corrosion is not very serious in the baseline test if the edge effect is excluded.

**Bottom of the line:** Figure 3-12 shows pictures of the weight loss coupons taken immediately after their removal from the loop. It has been seen that a thick but porous layer is always present on the coupon surface. The cracks of surface film shown on Figure 3-12b, c, and d are due to a thermal expansion effect in the dehydration process. SEM pictures and EDS analysis are shown in Figure 3-13 to Figure 3-16 for all the test durations (2, 7, 14 and 21 days). The amorphous layer present on all coupon surfaces is identified to be iron carbide ( $\text{FeC}_3$ )<sup>4</sup> by EDS analysis.

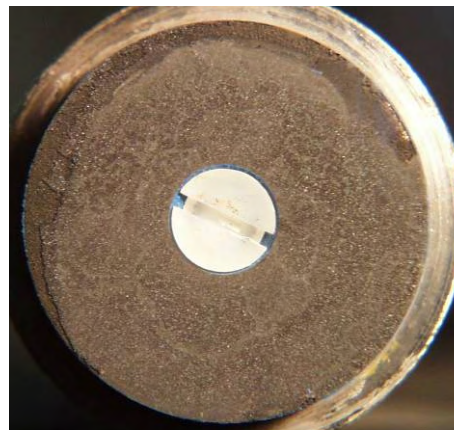
### Surface analysis (Pictures)

---

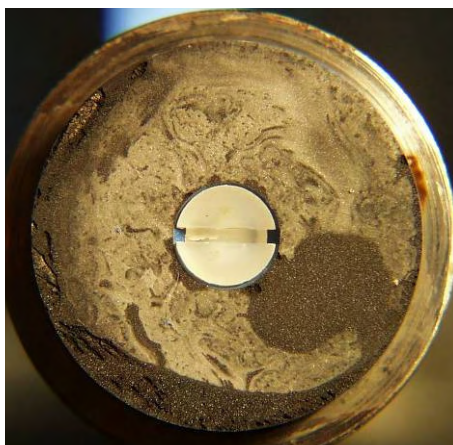
<sup>4</sup> In Table 3-1, it is known that carbon steel is a mixture of various elements, which constitute crystal lattices. Most iron atoms in the lattice dissolve in the liquid solution after the degradation due to corrosion. Although the remaining iron atoms and all atoms of other elements (C, Mn, Cr ...) are left on their original places, the lattices lose their characteristic properties. This remainder is so-called  $\text{FeC}_3$ , which can be identified if various elemental peaks can be found in the EDS spectrum.



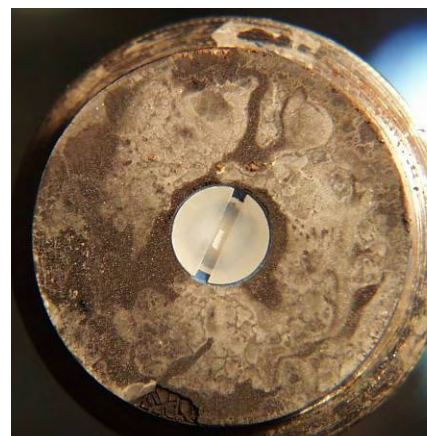
(a) Test duration: 2 days



(b) Test duration: 7 days



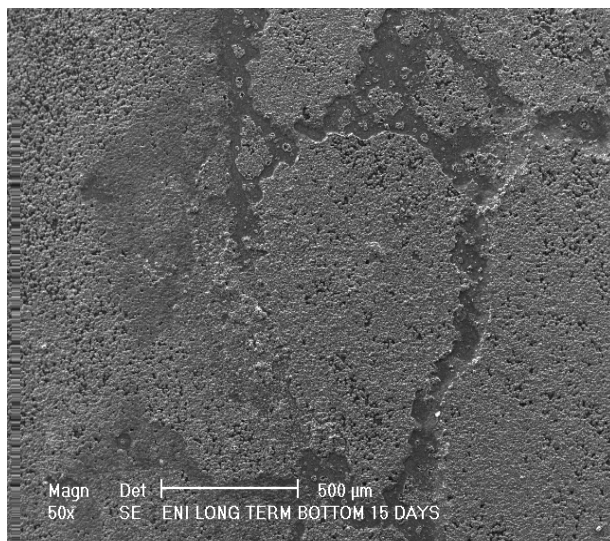
(c) Test duration: 14 days



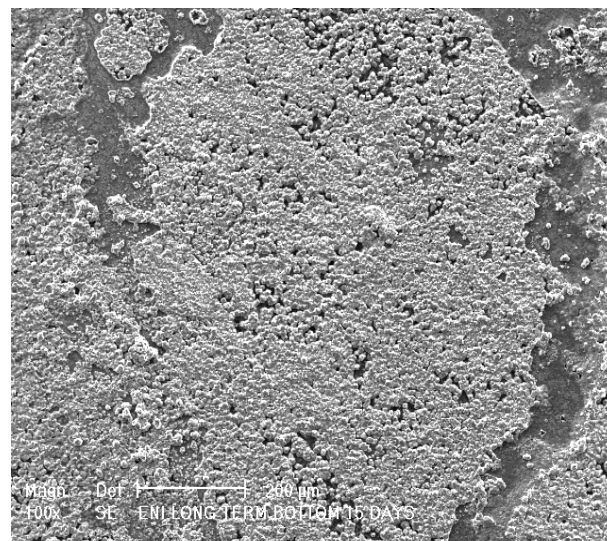
(d) Test duration: 21 days

Figure 3-6: Baseline – Top of the line

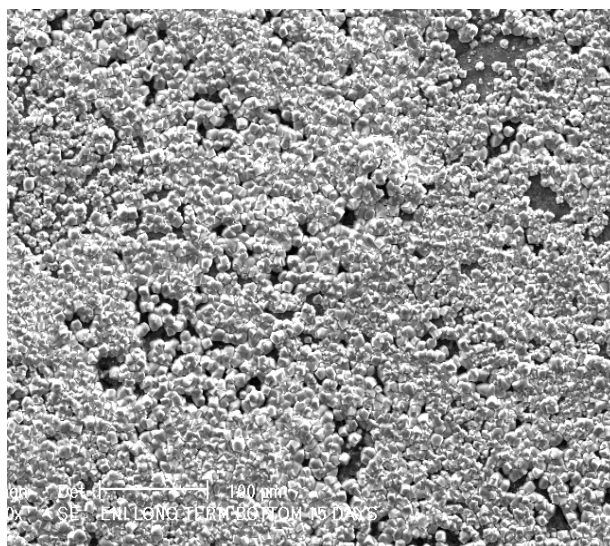
Weight loss coupons before the removal of the corrosion product layer



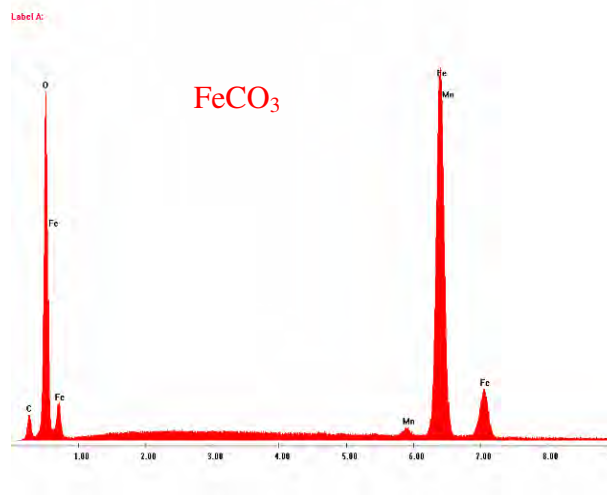
(a) SEM X50



(b) SEM X100



(c) SEM X200

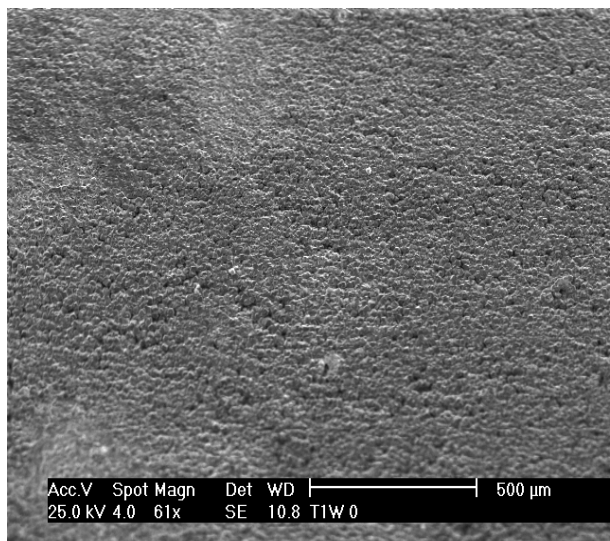


(d) Composition of the corrosion product

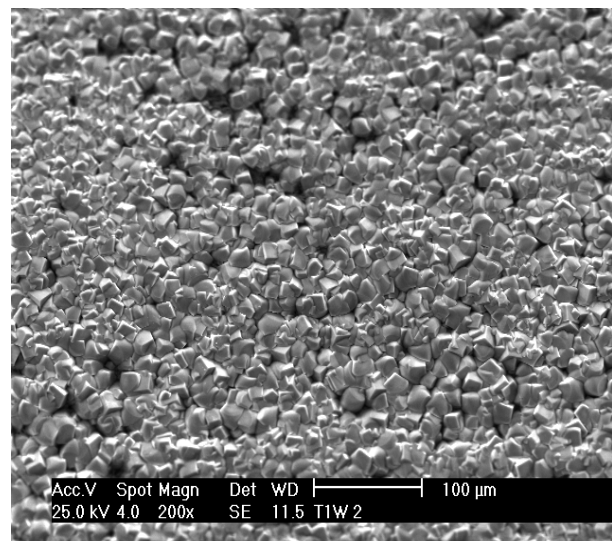
Figure 3-7: Baseline – Top of the line – Test duration: 2 days

SEM and EDS analysis of the corrosion product layer on the coupon surface

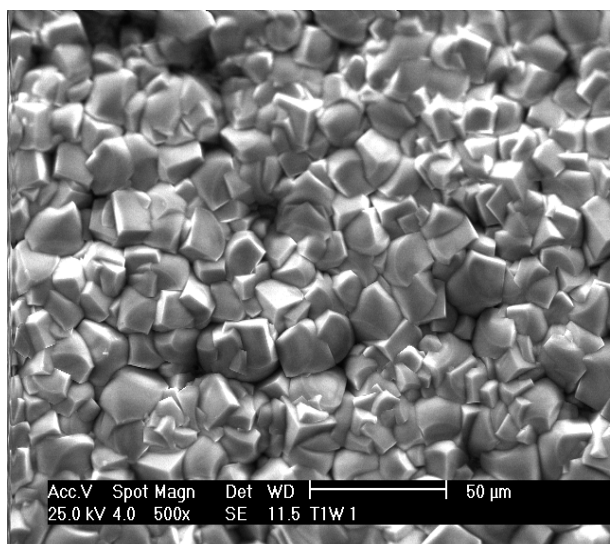
(The spreading of the  $\text{FeCO}_3$  film through precipitation under the droplets)



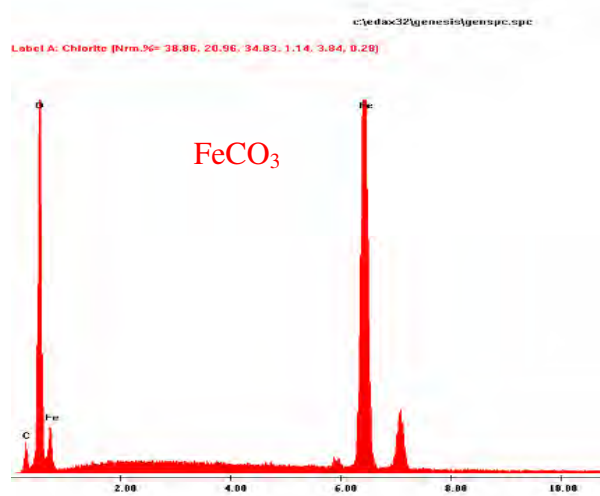
(a) SEM X61



(d) SEM X200



(c) SEM X500

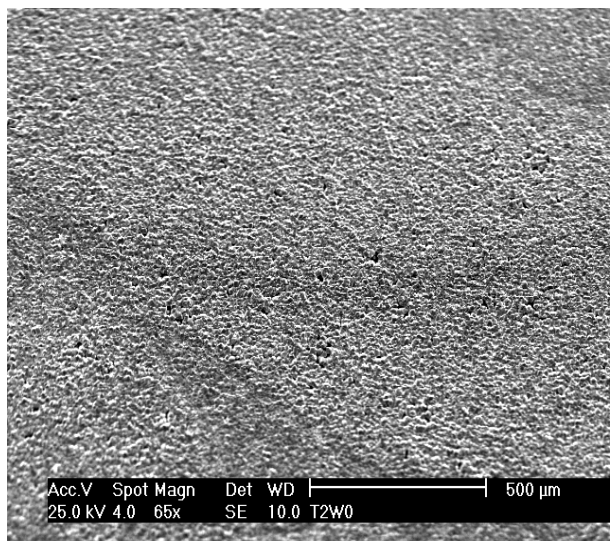


(d) Composition of the corrosion product

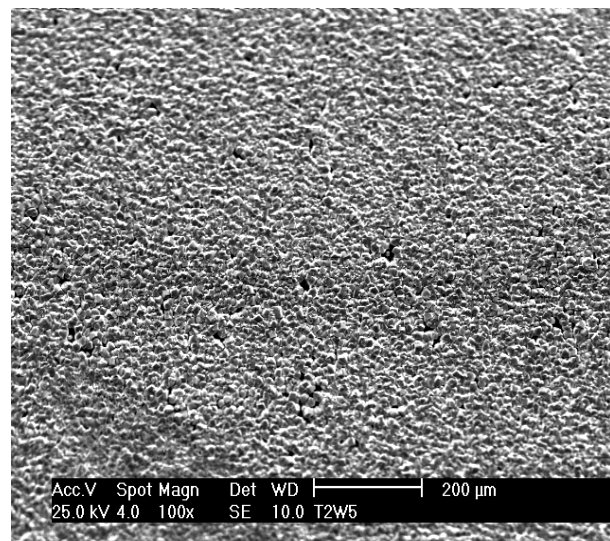
Figure 3-8: Baseline – Top of the line – Test duration: 7 days

SEM and EDS analysis of the corrosion product layer on the coupon surface

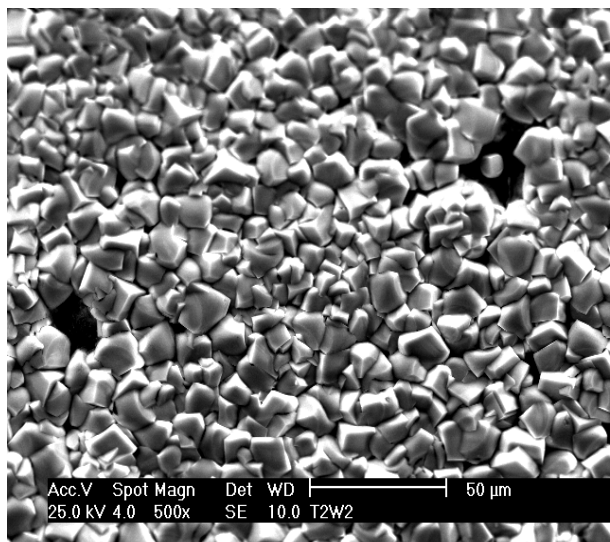
(A dense film with a number of defects where localized corrosion can happen)



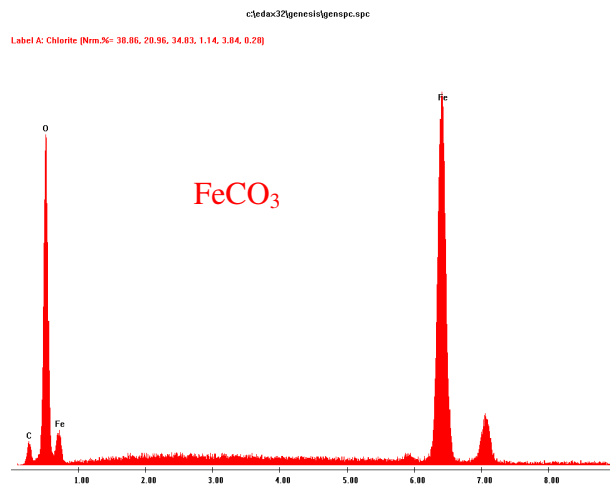
(a) SEM X66



(b) SEM X100



(c) SEM X500

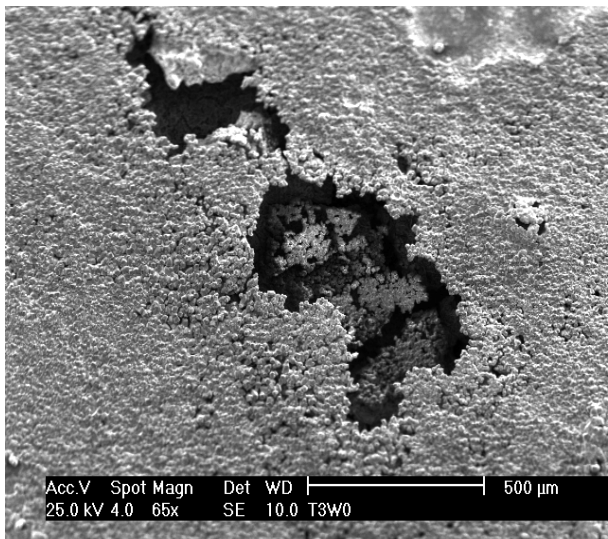


(d) Composition of the corrosion product

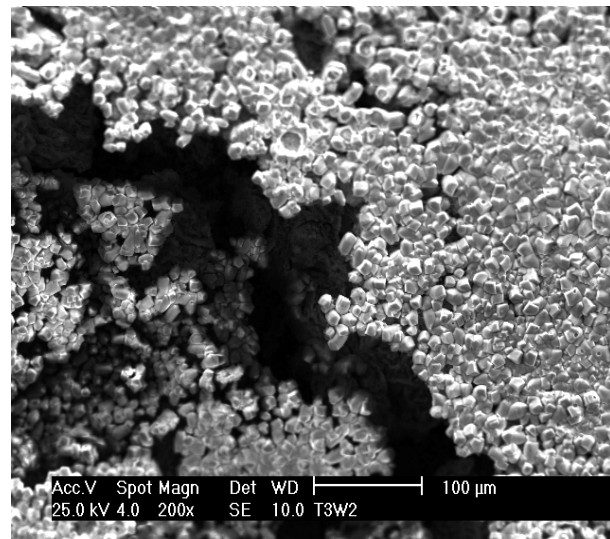
Figure 3-9: Baseline – Top of the line – Test duration: 14 days

SEM and EDS analysis of the corrosion product layer on the coupon surface

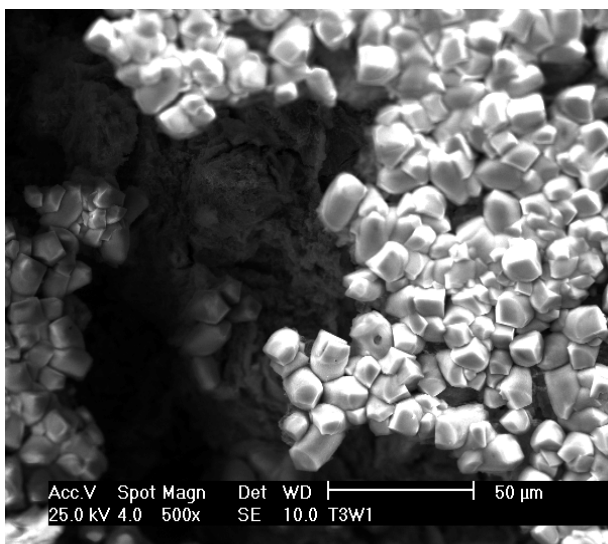
(A dense film with a number of defects where localized corrosion can happen)



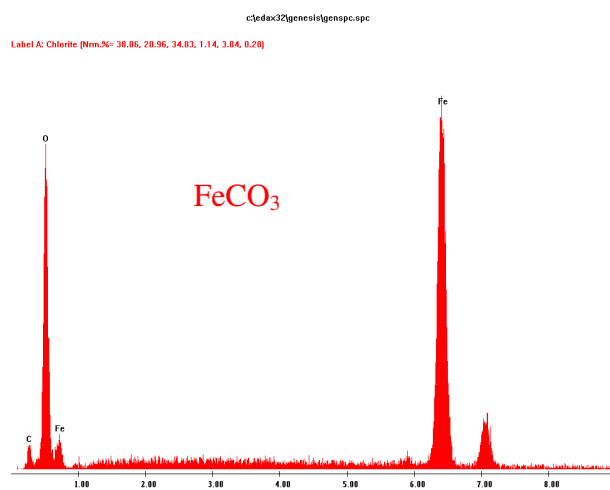
(b) SEM X65



(b) SEM X200



(c) SEM X500



(d) Composition of the corrosion product

Figure 3-10: Baseline – Top of the line – Test duration: 21 days

SEM and EDS analysis of the corrosion product layer on the coupon surface

(Film breakdown due to corrosion underneath the film in the defects)

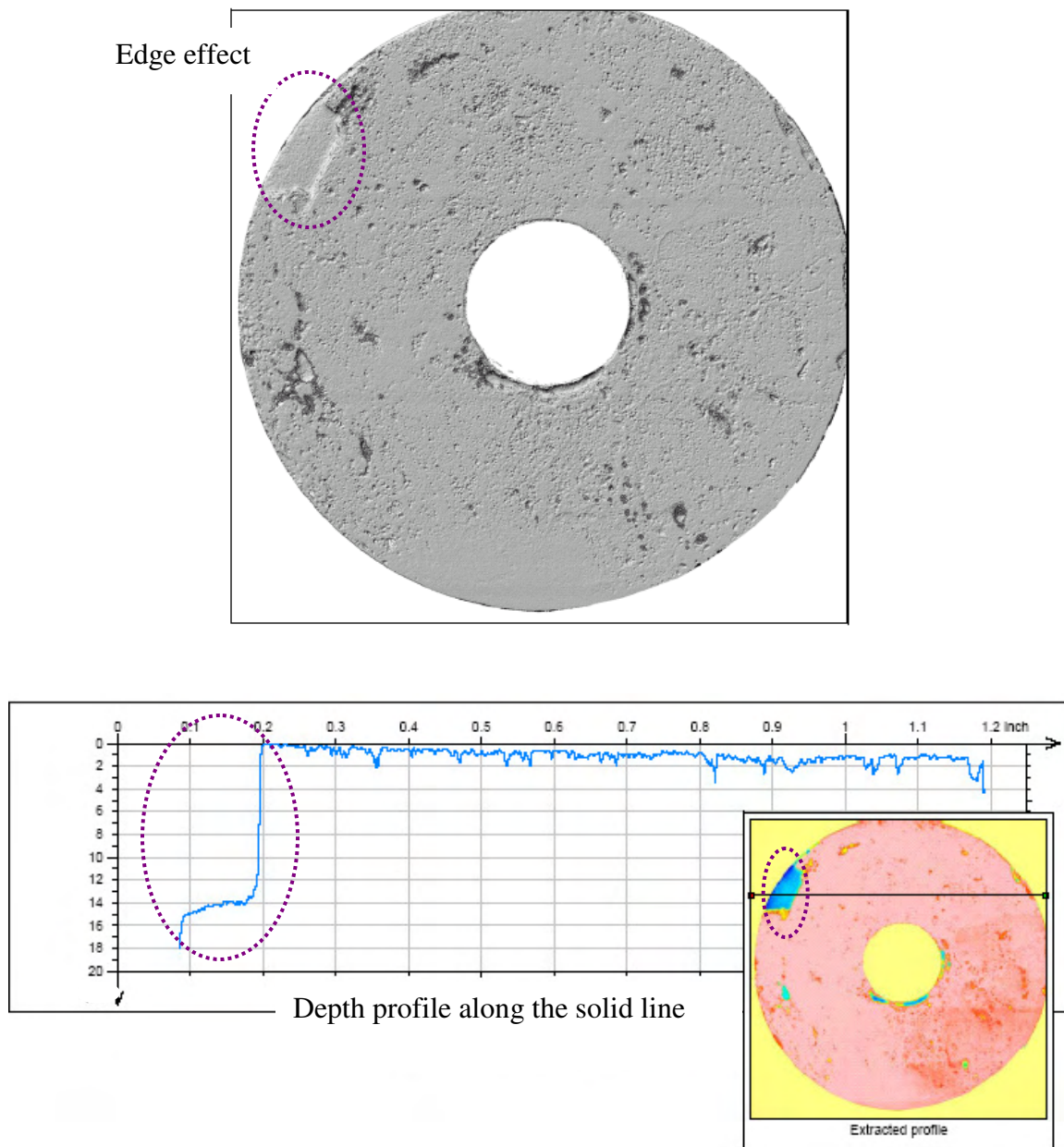
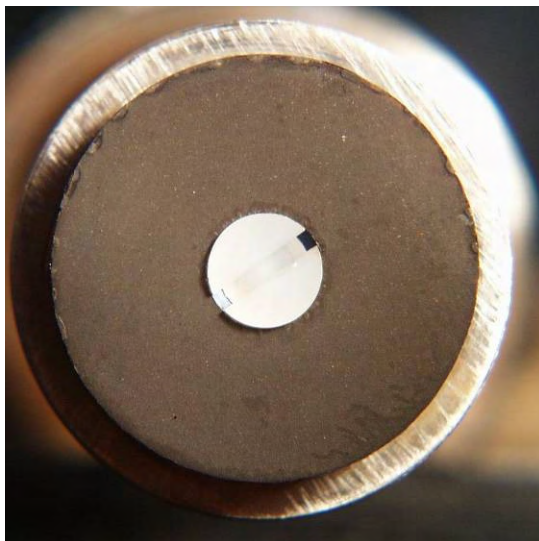
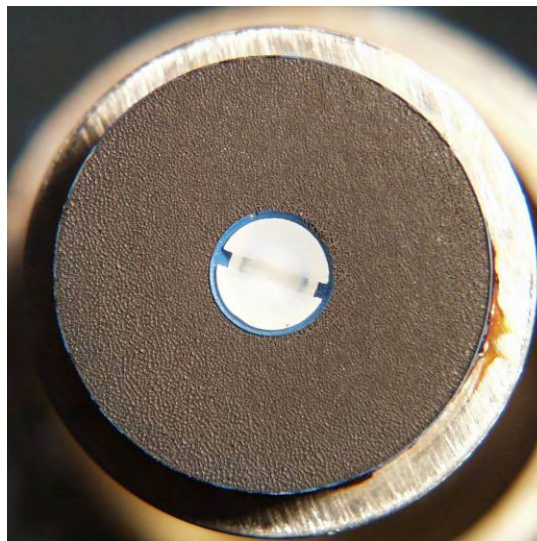


Figure 3-11: Baseline – Top of the line – Test duration: 21 days

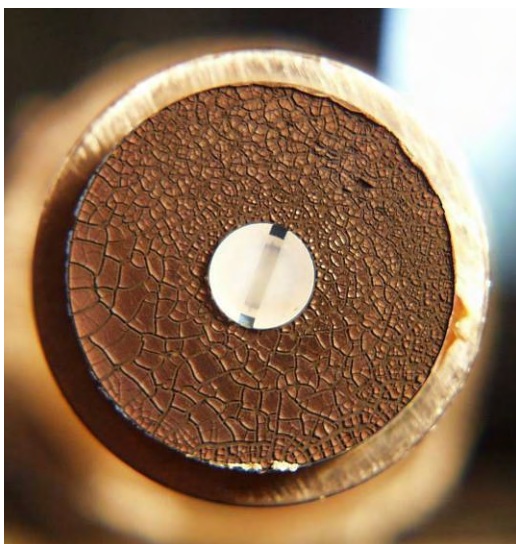
Surface profile of the coupon after the removal of the corrosion product layer



(a) Test duration: 2 days



(b) Test duration: 7 days



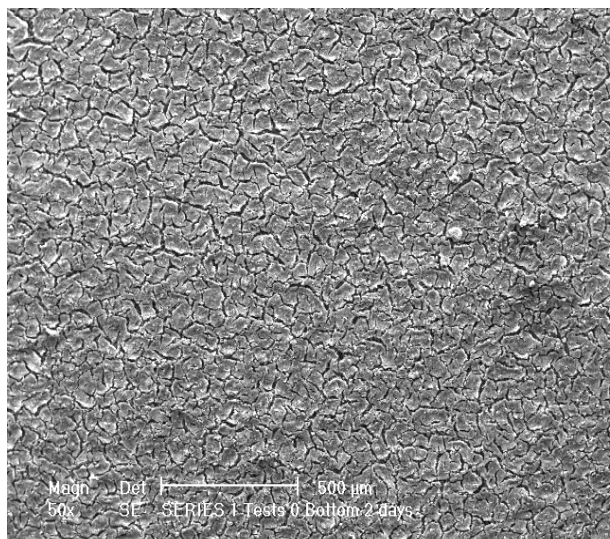
(c) Test duration: 14 days



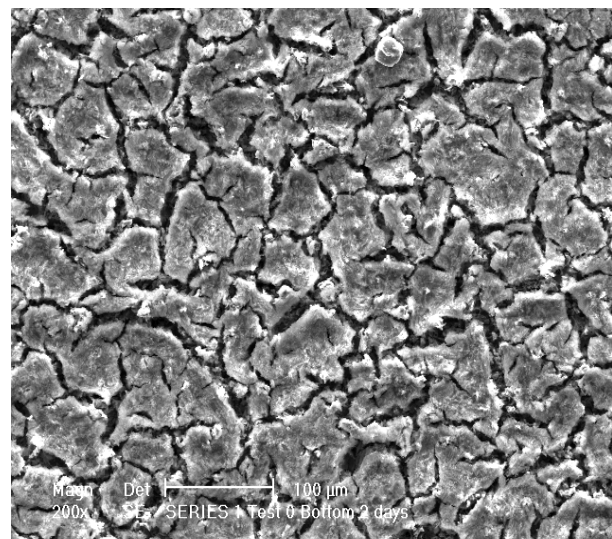
(d) Test duration: 21 days

Figure 3-12: Baseline – Bottom of the line

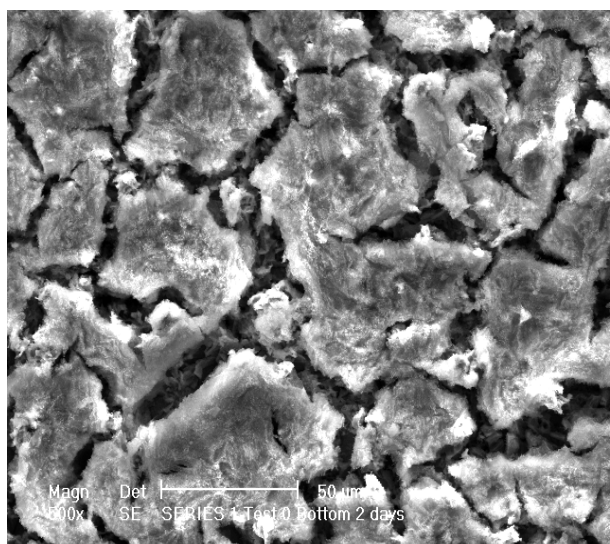
Weight loss coupons before the removal of the corrosion product layer



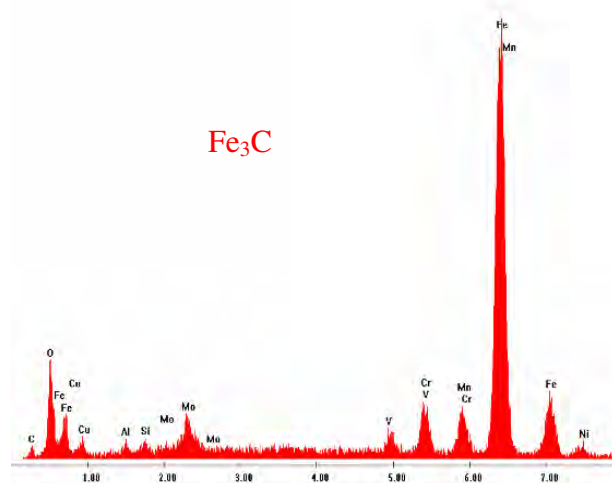
(a) SEM X50



(b) SEM X200



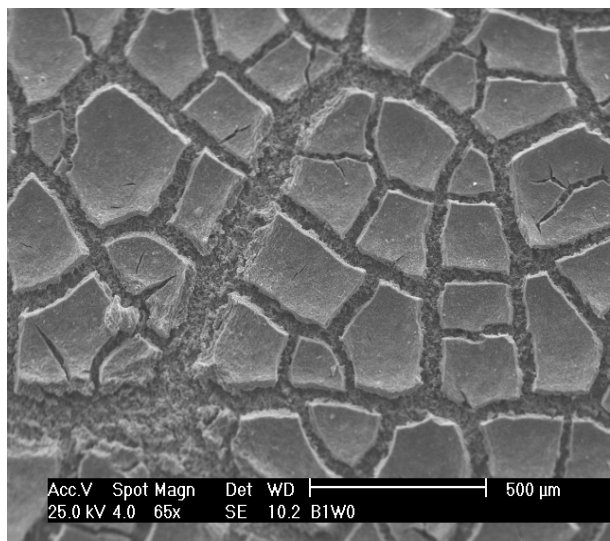
(c) SEM X500



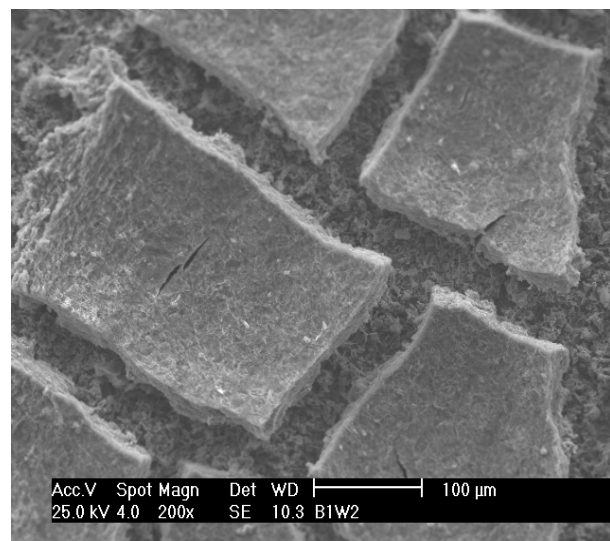
(d) Composition of the corrosion product

Figure 3-13: Baseline – Bottom of the line – Test duration: 2 days

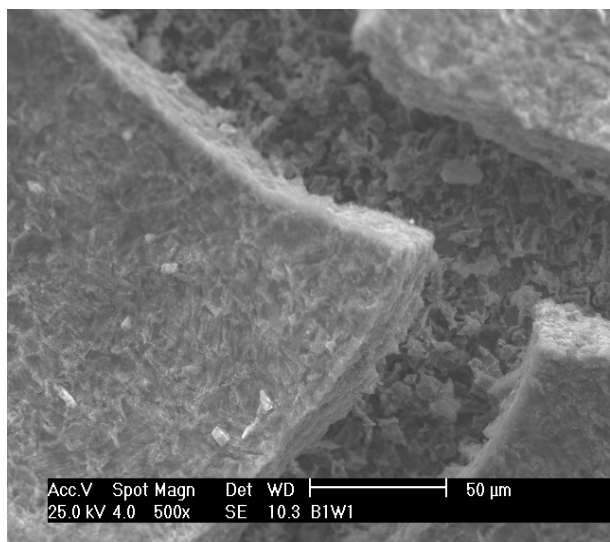
SEM and EDS analysis of the corrosion product layer on the coupon surface



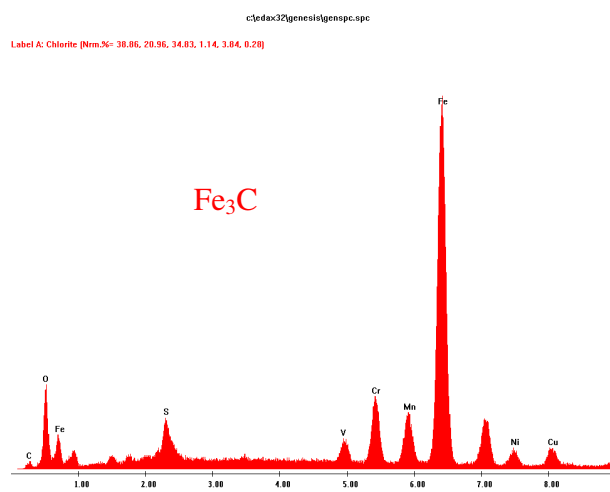
(a) SEM X65



(b) SEM X200



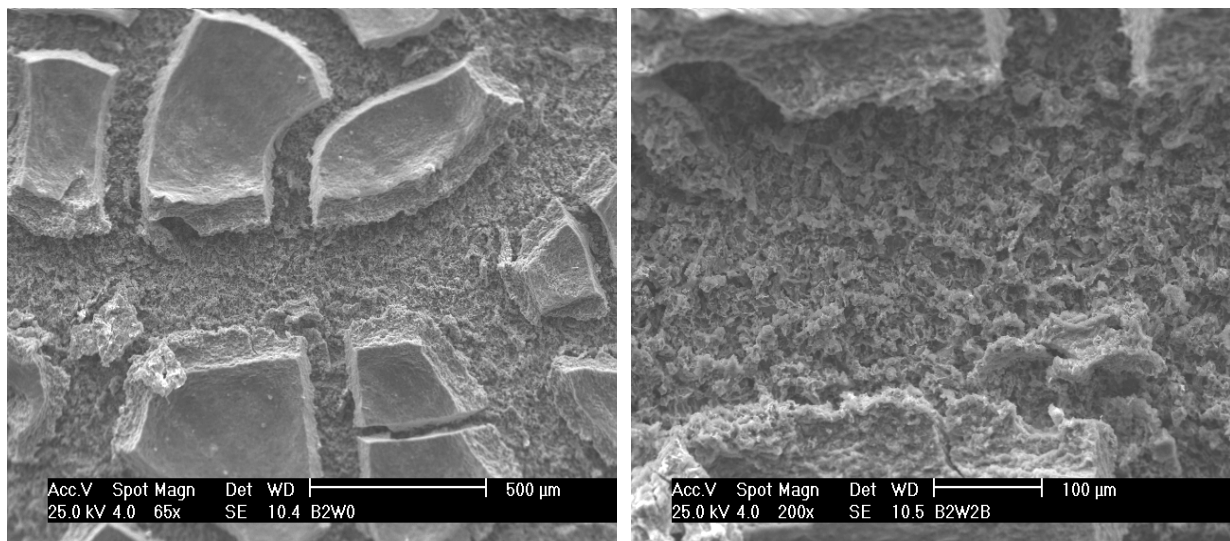
(c) SEM X500



(d) Composition of the corrosion product

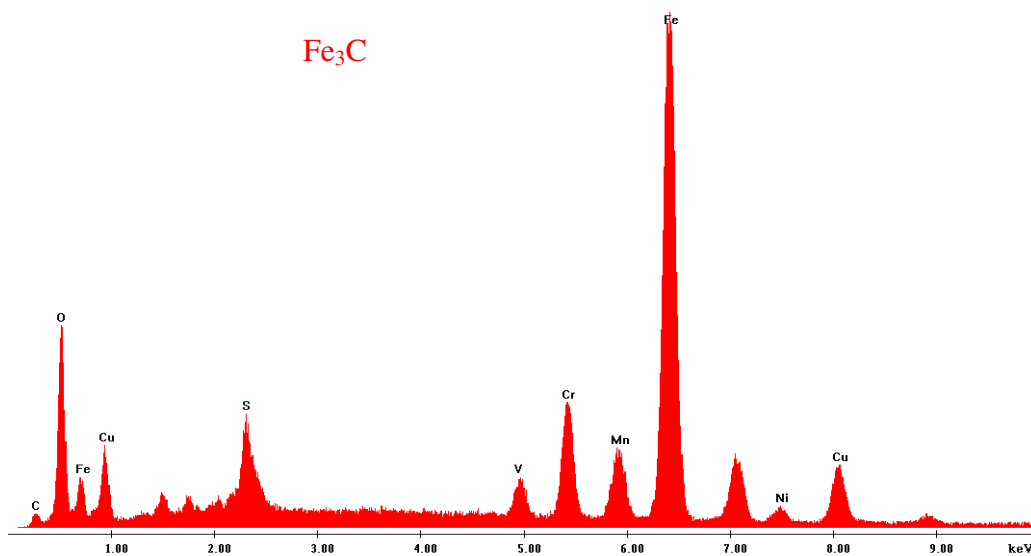
Figure 3-14: Baseline – Bottom of the line – Test duration: 7 days

SEM and EDS analysis of the corrosion product layer on the coupon surface



(a) SEM X100

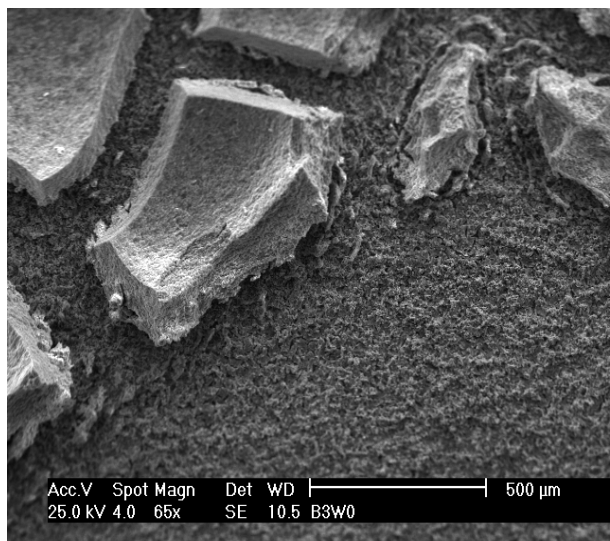
(b) SEM X200



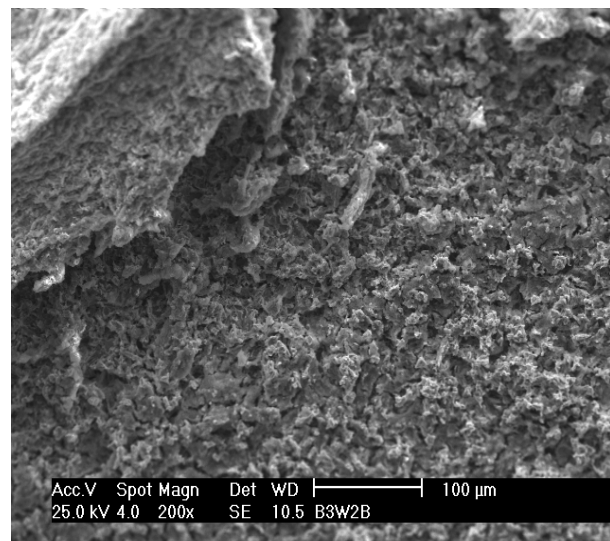
(c) Composition of the corrosion product

Figure 3-15: Baseline – Bottom of the line – Test duration: 14 days

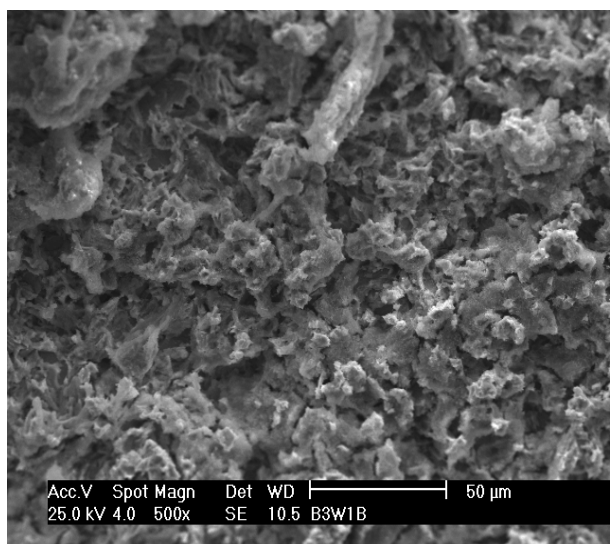
SEM and EDS analysis of the corrosion product layer on the coupon surface



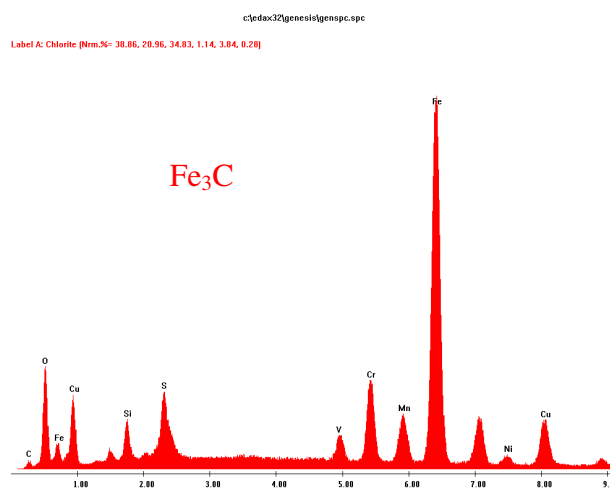
(a) SEM X66



(b) SEM X200



(c) SEM X500



(d) Composition of the corrosion product

Figure 3-16: Baseline – Bottom of the line – Test duration: 21 days

SEM and EDS analysis of the corrosion product layer on the coupon surface

### 3.3.2 Effect of gas temperature

**Top of the line:** Since the corrosion reactions follow the Arrhenius law, the average corrosion rate increases with the increasing gas temperature. This is usually true at the bottom of the line, where there is no protective film formed on the steel surface. At top of the line, however, the enhancing effect of the temperature on corrosion is reduced due to the presence of a protective corrosion product film. In all experiments at different temperatures, it has been observed that a  $\text{FeCO}_3$  film is present at the top of the line, but its protectiveness is different. The  $\text{FeCO}_3$  film is expected to be denser and more protective at higher temperature since the  $\text{FeCO}_3$  precipitation is faster. From Figure 3-17, it can be seen that corrosion rate in 85 °C starts at 0.6 and is decreased to around 0.1 after 21 days. On the contrary, at 40 °C the corrosion rate starts at a low value (0.28) but is still very high (0.3) after 21 days. The corrosion rate at 70 °C is decreased with time, but the reduction of the corrosion rate after 21 days is not as significant as that at 85 °C.

Moreover, at the top of the line, there was no sign of localized corrosion at 40°C or 85°C while there was strong evidence of pitting corrosion at 70°C. It is clear that the properties of the corrosion product film (rate of formation, density, integrity ...) are strongly linked to the pitting corrosion. The breakdown of a protective film at some locations (which is ordinarily observed at top of the line coupons, for example, a coupon in the baseline test in Figure 3-10) provides ideal seedbeds for the initiation and propagation of pits.

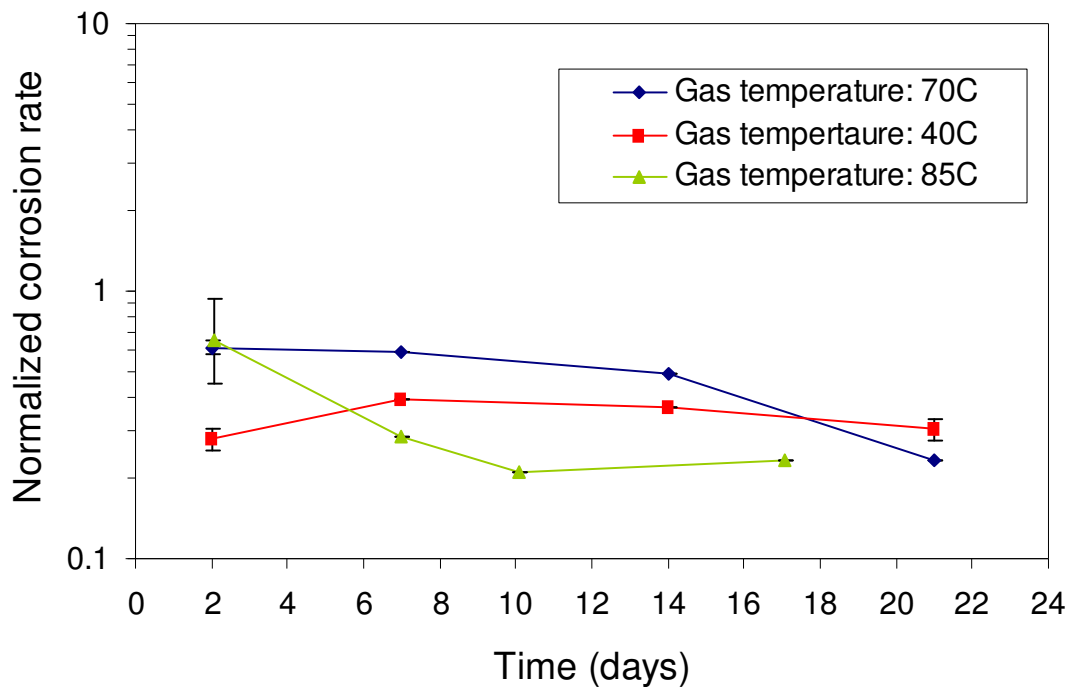


Figure 3-17: Effect of gas temperature on the general corrosion rate at the top of the line ( $P_T = 3$  bar,  $pCO_2 = 2$  bar,  $WCR = 0.25$  mL/m<sup>2</sup>/s,  $U_{SG} = 5$  m/s,  $Free\ HAc = 0$  ppm)

**Bottom of the line:** At the bottom of the line, the corrosion rate is and remains lower at 40°C compared to 70°C and 85°C throughout the test. The relative high corrosion rate at the bottom of the line is due to the presence of an un-protective Fe<sub>3</sub>C scale on the steel surface. With the high uniform corrosion, no localized corrosion was observed at the bottom of the line.

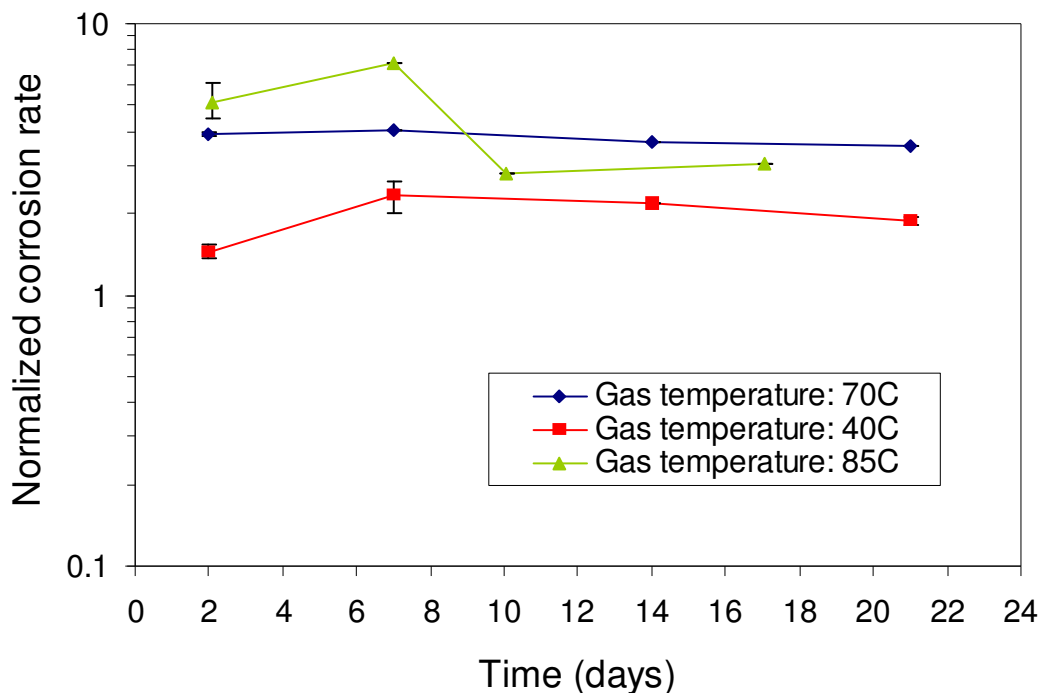
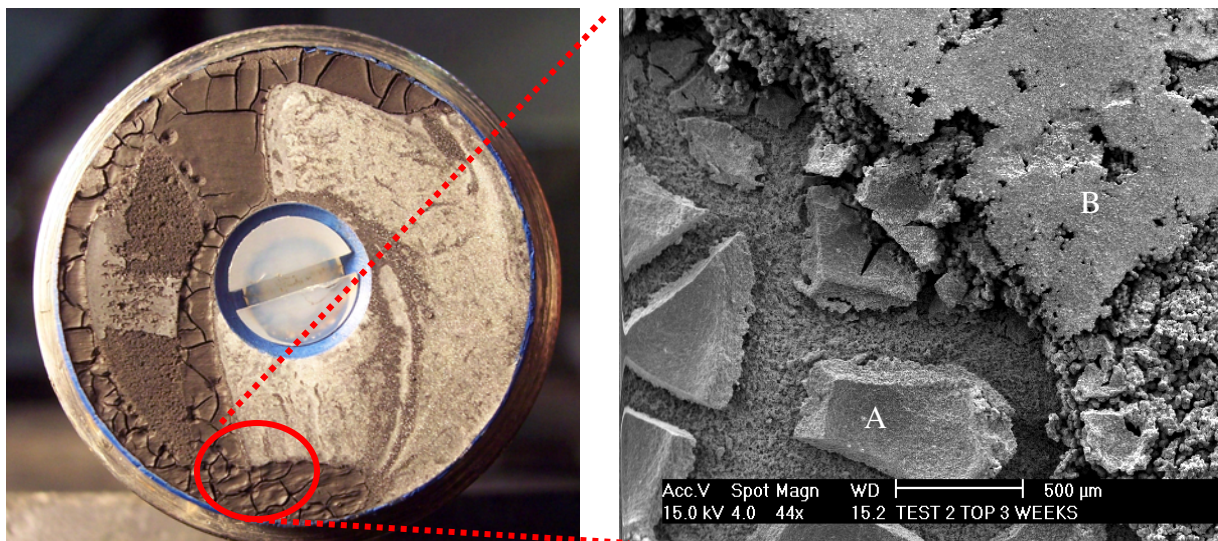


Figure 3-18: Effect of gas temperature on the general corrosion rate at the bottom of the line ( $P_T = 3$  bar,  $pCO_2 = 2$  bar,  $WCR = 0.25$  mL/m<sup>2</sup>/s,  $U_{SG} = 5$  m/s,  $Free\ HAc = 0$  ppm)

### 3.3.3 Effect of gas velocity

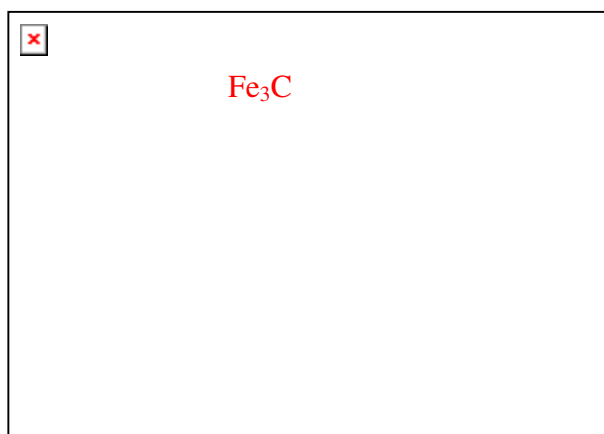
**Top of the line:** The most visible influence of the gas velocity appears on the condensation regime. At low velocity (<10 m/s), the vapor condenses by forming stagnant droplets at the top of the pipe. In these stagnant droplets, very high level of the  $FeCO_3$  supersaturation can be easily achieved, resulting in the formation of a dense and protective film on the metal surface. As the gas velocity increases, the condensation regime transits gradually from a *stagnant* to *sliding* droplet. In the sliding droplet mode, the droplets of condensed liquid flow along the top of the line and eventually slide to the bottom due to the force of gravity. The sliding droplets are not generally in contact with

the pipe steel long enough to create a  $\text{FeCO}_3$  film (as opposed to the stagnant droplet condensation regime). Instead, a thick but non protective  $\text{Fe}_3\text{C}$  is formed on the liquid path ways that the sliding droplets create. It leads to the formation of two different types of film at the top of the line: protective  $\text{FeCO}_3$  on most of the coupon area and non-protective  $\text{Fe}_3\text{C}$  on the preferential liquid path ways (shown in Figure 3-19). The weight loss method, used as a corrosion monitoring tool for most of the experiments, does not differentiate between the types of film and only gives a space average corrosion rate over the entire surface of the coupon. These space average corrosion rates are displayed in all graphs of corrosion rates in this chapter, which are represented by solid lines.

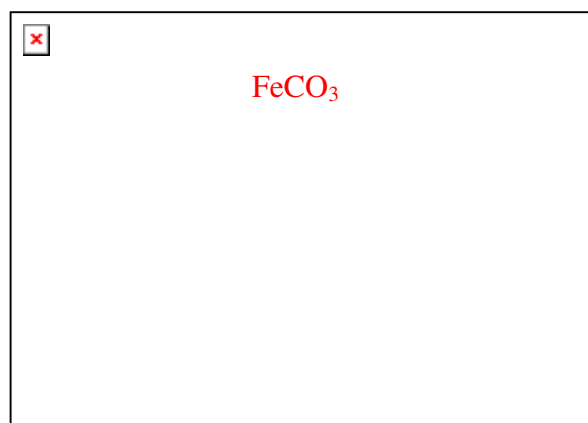


(a) Coupon surface

(b) SEM picture of the circled area



(c) Composition of the corrosion product at location A



(d) Composition of the corrosion product at location B

Figure 3-19: Surface analysis on a coupon at high gas velocity (15m/s) by SEM and EDS

( $T_g = 70\text{ }^\circ\text{C}$ ,  $P_T = 3\text{ bar}$ ,  $p\text{CO}_2 = 2\text{ bar}$ ,  $\text{WCR} = 0.25\text{ mL/m}^2/\text{s}$ ,  $\text{Free HAc} = 0\text{ ppm}$ )

However, it is possible to correct the space average corrosion rate by evaluating the percentage of surface coverage of these two types of film on the coupon surface and

assigning an estimated corrosion rate under either of them. The corrosion rate under a  $\text{Fe}_3\text{C}$ , which often corresponds to the bottom of the line, is usually at least an order of magnitude higher than the corrosion rate under a  $\text{FeCO}_3$  film, which is more typical in TLC. The space average corrosion rates are therefore corrected by assuming that the area of the coupons under a  $\text{Fe}_3\text{C}$  film corrodes at the same rate with the corresponding bottom of the line corrosion rate. For example, consider a fictitious experiment where the coupon at the bottom of the line is evenly corroded at a rate of 10 mm/year and is fully covered by a  $\text{Fe}_3\text{C}$  film. At the top of the line, the space average corrosion rate is measured at 2 mm/year but 5% of the coupon is covered by  $\text{Fe}_3\text{C}$  (and 95% by  $\text{FeCO}_3$ ). By assuming that the part of the coupon at the top of the line covered by  $\text{Fe}_3\text{C}$  corrodes at 10 mm/year, a corrected corrosion rate under  $\text{FeCO}_3$  can be estimated at  $2 - 5\% \cdot 10 = 1.5$  mm/year. Therefore, for each condition, three corrosion rates can be extracted from one coupon: the space average corrosion rate, the corrected average corrosion rate under  $\text{Fe}_3\text{C}$  film, and a corrected average corrosion rate under  $\text{FeCO}_3$  film. There is obvious inherent error in this method of calculation and the actual corrosion rate lies most probably between the space average and the corrected values. The corrected corrosion rates are displayed, when applicable, in the graphs with a dotted line in the same color of its corresponding experiment. In order to make all corrosion rates at the top of the line comparable, the corrected corrosion rate shown for the top of the line (dotted line) represents the corrosion rate under a  $\text{FeCO}_3$  film. For the similar reason, the corrected corrosion rate (represented by a dotted line) at the bottom of the line shows the average corrosion rate under a  $\text{Fe}_3\text{C}$  film. It is important to keep in mind that some parts of the

coupons (covered with  $\text{Fe}_3\text{C}$ ) at the top of the line were corroded at a much higher rate (similar to the bottom of the line).

As the condensation regime starts to transit from stagnant droplet to sliding droplet at a gas velocity equal or above 10 m/s (rivulets of liquid are formed on the coupon surface), some parts of the coupons are heavily corroded in sliding droplet condensation. As the gas velocity increases, more and more of the coupon surface is covered with  $\text{Fe}_3\text{C}$  leading to an overall increase of the space-averaged corrosion rate. However, the corrected corrosion rate under  $\text{FeCO}_3$  (dotted line) does not seem to be greatly affected by the gas velocity (Figure 3-20). The starting corrected corrosion is around 0.75 – 1 and decreases gradually with time below 0.1 after 20 days of testing, whatever the gas velocity is. It means that as long as the conditions for  $\text{FeCO}_3$  supersaturation are met at the top of the line, the gas velocity does not have any visible effect on the corrosion attack.

From the experiments, it seems that there is a critical gas velocity for the transition from stagnant droplet condensation to sliding droplet condensation. A protective film is always present at the top of the line (which means low corrosion rate) when the condensation regime is sliding droplet condensation. It would be desired that the critical value for the transition can be determined by theoretical and experimental studies, which prompted us to explore the mechanism for the transition of condensation regimes (covered in Chapter 4).

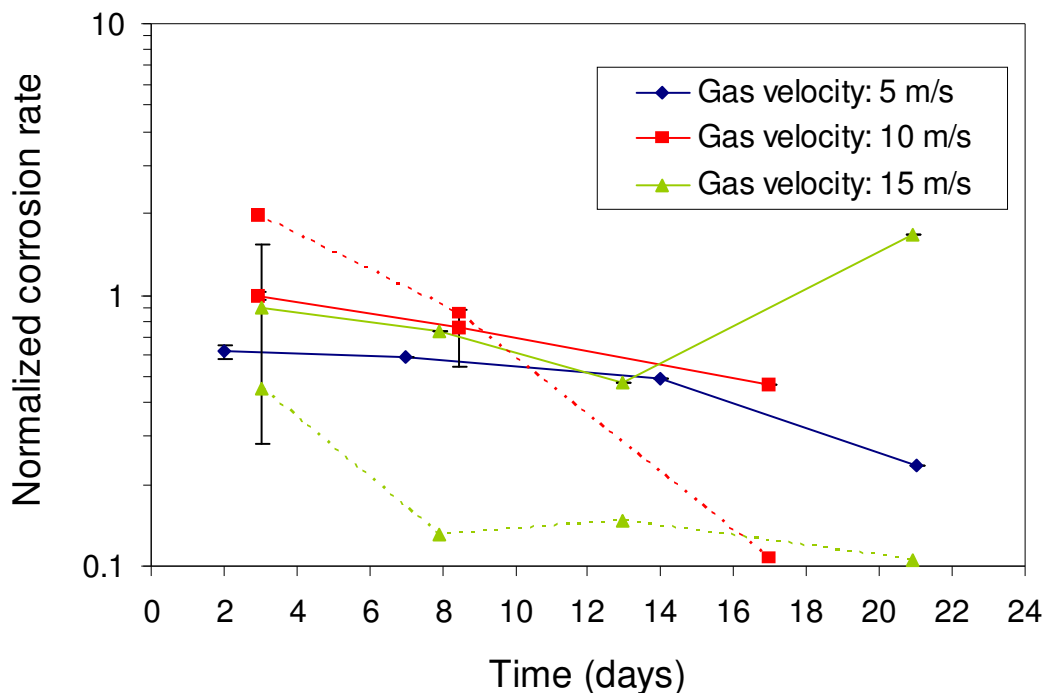


Figure 3-20: Effect of gas velocity on the general corrosion rate at the top of the line (The corrected corrosion rates and space average corrosion rates are represented by dashed lines and solid lines respectively. The definitions of these two corrosion rates can be found in the text.)

( $T_g = 70$  °C,  $P_T = 3$  bar,  $pCO_2 = 2$  bar,  $WCR = 0.25$  mL/m<sup>2</sup>/s, *Free HAc* = 0 ppm)

**Bottom of the line:** At the bottom of the line, the liquid flowing on the pipe is exclusively made of accumulated condensed liquid. Due to the limited amount of water at the bottom of the line, only a small portion of the bottom surface is covered by a thin and narrow liquid film. Consequently, the coupons at the bottom of the line might not be completely wetted by the water when the liquid film thickness is very thin. At a gas velocity of 5 m/s, it was observed that the coupon is completely immersed in the liquid stream. According to the same theory mention above, a thick and uniform Fe<sub>3</sub>C is formed

on the surface. As the gas velocity increases, the liquid stream gets thinner and narrower with the increasing liquid velocity. It leads to the creation of preferential liquid path ways as the coupon cannot be completely immersed in water. Around these liquid pathways, the liquid is more or less stagnant and condition of  $\text{FeCO}_3$  precipitation can be met like at the top of the line. This phenomenon, which is a pure artifact of the experimental setup (specifically, the imperfect match of coupons and holes in the test section), gets stronger as the velocity increases. For the same reason mentioned above, a space average corrosion rate cannot differentiate between the two types of film and the corrosion rates need to be corrected. Once the corrosion rates are corrected, they show a stable value around 4 independent of the gas velocity, which is quite expected.

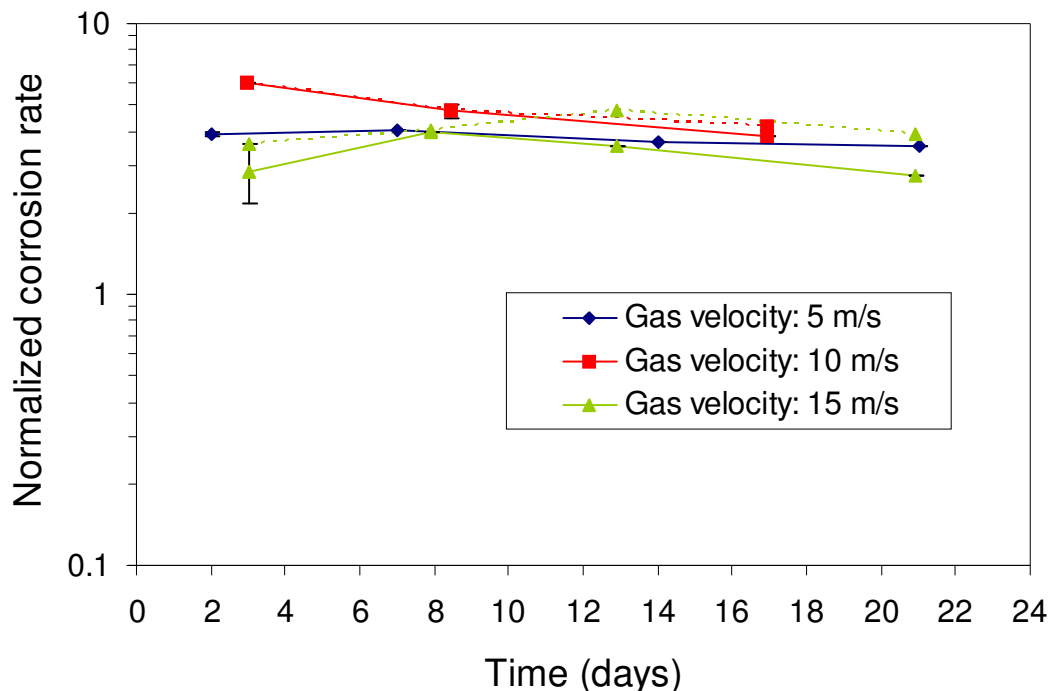


Figure 3-21: Effect of gas velocity on the general corrosion rate at the bottom of the line  
(The corrected corrosion rates and space average corrosion rates are represented by dashed lines and solid lines respectively. The definitions of these two corrosion rates can be found in the text.)

( $T_g = 70$  °C,  $P_T = 3$  bar,  $pCO_2 = 2$  bar,  $WCR = 0.25$  mL/m<sup>2</sup>/s,  $Free\ HAc = 0$  ppm)

### 3.3.4 Effect of CO<sub>2</sub> partial pressure

**Top of the line:** In general, the higher the partial pressure of CO<sub>2</sub>, the higher the general corrosion rate, both at the top and the bottom of the line. At the top of the line, a protective FeCO<sub>3</sub> film is formed on the coupon surface and leads to a stop of the corrosion attack after 18 days of testing. At lower partial pressure of CO<sub>2</sub> (0.13 bar), it seems more difficult to achieve the supersaturation of FeCO<sub>3</sub> due to the low concentration of Fe<sup>2+</sup> and CO<sub>3</sub><sup>2-</sup> ions. Compared to the initial corrosion rate (2 days),

corrosion rate after 21 days is still high although the absolute value is pretty low (around 0.17). At highest partial pressure of CO<sub>2</sub> (7 bar), the corrosion attack is supposed to be more aggressive but the uniform corrosion rate decreases with time to reach 0.15 after 21 days of testing. Since all the conditions for achieving FeCO<sub>3</sub> supersaturation are met easily at 7 bar of CO<sub>2</sub> (high Fe<sup>2+</sup> and CO<sub>3</sub><sup>2-</sup> concentrations), a dense protective film is formed on the metal surface.

Pitting corrosion was observed at partial pressures of 2 and 7 bars and was more serious at 7 bars of CO<sub>2</sub>. But only light pitting was observed at 0.13 bar of CO<sub>2</sub> after 21 days of testing.

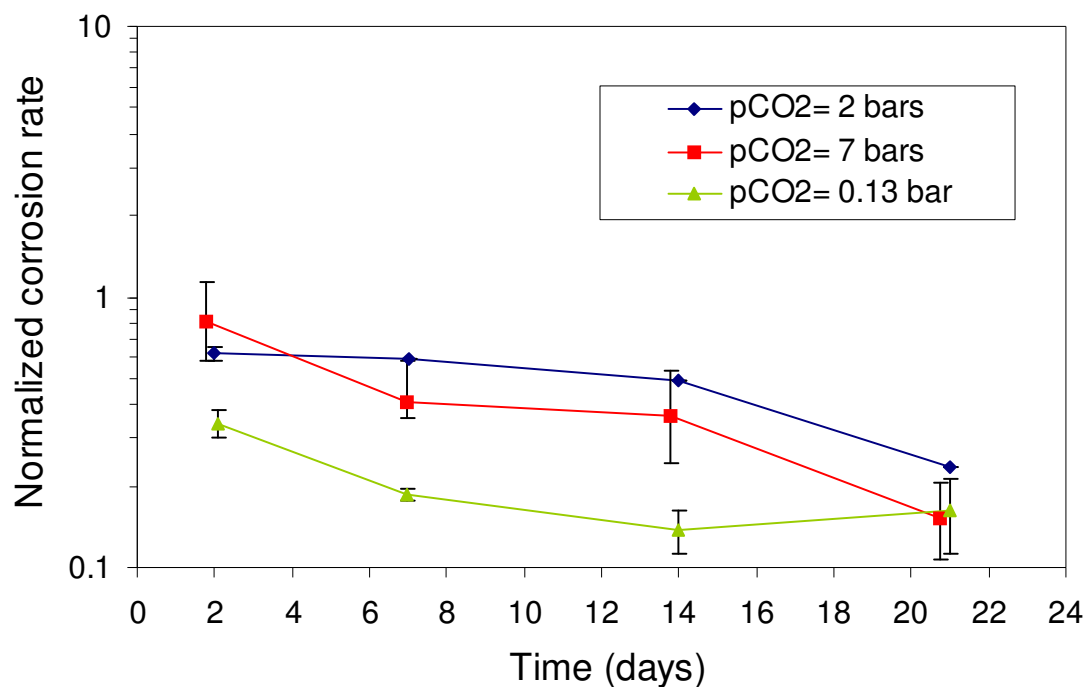


Figure 3-22: Effect of CO<sub>2</sub> partial pressure on the general corrosion rate at the top of the line ( $T_g = 70$  °C,  $WCR = 0.25$  mL/m<sup>2</sup>/s,  $U_{SG} = 5$  m/s,  $Free\ HAc = 0$  ppm)

**Bottom of the line:** At the bottom of the line, the corrosion rate increases with increasing  $\text{CO}_2$  partial pressure (Figure 3-23). More  $\text{CO}_2$  is present in the gas phase; more  $\text{CO}_2$  can dissolve and then hydrate with water to produce more carbonic acid in the solution. In all cases, the corrosion rate remains globally constant with time since the  $\text{Fe}_3\text{C}$  layer on the steel surface is thick but non-protective. Meanwhile, no localized corrosion was observed at the bottom of the line.

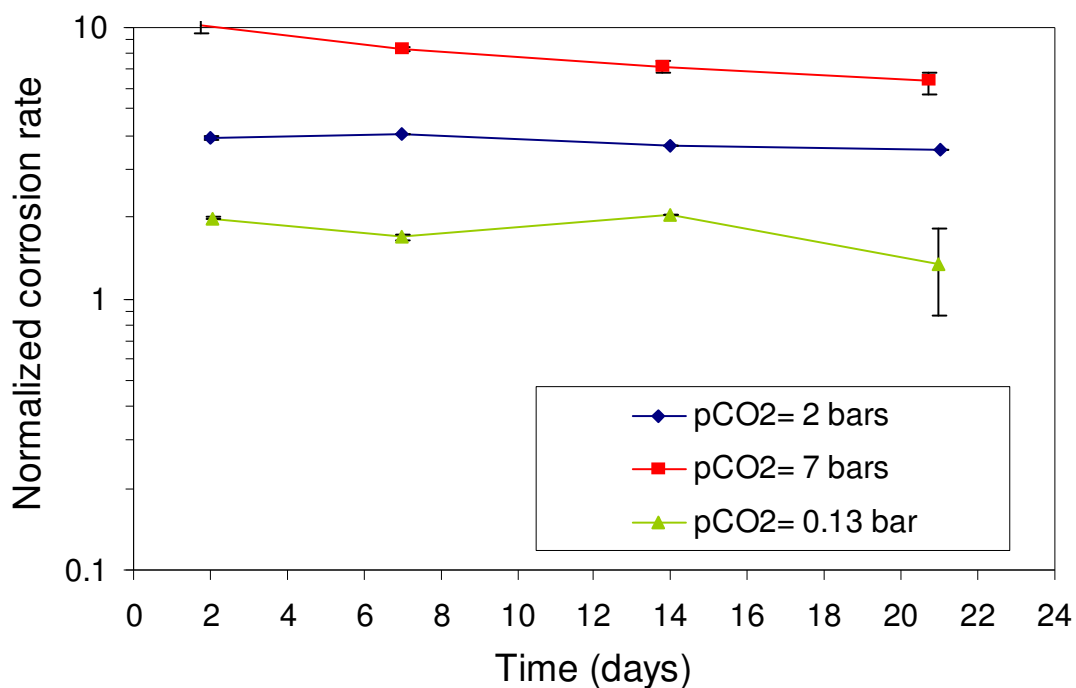


Figure 3-23: Effect of  $\text{CO}_2$  partial pressure on the general corrosion rate at the bottom of the line ( $T_g = 70^\circ\text{C}$ ,  $WCR = 0.25\text{ mL/m}^2/\text{s}$ ,  $U_{SG} = 5\text{ m/s}$ ,  $Free\ HAc = 0\text{ ppm}$ )

### 3.3.5 Effect of condensation rate

**Top of the line:** The average corrosion rate at the top of the line is generally the lowest at the lowest condensation rate (Figure 3-24). The reason for this is probably that there is more fresh liquid available at higher condensation rate. Moreover, the saturation of  $\text{FeCO}_3$  is easier to achieve when there is less liquid (at lower condensation rate the droplet grows slower and is refreshed in less frequency).

Nevertheless, there is not any significant difference in the corrosion rate between 0.25 and 1  $\text{mL/m}^2/\text{s}$ . The corrosion rates have very similar values over time and in these two cases, the corrosion attack seems to be stopped after 21 days due to the formation of a protective  $\text{FeCO}_3$  scale at the steel surface. In all cases, the condensation regime seems to be stagnant droplet condensation, which means that the overall decreasing trend of the corrosion rate should be the same.

The influence of the condensation is much stronger on the localized attack. Both pitting rate and surface coverage by localized attack increase dramatically with the condensation rate.

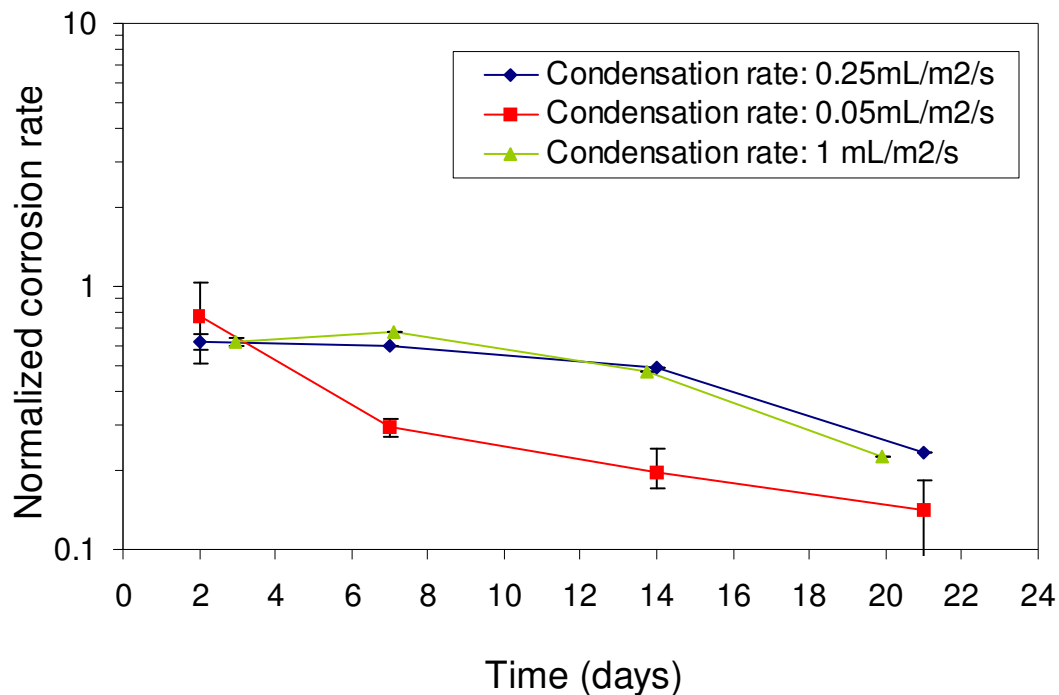


Figure 3-24: Effect of the condensation rate on the general corrosion rate at the top of the line ( $T_g = 70$  °C,  $P_T = 3$  bar,  $pCO_2 = 2$  bar,  $U_{SG} = 5$  m/s,  $Free\ HAc = 0$  ppm)

**Bottom of the line:** Obviously, the corrosion rate at the bottom of the line is independent of the condensation rate (Figure 3-25) because the water flow rate at the bottom of the line is decided by the amount of water condensed in the whole upstream. In all three experiments, there is always a fair amount of liquid flowing at the bottom of the line, which is from the condensate accumulated on the connection pipeline between the tank and the test section (Figure 3-1). The film formed on the coupon surface is usually a porous and un-protective  $Fe_3O_4$  scale. Therefore, no localized corrosion was reported in any tests at the bottom of the line.

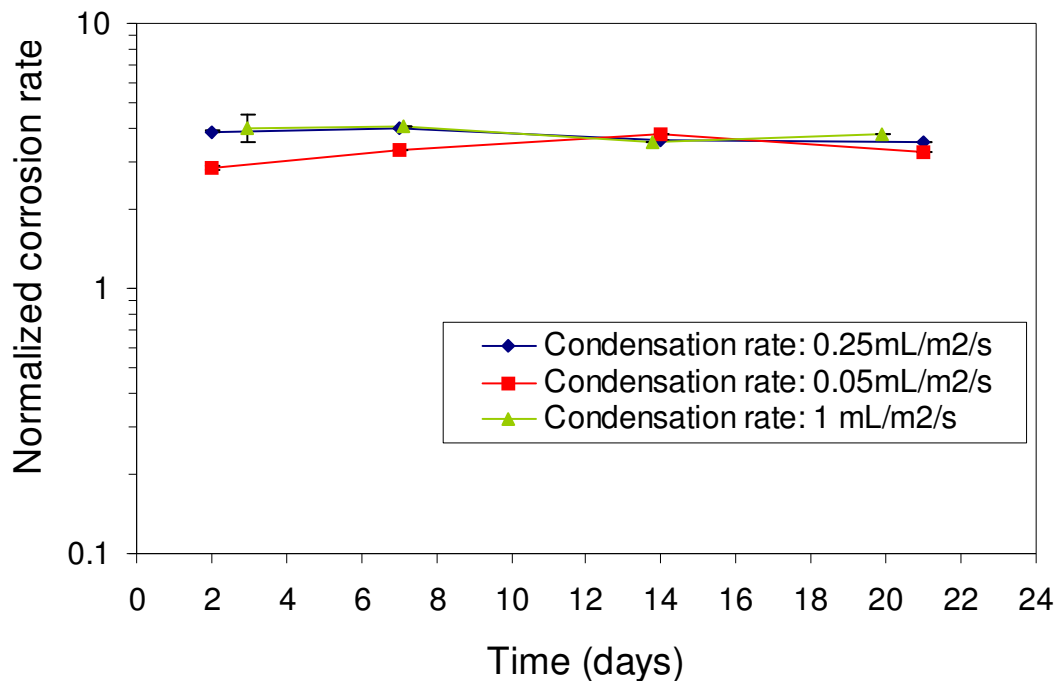


Figure 3-25: Effect of the condensation rate on the general corrosion rate at the bottom of the line ( $T_g = 70\text{ }^\circ\text{C}$ ,  $P_T = 3\text{ bar}$ ,  $pCO_2 = 2\text{ bar}$ ,  $U_{SG} = 5\text{ m/s}$ ,  $Free\ HAc = 0\text{ ppm}$ )

### 3.3.6 Effect of acetic acid concentration

**Top of the line:** From the electrochemical theory, when acetic acid is present, another cathodic reaction occurs in addition to the reduction of the carbonic acid resulting in extra metal loss. Therefore, more acetic acid means higher corrosion rate. However, the presence of 100 ppm of free acetic acid in the liquid phase does not seem to have a strong effect on the average corrosion rate at the top of the line. The contribution to the overall cathodic reaction of such a small amount of acetic acid is minimal. As the free acetic acid concentration is increased to 1000 ppm, the average corrosion rate is increased dramatically at every point in respect to time, which is shown in Figure 3-26.

Moreover, even after 3 weeks of testing the corrosion rate at 1000 ppm acetic acid is still very high (around 1).

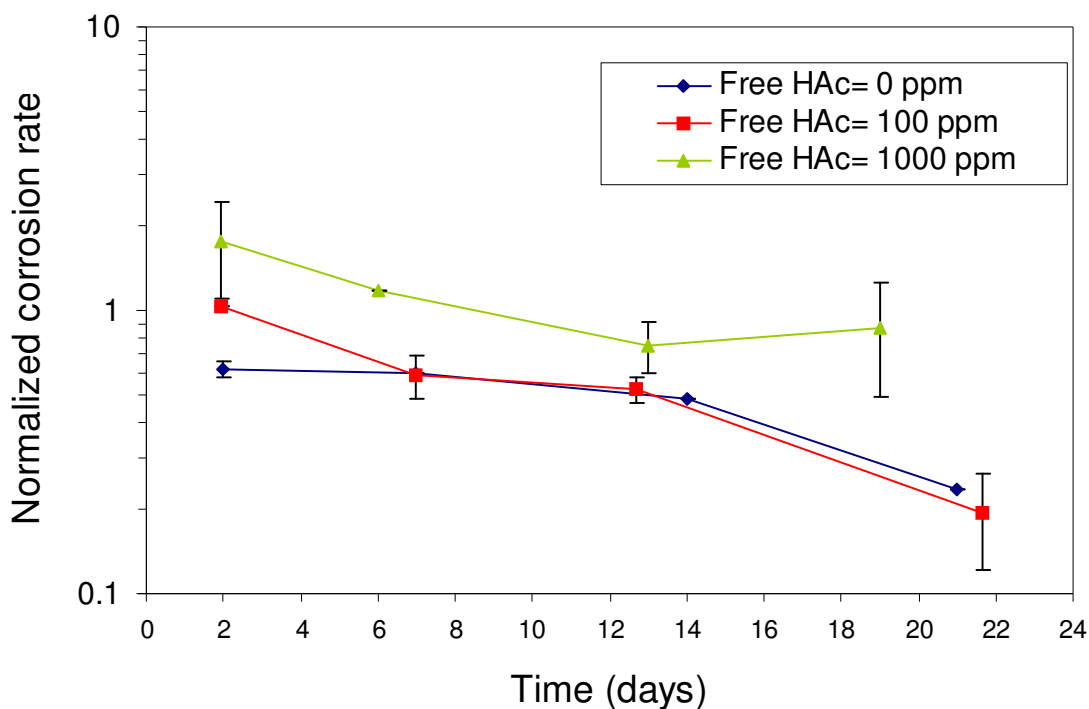


Figure 3-26: Effect of HAc concentration on the general corrosion rate at the top of the line ( $T_g = 70\text{ }^\circ\text{C}$ ,  $P_T = 3\text{ bar}$ ,  $pCO_2 = 2\text{ bar}$ ,  $WCR = 0.25\text{ mL/m}^2/\text{s}$ ,  $U_{SG} = 5\text{ m/s}$ )

Meanwhile, although traces of localized corrosion were found in all three tests, the presence of acetic acid promotes definitively the occurrence of pitting corrosion and the extent of enhancement is proportional to the acid concentration in the solution. The 3D coupon surface profile in the test with 1000 ppm HAc is shown in Figure 3-27. By comparison (Figure 3-11 and Figure 3-27), it seems that 1000 ppm HAc can enhance the localized corrosion dramatically.

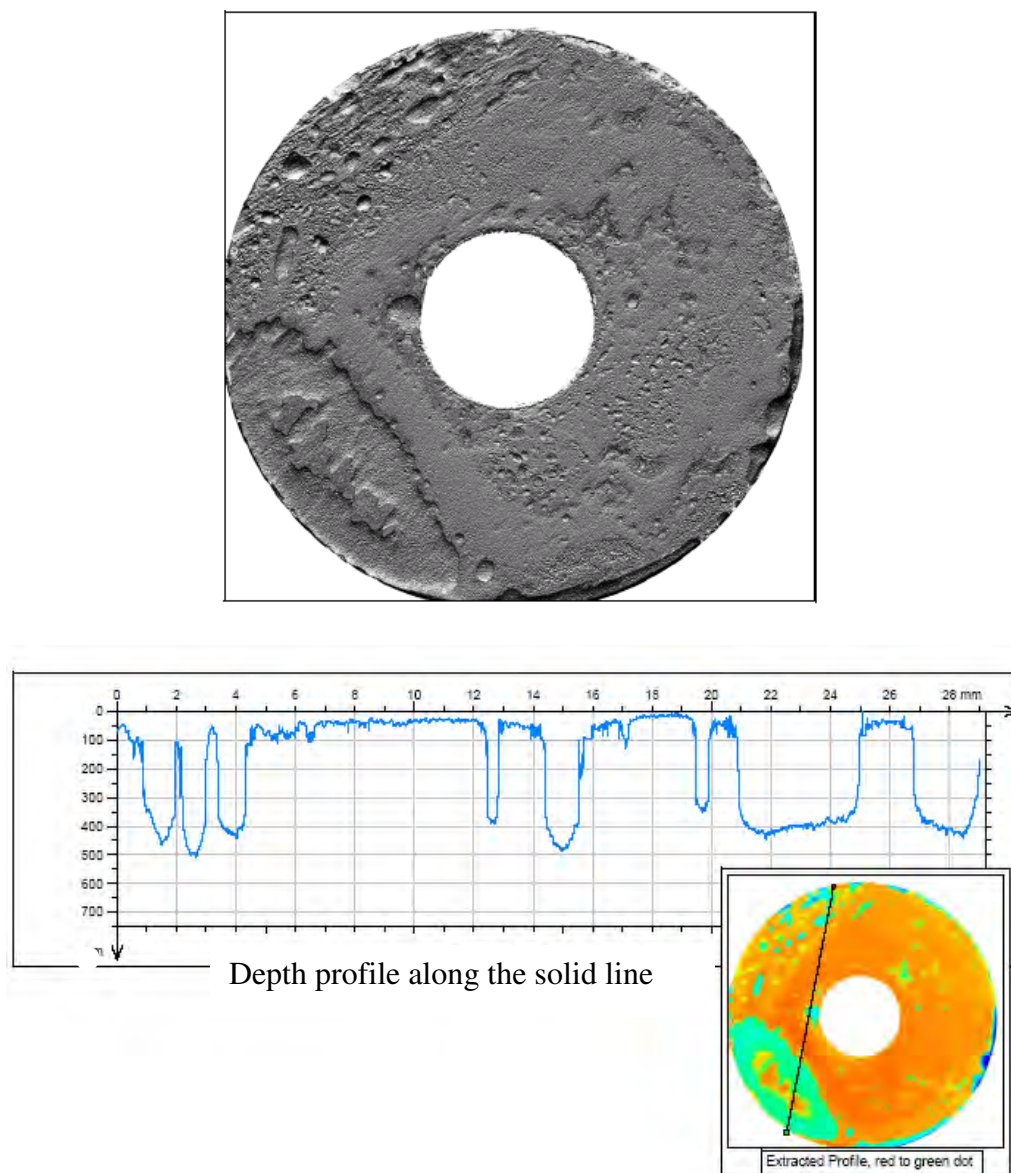


Figure 3-27: Test with 1000 ppm free HAc – Top of the line – Test duration: 21 days  
Surface profile of the coupon after the removal of the corrosion product layer

**Bottom of the line:** At the bottom of the line, the presence of acetic acid seems to increase the corrosion rate, which is proportional to the amount of acid present (Figure 3-28). Although the enhancement of the corrosion rate by 100ppm HAc is not significant, it

is more evident when the HAc concentration is increased to 1000ppm. No localized corrosion was observed in the surface analysis. It is not surprising since the localized corrosion even if it exists is overshadowed by the high level of uniform corrosion.

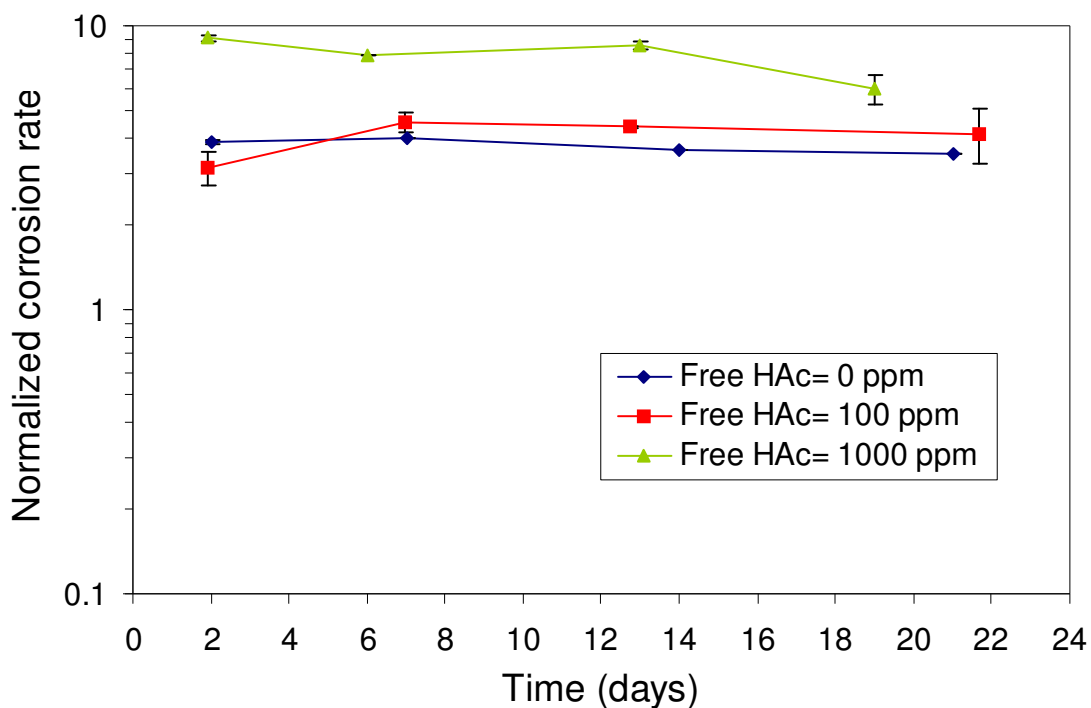


Figure 3-28: Effect of HAc concentration on the general corrosion rate at the bottom of the line ( $T_g = 70$  °C,  $P_T = 3$  bar,  $pCO_2 = 2$  bar,  $WCR = 0.25$  mL/m<sup>2</sup>/s,  $U_{SG} = 5$  m/s)

### 3.4 Summary

In the last four years of TLC JIP, around 35 short term tests were performed for the Phase I and 20 long term tests (11 shown in this dissertation) have been completed for

the Phase II. After the analysis of the experimental data gained in large scale flow loop, several general conclusions on the effects of all important parameters are summarized below:

- Generally, the corrosion rate at the top of the line starts at relatively high value and then gradually decreases with time. This is due to the increasing protection of the  $\text{FeCO}_3$  film which continuously precipitates on the metal surface at very high  $\text{FeCO}_3$  supersaturation level in the droplets.
- Through the surface analysis, the evolution of the film formation process has been clarified. Furthermore, EDS results have shown that different films are formed at the top and the bottom. It confirmed that the protective film at the top of the line is made up of  $\text{FeCO}_3$  crystals. By contrast, the film at the bottom of the line is identified to be  $\text{Fe}_3\text{C}$ , and therefore it is non-protective.
- The long term experiments not only provide a reliable and consistent experimental database for the verification of the corrosion model but also lead to some new visions on the theoretical study of TLC. For example, the findings on the effect of gas velocity on condensation and corrosion prompt us to explore the mechanism for the transition of condensation regimes.

## **CHAPTER 4: A MECHANISTIC MODEL OF DROPWISE CONDENSATION AT THE TOP OF THE LINE**

### **4.1 Introduction**

Filmwise condensation and dropwise condensation are two main condensation regimes that may happen on a metal surface. Which one is prevailing depends on the wettability and the orientation of the surface. The condensation type in Top of the Line Corrosion (TLC) has been proved to be dropwise by reported field cases (Gunaltun, 1999); our own experimentation including in-situ visual observation (Figure 2-2); coupon analysis (Figure 2-6); and heat transfer analysis of dropwise and filmwise condensation (Utaka and Saito, 1988). Essentially, dropwise condensation is a typical heat transfer problem if the vapor phase is stagnant without any non-condensable impurities. However, this is not the condition seen in natural gas pipelines, in which the gas mixture is always dynamic. Only small quantities of water vapor are present in the natural gas with a large amount of non-condensable and condensable hydrocarbon fractions. In these cases, dropwise water condensation depends not only on heat transfer but also mass transfer and hydrodynamics as well.

In previous studies, most of researchers did not cover the most difficult part in dropwise condensation modeling: presence of a non-condensable gas phase, since they assumed that the vapor phase in their systems was pure and stagnant, which was in some cases a reasonable assumption i.e. for some simple heat exchange systems. A few investigators have signaled the problem associated with the presence of non-condensable

gas. They (Gener and Tien, 1990; Wang and Tu, 1988; Wang and Utaka, 2004) observed that 10% of non-condensable gas can reduce the heat transfer rate by ~60% and 500 ppm of nitrogen gas in the vapor-ethanol mixture could reduce the heat flux by ~50%. However, no mechanism was developed by these researchers from their experiments although they used some simple equations to correlate their experimental data.

In the present study, a new mechanistic model of dropwise condensation is established for the unique pipeline system with a trace amount of water vapor. Heat transfer and droplet distribution equations from the model of pure vapor dropwise condensation were adopted after some modifications to account for the effect of pipeline flow configuration. New equations were derived for the mass transfer through the gas boundary layer built up around the droplets. The connection between heat transfer and mass transfer balance equations was established through those mass transfer and heat transfer coefficients in the hydrodynamic part of the analysis. In addition, a force analysis on a single droplet was conducted to determine the maximum droplet size and the criteria for droplet motion. Based on the theoretical study and our unique experiments using an *in situ* camera, several condensation regimes were defined. A preliminary condensation regime map was then constructed to predict transitions of different condensation regimes.

## **4.2 Model development**

After several decades of studies on TLC and dropwise condensation, various factors that have been identified to influence the condensation rate in the wet gas pipeline include:

- Gas temperature;
- Subcooling temperature (defined as  $\Delta T = T_b^g - T_i^w$ ) where  $T_b^g$  is bulk gas temperature and  $T_i^w$  is inner wall temperature;
- Non-condensable gas concentration;
- Gas velocity;
- System pressure;
- Internal pipe diameter.

Since the liquid nucleation of embryos in dropwise condensation is a random process, a statistical method (droplet size distribution function) is employed to model the overall heat transfer process. In order to calculate the condensation rate for dropwise condensation, two crucial parameters must first be obtained: droplet size distribution and heat transfer rate through each droplet of a given radius,  $r$ .

#### 4.2.1 Droplet-size distribution function

At any given time, a family of droplets with different diameters occupies the pipe inner surface. This is called the droplet-size distribution in dropwise condensation. Equation (4-1) was first proposed by Rose and Glicksman (1973) and is one of the most commonly used droplet-size distribution functions.

$$N(r)dr = \frac{n}{\pi r^2 r_{max}} \left( \frac{r}{r_{max}} \right)^{n-1} dr \quad (4-1)$$

where:

$N(r)dr$	number of droplets at radius, $r$ , over $1 \text{ m}^2$ surface area, $\text{m}^{-2}$
$n$	exponent constant, typically as $1/3$
$r_{max}$	the maximum droplet radius, $\text{m}$

#### 4.2.2 Heat flux in dropwise condensation

The overall heat transfer process in dropwise condensation should take into account several crucial phenomena (Rose, 1988; Abu-Orabi, 1998; Crahan and Griffith, 1973) as shown in Figure 4-1:

- 1) Heat transfer resistance in the gas phase boundary layer.
- 2) Water vapor condensation at the droplet surface.
- 3) The influence of droplet surface curvature on the phase equilibrium temperature.  
This is important especially for small droplets.
- 4) Vapor-liquid interfacial resistance. In the condensation process only part of the vapor molecules which are striking the liquid surface can enter the liquid phase.  
This causes a thermal resistance to heat transfer.
- 5) Heat conduction resistance through the droplets. It is important to point out that the heat conduction resistance is not uniform through a droplet since the distance from the droplet surface (gas-liquid interface) to the inner pipe wall changes from the apex to the drop base perimeter (gas-liquid-solid three phase interface).
- 6) Heat conduction resistance through the pipe wall and the insulation layer to the environment.

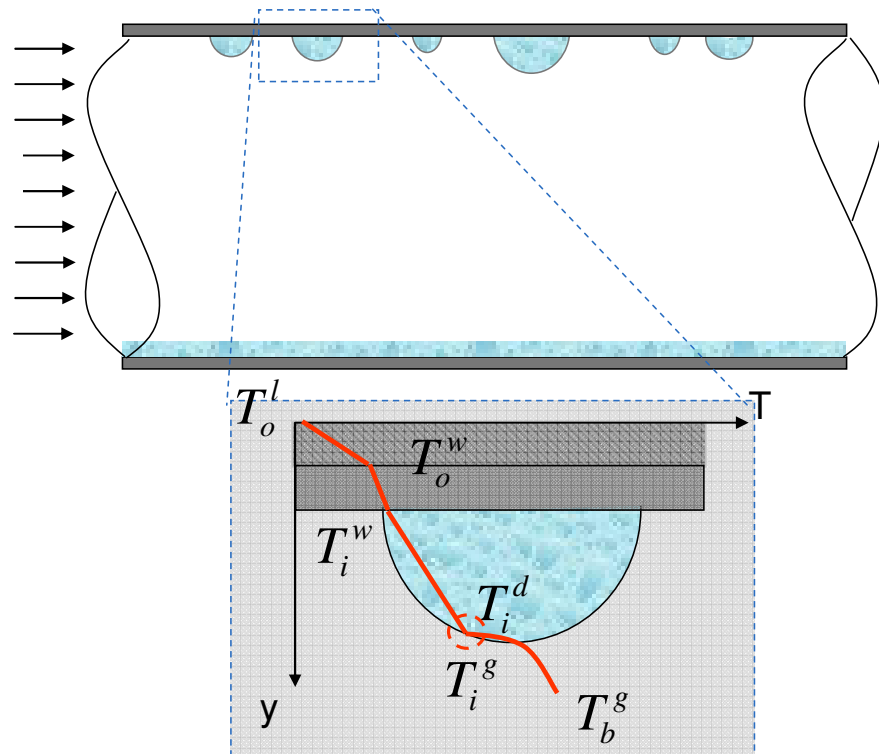


Figure 4-1: Temperature gradient in a single droplet where the bulk temperature can be assumed to be constant for a very short distance in flow direction.

( $T_o^l$ : outer insulation layer temperature;  $T_o^w$ : outer wall temperature;  $T_i^w$ : inner wall temperature;  $T_i^d$ : interfacial temperature in the liquid side;  $T_i^g$ : interfacial temperature in the gas side;  $T_b^g$ : bulk gas temperature)

### 4.2.3 Heat balance

Due to the fact that the heat transfer resistance in the gas phase is significant when non-condensable gases are present and that the phase change (vapor condensation) happens at the interface, the total flux of heat  $Q$  between the gas phase and the droplets can be written as:

$$Q = Q_g + Q_c \quad (4-2)$$

where:

$Q_g$ : heat flux through the gas boundary layer to the droplet surface,  $W/m^2$

$Q_c$ : latent heat flux released by the phase change at the droplet surface,  $W/m^2$

1) For a fully developed gas boundary layer the heat flux  $Q_g$  can be calculated by:

$$Q_g = h_g \cdot (T_b^g - T_i^g) \quad (4-3)$$

where:

$h_g$ : heat transfer coefficient for the gas boundary layer,  $W/m^2 /K$

$T_b^g$ : temperature of the bulk gas, K

$T_i^g$ : temperature of the gas at the droplet interface, K

Here the heat transfer coefficient of the gas boundary layer in a pipeline can be estimated by empirical correlations (Dittus and Boetler, 1930).

$$Nu = 0.023 Re^{0.8} Pr^{0.4} \quad (4-4)$$

where:

$Nu = h_g d / k_g$  : Nusselt number

$Re = U_g d \rho_g / \mu_g$  : Reynolds number

$Pr = \hat{C}_p \mu / k_g$  : Prantl number

$d$  : internal pipeline diameter, m

$k_g$ :	thermal conductivity of the gas, W/m·K
$U_g$ :	actual gas velocity, m/s
$\rho_g$ :	gas density, kg/m <sup>3</sup>
$\mu_g$ :	gas viscosity, Pa·s
$\hat{C}_p$ :	heat capacity of the gas, J/K·kg

2) The latent heat flux is related to the condensation rate:

$$Q_c = \dot{m} H_{fg} \quad (4-5)$$

where:

$\dot{m}$  : condensation rate, kg<sub>g</sub>/m<sup>2</sup>/s

$H_{fg}$  : latent heat of evaporation/condensation for water, J/kg

The total heat flux between the gas phase and the droplets becomes:

$$Q = h_g \cdot (T_b^g - T_i^g) + \dot{m} H_{fg} \quad (4-6)$$

To calculate the condensation rate  $\dot{m}$  from this equation one needs to know the heat flux  $Q$  and find the unknown temperature of the gas at the interface with the droplets  $T_i^g$  by considering that the heat transferred from the gas to the droplets, passes through the droplets and the pipe wall to the outside environment.

3) The temperature drop  $\Delta T_c$  at the droplet interface due to droplet curvature is defined as (the derivation discussed below):

$$\Delta T_c = \frac{\rho_l - \rho_g}{H_{fg} r \rho_g \rho_l} 2T_i^g \sigma \quad (4-7)$$

where:

- $r$ : radius of the droplet, m
- $\sigma$ : vapor-liquid surface tension, N/m
- $\rho_l$ : water density, kg/m<sup>3</sup>
- $\rho_g$ : water vapor density, kg/m<sup>3</sup>

4) The amount of heat  $q$  in W, carried through the interface of a droplet with a radius  $r$  is (Abu-Orabi, 1998):

$$q(r) = 2\pi r^2 h_i (T_i^g - T_i^d) = 2\pi r^2 h_i \Delta T_i \quad (4-8)$$

where

- $h_i$ : heat transfer coefficient at the droplet interface, W/m<sup>2</sup>/K
- $T_i^d$ : temperature of the droplet at the interface with the gas, K
- $\Delta T_i$ : temperature drop due to vapor-liquid interfacial resistance for a hemispherical droplet, K

5) Then the heat is conducted through the bulk of the droplet (Graham and Griffith, 1973):

$$q(r) = \frac{4\pi r^2 k_{H_2O}}{r} (T_i^d - T_i^w) = 4\pi r k_{H_2O} \Delta T_d \quad (4-9)$$

where

$k_{H_2O}$ : thermal conductivity of the water, W/m/K

$T_i^w$ : temperature of the droplet at the interface with the pipe wall, K

$\Delta T_d$ : temperature drop due to heat conduction through a hemispherical droplet,  
K

6) The heat goes through the pipe wall:

$$q(r) = \frac{2\pi r^2 k_w}{d_w} (T_i^w - T_o^w) = \frac{2\pi r^2 k_w}{d_w} \Delta T_w \quad (4-10)$$

where:

$k_w$ : thermal conductivity of the steel pipe wall, W/m/K

$d_w$ : thickness of pipe wall, m

$T_o^w$ : temperature of the outer pipe wall, K

$\Delta T_w$ : temperature drop due to heat conduction through the pipe wall, K

7) Finally, the same amount of heat exits through the insulation/protection layer (commonly used to cover up the outer surface of the oil and gas pipelines) out to the environment:

$$q(r) = \frac{2\pi r^2 k_l (T_o^w - T_o^l)}{d_l} = \frac{2\pi r^2 k_l}{d_l} \Delta T_l \quad (4-11)$$

where:

$k_l$ : thermal conductivity of the insulation/protection layer, W/m/K

$d_l$ : thickness of the insulation/protection layer, m

$T_o^l$ : temperature of the outer insulation/protection layer, K

$\Delta T_l$ : temperature drop due to heat conduction through the pipe wall, K

One can write the overall temperature difference between the surface of the droplet  $T_i^s$  and the outer insulation/protection layer  $T_o^l$  as:

$$T_i^s - T_o^l = \Delta T_c + \Delta T_i + \Delta T_d + \Delta T_w + \Delta T_l \quad (4-12)$$

By substituting the various  $\Delta T$  from Equations (4-7) to (4-11) into Equation (4-12), the amount of heat  $q(r)$  transferred through a single droplet of radius  $r$  can be expressed as:

$$q(r) = \frac{T_i^s \left( 1 - \frac{2\sigma(\rho_l - \rho_g)}{H_{fg} r \rho_g \rho_l} \right) - T_o^l}{\frac{r}{4\pi r^2 k_{H_2O}} + \frac{1}{2\pi r^2 h_i} + \frac{d_w}{2\pi r^2 k_w} + \frac{d_w}{2\pi r^2 k_w}} \quad (4-13)$$

The total heat flux for a unit area of the pipe wall covered by a large number of droplets of various sizes can be calculated by summing all the fluxes, which can be written as (Rose, 1988):

$$Q = \int_{r_{min}}^{r_{max}} q(r)N(r)dr \quad (4-14)$$

where:

$r_{max}$  : maximum radii of droplet, m

$r_{min}$  : minimum radii of droplet, m

There are two flux equations (4-6) and (4-13) and three unknowns,  $Q$ ,  $T_i^g$  and  $\dot{m}$ . Writing the mass balance closes the equation system and enables the calculation of the condensation rate  $\dot{m}$  for the case of dropwise condensation.

It should be noted that the gas phase in either laboratory experiments or a real field pipeline is a mixture of various components which dramatically deviates from an ideal state when system pressure is much greater than the atmospheric pressure. Therefore, the gas properties should be calculated with considering the effect of the pressure. The equations for the calculations of gas properties in a non-ideal gas mixture such as density, viscosity, diffusivity, heat capacity, and thermal conductivity and their derivation are described in Appendix II.

#### 4.2.4 Mass balance

All liquid water condensing at the pipe wall comes from the gas phase, i.e. the water vapor needs to pass through the mass transfer boundary layer to get to the wall. Therefore one can equate the condensation rate to the mass flux of water through the gas phase. When non-condensable gases are present, the resistance to mass transfer of water

vapor in the boundary layer can be rather significant. This makes the heat and mass transfer coupled and therefore they have to be resolved simultaneously. One can write:

$$\dot{m} = \rho_g \beta_g (x_b^g - x_i^g) \quad (4-15)$$

where:

$\beta_g$ : mass transfer coefficient in the gas boundary layer, m/s

$x_b^g$ : mass fraction of water vapor in the bulk gas flow,  $\text{kg}_v/\text{kg}_g$

$x_i^g$ : mass fraction of water vapor at the gas-liquid interface,  $\text{kg}_v/\text{kg}_g$

$\rho_g$ : density of gas,  $\text{kg}_g/\text{m}^3$

The mass transfer coefficient for the gas boundary layer can be estimated using the analogy (Stephan, 1992) between heat and mass transfer, according to

$$\rho_g \beta_g = \frac{h_g}{\hat{C}_p} Le^{2/3} \quad (4-16)$$

where:

$Le = k_g / \rho_g \hat{C}_p D_v$ : Lewis number

$D_v$ : diffusivity of water vapor in the gas phase,  $\text{m}^2/\text{s}$

The mass fraction of water vapor in a saturated gas mixture  $x(T)$  is a function of temperature T and can be calculated according to:

$$x(T) = \frac{p_{sat}(T)}{p_{tot}} \quad (4-17)$$

where:

$p_{sat}(T)$ : saturation vapor pressure as a function of temperature, kPa

$p_{tot}$ : total pressure, kPa

Therefore this constitutes another way that the heat and mass transfer processes are coupled:

$$x_b^g = x(T_b^g) = \frac{p_{sat}(T_b^g)}{p_{tot}} \quad (4-18)$$

$$x_i^g = x(T_i^g) = \frac{p_{sat}(T_i^g)}{p_{tot}} \quad (4-19)$$

To be able to solve the set of coupled heat and mass equations (4-6), (4-14) and (4-15) and obtain the condensation rate, one needs to know the minimum and maximum size of the droplets that are found on a condensing steel surface.

## 4.2.5 Determination of minimum and maximum radii of droplets

### 4.2.5.1 Minimum radius (Glicksman, 1972)

The saturation temperature and pressure in equilibrium are slightly dependent on the shape of the interface between the gas and the liquid. The difference of saturation temperature between curved surface and flat surface is thought of as the minimum

driving force (i.e. subcooling temperature) to form a droplet on the solid surface. From Clausius-Clapeyron relation, the pressure difference ( $\Delta P$ ) can be calculated through:

$$\Delta P = \frac{H_{fg}}{V_m^l - V_m^g} \frac{\Delta T}{T_s} \quad (4-20)$$

where:

$\Delta T$ : temperature difference, K

$V_m^l$ : specific volume of water liquid, m<sup>3</sup>/kg

$V_m^g$ : specific volume of water vapor, m<sup>3</sup>/kg

$T_s$ : saturation temperature, K

From Young-Laplace equation, the pressure difference of a curvature can be also calculated through:

$$\Delta P = \sigma \left( \frac{1}{R_1} + \frac{1}{R_2} \right) \quad (4-21)$$

where:

$R_1$  and  $R_2$ : characteristic radii to define a curvature, ( $R_1 = R_2 = r_{\min}$  for a spherical curvature), m

Substituting equation (4-21) to equation (4-20), for a hemispherical droplet one can get:

$$r_{\min} = \frac{V_m^l - V_m^g}{H_{fg}} \frac{2T_s \sigma}{\Delta T} = \frac{\rho_l - \rho_g}{H_{fg} \rho_g \rho_l} \frac{2T_s \sigma}{\Delta T} \quad (4-22)$$

#### 4.2.5.2 Maximum droplet radius and the condensation regimes

It is well known that gas velocity has a great influence on TLC. On one hand it affects the heat and mass transfer in the gas boundary layer (see equations (4-3) and (4-

15)), which are some of the most important steps in the whole condensation process. On the other hand the drag force exerted by the flowing gas onto the droplets is the key factor for determining droplet size and their mode of motion at the top of the line (condensation regimes). Through an analysis of the forces acting on a suspended droplet, it is possible to gain some insight into the mechanics of droplet growth and motion. In Figure 4-2, forces are considered as acting on a single hemispherical suspended droplet at the top of the line.

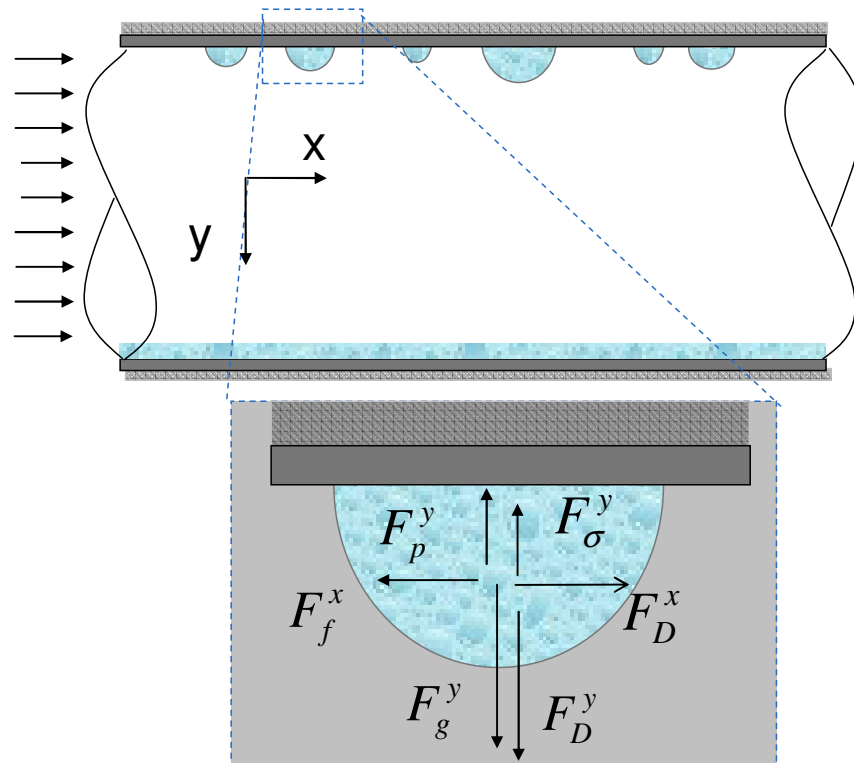


Figure 4-2: Force analysis on a single droplet.

( $F_B^y$  : buoyancy;  $F_\sigma^y$  : surface tension force;  $F_g^y$  : gravity force;  $F_D^y$  : flow drag force in y direction;  $F_f^x$  : friction force between the liquid droplet and the solid wall;  $F_D^x$  : flow drag force in x direction)

- The drag force  $F_D^x$  represents the pull by the flowing gas exerted on the droplet. It can be expressed by (Bikerman, 1950):

$$F_D^x = \frac{1}{2} C_D \rho_g A_{drop} U_g^2 \quad (4-23)$$

where:

$C_D$ : drag coefficient

$A_{drop} = r^2 \pi / 2$ : frontal area of a hemispherical droplet,  $m^2$

$U_g$ : gas velocity, m/s

The drag coefficient  $C_D$  depends on the shape of the droplet. For a sphere, the  $C_D$  is dependent on the Reynolds number and varies from 0.07 to 0.5. However, in the range of Reynolds numbers typical for TLC, the  $C_D=0.44$ .

- The “friction” force  $F_f^x$  represents the adhesion between droplet and the steel wall that opposes the drag force and keeps the droplet in place. For a suspended droplet, an empirical equation is adopted from Bikerman (1970):

$$F_f^x = k_f \cdot \sigma \cdot r \quad (4-24)$$

where:

$\sigma$ : surface tension, N/m

$k_f$ : friction coefficient which is a function of inner pipe surface roughness  $h$ :

$$k_f = f(h) \quad (4-25)$$

Bikerman (1970) performed a series of experiments on the surface of steel to determine the effect of surface roughness on the sliding droplets. It was found that when  $h$  is less than  $0.5 \mu m$  the coefficient  $k_f$  changes significantly with roughness. But when  $h$  is in the range  $0.5$  to  $3.0 \mu m$ , the coefficient  $k_f$  is approximately constant around 1.5.

- Gravity force  $F_g^y$  tends to either detach the droplet from the top of the pipe or cause it to slide down the sides of the pipe:

$$F_g^y = \rho \frac{4}{6} \pi r^3 g \quad (4-26)$$

- The downward drag force  $F_D^y$  arises due to the hemispherical shape of the droplets. No explicit expressions for calculation of this force have been found and in this study it is assumed:

$$F_D^y = \frac{1}{2} F_D^x \quad (4-27)$$

- The surface tension force  $F_\sigma^y$  keeps the droplet attached to the pipe wall and counters the effect of gravity. For a hemispherical droplet it can be calculated as (Adamsn, 1990):

$$F_\sigma^y = \pi r^2 \frac{2\sigma}{r} \quad (4-28)$$

- The buoyancy  $F_B^y$  for a suspended hemispherical droplet can be calculated as:

$$F_B^y = \frac{4}{6} \pi r^3 \rho_g \quad (4-29)$$

Very small droplets are firmly attached to the steel surface i.e. the friction force is much larger than the drag force:  $F_f^x > F_D^x$  and the droplet cannot slide along the pipe wall.

Also, the surface tension and the pressure forces exceed the gravity and downward drag forces:  $F_{\sigma}^y + F_B^y > F_g^y + F_D^y$  so the droplet does not detach and fall. Clearly all the forces are a function of the droplet diameter. As condensation proceeds and a droplet grows the effect of gravity increases fastest (with  $r^3$ ). When the droplet reaches a critical size, a force balance in either  $x$  direction or  $y$  direction is reached. If the force balance in  $y$  direction is established before that in  $x$  direction, the droplet will fall down before it slides away. If the force balance in  $x$  direction is established before that in  $y$  direction, the droplet will slide along the pipe before it detaches and falls down. In either case, this represents the end of the lifetime of a single droplet and the maximum radius  $r_{max}$  of the droplet can be calculated. In addition, the mode of motion of droplets could enable us to determine the condensation regime: either the falling droplet condensation regime or the sliding droplet condensation regime.

#### 4.2.6 Numerical method

All equations presented above which are heavily coupled with each other cannot be solved without an iteration. An algorithm is invoked to solve the non-linear equation system. In Figure 4-3, the detailed procedure of the calculation is given as:

- 1) Guess the interfacial temperature  $T_i^g$ ;
- 2) Calculate the maximum (Equation (4-23) to (4-29)) and minimum (Equation (4-22)) droplet sizes (Equation (4-22));
- 3) Compute all unknown independent parameters:  $Q$  (Equation (4-14)),  $Q_g$  (Equation (4-3)),  $x_i$  (Equation (4-18) and (19)) except the condensation rate;

- 4) Calculate the two condensation rates:  $\dot{m}_{mass}$  and  $\dot{m}_{heat}$  by mass balance equation (Equation (4-15)) and heat balance equation (Equation (4-6)), respectively;
- 5) Generate a new value of the interfacial temperature through Newton-Raphson iteration if two condensation rates in the last step are not equal;
- 6) Output results when two condensation rates in the fourth step are equal.

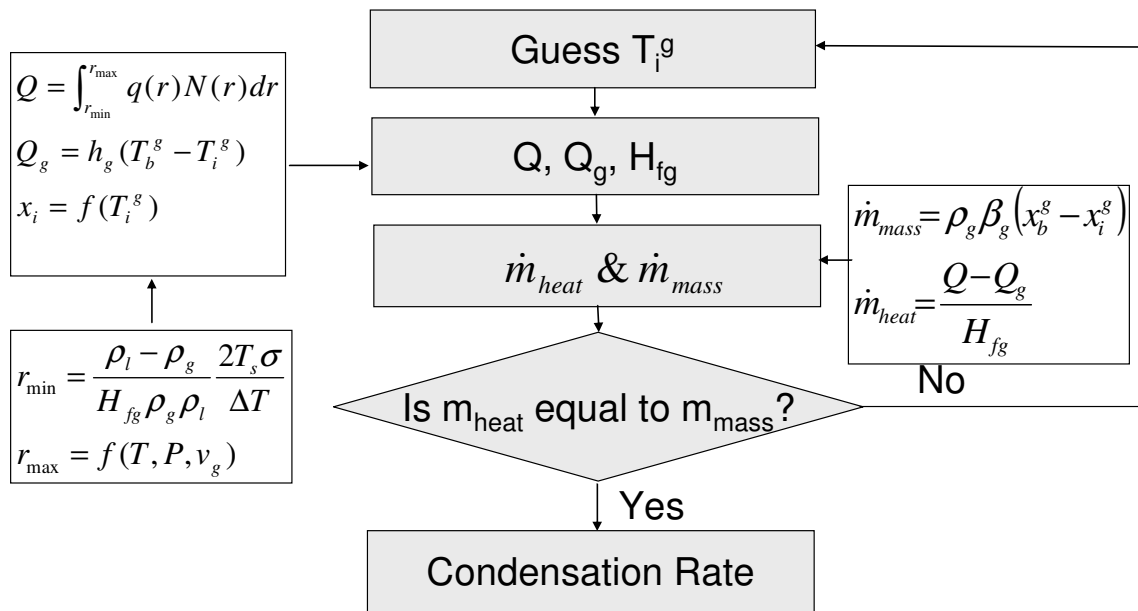


Figure 4-3: Flow chart for the numerical calculation in the condensation model

### 4.3 Verification of the condensation model

#### 4.3.1 Condensation rate and heat flux

With the model described above, the condensation rate for a dropwise condensation regime could be calculated for a wide range of experimental conditions. In order to verify the model some experiments have been performed in large scale, high

temperature, high pressure flow loops. The test section (shown in Figure 3-2) where the data were collected was equipped with cooling system, which was used to control the inner wall temperature through adjustment of flow rate of cooling water. When hot wet gas flow contacted with the cooler inner wall, condensation happened and the condensed water was drained to the liquid collector on the down stream. If the condensation rate for the whole inner surface of the text section was assumed to be uniform, it could be calculated in  $\text{mL/m}^2/\text{s}$  (the total volume of the liquid divided by surface area and time). The parameters and their ranges were listed in Table 4-1. More detail about the experimental setup and procedure was described in Vitse's work (2002). The comparisons between experiments and model prediction (Figure 4-4) show that the model's performance is reasonably good.

Table 4-1: Test conditions on condensation in large scale loop

Variables	Range	
	Minimum	Maximum
Absolute pressure (bara)	3	8
CO <sub>2</sub> partial pressure (bara)	2	7
Gas temperature (°C)	40	90
Subcooling temperature (°C)	1	13
Gas velocity (m/s)	3	8

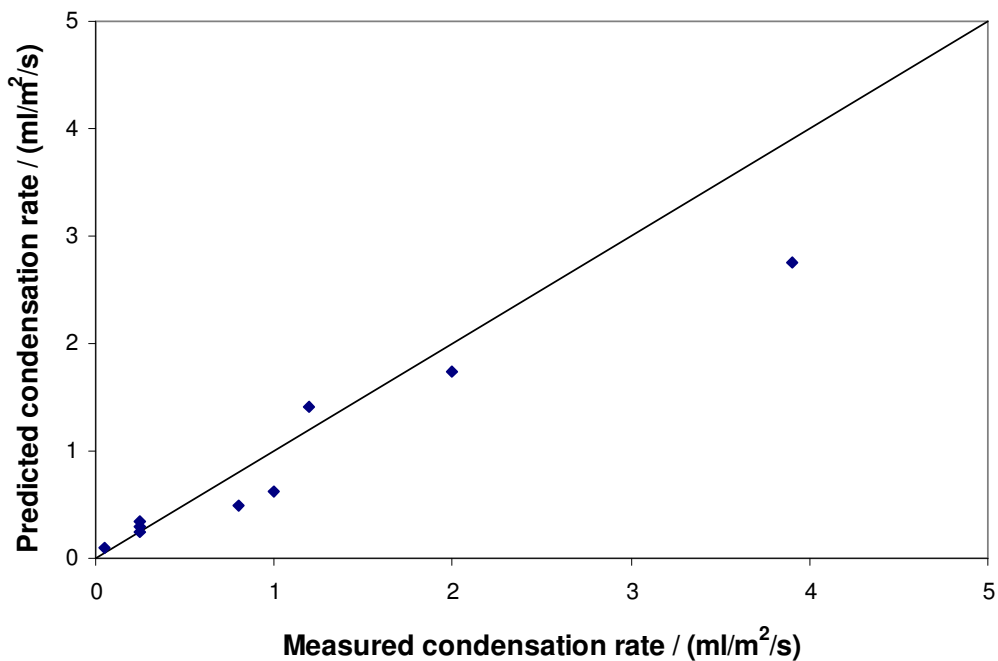


Figure 4-4: Comparison of the measured and predicted condensation rate

#### 4.3.2 Maximum droplet size and the dropwise condensation regimes

In order to verify the model for the maximum droplet size, two series of experiments have been done in different experimental setups: a transparent flow loop (Figure 4-5) and a stainless steel test section (Figure 3-2). In the transparent loop, a digital camera was used to take pictures of the droplet from the outside. The droplet size was measured through a scale inside the pipeline. The motion of droplets could be determined by direct observation. The detailed description of the experimental setup and procedure could be found elsewhere (Singer et al., 2004-2007). In a separate series of experiments (Sapaly, 2007), an *in situ* video camera was inserted into the stainless test section in one probe port at the bottom of the line (Figure 3-2) in order to record the

information about the lifetime of droplets, motion of droplets, and the maximum size of droplets at different conditions. In various experiments, all parameters except gas velocity were kept constant and the maximum size of droplets then measured as a function of the gas velocity. In the model development, it seemed that gas temperature, gas velocity, and gas pressure are the most important factors for determining the maximum size and motion of droplets. The effect of all these major parameters was examined through either experiments or numerical tests.

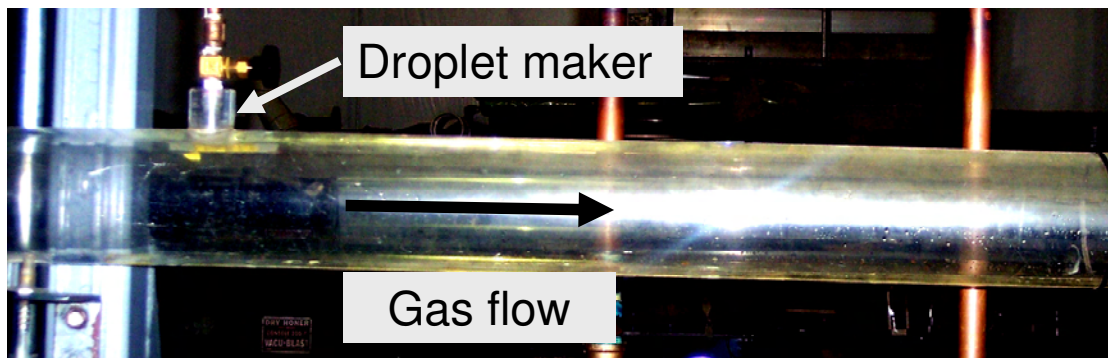


Figure 4-5: Experimental setup of a transparent flow loop

The measured maximum size of droplet is compared with the predictions in all graphs with the gas velocity as the  $x$  axis and the droplet diameter as the  $y$  axis. From Figure 4-6, it can be seen that a very good agreement is achieved between the model prediction and experimental data in the transparent loop. Note how under the given set of conditions, the droplet lifetime ends due to dislodgement by gravity at low velocities while at high velocity this happens due to the gas drag force. Assisted by the in situ camera, the data from the dynamic growth process of a droplet in dropwise condensation

were collected from the test section in large scale stainless steel loop, which are plotted in Figure 4-7 and Figure 4-8 at different system pressures. From both graphs, it appears that the model can predict the overall trend seen in the experiments except for several deviating points close to the transition zone.

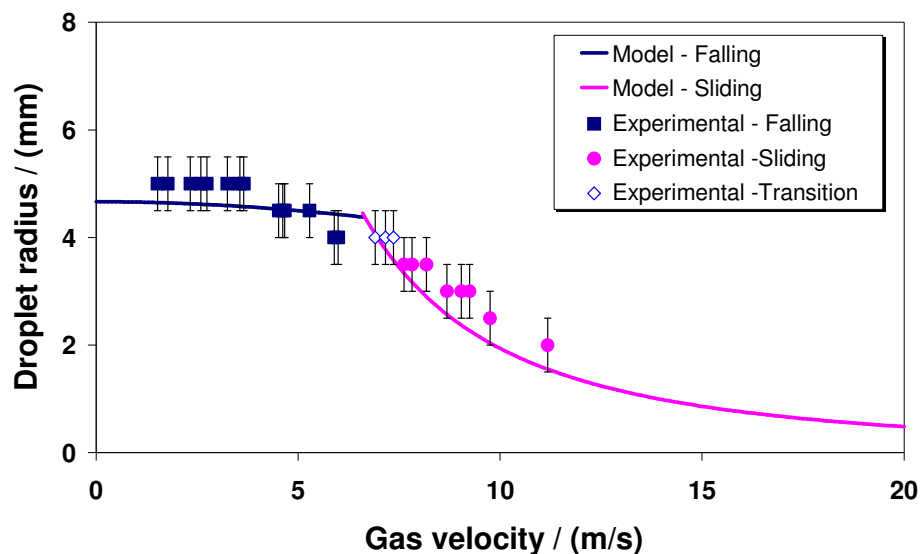


Figure 4-6: Comparison between experimental results and the model prediction on the maximum droplet and condensation regimes in transparent flow loop  
 $(T_g = 25 \text{ }^\circ\text{C}, P_T = 1 \text{ bar})$

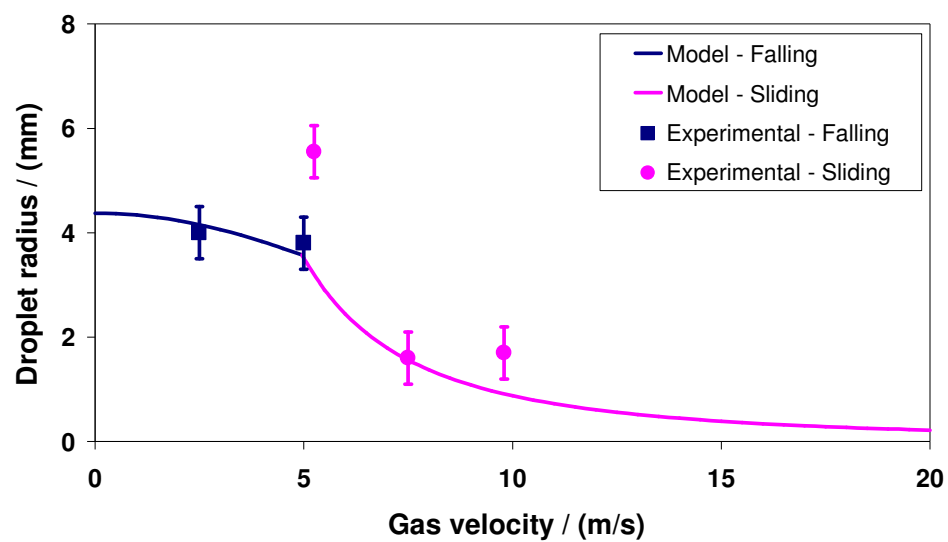


Figure 4-7: Comparison between experimental results and the model prediction on the maximum droplet size and condensation regimes in stainless flow loop at low pressure ( $P_T = 3 \text{ bar}$   $T = 75 \pm 5 \text{ }^\circ\text{C}$ )

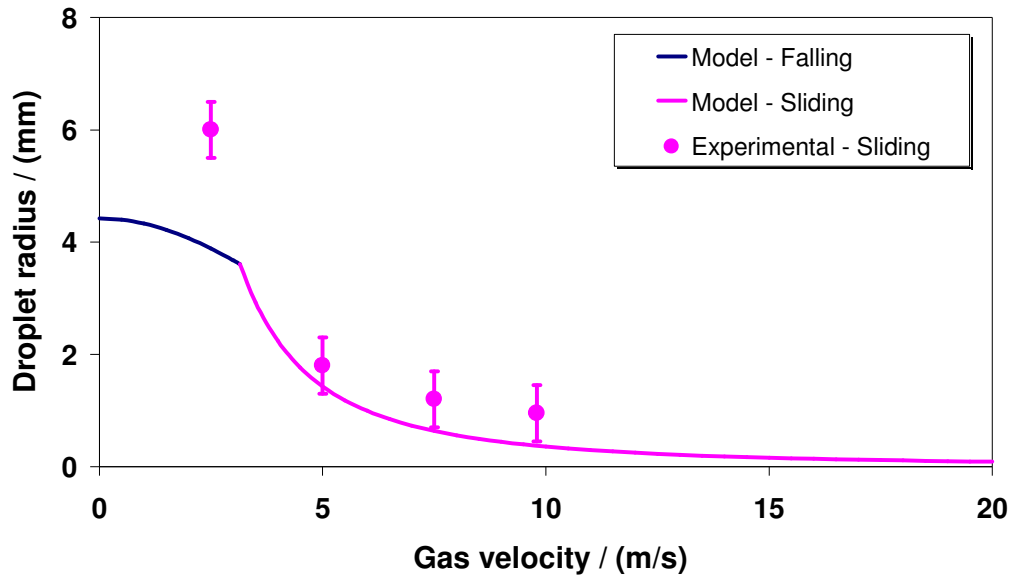


Figure 4-8: Comparison between experimental results and the model prediction on the maximum droplet size and condensation regimes in stainless flow loop at high pressure ( $P_T = 7$  bar,  $T = 70 \pm 5$  ° C)

#### 4.4 Parametric study

One of the advantages of having a mechanistic model (such as the dropwise condensation model) is that it could be used to carry out numerical tests, in which the effect of various parameters could be revealed. Furthermore, the parametric study provided a theoretical guidance for our ongoing experiments in corrosion and condensation studies.

##### 4.4.1 Parametric study of the condensation model

As mentioned above, dropwise condensation is a combined process of heat and mass transfer. All factors which could either increase driving forces (concentration

difference for mass transfer and/or temperature difference for heat transfer) or decrease the respective transfer resistances (in heat and/or mass) can promote the condensation process. As the driving force (the water vapor concentration difference) is increased with increased gas temperature, the condensation process will be enhanced (Figure 4-9). Although water vapor pressure, which exclusively depends on temperature, is constant at different gas pressures, more non-condensable gas at higher total pressure can dilute the gas mixture, resulting in the reduction of the water vapor fraction in the gas mixture. Consequently, the condensation rate is decreased with increased total pressure (Figure 4-10). Since both heat and mass transfer resistances are reduced by more turbulent gas flow at higher gas velocities, condensation rate increased (Figure 4-11). It is obvious that the subcooling temperature is an important factor for enhancing the condensation rate (Figure 4-12). Among all these parameters, total pressure is the most important practical influence since mass transfer in the gas boundary layer is the rate controlling process. The condensation rate for a pure water vapor condensation system is almost tenfold that in system with non-condensable gases (Figure 4-10).

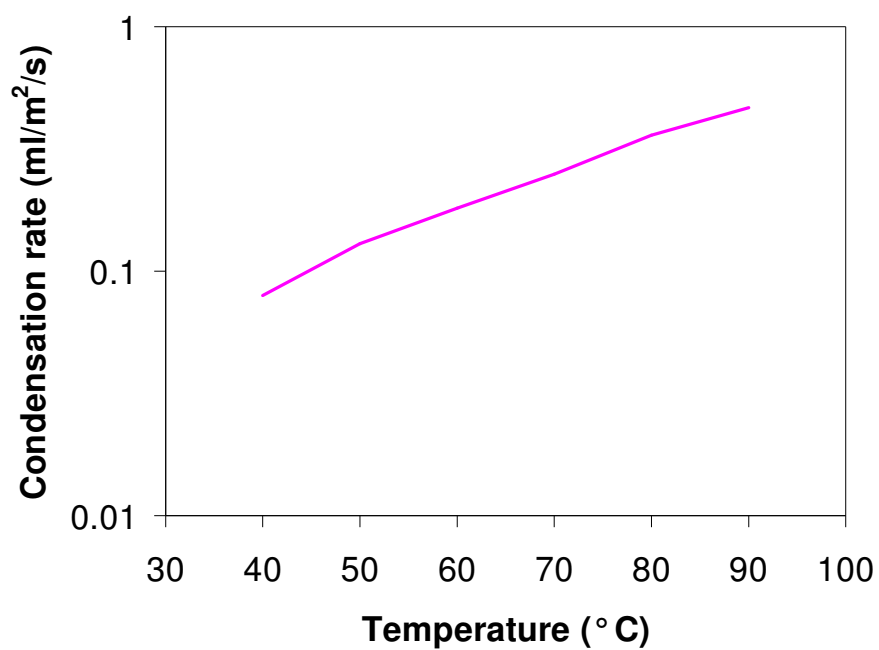


Figure 4-9: Effect of gas temperature on the condensation rate

( $\Delta T = 2$  °C,  $U_{SG} = 5$  m/s,  $P_T = 3$  bar, and  $p_{CO_2} = 2$  bar)

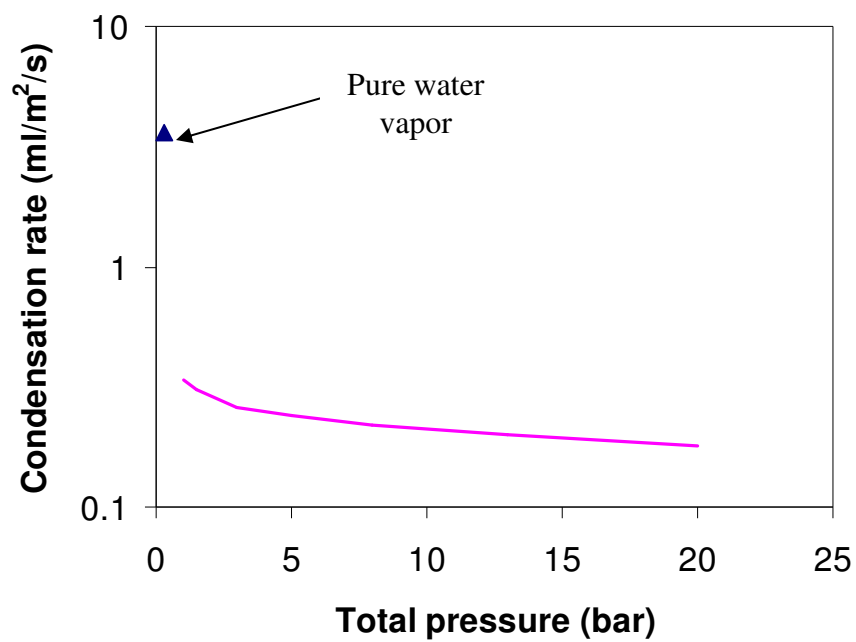


Figure 4-10: Effect of total pressure on the condensation rate

( $T_{gas} = 70\text{ }^{\circ}\text{C}$ ,  $U_{SG} = 5\text{ m/s}$ ,  $\Delta T = 2\text{ }^{\circ}\text{C}$ , and  $pCO_2 = 2\text{ bar}$ )

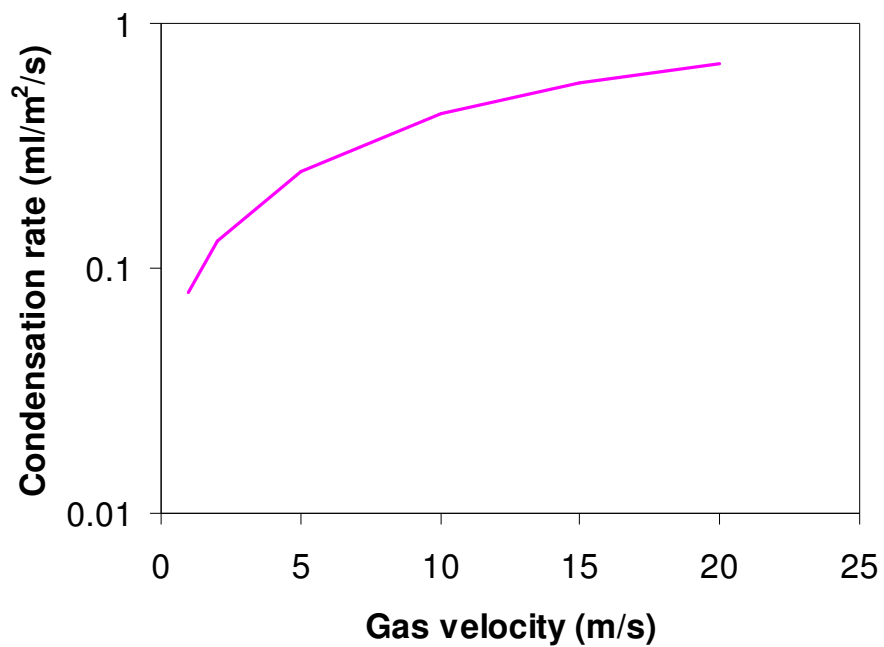


Figure 4-11: Effect of gas velocity on the condensation rate

( $T_{gas} = 70\text{ }^{\circ}\text{C}$ ,  $\Delta T = 2\text{ }^{\circ}\text{C}$ ,  $P_T = 3\text{ bar}$ , and  $p_{CO_2} = 2\text{ bar}$ )

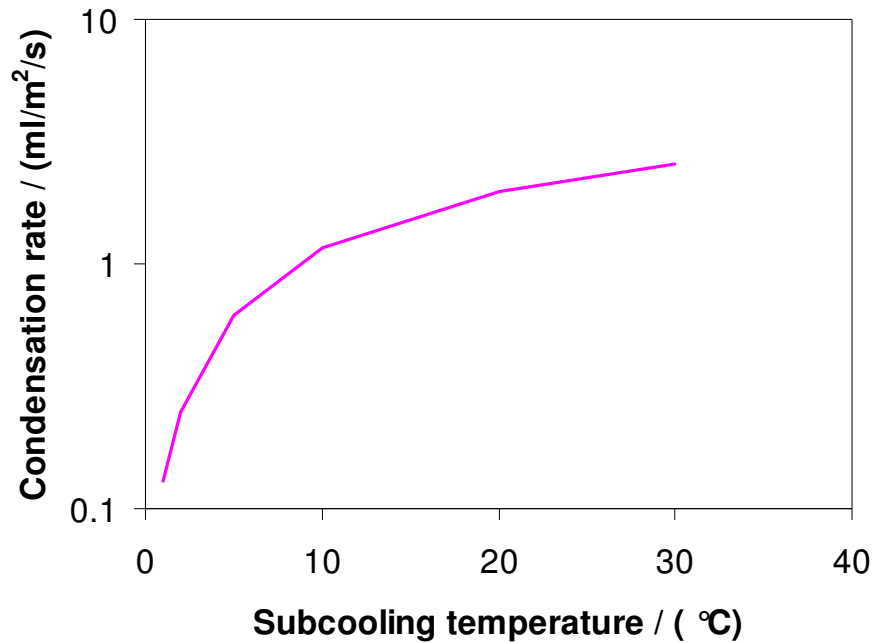


Figure 4-12: Effect of subcooling temperature on the condensation rate

$$(T_{gas} = 70 \text{ } ^\circ\text{C}, U_{SG} = 5 \text{ m/s}, P_T = 3 \text{ bar, and } pCO_2 = 2 \text{ bar})$$

#### 4.4.2 Maximum droplet and condensation regimes

The theoretical analysis of forces on a single droplet can provide not only the maximum droplet size but also the prediction of the condensation regimes. In fact, the model was developed before the establishment of the experimental setup with an *in situ* camera. Through a parametric study, key influencing factors have been identified in the determination of the maximum droplet size. The result of numerical tests assisted the design of the test matrix in the flow loop.

In both theoretical and experimental studies, condensation regimes associated with the droplet motion have been found to be of particular importance for corrosion

process. The results obtained from numerical tests performed in various conditions can be used to create a condensation regime map, in which the flow conditions (total pressure and gas velocity) for the transition from one condensation regime to another are clearly indicated.

#### **4.4.2.1 Parametric study of the model for the maximum droplet size**

In the model development, several parameters: the gas temperature, the gas velocity, and the total pressure have been included. Their relative importance on the maximum droplet size and the condensation regime could be evaluated by a parametric study. In Figure 4-13 it is shown that the influence of gas pressure on the maximum droplet size is significant, especially in the sliding zone. The transition from falling droplet condensation to sliding droplet condensation happens at much smaller gas velocity at higher gas pressure. The increased gas density at high gas velocity makes the drag force increase dramatically. Thus, the force balance in horizontal direction can be established at lower gas velocities. In contrast, it seems that gas temperature only has a minor effect on the maximum droplet size and the critical gas velocity (Figure 4-14). It should be noted that, based on field experience, the magnitude of gas temperature change which is practically possible is rather small (e.g. from 30 to 90 °C) while the gas pressure can change by three orders of magnitude (from 1 to 100 bar).

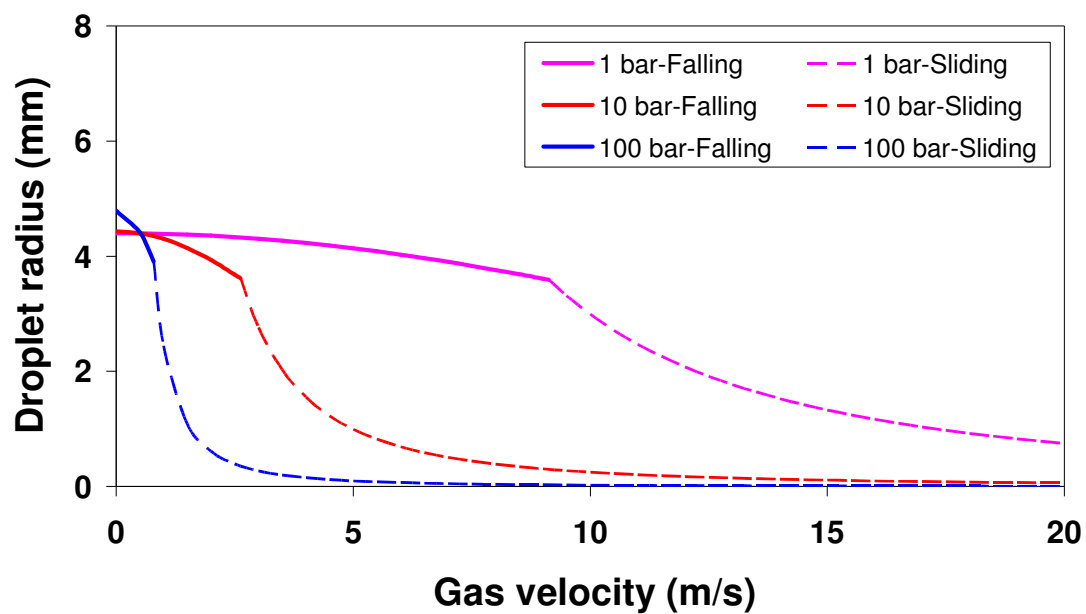


Figure 4-13: Effect of gas pressure on the maximum droplet size and condensation regimes ( $T_g = 70$  °C)

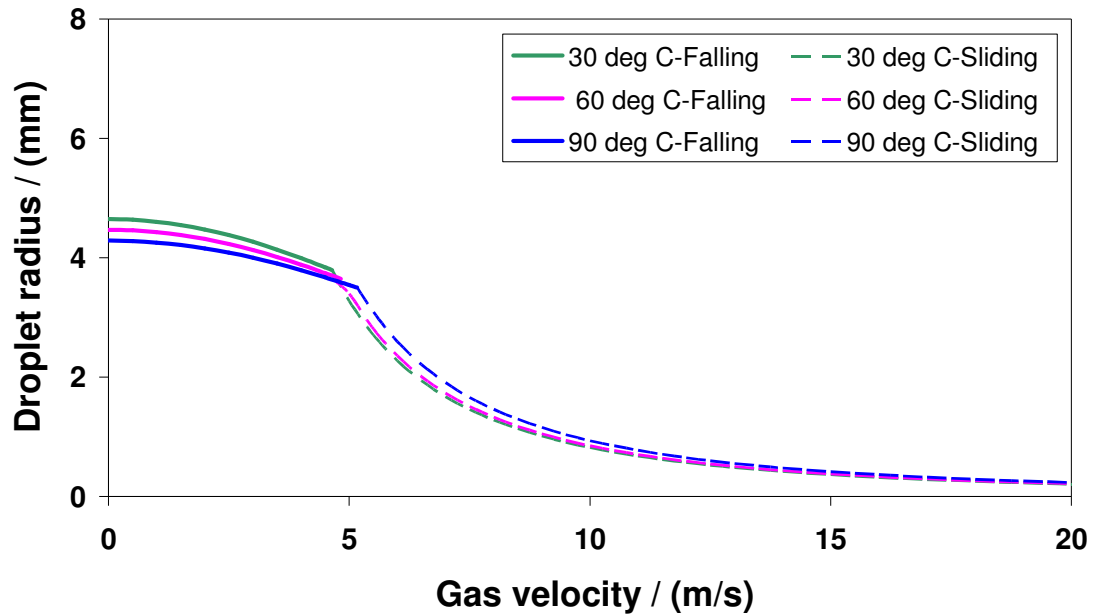


Figure 4-14: Effect of gas temperature on the maximum droplet size and condensation regimes ( $P_T = 8$  bar)

#### 4.4.2.2 Condensation regimes

In the literature review, two different condensation types, filmwise and dropwise, and their characteristics have been described in detail. Through experiments and theoretical analysis, it is found that dropwise condensation can be further divided into several different sub-categories: falling droplet, sliding droplet, and water rivulet. All these condensation regimes and their transitions against gas velocity are delineated in Figure 4-15.

- Falling droplet condensation:** In falling droplet condensation, droplets, which are separated from each other in both the side view and the cross section, are

removed only through falling due to the gravity.

- **Sliding droplet condensation:** When gas velocity is increased, droplets are pushed by flowing gas to slide along the surface. Sliding droplet condensation ensues. In the side view, droplets move along the surface.
- **Water rivulet condensation:** When more and more droplets slide along the pipe in a relay, a number of rivulets are formed in different locations. Since these rivulets are separated from each other, they still look like droplets in the cross section. However, they look like liquid films in the side view. In addition the liquid at the bottom of the line at high gas velocity can be swept up along the pipe wall. More surface area at the bottom has been covered by the liquid.
- **Filmwise condensation:** Eventually, when water rivulets join together side by side. This film will be connected with the bulk liquid at the bottom of the line. The whole inner surface of the pipeline is then completely covered by a liquid film. This is called filmwise condensation in heat transfer and annular flow in hydrodynamics.

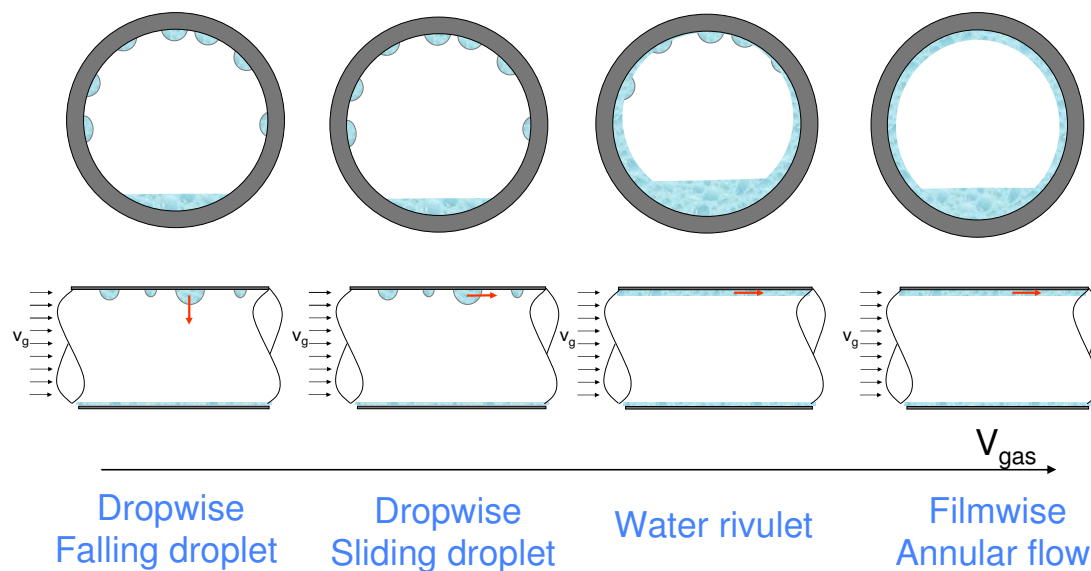


Figure 4-15: Condensation regimes at the top of the line

The transition from one regime to another is important not only for the condensation process but also for the corrosion process. In order to explain the problem in a simple way, a condensation regime map (Figure 4-16), similar to the flow regime map, is drawn with various transition lines. The model of the maximum droplet size provides a criterion for the transition from falling droplet to sliding droplet condensation. The transition from rivulet to filmwise (or from stratified to annular flow) could be determined through a hydrodynamic analysis (discussed in Chapter 6). However, the mechanism behind the transition from sliding droplet to water rivulet condensation is still not completely understood. Further study of the physical processes governing this transition will be very important in the future developments of this model.

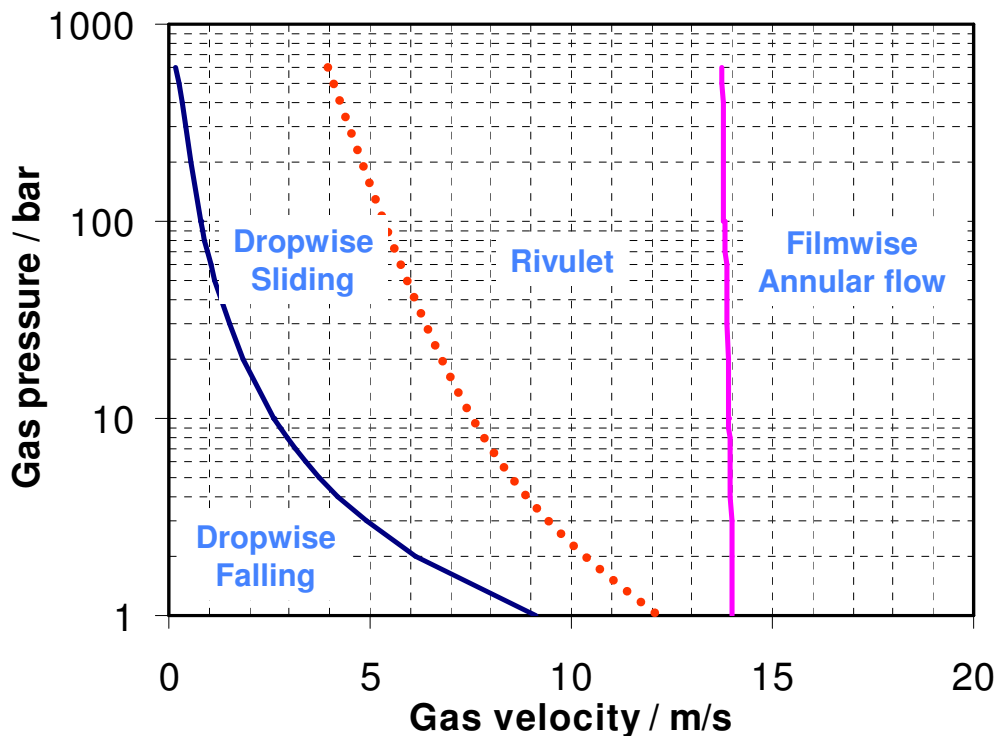


Figure 4-16: Condensation regime map

#### 4.5 Summary

Dropwise condensation at the top of the line is a complicated process due to the presence of large amount of non-condensable gas components in the natural gas. Neither the filmwise condensation model nor the pure vapor dropwise condensation model, which were found in the open literature, could precisely describe the condensation process. Through a coupled analysis of heat transfer, mass transfer, hydrodynamics, and forces acting on a single droplet, all important factors have been included in the newly developed mechanistic model. The model performance on the prediction of condensation rate, the maximum droplet size, and condensation regimes has been verified by

experiments in large scale loops with a specially designed test section. The present condensation model presents a sound theoretical base for the development of a corrosion model at the top of the line, which was the ultimate goal of this project.

## CHAPTER 5: A MECHANISTIC MODEL OF TOP OF THE LINE CORROSION

### 5.1 Introduction

In the last couple of decades, several empirical or semi-empirical models have been developed to predict the corrosion rate at the top of the line. Among them, the simple de Waard's model (1993) and Pots and Hendriksen's (2000) model have been accepted by the industry for a period of time. However, more and more questions have been raised about the validity of both models due to their inherent limitations. For example, the introduction of a TLC correction factor in de Waard's model (1993) indicated a serious lack of understanding of the mechanism behind the phenomenon of TLC, which could not satisfy entirely the need of the industry. Pots and Hendriksen's model (2000) represented a significant improvement, but without being able to reliably predict the condensation rate and regimes, and by ignoring some other important parameters related to mass transfer and electrochemistry, it can only be seen as a first crude attempt to predict TLC. More recently, Vitse (2002) proposed a quasi-mechanistic model to predict the corrosion rate in TLC, however, his efforts would have been useful at best in describing corrosion during the filmwise condensation process, which is not common for TLC.

Based on the sound theory, the mechanistic model of dropwise condensation at the top of the line described in the previous chapter can meet the need for the development of TLC models. Moreover, the mechanistic model at the bottom of the line developed by Nestic and his co-workers (Nestic, 1996; Nordsveen and Nestic, 2003; Nestic,

2003; Nescic and Lee, 2003), which covers corrosion, chemistry, and film formation, provided a powerful platform for further development fit for various purposes. After a thorough analysis it was concluded that the core theory presented in the Nescic's model was fully applicable and could be transplanted to the TLC scenario.

In essence, the corrosion mechanism at the top of the line is not different from that at the bottom of the line. In both locations metal loss is caused by the attack of aggressive species in the water solution through the same electrochemical reactions on the metal surface. From the point view of corrosion kinetics, the corrosion reaction rate depends on the surface concentrations of the reactants and products rather than the bulk concentrations. At the bottom of the line, these surface concentrations are determined by the nature of the turbulent stratified flow. Based on the bulk species concentrations in the water layer at the bottom of the line, which are determined to be in equilibrium with the gas phase through Henry's law, and the steel surface concentrations could be established by solving one-dimensional mass transfer equations through a liquid boundary layer near the metal surface.

In contrast to the continuous liquid phase at the bottom of the line, randomly distributed droplets cover the whole surface at the top of the line. The liquid inside a droplet is stagnant while the whole liquid volume of the droplet changes with time due to the condensation. Mathematically speaking, this amounts to a transient three dimensional problem with a moving boundary.

In the present study, this complicated three-dimensional problem is simplified to a one-dimensional problem after an assumption (discussed below) is made. A non-uniform

mesh with a fixed computation domain, which has the same size as the maximum droplet, is defined to cover both the liquid and gas phase. The mass conservation equation without the convection term is then solved to calculate the concentration profile of various species in the droplets. The boundary conditions at either side of the computation domain are determined by Henry's law and the electrochemical reactions, respectively. In order to include the effect of corrosion product film, porosity and its calculation are adopted from Nescic's work, which provides another equation in addition to the equation system above. Eventually, the solution of the complicated mathematic matrix at each time step enables us to calculate the instantaneous corrosion rate.

A software package (TOPCORP), in which all the equations and their calculations are hidden behind a user friendly interface, was designed and developed to predict TLC related risks in wet gas pipelines. It represents a convenient tool for corrosion engineers in the design of their field facilities and is actually already in use in the oil and gas industry today.

## **5.2 Model development**

It is well known that the dropwise condensation is a random process. From a statistical point of view, every point on the metal surface has the same probability to be covered by a certain size of droplets at any given point in time. Therefore the condensation rate can be assumed to be uniform over the entire surface. Although one point can corrode more than another at the beginning of the process, the entire surface will be corroded uniformly after some time. This way, the calculations can be carried out

as if the surface was covered by a uniform liquid layer which follows continuous cycles of growth and detachment (just like a single droplet).

In order to make it a feasible task, one needs to simplify the mathematical challenge in describing a complex random corrosion process occurring under a family of growing hemispherical droplets with a known size distribution. Following the argument presented above, a family of two-dimensional hemispherical droplets is represented with a one-dimensional liquid layer (as shown in Figure 5-1). Droplet/layer growth due to condensation is represented by the increase in the height of the water column until the maximum size of the droplet,  $r_{max}$ , is reached. At that point the droplet is dislodged and new droplet starts growing in its place; this is simulated by reducing the size of the water column to minimum size of the droplet,  $r_{min}$ , and the cycle starts all over again.

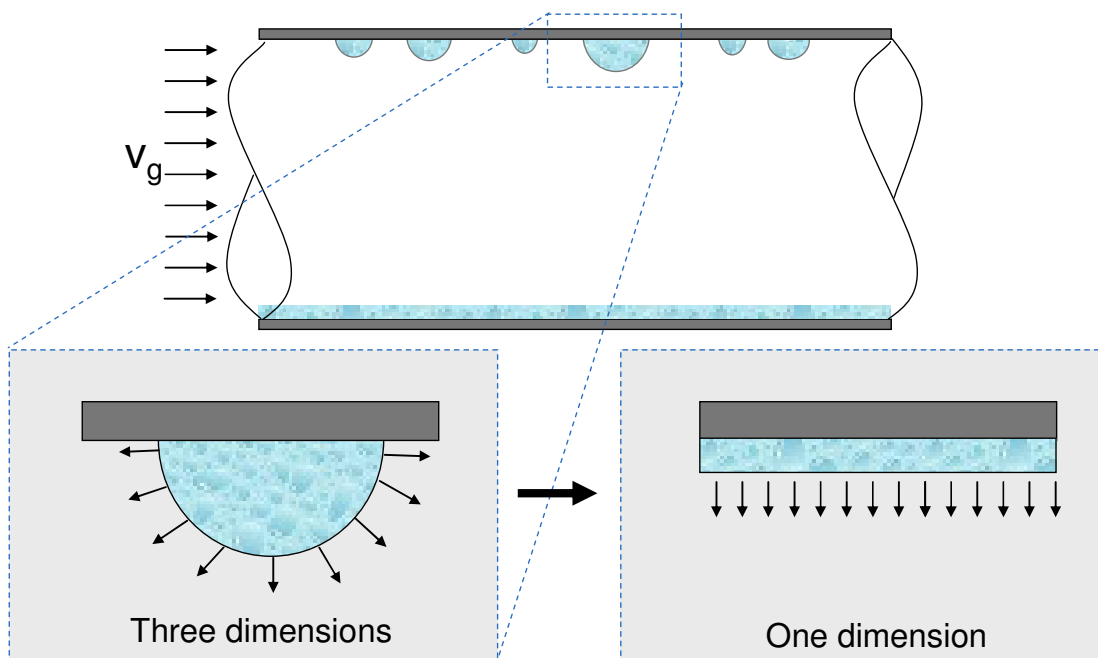


Figure 5-1: The simplification from a three-dimension problem to a one dimensional problem

The corrosion at the top of the line (or anywhere else in the line for that matter) involves three important processes occurring simultaneously:

- chemical reactions, including homogeneous (dissociation, dissolution, etc.) and heterogeneous (precipitation of corrosion product scales),
- electrochemical reactions at the metal surface and
- transport of species in the liquid droplet.

Since these processes occur at different rates, the slowest one will be the rate controlling process which will determine the corrosion behavior. These processes are modeled according to the physics underlying the different phenomena. Fundamental equations, already published by Nescic and his coworkers (Nescic, 1996; Nordsveen and

Nesic, 2003; Nesic, 2003; Nesic and Lee, 2003) are used to quantify the whole process mathematically. All constants in the equation system, such as equilibrium constants, reaction rate constants and diffusion coefficients, are taken from the open literature referenced by Nesic's papers (Nesic, 1996; Nordsveen and Nesic, 2003; Nesic, 2003; Nesic and Lee, 2003).

### 5.2.1 Chemical reactions

Water dissociation	$\text{H}_2\text{O} \Leftrightarrow \text{H}^+ + \text{OH}^-$
Dissolution of carbon dioxide	$\text{CO}_2 (\text{g}) \Leftrightarrow \text{CO}_2 (\text{aq})$
Carbon dioxide hydration	$\text{CO}_2 + \text{H}_2\text{O} \Leftrightarrow \text{H}_2\text{CO}_3$
Carbonic acid dissociation	$\text{H}_2\text{CO}_3 \Leftrightarrow \text{H}^+ + \text{HCO}_3^-$
Bicarbonate anion dissociation	$\text{HCO}_3^- \Leftrightarrow \text{H}^+ + \text{CO}_3^{2-}$
Acetic acid liquid / vapor equilibrium	$\text{HAc} (\text{aq}) \Leftrightarrow \text{HAc} (\text{vap})$
Acetic acid dissociation	$\text{HAc} \Leftrightarrow \text{H}^+ + \text{Ac}^-$

All the reactions shown above (reactions and their reaction constants shown in detail in Appendix I) can be in equilibrium if the reaction rates are fast compared to other processes in the corroding system. According to stoichiometry, the reaction rate for species  $j$  can be calculated in the  $k$ -th chemical reaction with tensor notation applies for the subscripts:

$$R_j = A_{jk} \mathfrak{R}_k, \quad j = 1, 2, \dots, n_s; \quad k = 1, 2, \dots, n_r \quad (5-1)$$

where:

$A_{jk}$ : stoichiometric matrix ( $n_s \times n_r$  size) where row  $j$  represents the  $j$ -th species, column  $k$  represents the  $k$ -th chemical reaction

$\mathfrak{R}_k$ : reaction rate vector

$n_s$ : the number of species

$n_r$ : the number of reactions

### 5.2.2 Transport processes (Nesic, 1996)

In the droplets, the transport of species can be described using a species conservation equation. The expression for transport of species  $j$  in the presence of chemical reactions is valid for the pure liquid in the droplet as well as for the liquid in the porous surface scale:

$$\frac{\partial \varepsilon C_j}{\partial t} = -\frac{\partial (\kappa N_j)}{\partial y} + \varepsilon R_j \quad (5-2)$$

where:

$C_j$  concentration of species  $j$ , moles/m<sup>3</sup>

$\varepsilon$ : volumetric porosity a of the scale respectively (=1, bulk solution);

$\kappa$ : surface permeability of the scale(=1, bulk solution).

$N_j$  flux of species  $j$ , moles/m<sup>2</sup>·s

$R_j$  source or sink of species  $j$  due to chemical reaction, moles/m<sup>3</sup>·s

$t$  time, s

$y$  spatial coordinate.

The transport of species has three components: diffusion, convection and electromigration. In the first approximation it can be assumed that the liquid in the droplets is stagnant, and therefore no convection term exists in the species conservation equation. The electromigration is neglected as well and the electroneutrality equation is used instead:

$$\sum_1^{n_s} z_j \cdot C_j = 0 \quad (5-3)$$

where:

$z_j$       number of charge for species  $j$ ,

Therefore, the flux contains only a diffusion term and can be expressed using Fick's law:

$$N_j = -D_j \frac{\partial C_j}{\partial y} \quad (5-4)$$

where:

$D_j$ :      molecular diffusivity of species  $j$ ,  $m^2/s$

Combining all equations above, the overall species conservation equation in the droplet becomes:

$$\frac{\partial \epsilon C_j}{\partial t} = D_j \frac{\partial^2 (\kappa C_j)}{\partial^2 y} + \epsilon R_j \quad (5-5)$$

The permeability  $\kappa$  of the surface scale is a function of porosity and tortuosity of the film. An empirical correlation  $\kappa = \varepsilon^{1.5}$  from Netic (1996) can be adopted to calculate the permeability.

### 5.2.3 Scale growth

The calculation of the porosity  $\varepsilon$  and the overall scale growth model is taken entirely from Netic's paper (Netic, 1996; Nordsveen and Netic, 2003; Netic, 2003; Netic and Lee, 2003). For  $\text{FeCO}_3$ , there is an additional species conservation equation written in the same form as for other species (with the diffusion term neglected as  $\text{FeCO}_3$  is a solid).

$$\frac{\partial C_{\text{FeCO}_3}}{\partial t} = R_{\text{FeCO}_3} \quad (5-6)$$

where:

$R_{\text{FeCO}_3}$ : precipitation/dissolution rate of iron carbonate, moles/m<sup>3</sup>/s

The volumetric porosity  $\varepsilon$  describes the morphology of the  $\text{FeCO}_3$  scales and is the principal scale parameter affecting the transport of species.

$$\varepsilon = \frac{V_{\text{void}}}{V_{\text{total}}} = \frac{(V_{\text{total}} - V_{\text{FeCO}_3})}{V_{\text{total}}} = 1 - \frac{V_{\text{FeCO}_3}}{V_{\text{total}}} = 1 - \frac{C_{\text{FeCO}_3} \cdot M_{\text{FeCO}_3}}{\rho_{\text{FeCO}_3}} \quad (5-7)$$

where:

$M_{\text{FeCO}_3}$ : iron carbonate's molecular weight (115.8 kg/mol)

$\rho_{\text{FeCO}_3}$ : iron carbonate's density (3.9 kg/m<sup>3</sup>)

The scale growth equation (5-6) can be then expressed as a function of porosity:

$$\frac{\partial \varepsilon}{\partial t} = -\frac{M_{FeCO_3}}{\rho_{FeCO_3}} R_{FeCO_3} \quad (5-8)$$

The  $FeCO_3$  precipitation/dissolution reaction is modeled using Van Hunnik's equation (1996):

$$R_{FeCO_3} = \frac{A}{V} \cdot e^{\frac{52.4 - 119.8}{RT}} \cdot K_{sp} \cdot (S - 1) \cdot (1 - S^{-1}) \quad (5-9)$$

where:

$K_{sp}$  solubility product constant for iron carbonate,  $(\text{moles}/\text{m}^3)^2$

$S$  supersaturation ( $S = \frac{C_{Fe^{2+}} \cdot C_{CO_3^{2-}}}{K_{sp}}$ )

A latest equation for the calculation of the solubility product constant is adopted from Sun (2007), which is shown as:

$$\log(K_{sp}) = -59.3498 - 0.041377T - \frac{2.1963}{T} + 24.5724 \log(T) + 2.518I^{0.5} - 0.657I \quad (5-10)$$

where:

$I$  ionic strength

The surface to volume ratio  $A/V$  for the porous scale is calculated locally throughout the porous scale as:

$$\frac{A}{V} = \frac{\varepsilon^2 \cdot (1 - \varepsilon)}{\Delta x} \quad (5-11)$$

where:

$\Delta x$ : characteristic size of iron carbonate crystals, m

## 5.2.4 Initial and boundary conditions

### 5.2.4.1 Initial conditions

Uniform concentrations of species as determined by chemical equilibria (shown in Appendix I) are used as initial conditions for all species.

### 5.2.4.2 Boundary conditions

On the outer boundary of the droplet, which is in contact with the gas, the boundary conditions are different for different species. For “volatile” species including CO<sub>2</sub>, HAc and H<sub>2</sub>S, the concentrations ( $C_j$ ) are held constant as calculated by Henry’s law:

$$C_j = H_j p_j \quad (5-12)$$

where:

$H_j$  Henry’s law constant for species  $j$ ,

$p_j$  partial pressure of species  $j$  in gas phase, kPa

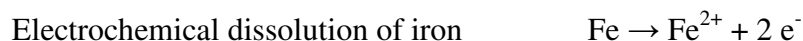
For other species found only in the liquid phase a zero flux boundary condition is imposed at the droplet outer boundary.

A number of electrochemical reactions are happening at the metal surface:

*Cathodic reactions:*



*Anodic reactions:*



If the species  $j$  is not a participant in an electrochemical reaction, the flux is zero ( $N_j = 0$ ) at the metal surface. On the other hand, the flux for species  $j$  involved in electrochemical reactions can be calculated through:

$$N_j = -\frac{i_j}{n_j F} \quad (5-13)$$

where:

$i_j$ : partial current for species  $j$ ,  $\text{A/m}^2$

$n_j$ : number of mols of electrons exchanged per mol of species  $j$

From the Volmer-Butler equation, the correlation between the current density  $i_j$  and potential  $E$  for a cathodic/anodic reaction involving species  $j$  can be expressed as:

$$i_j = \pm i_{0,j} \cdot 10^{\pm \frac{E - E_{rev,j}}{b_j}} \quad (5-14)$$

where

$i_{0,j}$  exchange current density,  $\text{A/m}^2$

$E_{rev,j}$  reversible potential, V

$b_j$  Tafel slope, V

In a spontaneous corrosion process, the open circuit potential  $E$  (also called corrosion potential) is the same for all involved cathodic and anodic reactions. Therefore, it can be calculated through the charge conservation equation below:

$$\sum_1^{n_a} i_j^a = \sum_1^{n_c} i_j^c \quad (5-15)$$

where:

$n_a$ : total number of anodic reactions

$n_c$ : total number of cathodic reactions

### 5.2.5 Numerical method

Since all equations are strongly and nonlinearly coupled through the chemical reaction term, they have to be solved simultaneously, together with the boundary conditions and initial conditions. The species conservation equations and the scale growth equation are discretized using a finite difference method and a non-uniform grid. A fully implicit time discretization scheme is used here for reasons of stability, and all nonlinear terms are linearized in variable space.

Most of the equations and techniques described above for the corrosion model are the same as proposed originally by Nordsveen and Nesic (2003). However, the domain of calculation had to be adapted to the TLC scenario in order to take into account the growth and demise of droplets with time.

The growth of the droplet is simulated by controlling (moving) the position of the vapor/liquid interface i.e. the outer boundary of the droplet. In reality, when the droplet reaches its maximum size and is removed from the top of the line, some liquid remains. This is even more true in the presence of porous corrosion product scales which hold water in the pores much like a sponge. This effect is included in the model. At the very beginning of the calculation when a first droplet with a minimum radius is generated, the initial concentrations in the droplet are set by equilibria for pure freshly condensed water. When this droplet grows the outer boundary of the computational domain is extended. When the droplet detaches, the computational domain is shrunk back to match the initial (minimum) droplet size while the concentrations of species in that small droplet are unchanged from what they were before detachment. The same is true if there is a corrosion scale, the species concentrations in the porous scale are retained after droplet detachment. The new freshly condensed droplet starts its lifetime on the outer side of the existing scale, i.e. the computational domain has the initial thickness equal to thickness of scale plus minimum droplet size. The detailed algorithm is described in Figure 5-2.

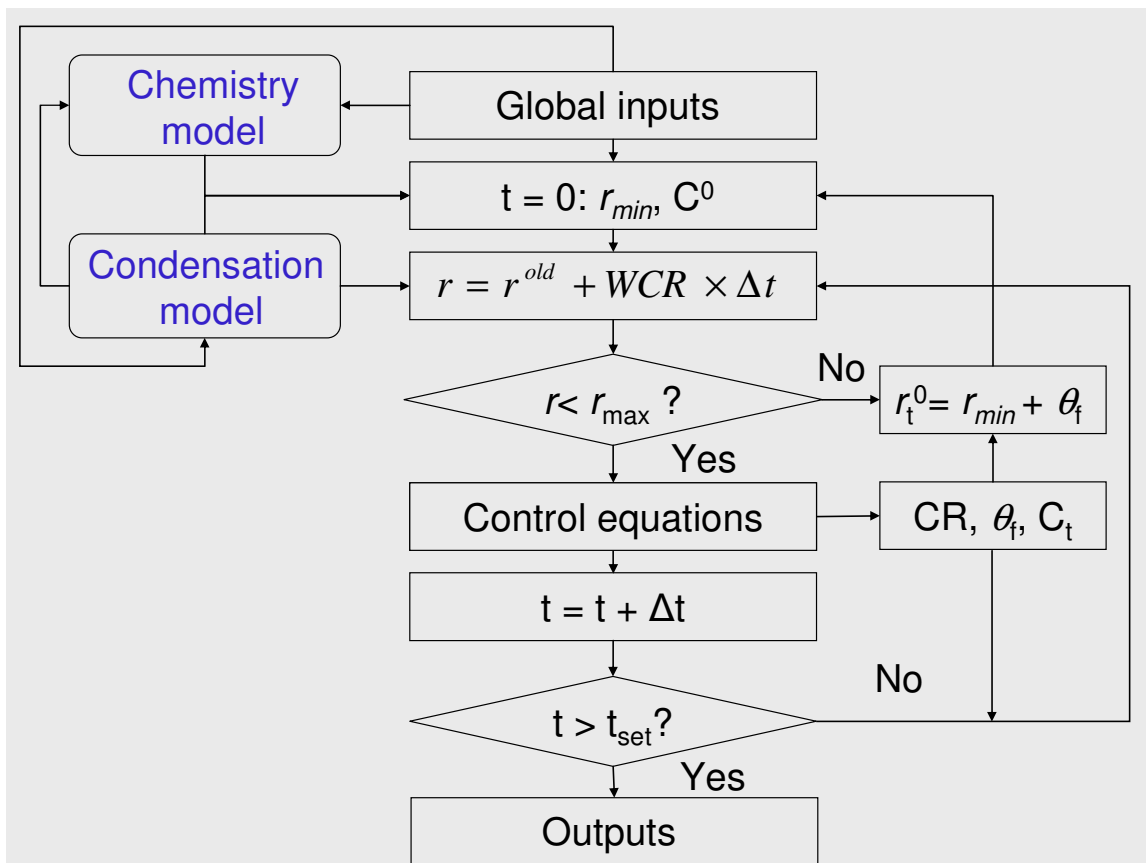


Figure 5-2: Flow chart for the calculation of corrosion rate

(t: time,  $\Delta t$ : time step, r: droplet radius,  $\theta$ : scale thickness, C: concentration, WCR: condensation rate, CR: corrosion rate, 0: initial time/first time step, old: last time step)

### 5.3 Verification of the corrosion model

Several large-scale flow loops have been built at the Institute for Corrosion and Multiphase Technology to try to simulate as closely as possible the real field conditions. The description of these loops and the results were given in detail in Chapter 3. The parameters, which are covered in the experiments discussed below, are shown in Table 5-

1. In these experiments, after the system at the set conditions reaches the equilibrium, weight loss coupons are mounted on the probe, which are inserted into the test section through the probe ports. All the experiments were conducted over long periods of time, up to three weeks, with weight loss coupons collected during the 2<sup>nd</sup>, 7<sup>th</sup>, 14<sup>th</sup> and 21<sup>st</sup> day of exposure. The influence of several parameters including gas temperature (T), gas velocity ( $U_{SG}$ ), CO<sub>2</sub> partial pressure ( $pCO_2$ ), condensation rate (WCR) and free HAC concentration were investigated in more than 20 long term experiments and at least 40 short term tests.

Table 5-1: Test conditions on corrosion in large scale loop

Variables	Range	
	Minimum	Maximum
Absolute pressure (bara)	3	8
CO <sub>2</sub> partial pressure (bara)	0.13	7
Gas temperature (°C)	40	85
Condensation rate (mL/m <sup>2</sup> /s)	0.05	1
Gas velocity (m/s)	5	15
Free HAC concentration in the tank (ppm)	0	1000

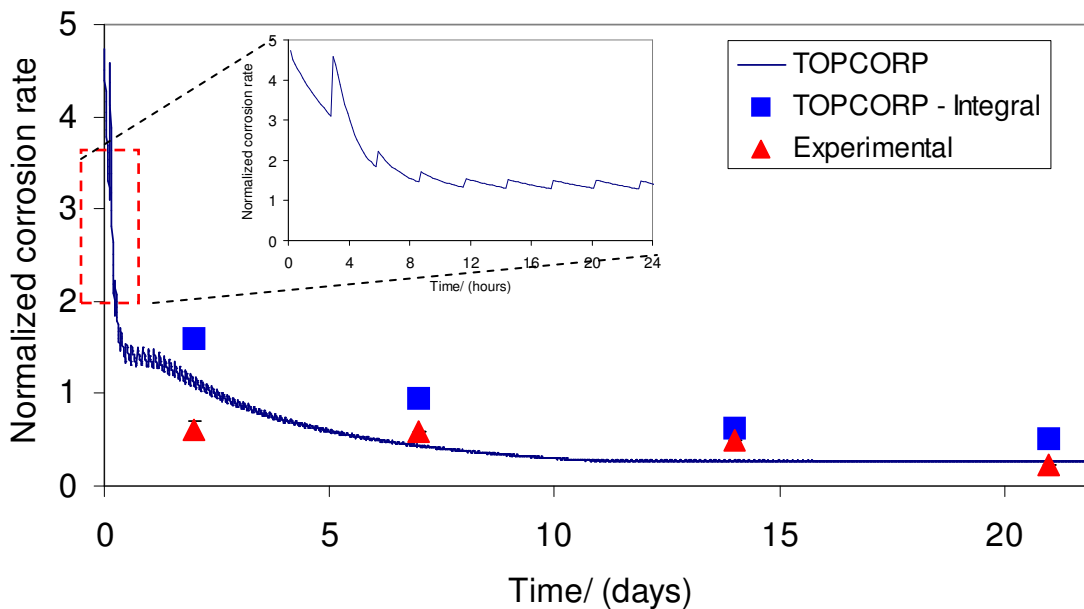


Figure 5-3<sup>5, 6</sup>: Comparison between a long term test and model prediction on the corrosion rate ( $T = 70\text{ }^{\circ}\text{C}$ ,  $P_T = 3\text{ bar}$ ,  $pCO_2 = 2\text{ bar}$ ,  $WCR = 0.25\text{ mL/m}^2/\text{s}$ ,  $U_{SG} = 5\text{ m/s}$ ,  $Free\ HAc = 0\text{ ppm}$ )

From Figure 5-3 which shows a typical simulation result at specific conditions, it can be seen that the corrosion rate at the very beginning is very high because the fresh condensed water is very corrosive. The corrosion rate, however, decreases dramatically as the protective scale forms on the metal surface in the first day. As the scale grows and becomes denser, the corrosion rate is further decreased and remains at a very low “steady

<sup>5</sup> TOPCORP calculates instantaneous corrosion rate ( $CR_{TOP}$ ) while experimental corrosion rate from weight loss coupons is average value over the exposure time ( $t^{\#}$ ). Therefore, only an integral corrosion rate ( $= \int_0^{t^{\#}} CR_{TOP} dt$ ) is comparable to the experimental result.

<sup>6</sup> Both experimental and predicted corrosion rates have been normalized by a factor for the protection of confidential data

state” value in long exposure. The jagged appearance of the predicted corrosion rate curve is due to the many droplets that form, grow and detach during the course of the simulation, each “fluctuation” representing a single droplet’s lifetime. Clearly when a new freshly condensed droplet forms the corrosion rate increases temporarily and then rapidly decreases as the droplet saturates with iron carbonate leading to a pH increase.

In most of TLC cases, the general corrosion rate is expected to decrease rapidly to a very small value since the chemistry in the droplets is ideal for the formation of protective corrosion product scale (small liquid volume, large corrosion rate leading to rapid iron carbonate supersaturation). From Figure 5-4 it follows that even at low gas temperature (40 °C), the formation of the corrosion scale still retards the corrosion rate dramatically. In the simulation, it is found that both the concentration of iron ions and pH are always very high. For example at these conditions (Figure 5-4) the pH in fresh condensed water is pH3.8, which is also the boundary condition at the interface of the droplets. But at the metal surface the iron ion concentration builds up due to corrosion and can be as high as 600 ppm (w/w). Due to the corrosion process the pH increases and rapidly reaches pH6.3, which leads to rapid protective film formation.

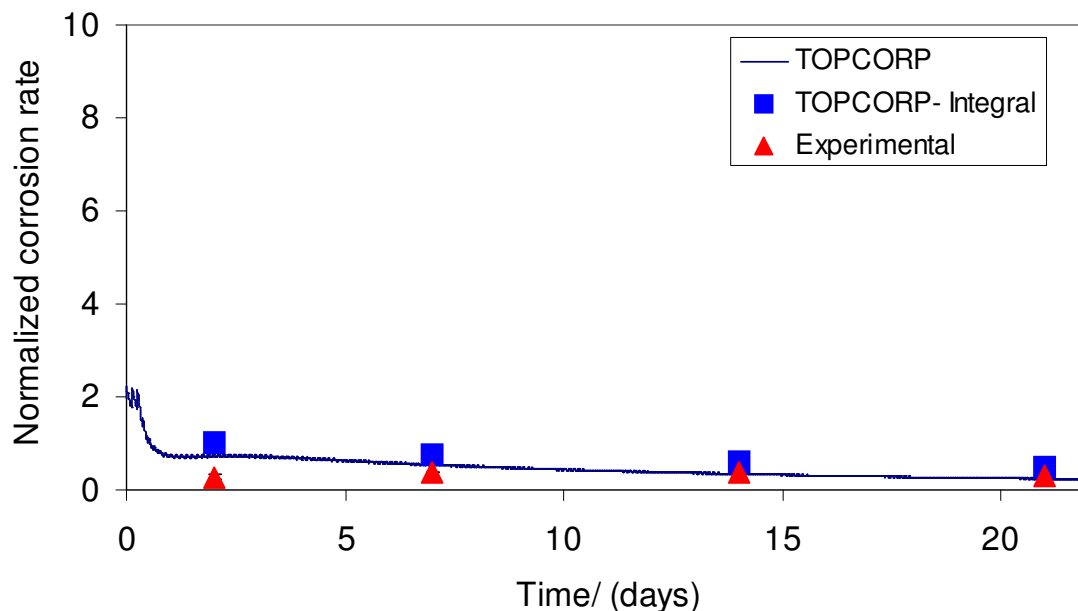


Figure 5-4<sup>3,4</sup>: Comparison between a long term test and model prediction on the corrosion rate ( $T=40\text{ }^{\circ}\text{C}$ ,  $P_T=3\text{ bar}$ ,  $p\text{CO}_2=2\text{ bar}$ ,  $\text{WCR}=0.25\text{ mL/m}^2/\text{s}$ ,  $U_{SG}=5\text{ m/s}$ ,  $\text{Free HAc}=0\text{ ppm}$ )

From the comparison between the experimental data and simulation results (Figure 5-3 & Figure 5-4), it is seen that the model can accurately predict the trend of corrosion rate with time. Although the model overpredicts the corrosion rate for short term experiments (2 days), it gives a reasonable prediction for long term experiments. The discrepancy for short term experiments probably results from the introduced approximation of a 3D problem in a 1D approach.

Other comparisons (Figure 5-5 to 13) between experiments and model prediction at different conditions, which are presented to evaluate the effect of various parameters including temperature,  $\text{CO}_2$  partial pressure, gas velocity, condensation rate, and free

HAc concentration, show a satisfactory agreement. It is worth mentioning that discrepancy of the experimental and predicted corrosion rate at 21 days in Figure 5-9 is due to the change of condensation regime from stagnant to sliding droplet mode.

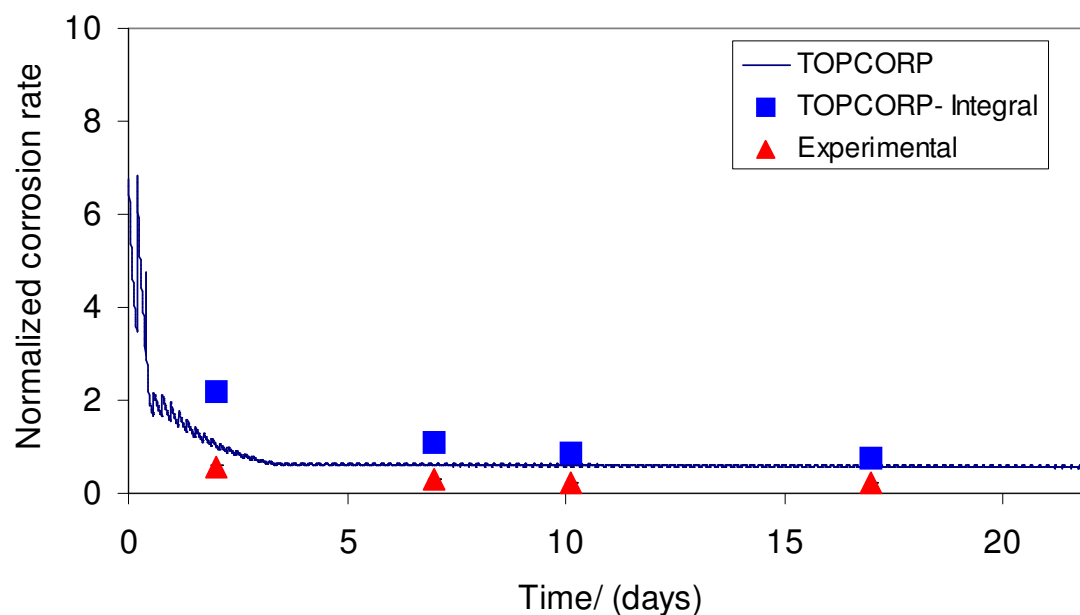


Figure 5-5<sup>3,4</sup>: Comparison between a long term test and model prediction on the corrosion rate ( $T=85\text{ }^{\circ}\text{C}$ ,  $P_T=3\text{ bar}$ ,  $pCO_2=2\text{ bar}$ ,  $WCR=0.25\text{ mL/m}^2/\text{s}$ ,  $U_{SG}=5\text{ m/s}$ ,

*Free HAc = 0 ppm*)

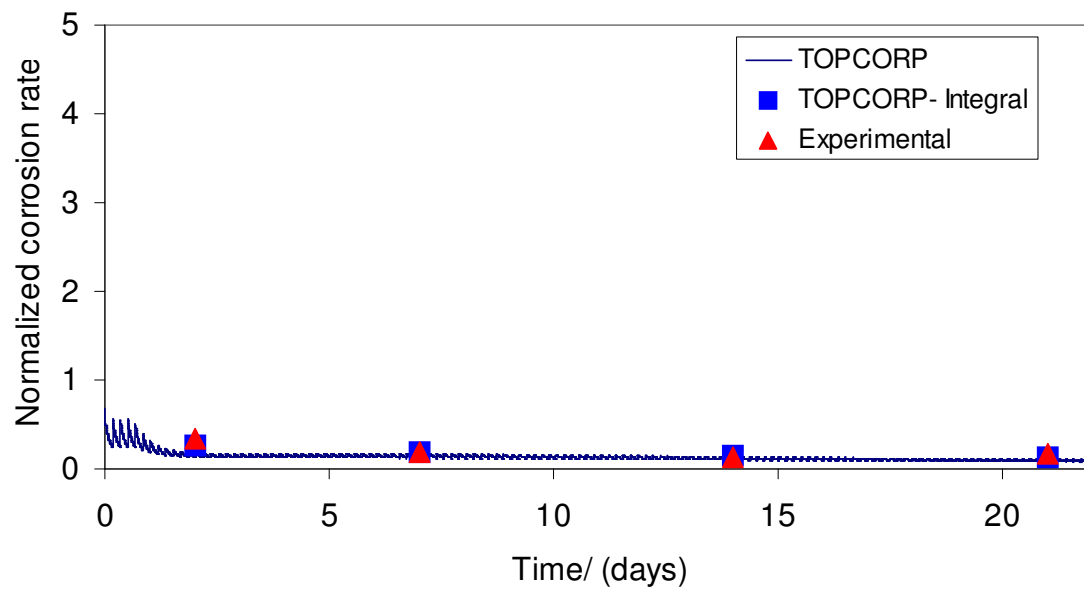


Figure 5-6<sup>3, 4</sup>: Comparison between a long term test and model prediction on the corrosion rate ( $T=70\text{ }^{\circ}\text{C}$ ,  $P_T=3\text{ bar}$ ,  $p\text{CO}_2=0.13\text{ bar}$ ,  $\text{WCR}=0.25\text{ mL/m}^2/\text{s}$ ,  $U_{SG}=5\text{ m/s}$ ,  $\text{Free HAc}=0\text{ ppm}$ )

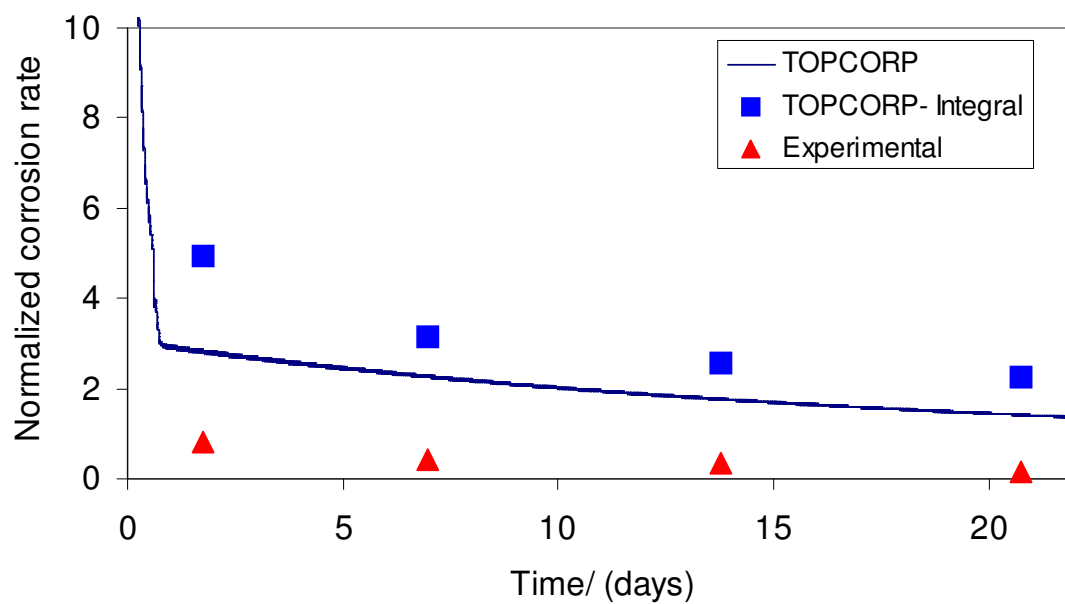


Figure 5-7<sup>3,4</sup>: Comparison between a long term test and model prediction on the corrosion rate ( $T=70\text{ }^{\circ}\text{C}$ ,  $P_T=8\text{ bar}$ ,  $pCO_2=7\text{ bar}$ ,  $WCR=0.25\text{ mL/m}^2/\text{s}$ ,  $U_{SG}=5\text{ m/s}$ ,  
 $Free\ HAc=0\text{ ppm}$ )

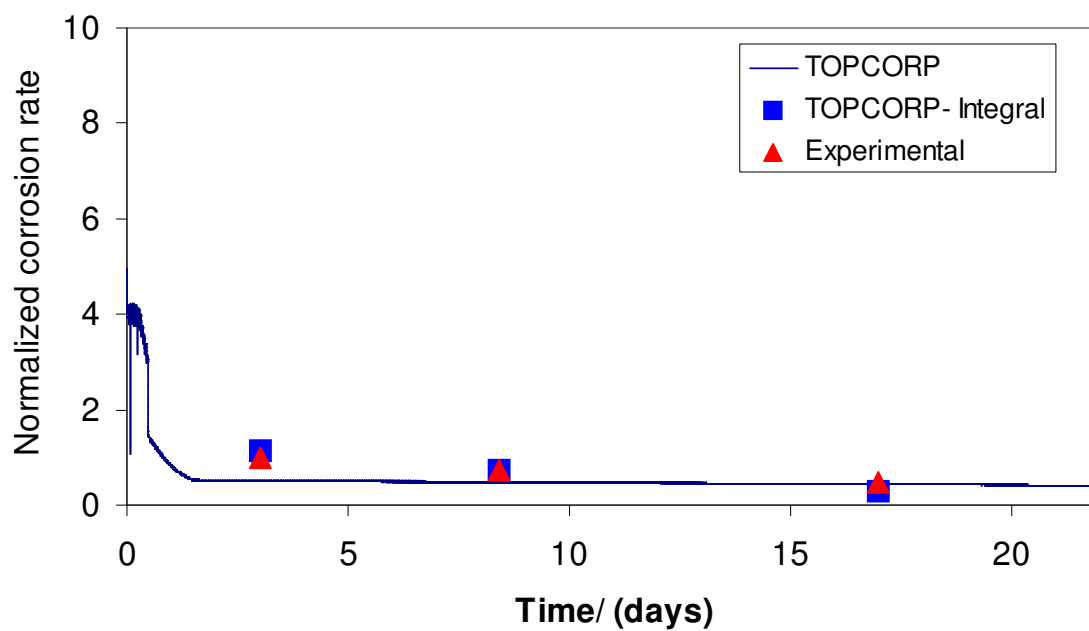


Figure 5-8<sup>3,4</sup>: Comparison between a long term test and model prediction on the corrosion rate ( $T = 70$  °C,  $P_T = 3$  bar,  $pCO_2 = 2$  bar,  $WCR = 0.25$  mL/m<sup>2</sup>/s,  $U_{SG} = 10$  m/s,  $Free\ HAc = 0$  ppm)

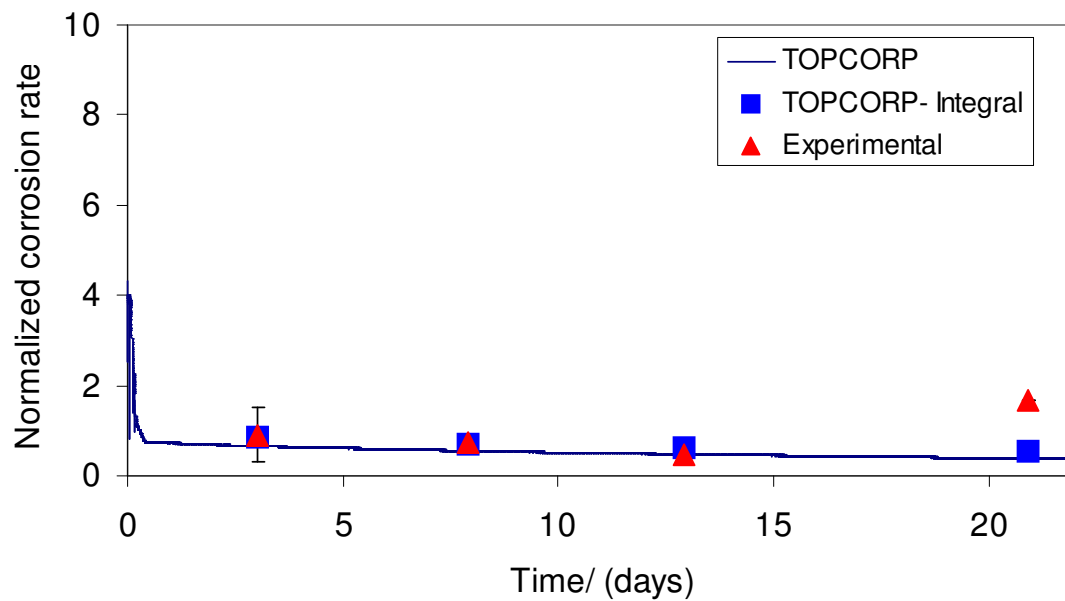


Figure 5-9<sup>3,4</sup>: Comparison between a long term test and model prediction on the corrosion rate ( $T = 70\text{ }^{\circ}\text{C}$ ,  $P_T = 3\text{ bar}$ ,  $p\text{CO}_2 = 2\text{ bar}$ ,  $\text{WCR} = 0.25\text{ mL/m}^2/\text{s}$ ,  $U_{SG} = 15\text{ m/s}$ ,  
 $\text{Free HAc} = 0\text{ ppm}$ )

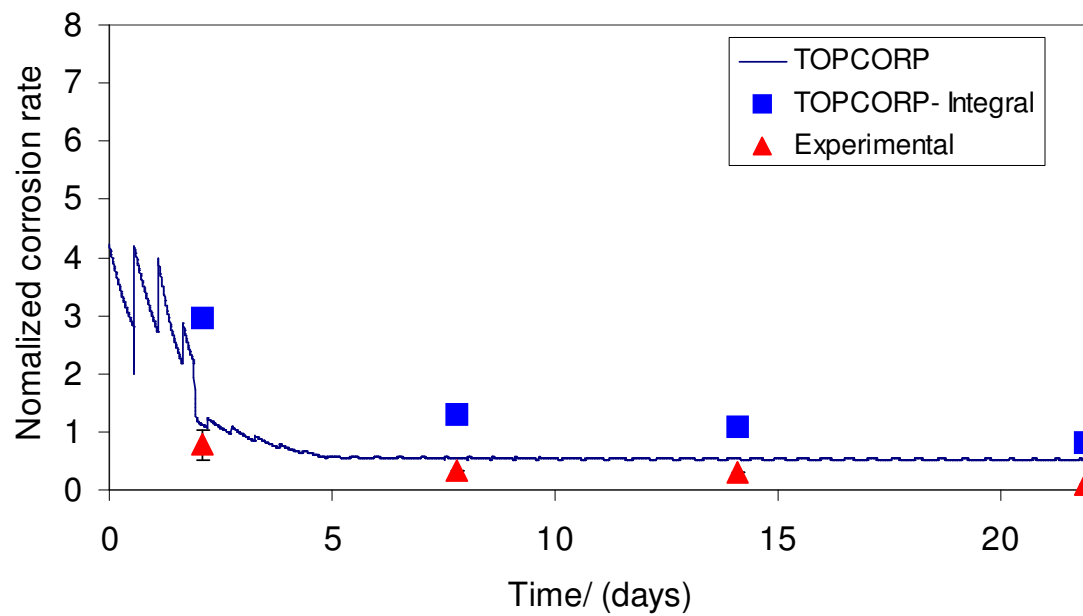


Figure 5-10<sup>3,4</sup>: Comparison between a long term test and model prediction on the corrosion rate ( $T=70\text{ }^{\circ}\text{C}$ ,  $P_T=3\text{ bar}$ ,  $p\text{CO}_2=2\text{ bar}$ ,  $\text{WCR}=0.05\text{ mL/m}^2/\text{s}$ ,  $U_{SG}=5\text{ m/s}$ ,  
 $\text{Free HAc}=0\text{ ppm}$ )

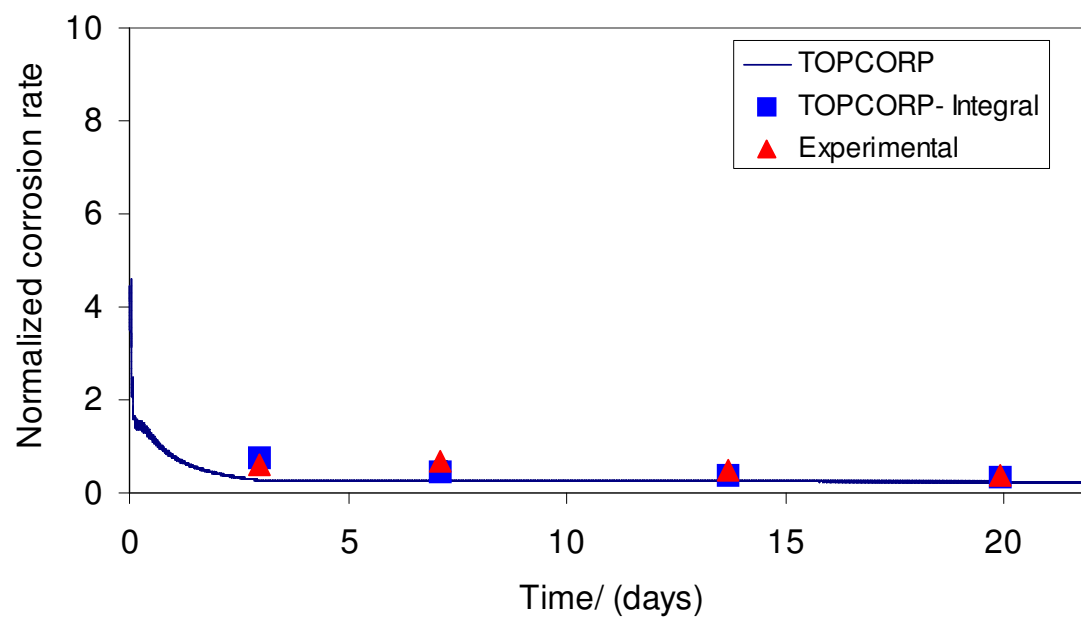


Figure 5-11<sup>3,4</sup>: Comparison between a long term test and model prediction on the corrosion rate ( $T = 70\text{ }^{\circ}\text{C}$ ,  $P_T = 3\text{ bar}$ ,  $p\text{CO}_2 = 2\text{ bar}$ ,  $\text{WCR} = 1\text{ mL/m}^2/\text{s}$ ,  $U_{SG} = 5\text{ m/s}$ ,  $\text{Free HAc} = 0\text{ ppm}$ )

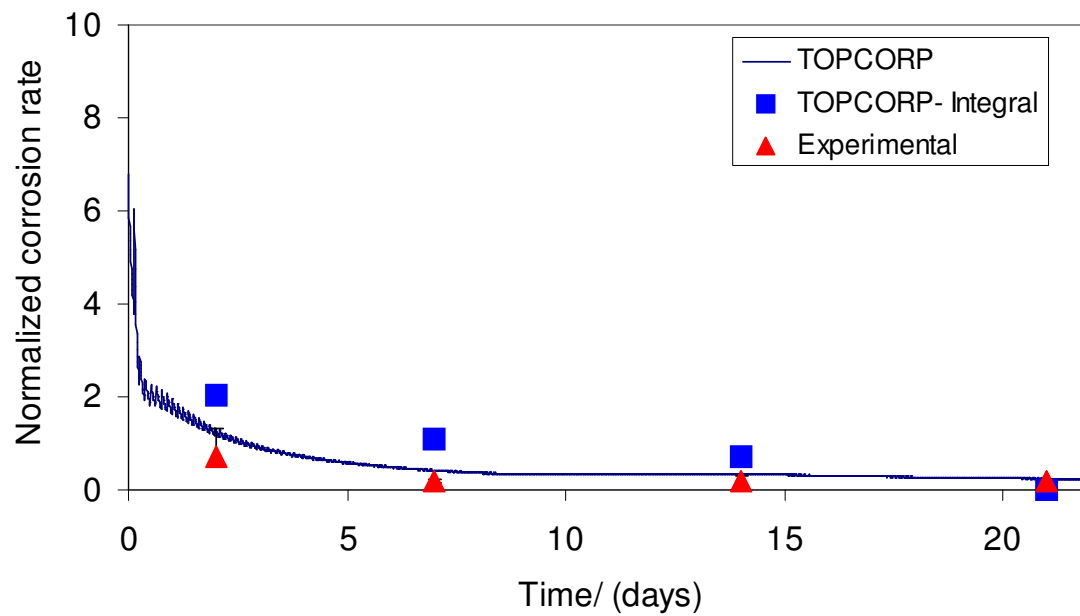


Figure 5-12<sup>3,4</sup>: Comparison between a long term test and model prediction on the corrosion rate ( $T=70\text{ }^{\circ}\text{C}$ ,  $P_T=3\text{ bar}$ ,  $p\text{CO}_2=2\text{ bar}$ ,  $\text{WCR}=0.25\text{ mL/m}^2/\text{s}$ ,  $U_{SG}=5\text{ m/s}$ ,  
*Free HAc* = 100 ppm)

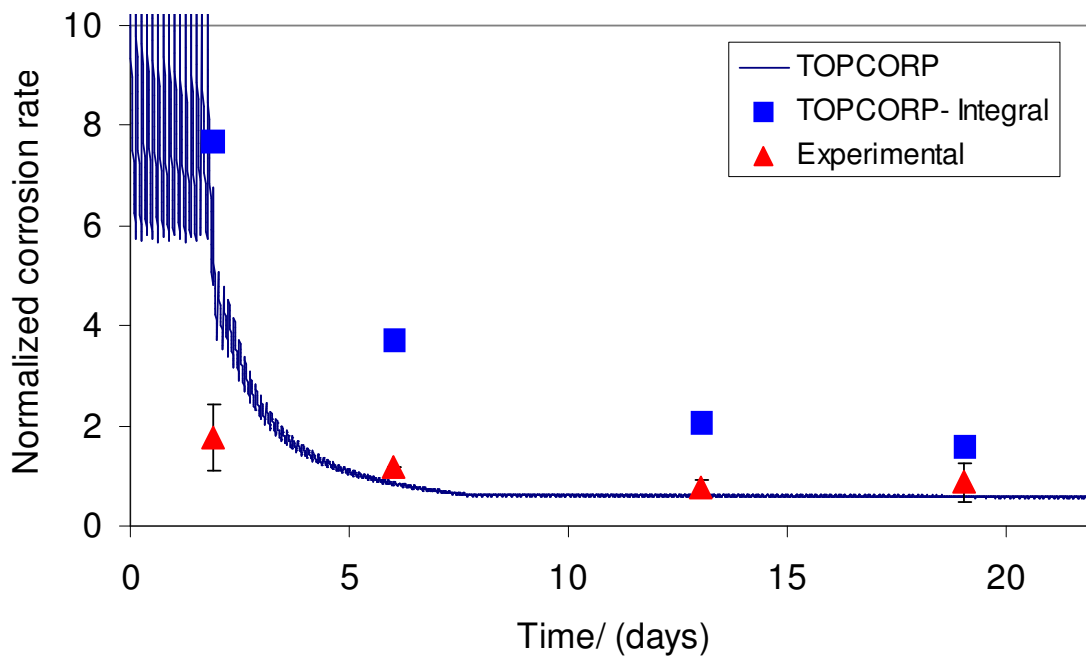


Figure 5-13<sup>3,4</sup>: Comparison between a long term test and model prediction on the corrosion rate ( $T=70\text{ }^{\circ}\text{C}$ ,  $P_T=3\text{ bar}$ ,  $pCO_2=2\text{ bar}$ ,  $WCR=0.25\text{ mL/m}^2/\text{s}$ ,  $U_{SG}=5\text{ m/s}$ ,  
*Free HAc = 1000 ppm*)

#### 5.4 Prediction software package (TOPCORP)

In order to meet the specific need of the sponsor companies, a software package (TOPCORP) with a user friendly interface (Figure 5-14 with more detail in Appendix III) was designed and developed. Without dealing with the complicated calculation process, users can easily operate the software to obtain the results on their specified cases. As a carrier of established knowledge based on a theoretical model and laboratory

experimental experience, TOPCORP will become a reliable tool in prediction of TLC related risks for corrosion engineers in the design of their field facilities.

Global input		
Gas temperature	25	C
Total pressure	1	bar
Internal diameter	0.1	m
CO2 partial pressure	0.96	bar
H2S partial pressure	0	bar
Gas velocity	5	m/s
Environmental temperature	68	C

Modules

Condensation      Chemistry

Localized corrosion    General corrosion    Help    Cancel

Figure 5-14: Main window of TOPCORP: Outputs including the condensation rate, the chemistry in droplets, and the corrosion rate can be calculated by different modules with provided case conditions, which are specified in global inputs.

## 5.5 Summary

Previously developed empirical and semi-empirical models could not precisely predict the corrosion rate at the top of the line. Based on the solid foundation (the dropwise condensation model), a mechanistic model has been developed to predict the corrosion at the top of the line. The comparison between model prediction and

experimental data has shown that the model can reasonably predict the corrosion rate at the top of the line. A software package (TOCORP) with a user friendly interface was built to help the transfer the knowledge in our laboratory to the corrosion engineers in the oil and gas industry.

## CHAPTER 6: DROPLET TRANSPORT IN GAS-LIQUID TWO-PHASE CONCURRENT FLOW

### 6.1 Introduction

Droplet transport is one of the most important topics in flow dynamics. The pressure drop related to the droplet entrainment rate in annular flow is a big concern for flow assurance engineers. But, in contrast, liquid atomization and droplet deposition are of particular interest in corrosion study. One obstacle for corrosion control at the top of the line is that corrosion inhibitors, which are injected to pipelines at the bottom of the line for corrosion prevention, can not be transported to the top of the line since the liquid connection between the top and the bottom is obstructed by gas flow. However, through droplet transport the mass transfer between the bottom and the top of the line might be established and inhibitors can then reach the top with the deposition of the entrained droplets to prevent TLC. Therefore, a mathematic criterion to predict the occurrence of such effective droplet transport is required for the establishment of such a practical solution for TLC prevention.

Studies on hydrodynamics showed that droplets are formed from turbulent waves at stratified flow with a relative high gas velocity. Almost at the same time droplets start to be deposited on the pipe wall at the top. When the gas velocity is further increased, more and more droplets are deposited and accumulated at the top of the line. Eventually, a liquid film is formed and annular flow ensues. Based on the experimental results, Lin and Hanratty (1987) proposed a mechanism that the deposition of the droplets could lead

to the transition from stratified flow to annular flow. However, the inception of droplet deposition happens at much smaller gas velocity than is needed for the development of a stable liquid film. On the other hand, liquid atomization starts earlier than droplet deposition when gas velocity is increased. In other words, effective droplet deposition for corrosion prevention happens between the onset of atomization and the transition to annular flow with respect to the gas velocity.

In order to define the conditions under which effective deposition of the droplets is possible, a so-called “effective zone” with the involvement of three different criteria is established in a Mandhane plot (flow regime map, 1974).

- **Onset of droplets:** The inception criterion of atomization provides the left and lower boundaries.
- **Transition to non-stratified flow by waves:** The well known wave-mixing mechanism (Taitel and Dukler, 1976) determines the upper and/or the right boundary.
- **Transition to non-stratified flow by deposited droplets:** The right boundary could be set alternatively by the entrainment-deposition mechanism (Lin and Hanratty, 1987) if this mechanism, instead of wave-mixing mechanism, is dominant.

Any point residing inside this zone means that at these gas and liquid flow conditions entrained droplets can be deposited at the top of the line. The practical meaning of the “effective zone” to the corrosion engineers is that the injection of corrosion inhibitor at the bottom of the line is able to prevent the corrosion at the top of the line.

## 6.2 Model development

Although theories and their numerical model behind the three different criteria are developed individually, their connections can be established through the investigation of the momentum balance on the gas and liquid phase in the presence of roll waves at the interface.

### 6.2.1 Momentum balance in stratified flow

In stratified flow, liquid flows at the bottom of the line while gas flows concurrently at the top. As the cross section of a pipeline drawn in Figure 6-1, part of the whole area is occupied by the liquid and the gas fills the remaining area. Momentum balance equations could be established on both phases as (Taitel and Dukler, 1976):

$$-A_L \left( \frac{dP}{dx} \right) - \tau_{wL} S_L + \tau_i S_i + \rho_L A_L g \sin \alpha = 0 \quad (6-1)$$

$$-A_G \left( \frac{dP}{dx} \right) - \tau_{wG} S_G + \tau_i S_i + \rho_G A_G g \sin \alpha = 0 \quad (6-2)$$

where:

$\tau$  shear stress at the interface of liquid-wall ( $\tau_{wL}$ ), gas-liquid ( $\tau_i$ ), and wall-gas ( $\tau_{wG}$ ), Pa m

$\alpha$  inclination angle, degree

$A$ : area of the different phases in a cross section, m<sup>2</sup>

$S$ : wetted length of different phases, m

$\rho_L$ : liquid density, kg/m<sup>3</sup>

$\mu_L$ : liquid viscosity, Pa s

$\rho_G$ : gas density, kg/m<sup>3</sup>

$\mu_G$ : gas viscosity, Pa s

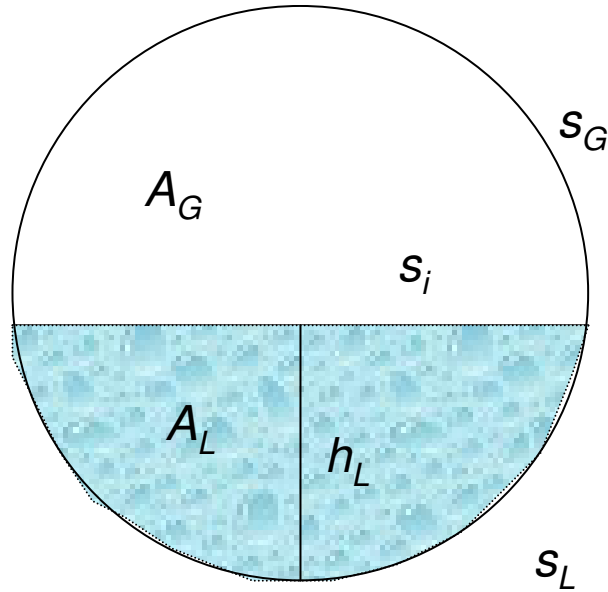


Figure 6-1: Schematic of the cross section of a pipe in gas-liquid two-phase flow

( $A_G$ : area covered by gas,  $A_L$ : area covered by liquid,  $S_G$ : wetted length of the gas phase,  $S_L$ : wetted length of the liquid phase,  $S_i$ : the boundary length at gas-liquid interface,  $h_L$ : liquid holdup)

Their specific meaning of  $A$  and  $S$  with different subscripts have been defined in Figure 6-1. Pressure drop is the same for these two equations. Substituting one equation to another one, one can get an equation with only one unknown liquid holdup ( $h_L$ ):

$$\tau_{wG} \frac{S_G}{A_G} - \tau_{wL} \frac{S_L}{A_L} + \tau_i S_i \left( \frac{1}{A_L} + \frac{1}{A_G} \right) + (\rho_L - \rho_G) g \sin \alpha = 0 \quad (6-3)$$

From the basic definition in flow dynamics, the conventional equation of the shear stress on the gas side of a gas-liquid interface is:

$$\tau_{iG} = f_{iG} \frac{\rho_G U_G^2}{2} \quad (6-4)$$

where:

$f_{iG}$ : interfacial friction factor at the gas side

$U_G$ : actual gas velocity, m/s

Similarly, equations of the interfacial shear stress between gas and pipe wall and between liquid and pipe wall are given, respectively:

$$\tau_G = f_G \frac{\rho_G U_G^2}{2} \quad (6-5)$$

$$\tau_L = f_L \frac{\rho_L U_L^2}{2} \quad (6-6)$$

where:

$f_G$ : gas friction factor

$f_L$ : liquid friction factor

$U_L$ : actual liquid velocity, m/s

Usually, friction factors can be calculated through:

$$f_L = C_L \left( \frac{\rho_L D_L U_L}{\mu_L} \right)^{-n} \quad (6-7)$$

$$f_G = C_G \left( \frac{\rho_G D_G U_G}{\mu_G} \right)^{-m} \quad (6-8)$$

where:

$C_L$ : a constant (= 0.046 for turbulent flow or = 16 for laminar flow)

$C_G$ : a constant (= 0.046 for turbulent flow or = 16 for laminar flow)

$m$ : a constant (= 0.2 for turbulent flow or = 1 for laminar flow)

$n$ : a constant (= 0.2 for turbulent flow or = 1 for laminar flow)

$D_L$ : liquid hydraulic diameter, m

$D_G$ : gas hydraulic diameter, m

When the interface is very smooth  $f_i$  could be assumed to be equal to  $f_G$ . However, this assumption ( $f_i = f_G$ ) is not applicable when droplets are atomized from the gas-liquid interface. As discussed in Chapter 2, the presence of waves is a prerequisite for droplet entrainment. Due to the curvature of the gas-liquid interface in the presence of these large amplitude irregular waves, the pressure and velocity gradients in the area close to the interface are changed.

Obviously, the pattern and the shape of the waves on the liquid film are two crucial factors. A direct correlation between the interfacial shear stress and these two factors is not available due to the complexity of characterizing of an irregular wave. An empirical correlation between the ratio of  $f_i$  to  $f_G$  and some characteristic parameters (the liquid film thickness, gas density, and gas velocity) in multiphase flow was developed by Andrisos and Hanratty (1987a). Validated with a large experimental database, this correlation for the interfacial shear stress has been widely accepted:

$$\frac{f_i}{f_G} = 1 + 15 \left( \frac{h_L}{D} \right)^{0.5} \left( \frac{U_{SG}}{U_{SG,R}} - 1 \right) \quad (6-9)$$

where:

$U_{SG,R}$ : reference superficial gas velocity, m/s

$D$ : pipeline diameter, m

$h_L$ : liquid holdup, m

The reference superficial gas velocity introduced by Andritsos and Hanratty (1987a) is a function of  $(\rho_G)^{0.5}$ . An empirical equation with a satisfactory accuracy was given as:

$$U_{SG,R} = 5 \left( \frac{\rho_{G,A}}{\rho_G} \right)^{1/2} \quad (6-10)$$

where:

$\rho_{G,A}$ : gas density at atmospheric pressure, kg/m<sup>3</sup>

Substituting all these equations for the friction calculation into Equation (6-1), liquid holdup can be determined at any specified gas and liquid velocities.

### 6.2.2 Onset of atomization

Two different mechanisms (e.g. tearing and undercutting) are responsible for droplet formation in two-phase flow. A critical liquid Reynolds number ( $Re_{LCI}$ ) was suggested for the transition between two different mechanisms. When the liquid Reynolds number is less than  $Re_{LCI}$ , the undercutting mechanism is dominant. However,  $Re_{LCI}$  from various studies covered a quite wide of range. The correlation in which the critical liquid Reynolds number was a function of gas and liquid properties from Andreussi's work (1985) seemed more reasonable than any other fixed numbers. Thus, it is adopted in this study.

$$Re_{LCI} = 7.30(\log \omega)^3 + 44.2(\log \omega)^2 - 263(\log \omega) + 439 \quad (6-11)$$

where:

$$\omega = \frac{\mu_L}{\mu_G} \sqrt{\frac{\rho_G}{\rho_L}} \quad (6-12)$$

When the liquid Reynolds number is greater than the critical value ( $Re_{LC1}$ ) the tearing mechanism is dominant. In the tearing mechanism, the relative importance of liquid and gas turbulence is different, which leads to another critical liquid Reynolds number ( $Re_{LC2}$ ). At moderate liquid Reynolds number ( $Re_{LC1} < Re < Re_{LC2}$ ), both liquid and gas turbulences are important for the formation of droplets since the liquid flow is still laminar. When liquid Reynolds number is greater than  $Re_{LC2}$ , the fully developed turbulent liquid flow has no further effect on the atomization process. Finally, the scopes of application for these different controlling mechanisms can be defined according to the liquid Reynolds number:

- **Low liquid Reynolds number:** Undercutting mechanism
- **Moderate liquid Reynolds number:** Tearing mechanism under the combined effect of liquid and gas flow
- **High liquid Reynolds number:** Tearing mechanism exclusively influenced by gas flow

#### 6.2.2.1 Low liquid Reynolds number ( $Re_L < Re_{LC1}$ )

When the liquid Reynolds number is very low, liquid atomization is similar to the droplet disintegration. The mechanism of undercutting is dominant and a dimensionless group, Weber number, was suggested to evaluate the relative importance of drag force

and surface tension. According to van Rossum' work (1959), when the Weber number ( $We$ ) was greater than a critical value ( $We_c$ ) droplets were formed. Thus, one can get:

$$We = \frac{\rho_G U_G^2 h_L}{\sigma} > We_c \quad (6-13)$$

where:

$\sigma$ : surface tension, N/m

van Rossum found  $We_c$  is around 17 which is very close to 22 identified in Hinze's experiments (1955). In Equation (6-13), liquid holdup  $h_L$  is calculated by solving Equation (6-1).

### 6.2.2.2 Moderate liquid Reynolds number-Transition zone ( $Re_L > Re_{LC2}$ )

When the increasing liquid Reynolds number is greater than the critical liquid Reynolds number ( $Re_{LC1}$ ) another mechanism (tearing mechanism) will control the atomization process. According to the mechanism of tearing (Zuber, 1962), a droplet will be formed when the drag force is greater than the force from the surface tension:

$$\frac{1}{2} C_D \rho_G \lambda b U_r^2 > C_{shape} \lambda \sigma \quad (6-14)$$

where:

$U_r$ : relative velocity between gas and liquid ( $=U_g - U_L$ ), m/s

$C_D$ : drag coefficient ( $\sim 1$ )

$b$ : amplitude of a wave, m

$\lambda$ : base length of a wave, m

$C_{shape}$  coefficient of shape on surface tension (0.77 suggested in Ishii and Grolmes, 1975)

The internal flow caused by the shear stress could be defined as (Ishii and Grolmes, 1975):

$$\tau_i = C_\sigma \mu_L \frac{U_f}{b} \quad (6-15)$$

where:

$U_f$ : film velocity (assumed to be equal to  $U_L$ ), m/s

The coefficient  $C_\sigma$  is a function of viscosity and surface tension, Ishii and Grolmes (1975) developed an equation by fitting experimental data, which was given as:

$$\begin{aligned} C_\sigma &= 0.0153 N_\mu^{-0.8} & N_\mu < 1/15 \\ C_\sigma &= 0.1335 & N_\mu > 1/15 \end{aligned} \quad (6-16)$$

where:

$N_\mu$ : viscosity number.

The viscosity number was defined by Hinze (1955) as:

$$N_\mu = \frac{\mu_L}{\left( \rho_L \sigma \sqrt{\frac{\sigma}{g(\rho_L - \rho_G)}} \right)^{0.5}} \quad (6-17)$$

When the liquid Reynolds number is moderate, both liquid and gas flow have the equivalent effect on the interfacial shear stress, which could be calculated either by the equation described in the previous part (Equation (6-9)) or by the equation listed below:

$$\tau_{iL} = f_{iL} \frac{\rho_L U_L^2}{2} \quad (6-18)$$

where:

$f_{iL}$ : interfacial friction factor evaluated at the liquid side.

At moderate liquid Reynolds number, the interfacial friction coefficient  $f_{iL}$  at the liquid side can be calculated from Hughmark's method (1973):

$$\sqrt{f_{iL}} = 1.962 \text{Re}_f^{-1/3} \quad (6-19)$$

At moderate liquid Reynolds number, both liquid and gas flow affect the interfacial friction. Thus, one can assume:

$$\tau_i = \tau_{iL}^w \tau_{iG}^{1-w} \quad (6-20)$$

where:

$w$ : weighing factor for the liquid Reynolds number ( $0 < w < 1$ , assumed to be 0.5 in the work of Ishii and Grolmes, 1975)

When Equations (6-15), (6-18), and (6-20) with their friction coefficient calculation equations (Equations (6-9) and (6-19)) are substituted into the inequality (Equation (6-14)), finally one can get:

$$\frac{\mu_f (U_G - U_L)^2}{\sigma U_G} \sqrt{\frac{\rho_G}{\rho_L}} \geq \frac{2.55 \sqrt{\left[ 1 + 15 \left( \frac{h_L}{D} \right)^{0.5} \left( \frac{U_{SG}}{U_{SG,R}} - 1 \right) \right] f_G}}{C_\sigma} \text{Re}_L^{-1/3} \quad (6-21)$$

Usually, liquid velocity is much less than gas velocity ( $U_L \ll U_G$ ) at the onset of liquid atomization. Therefore, Equation (6-21) can be simplified to:

$$\frac{\mu_f U_G}{\sigma} \sqrt{\frac{\rho_G}{\rho_L}} \geq \frac{2.55 \sqrt{\left[1 + 15 \left(\frac{h_L}{D}\right)^{0.5} \left(\frac{U_{SG}}{U_{SG,R}} - 1\right)\right] f_G}}{C_\sigma} \text{Re}_L^{-1/3} \quad (6-22)$$

### 6.2.2.3 High liquid Reynolds number ( $Re_L > Re_{LC2}$ )

At high liquid Reynolds number, the further increase in the liquid turbulence can not unlimitedly reduced the dependence of liquid atomization on the gas turbulence. When the liquid Reynolds number is greater than a critical value (e.g.  $Re_{LC2}$ ), turbulent liquid flow is fully developed, in which the inception of liquid atomization was completely controlled by the turbulence in gas phase. Ishii and Grolmes (1975) suggested that  $Re_{LC2}$  was around 1635. Consequently, the criterion at high liquid Reynolds number can be changed to:

$$\frac{\mu_f (U_G - U_L)^2}{\sigma U_G} \sqrt{\frac{\rho_G}{\rho_L}} \geq \frac{2.55 \sqrt{\left[1 + 15 \left(\frac{h_L}{D}\right)^{0.5} \left(\frac{U_{SG}}{U_{SG,R}} - 1\right)\right] f_G}}{C_\sigma} (1635)^{-1/3} \quad (6-23)$$

Similarly, the equation above can be simplified to:

$$\frac{\mu_f U_G}{\sigma} \sqrt{\frac{\rho_G}{\rho_L}} \geq \frac{2.55 \sqrt{\left[1 + 15 \left(\frac{h_L}{D}\right)^{0.5} \left(\frac{U_{SG}}{U_{SG,R}} - 1\right)\right] f_G}}{C_\sigma} (1635)^{-1/3} \quad (6-24)$$

### 6.2.3 Transition to non-stratified flow

#### 6.2.3.1 Entrainment-deposition mechanism

In order to achieve annular flow, the liquid height of the film at the top of the line should be large enough to fill the small “hills” on the rough metal surface. Therefore, the transition to annular flow occurs when the thickness ( $\delta$ ) of the stable film is greater than a minimum value ( $\delta_{min}$ ), which is a function of the roughness ( $\lambda$ ) of the metal:

$$\delta > \delta_{min} = f(\lambda) \propto \lambda \quad (6-25)$$

20  $\mu\text{m}$  was suggested by Baik and Hanratty (2003) based on their analysis of the laboratory experiments from Williams (1996). However, the roughness of a field pipeline can be as high as 150  $\mu\text{m}$ . Therefore, the minimum liquid thickness should be adjusted according to specific surface conditions of the pipelines.

The liquid source to maintain a stable film at the top of the line is from continuous deposition of the entrained droplets. Using a force balance and a mass balance (Laurinat, 1985) on this laminar film, the thickness of the liquid film resulting from droplet deposition can be calculated through (Baik and Hanratty, 2003):

$$\delta = \left( \frac{3R_D D \mu_L}{2g\rho_L^2} \right)^{1/3} \quad (6-26)$$

where:

$R_D$ : deposition rate,  $\text{kg/m}^2 \text{ s}$

$D$ : pipeline diameter, m

Similar to the mass flux in a diffusion process, the deposition rate ( $R_D$ ) can be calculated by:

$$R_D = k_D C_W \quad (6-27)$$

where:

$k_D$ : deposition constant, m/s

$C_W$ : droplet concentration at the wall, kg/m<sup>2</sup>

In order to predict the deposition rate, the droplet concentration and the deposition constant are calculated respectively below.

### ***Droplet concentration at the wall***

When ideal entrainment described in Karabelas' work (1977) happens, the droplet distribution in the gas core depends on the turbulent diffusion and the gravity. A mass balance of droplets with atomization as the source term and deposition as the sink term is given (Paras and Karabelas, 1991):

$$\varepsilon \frac{dC}{dy} + u_T C = a \quad (6-28)$$

where:

$C$ : droplet concentration, kg/m<sup>3</sup>

$\varepsilon$ : eddy diffusivity, m<sup>2</sup>/s

$u_T$ : droplet settling velocity, m/s

$a$ : constant accounting for a sink or source of droplets, kg/m<sup>2</sup> s

$y$ : spatial coordinate corresponding to the vertical direction

The eddy diffusivity of droplets is defined as:

$$\varepsilon = \zeta \times D \times U^* \quad (6-29)$$

where:

$\zeta$ : dimensionless droplet diffusivity, 0.09 is used in this work since 0.1 was suggested by Paras and Kaabelas (1991) and 0.08 was suggested by Pan and Hanratty(2002)

$U^*$ : friction velocity, m/s

After the integration, the droplet concentration at the top ( $C_w$ ) can be calculated through (Paras and Kaabelas, 1991):

$$\frac{C_w}{C_{mean}} = A + (1 - A) \frac{\frac{u_T}{\zeta U^*}}{\sinh\left(\frac{u_T}{\zeta U^*}\right)} \exp\left(-\frac{2u_T}{\zeta U^*}\right) \quad (6-30)$$

where:

$C_{mean}$ : mean concentration of droplets along the vertical pipe diameter,  $\text{kg/m}^3$

$A$ : a dimensionless flux ( $= a/U_T/C_{mean}$ )

In order to solve Equation (6-30), various procedures are developed or adopted to calculate several characteristic parameters, such as the friction velocity ( $U^*$ ), the settling velocity ( $U_T$ ), the dimensionless flux ( $A$ ), and the mean concentration of droplets along the vertical pipe diameter ( $C_{mean}$ ). Meanwhile, some of these parameters are used in the calculation of the deposition constant ( $k_D$ ) in the next section.

1) Friction velocity:

$$U^* = U_G (f_i / 2)^{0.5} \quad (6-31)$$

where:

$f_i$ : interfacial friction factor;

There are a number of correlations calculating the interfacial friction factor in droplet transport, one from Dallman (1979) is adopted:

$$\frac{f_i}{f_G} = \left[ 1 + (61F^{0.5})^2 \right]^{0.5} \quad (6-32)$$

$$F = \frac{\mu_L \rho_G^{0.5} \gamma \text{Re}_{LF}}{\mu_G \rho_L^{0.5} \text{Re}_G^{0.9}} \quad (6-33)$$

$$\gamma = \left[ (0.5 \text{Re}_{LF}^{0.5})^3 + (0.028 \text{Re}_{LF}^{0.9})^3 \right]^{1/3} \quad (6-34)$$

$$\text{Re}_{LF} = \frac{4W_{LF}}{\pi D \mu_L} = \frac{4(1-E)W_L}{\pi D \mu_L} \quad (6-35)$$

where:

$\text{Re}_{LF}$ : Reynolds number for the liquid film

$W_L$ : total liquid flow rate,  $\text{kg/m}^3 \text{ s}$

$W_{LF}$ : liquid flow rate in the film,  $\text{kg/m}^3 \text{ s}$

$E$ : entrainment

## 2) Settling velocity

Settling velocity is also called terminal velocity, which is a function of the gravity and the flow drag. For a spherical droplet, the terminal velocity can be calculated by:

$$U_T^2 = \frac{4dg\rho_L}{3C_D\rho_G} \quad (6-36)$$

where:

$C_D$ : drag coefficient

It is well known that the drag coefficient depends on the flow conditions. At a low Reynolds number ( $Re_{drop} < 1.62$ ), the drag coefficient could be calculated as:

$$C_D = \frac{24}{Re_{drop}} \quad (6-37)$$

where:

$$Re_{drop}: \text{ droplet Reynolds number } ( Re_{drop} = \frac{d_{50\%} u_T \rho_G}{\mu_G} )$$

$d_{50\%}$ : median diameter of droplets, m

At a moderate Reynolds number ( $1.62 < Re_{drop} < 500$ ), the equation for the drag coefficient is given as:

$$C_D = \frac{18.5}{Re_{drop}^{0.6}} \quad (6-38)$$

In order to calculate the median diameter of droplets, Al-Sarkhi and Hanratty (2002) proposed an empirical equation as:

$$\left( \frac{d_{50\%} U_{SG}^2 \rho_G}{\sigma} \right)^{0.37} \left( \frac{d_{50\%}}{D} \right)^{0.36} = 0.196 \quad (6-39)$$

It is worth noting that various droplet diameters have been used in different approaches. Baik and Hanratty (2003) found that choosing the median diameter, which is a function of gas velocity and the pipeline diameter, can reduce the dependence of the model on the dimensionless droplet diffusivity.

### 3) Dimensionless flux

The dimensionless flux is a constant from the model development in Paras and Kaabelas' work (1991), an empirical equation from experiments was given as:

$$A = 0.0134 + 0.532 \log_{10}(U_R) \quad (6-40)$$

where:

$U_R$ : reduced liquid superficial velocity ( $=U_{SL}/U_{SLC}$ );

$U_{SLC}$ : critical superficial liquid velocity below which there is no atomization at any gas velocity, m/s

In Baik and Hanratty's study (2003), the dimensionless flux A was assumed to be zero for simplification.

4) Mean concentration of droplets along the vertical pipe diameter

Through fitting with experimental data from both Paras and Kaabelas' work (1991) and Williams' work (1986), mean concentration of droplets could be calculated by:

$$C_{mean} = 0.85C^0 = 0.85 \frac{Q_E}{U_{SG}} \approx 0.85 \frac{EW_L}{U_{SG}} \quad (6-41)$$

where:

$Q_E$ : entrained liquid rate, kg/m<sup>2</sup> s.

$C^0$ : bulk mean concentration of droplets, kg/m<sup>3</sup>

On one hand,  $C^0$  can be calculated directly through the integration of local concentrations along the cross section:

$$C^0 = \frac{1}{A_c} \int C dA \quad (6-42)$$

where:

$A_c$ : cross section area,  $m^2$

On the other hand,  $C^0$  can be approximated if the entrainment rate can be calculated by the empirical equation from Pan and Hanratty (2002)

$$\frac{E/E_C}{1 - E/E_C} = K_E \frac{DU_G \rho_L^{1/2} \rho_G^{1/2}}{\sigma u_T} \quad (6-43)$$

where:

$E_C$ : entrainment at critical liquid velocity

$K_E$ : entrainment constant, (it was suggested by Pan and Hanratty to be 1E9)

### ***Deposition constant***

A procedure from Pan and Hanratty (2002) is adopted entirely in this study to determine the deposition constant. In Pan and Hanratty's work (2002) a Gaussian distribution was introduced to account for the velocity fluctuations. After integration the deposition constant can be calculated as:

$$k_D = \int_{-\psi}^{\infty} \frac{z}{\sqrt{2\pi}\sigma_p} \exp\left[\frac{-z^2}{2\sigma_p^2}\right] dz + \int_{-\psi}^{\infty} \frac{\psi}{\sqrt{2\pi}\sigma_p} \exp\left[\frac{-z^2}{2\sigma_p^2}\right] dz \quad (6-44)$$

where:

$\psi$ : gravity factor (=0 for vertical flow or =  $u_T \cos\theta$  for horizontal flow), m/s

$\theta$ : the angle deviating from the bottom of the line (= 0 at the bottom, =180° at the top), degree

$\sigma_p$ : standard deviation for Gaussian distribution, which is equal to the turbulent motion ( $\sigma_p^2 = \overline{v_p^2}$ ), m/s

In order to calculate the turbulent motion, Lee's method (1989a, b) was adopted when ideal entrainment is assumed, which is:

$$\overline{v_p^2} = \left( \frac{t_{LF}/\beta}{0.7 + t_{LF}/\beta} \right) \overline{v_G^2} \quad (6-45)$$

where:

$\beta$ : the inertial time constant to account for the response of a droplet to fluid turbulence, s

$t_{LF}$ : Lagrangian time constant to account for the gas turbulence, s

$\overline{v_G^2}$ : mean square of the gas velocity fluctuations, ( $= (0.9U^*)^2$ )

According to Hay (1996), the Lagrangian time constant can be calculated as:

$$t_{LF} = \frac{0.046D}{U^*} \quad (6-46)$$

And the inertial time constant can be calculated as (Pan and Hanratty, 2002):

$$\frac{1}{\beta} = \frac{3C_D \rho_G u_T}{4d_{50} \rho_L} \quad (6-47)$$

Substituting Equations (6-45), (6-46), and (6-47) into Equation (6-44), the deposition constant can be determined.

When the deposition constant from Equation (6-44) and the droplet concentration at the top of the line from Equation (6-30) are substituted into Equation (6-27), the deposition rate can be calculated and then the liquid thickness can be determined through

Equation (6-26). Finally, the transition conditions for the achievement of stable annular flow can be specified through the criterion of Equation (6-44).

### 6.2.3.2 Wave-mixing mechanism

When the turbulent waves on the liquid surface continues grow, the transition from stratified flow to annular flow or intermittent flow will take place. Milne-Thomson (1960) believed that turbulent waves grew on a horizontal flat rectangle channel if:

$$U_{SG} > \left[ \frac{g(\rho_L - \rho_G)h_G}{\rho_G} \right]^{1/2} \quad (6-48)$$

where:

$h_G$ : gas height in stratified flow, m.

The equation above was modified by Taitel and Dukler (1976) to account for the effect of the geometry of a round pipeline and the inclination as well. After a mathematic treatment, the criterion for the transition was given as:

$$U_G > C_{w-w} \left[ \frac{g(\rho_L - \rho_G) \cos \alpha A_G}{\rho_G \frac{dA_G}{dh_L}} \right]^{1/2} \quad (6-49)$$

where:

$C_{w-w}$ : a constant ( $= 1 - h_L/D$ ).

The inequality is coupled with Equation (6-1) through liquid holdup ( $h_L$ ). Liquid holdup is firstly calculated at different gas and liquid velocities, and the inequality is then applied to determine if the transition from stratified to annular/intermittent flow occurs.

#### 6.2.4 Numerical method

In order to identify the “effective zone”, three different criteria have to be applied simultaneously. The key factor for the numerical calculation is to determine liquid holdup ( $h_L$ ). Due to the non-linearity of the momentum balance equation (Equation (6-1)), Newton-Raphson iteration is applied. With the input of liquid holdup, the three criteria can calculate the onset of atomization and the transition from stratified to annular flow either by the wave-mixing mechanism or the entrainment-deposition mechanism, respectively. The flowchart (Figure 6-2) of the calculation process is drawn to assist the understanding of the detailed procedure.

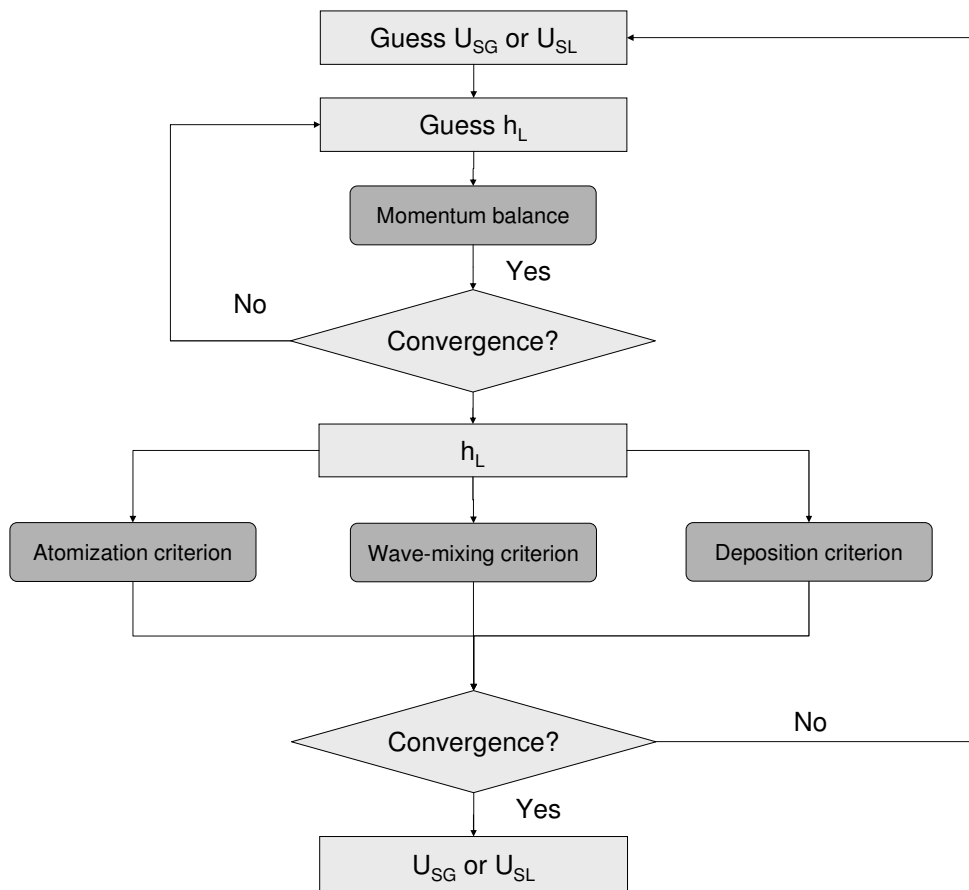


Figure 6-2: Flow chart for the numerical calculation in the determination of the “effective zone” ( $U_{SG}/U_{SL}$ : superficial gas/liquid velocity,  $h_L$ : liquid holdup)

## 6.3 Model prediction

### 6.3.1 Onset of atomization

A typical simulation result of the model for the onset of atomization is showed in Figure 6-3. Two turning points which can be identified clearly in the graph correspond to the critical Reynolds numbers:  $Re_{LC1}$  and  $Re_{LC2}$ . When the liquid Reynolds number is less than  $Re_{LC1}$ , atomization is very difficult and need much higher gas velocity according to undercutting mechanism. On the other hand, the increase of liquid velocity can not

infinitely reduce the dependence of droplet formation on the gas velocity. There is a minimum gas velocity for the onset of atomization, which is corresponding to the critical liquid Reynolds number ( $Re_{LC2}$ ). Compared to Lin and Hanratty's experiment (1987), the present model can predict the onset of liquid atomization precisely. However, more experiments are required to further verify the model in the future.

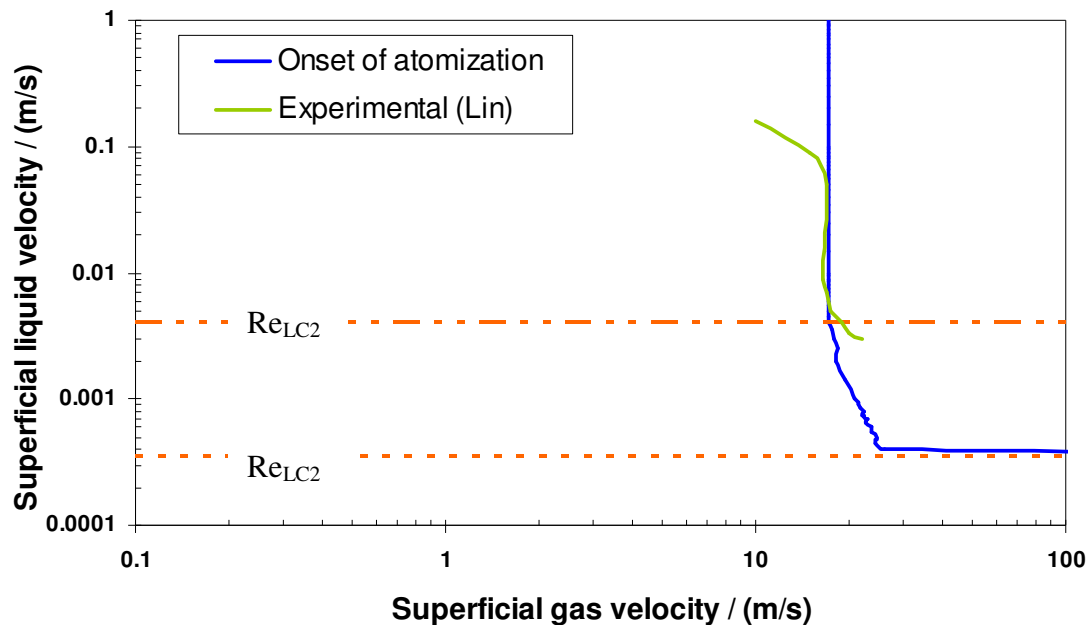


Figure 6-3: Comparison between an experiment and model prediction on the onset of atomization at such conditions  $T = 25\text{ }^{\circ}\text{C}$ ,  $P_T = 1\text{ bar}$ ,  $D = 0.1\text{ m}$ ,  $M_{Gas}$  (Molecular weight)  $= 0.029\text{ kg/mol}$  (Experimental data from Lin and Hanratty, 1987)

In order to figure out the effect of the total pressure and the pipeline diameter on the onset of atomization, numerical tests were carried out. The results are illustrated in Figure 6-4 and Figure 6-5, respectively. It can be seen that both these two factors have

great influences on the formation of droplets. Additionally, it is worth noting that the turning point in the transition zone between the two critical liquid Reynolds numbers (Figure 6-5) is not a computation error. In fact, it is due to the critical velocity introduced by Andrisos and Hanratty (1987a) in the calculation of the interfacial friction factor (Equation (6-9)). When gas velocity is greater than the critical velocity ( $U_{SG} > U_{SG,R}$ ), the friction at gas-liquid interface will be larger than the friction at the gas-wall interface.

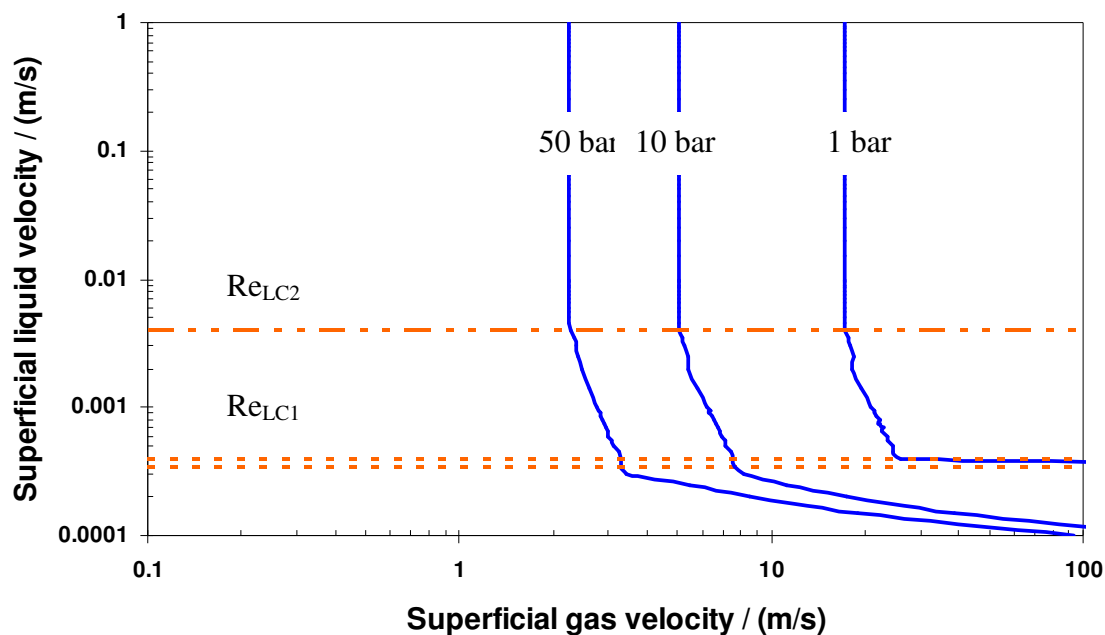


Figure 6-4: Onset of atomization at different pressures

$$(T = 25 \text{ } ^\circ\text{C}, D = 0.1 \text{ m}, M_{Gas} = 0.029 \text{ kg/mol})$$

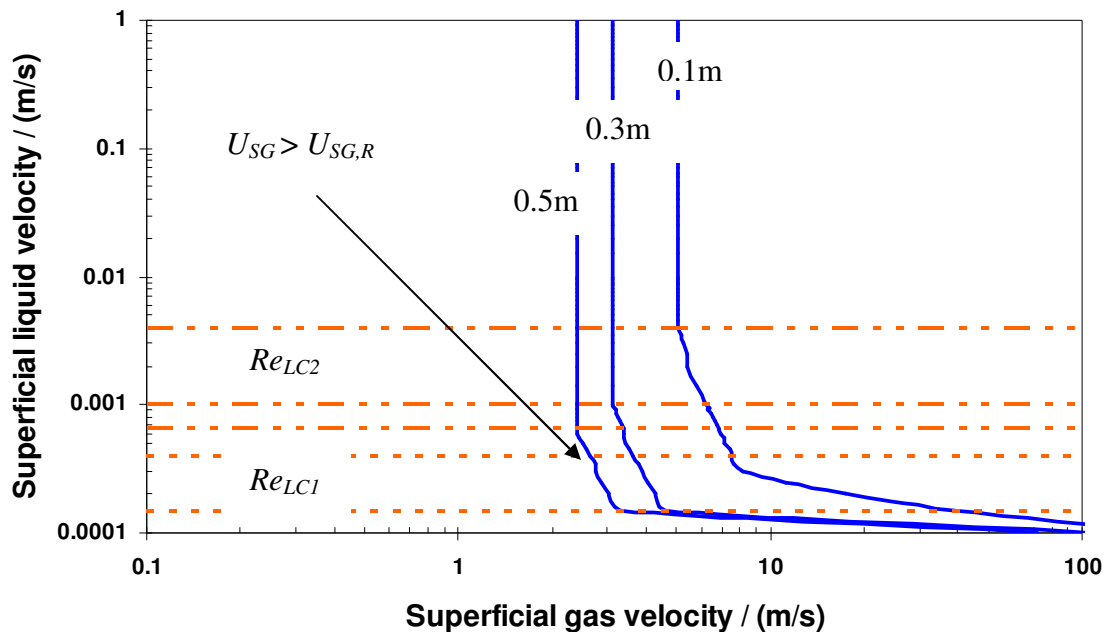


Figure 6-5: Onset of the atomization at different internal diameters

$$(T = 25 \text{ }^\circ\text{C}, P_T = 10 \text{ bar}, M_{Gas} = 0.029 \text{ kg/mol})$$

### 6.3.2 Transition to non-stratified flow

As discussed in the model development, two different mechanisms including wave-mixing and entrainment-deposition were proposed to predict the transition from stratified to non-stratified flow. In Figure 6-6 the predicted transitions by both these models are compared to the experimental results from Lin and Hanratty (1987) in a 9.53 cm pipeline. It is found that the entrainment-deposition mechanism under-predict gas velocity needed for the transition to annular flow while the wave-wetting mechanism can precisely predict the transition. In contrast, it is the entrainment-deposition mechanism, instead of the wave-mixing mechanism, that can provide an accurate prediction in the

transition from stratified to annular flow when the pipeline diameter is 30 cm (Figure 6-7). It seems that the entrainment-deposition mechanism dominates the transition process when the pipeline diameter is larger than a critical value which is between 9.53 cm and 30 cm. However, the conclusion is preliminary due to the limited amount of experimental data.

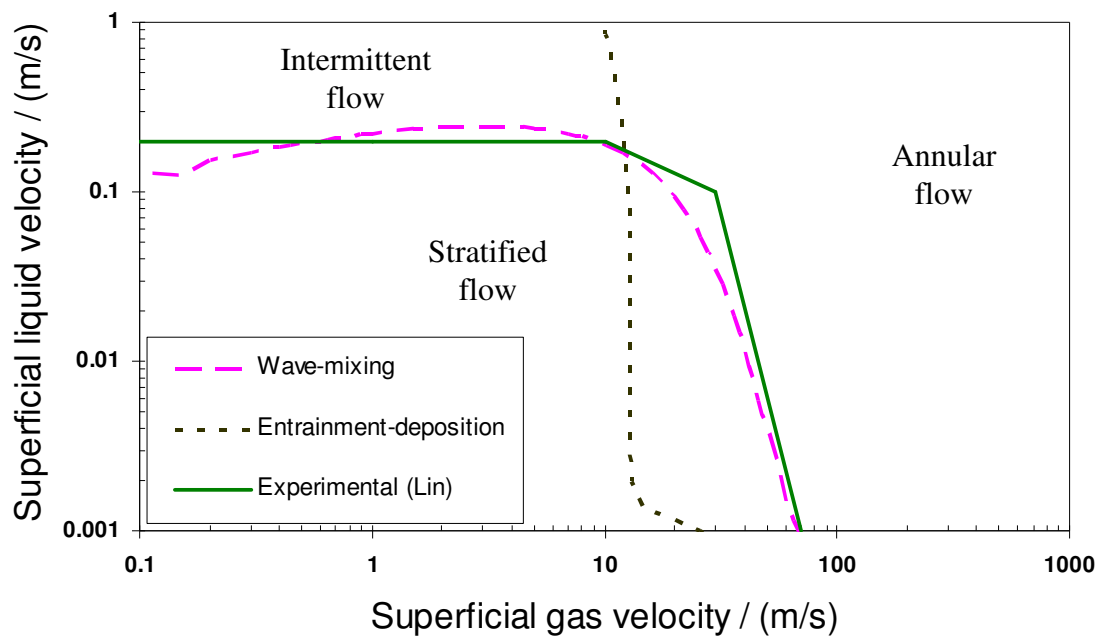


Figure 6-6: Transitions from stratified to non-stratified flow predicted by the wave-mixing and entrainment-deposition mechanism, and measured by Lin and Hanratty (1987) at such conditions as  $T = 25\text{ }^{\circ}\text{C}$ ,  $P_T = 1\text{ bar}$ ,  $M_{Gas} = 0.029\text{ kg/mol}$ , and  $D = 0.095\text{ m}$

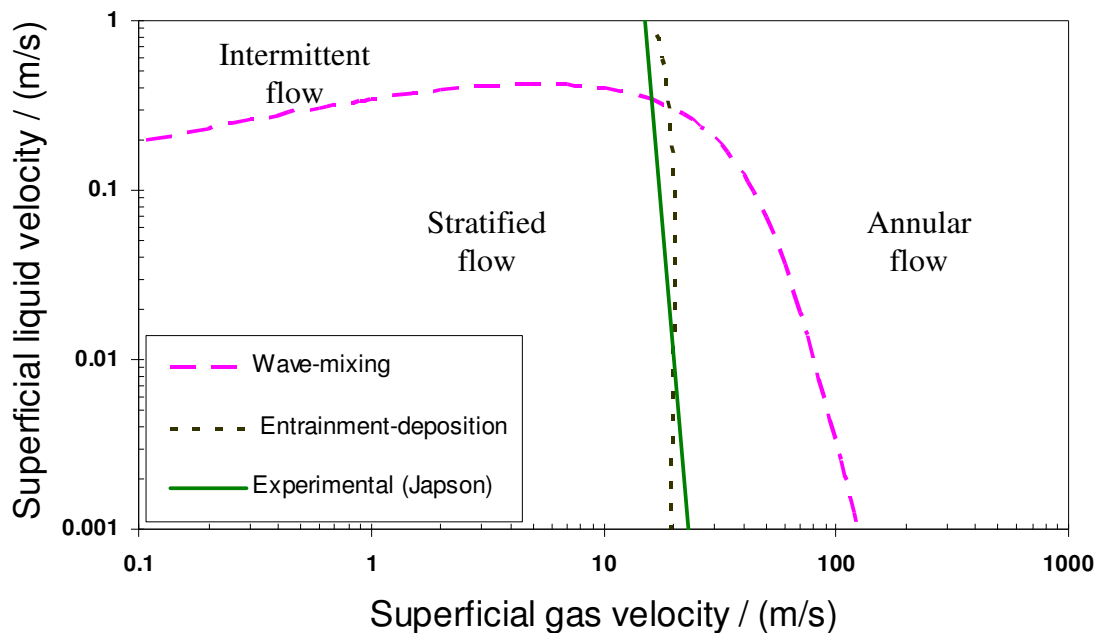


Figure 6-7: Transitions from stratified to non-stratified flow predicted by the wave-mixing and entrainment-deposition mechanism, and measured by Japson and Taylor (1993) at such conditions as  $T = 25\text{ }^{\circ}\text{C}$ ,  $P_T = 1\text{ bar}$ ,  $M_{Gas} = 0.029\text{ kg/mol}$ , and  $D = 0.3\text{ m}$

### 6.3.3 “Effective zone”

When these three different onset and transition criteria are presented in a flow map (Figure 6-8), the area surrounded by the prediction curves can form an “effective zone”, in which droplets can be atomized from the liquid at the bottom of the line and then be deposited at the top of the line. In other words, inhibitors injected at the bottom of the line can reach the top by effective droplet transport and TLC is able to be prevented with the protection of inhibitors. It should be pointed out that the turning point Figure 6-8 for the entrainment-deposition mechanism is due to the existing of a critical entrainment rate. In Pan and Hanratty’s model (2002), the critical entrainment rate in Equation (6-43),

which happens at the critical liquid Reynolds number ( $Re_{LC1}$ ), was introduced to act as a reference for droplet entrainment at higher liquid Reynolds number.

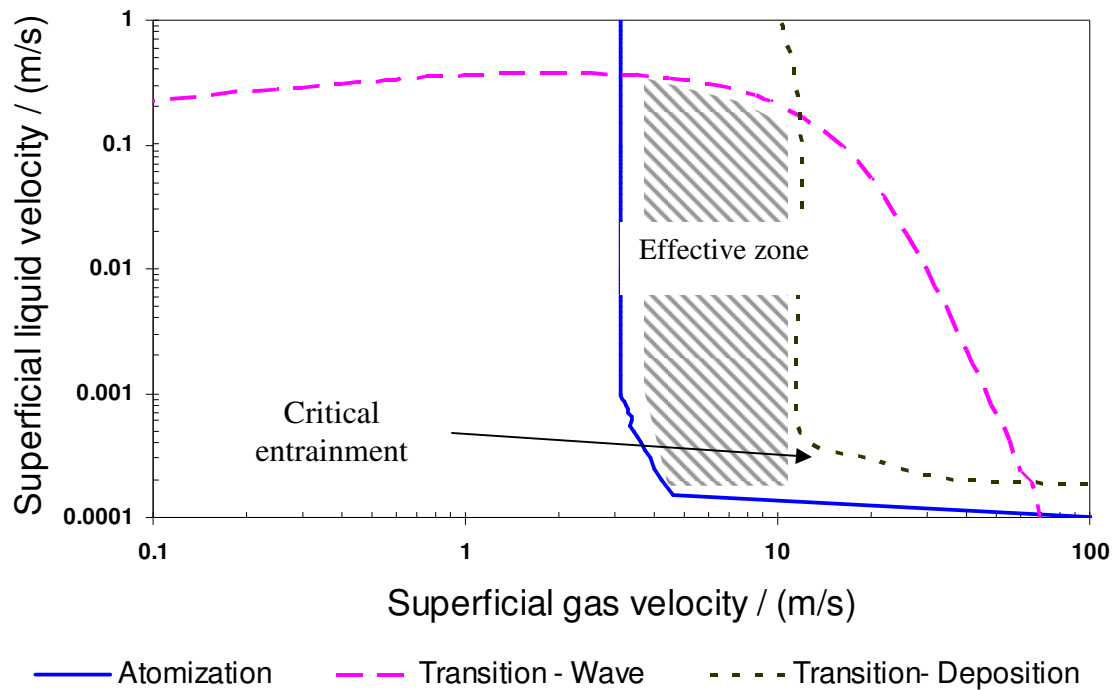


Figure 6-8: A flow map with an indicated “effective zone” in which inhibitors can be effectively transported to the top side of the pipeline through the deposition of entrained droplets ( $T = 25\text{ }^{\circ}\text{C}$ ,  $P_T = 10\text{ bar}$ ,  $D = 0.3\text{ m}$ )

#### 6.4 Summary

An inception criterion for the atomization in gas-liquid two phase flow has been established. Two different mechanisms responsible for droplet formation and their relative importance have been investigated. At low liquid Reynolds number, the

undercutting mechanism is dominant while the tearing mechanism is more important when the liquid Reynolds number is larger than a critical value.

At the same time, a new model from the entrainment-deposition mechanism has been developed to predict the transition from stratified to annular flow. When the pipeline diameter is large, the entrainment-deposition mechanism is dominant. However, the conventional mechanism (wave-mixing) is more important in small scale pipelines. According to the limited experimental data, the critical pipeline diameter likely lies between 0.095 and 0.300 m.

Finally, an “effective zone” with four boundaries determined by the three different onset and transition criteria has been defined in a flow map. This map can be an operational guidance in TLC prevention by utilizing corrosion inhibitors. In the future, experiments on large scale loops are required to further verify the model. In addition, it is worth carrying out the force analysis on an entrained droplet, which might lead to an exact deposition criterion rather than an effective zone.

## **CHAPTER 7: CONCLUSIONS AND RECOMMENDATIONS FOR FUTURE DEVELOPMENT**

A comprehensive study has been carried out to investigate the mechanism for top of the line corrosion (TLC) through experiments and modeling approaches. The effects of all important factors on TLC: gas temperature, CO<sub>2</sub> partial pressure, gas velocity, condensation rate, and HAc concentration were evaluated in long term tests (up to 21 days) in large scale flow loop. In all experiments a protective film was observed on the coupon surface by SEM and further identified to be made of iron carbonate crystals by EDS. With testing time, the uniform corrosion rate measured by weight loss coupons was gradually decreased due to the growing protection of the film on the coupon surface. However, in contrast, the localized corrosion associated with the damaged film appeared to be more evident when testing time was increased.

A mechanistic model has been developed which includes a fully mechanistic representation of the main processes in top of the line corrosion (TLC): dropwise condensation, gas liquid equilibria, corrosion processes, and force analysis on a single droplet. The effects of all these parameters tested in our long term experiments are described by mathematical equations which are firmly based on the physics behind the processes involved. The model can predict the dropwise condensation rate and the evolution of the uniform corrosion rate with time.

Both experimental and modeling studies indicated the possibility of different dropwise condensation regimes at the top of the line. Their transitions from one regime to

another were predicted through the force analysis on a single droplet. A condensation regime map defining transition conditions between different condensation regimes was built from our model and other work in hydrodynamics.

In comparisons with various corrosion and condensation experiments in large scale loop equipped with an *in situ* camera, the model showed satisfactory performance in the prediction of condensation rate, general corrosion rate, and condensation regimes. The mechanistic model and experimental experience in our laboratory have been incorporated into a software package (TOPCORP), in which all complicated and tedious computations were hidden behind a user friendly interface. The clean version of the model with reduced complexities to the utmost extent would be easily accepted by the industry.

At the same time, droplet transport and its effect on TLC have been examined through mathematical modeling. Conditions, under which droplets can reach the top of the line and the injection of corrosion inhibitors is able to prevent TLC issues, can be predicted by the model.

Reproducing the same conditions observed in the real field cases is a constant focus of our research work. However, a number of factors had to be neglected due to a variety of safety and technical reasons. In certain cases, some of these factors might be very important. For example, the co-condensation of hydrocarbons with water vapor could change not only heat transfer behavior for water vapor condensation but also the chemical speciation in water chemistry. The evaluation of these factors will be useful to broaden the applicability of the present model. Furthermore, the valuable information

hidden in the rich source of case failures has been ignored for a long time due mostly to lack of a reliable theoretical tool. As a mechanistic model, TOPCORP can be applied in the case analysis to theoretically explore the root cause responsible for these failures.

In a pipeline, localized corrosion is more complicated and dangerous than general corrosion which could be predicted by the present model. However, the mechanism for localized corrosion even at the bottom of the line is still not fully understood and debatable. Several mechanisms have been proposed for various corrosion scenarios. Among them, galvanic coupling seems to be dominant in CO<sub>2</sub> corrosion at bottom of the line based on the latest progress of another Joint Industry Project in our laboratory. Given the top side of the pipeline, galvanic corrosion might happen when the *concentration cell* is established in a single droplet. On the other hand, due to the randomness of droplet distribution in dropwise condensation, non-uniform condensation might be a more important mechanism for localized corrosion at the top of the line. Both mechanisms are worth examining through either experiments or modeling approaches, and their relative importance is required to be clarified as well. The extension of the present model's capability on localized corrosion prediction will further boost the recognition of the present model in industry.

Although the theoretical study on droplet transport has been accomplished, its validation with experiments in our laboratory is desperately needed. The knowledge gained from the theory would be helpful in the design of such experiments and the interpretation of experimental data. In addition, the force analysis on an entrained droplet

which might lead to an exact criterion, instead of an effective zone, for droplet deposition at the top of the line is worth to examine in the future.

**REFERENCES**

1. Adamson, A. W., Physical Chemistry of Surfaces, John Wiley & Sons, New York, NY, 1990, pp.21
2. Abu-Orabi, M., Modeling of Heat Transfer in Dropwise Condensation, International Journal of Heat Mass Transfer, 1998, 41: 81-87
3. Al-Sarkhi, A., Hanratty, T. J., Effect of Pipe Diameter on the Drop Size in a Horizontal Annular Gas-liquid Flow, International Journal of Multiphase Flow, 2002, 28 (5): 1617-1629
4. Andreussi, P., Asali, J., Hanratty, T. J., Initiation of Roll Waves in Gas-liquid Flows, AIChE Journal, 1985, 31: 126-134
5. Andritsos, N., Hanratty, T. J., Interfacial Instabilities for Horizontal Gas-liquid Flows, International Journal of Multiphase Flow, 1987a, 13 (5): 583-603
6. Andritsos, N., Hanratty, T. J., Influence of Interfacial Waves in Stratified Gas-liquid Flows, AIChE Journal, 1987b, 33 (5): 444-454
7. Baik, S., Hanratty, T. J., Concentration Profiles of Droplets and Prediction of the Transition from Stratified to Annular Flow in Horizontal Pipes, International Journal of Multiphase Flow, 2003, 29: 329-338
8. Bikerman, J. J., Sliding of Drops from Surfaces of Different Roughness, Journal of Colloid Science, 1950, 5: 349-359
9. Bikerman, J. J., Physical Surfaces, Academic Press, New York, NY, 1970, pp.278

10. Bird, R. B., Stewart, W. E., Lightfoot, E. N., Transport Phenomena, John Wiley & Sons, Inc., 2<sup>nd</sup> Edition, 2002, pp.522
11. Camacho, A., CO<sub>2</sub> Top of the Line Corrosion in the Presence of H<sub>2</sub>S, MS thesis, Ohio University, Athens, OH, 2006
12. Chato, J. C., American Society of Heating, Refrigerating, Air Conditioning Engineers Journal, 1962, pp.52 (a citation from Vitse, 2002)
13. CNN, Alaska Oil Shutdown Hikes Prices: Corrosion, Small Spill Leads to Loss of 400,000 Barrels a Day, <http://edition.cnn.com/2006/US/08/07/oilfield.shutdown/>
14. Dallman, J. C., Jones, B. G., Hanratty, T. J., Interpretation of Entrainment Measurements in Annular Gas-liquid Flows, Two-phase Momentum, Heat and Mass Transfer, (Edited by F. Durst, G. V. Tsiklauri, N. H. Afgan ), New Hemisphere, Washington DC, 1979, 2: 681-693
15. Dittus, F. W., Boetler, L. M. K., Public Engineering, University of California at Berkeley, 1930, 2: 443-447
16. de Waard, C., Lotz, U., Prediction of CO<sub>2</sub> Corrosion of Carbon Steel, Corrosion/93, NACE International, Houston, TX, 1993, Paper No. 69
17. Estavoyer, M., Corrosion Problems at Lack Sour Gas Field, H<sub>2</sub>S Corrosion in Oil and Gas production,, NACE publication, Houston TX, 1981, pp.905
18. Gerner, F.M., and Tien, C.L., Multi-Component Interfacial Condensation, International Journal of Heat Mass Transfer, 1990, 33: 2111-2120
19. Glicksman, L. R., Hunt, A. W, Numerical Simulation of Dropwise Condensation, International Journal of Heat and Mass Transfer, 1972, 15: 2251-2269

20. Graham, C., Griffith, P., Drop Size Distribution and Heat Transfer in Dropwise Condensation, *International Journal of Heat and Mass Transfer*, 1973, 16: 337-346
21. Gunaltun, Y. M., Supriyataman, D., Jumaludin, A., Top of the Line Corrosion in Multiphase Gas Lines: A Case History, *Corrosion/99*, NACE International, Houston, TX, 1999, Paper No. 36
22. Hanratty, T. J., Gas-liquid Flow in Pipelines, *Physicochemical Hydrodynamics*, 1987, 9 (1-2): 101-144
23. Hay, K. J., Liu, Z. C., Hanratty, H. J., Relation of Deposition to Drop Size When the Rate Law Is Nonlinear, *International Journal of Multiphase Flow*, 1996, 22: 829-848
24. Minkowycz, W. J., Sparrow, E. M., Condensation Heat Transfer in the Presence of Noncondensable Gas, Interfacial Resistance, Superheating, Variable Properties, and Diffusion, *International Journal of Heat and Mass Transfer*, 1966, 9: 1125-1144
25. Newitt, D. M., Dombrowski, N., Knelman, F. H., Liquid Entrainment: 1. The Mechanism of Drop Formation from Gas or Vapor Bubbles, *Transactions of the Institution of Chemical Engineers*, 1954, 32: 244-261
26. Hewitt D. M., Hall-Taylor, N. S., *Annular Two-Phase Flow*, Pergamon Press, Oxford, Great Britain, 1974, pp.136
27. Hinkson, D., Singer, M., Nestic, S., Zhang Z., A Study of the Chemical Composition and Corrosivity of the Condensate in Top of the Line Corrosion, *Corrosion/2008*, NACE International, Houston, TX, 2008
28. Hinze, J. O., Fundamentals of the Hydrodynamic Mechanism of Splitting in Dispersion Processes, *AIChE Journal*, 1955, 1(3): 289-295

29. Hughmark, G. A., Film Thickness, Entrainment, and Pressure Drop in Upward Annular and Dispersed Flow, *AIChE Journal*, 1962, 19(5): 1062-1065
30. Ishii, M., Grolmes, M. A., Inception criteria for Droplet Entrainment in Two-Phase Concurrent Film Flow, *AIChE Journal*, 1975, 21 (2): 308-318
31. Jepson, W. P., Taylor, R. E., Slug Flow and Its Transitions in Large-Diameter Horizontal Pipes, *International Journal of Multiphase Flow*, 1993, 19: 411-420
32. Jones, D. A., Principles and Prevention of Corrosion, 2<sup>nd</sup> edition, Prentice Hall, Upper saddle River, NJ, 1996
33. Karabelas, A. J., Vertical Distribution of Dilute Suspensions in Turbulent Pipe Flow, *AIChE Journal*, 1977, 23: 426-434
34. Koch G. H., Brongers M. P. H., Thompson N. G., Virmani Y. P., and Payer J. H., Corrosion Cost and Preventive Strategies in the United States, Appendix A, FHWA-RD-01-156, Federal Highway Administration, U.S. Department of Transportation, Washington, D.C., 2002
35. Lane, W. R., Shatter of Drops in Streams of Air, *Industrial Engineering Chemistry*, 1951, 43: 1312 -1321
36. Laurinat, J. E., Hanratty, T. J., Jepson, W. P., Film Thickness Distribution for Gas-Liquid Annular Flow in a Horizontal Pipe, *PhysicoChemical Hydrodynamics* 1985, 6: 179-195
37. Lee, M. M., Hanratty, T. J., Adrian, R. J., The Interpretation of Droplet Deposition Measurement with a Diffusion Model, *International Journal of Multiphase Flow*, 1989a, 15: 459-469

38. Lee, M. M., Hanratty, T. J., Adrian, R. J., An Axial Viewing Photographic Technique to Study Turbulence Characteristics of Particles, *International Journal of Multiphase Flow*, 1989b, 15: 787-802
39. Lin, P. Y., Hanratty, T. J., Effect of Pipe Diameter on Flow Patterns for Air Water-Flow in Horizontal Pipes, *International Journal of Multiphase Flow*, 1987, 13 (4): 549-563
40. Mandhane, J.M., Gregory, G. A. and Aziz, K., 1974. A Flow Pattern Map for Gas-Liquid Flow in Horizontal Pipes, *International Journal of Multiphase Flow*, 1974, 1: 537-553
41. Mendez, C., Singer, M., Camacho, A., Hernandez, S., Nestic, S., Gunaltun, Y., Jossten, M., Sun, Y., Gabbetta, P, Effect of Acetic Acid, pH and MEG on CO<sub>2</sub> Top of the Line Corrosion, *Corrosion/2005*, NACE International, Houston, TX, 2005, Paper No. 05278
42. Mine-Thomson, L. M. *Theoretical Hydrodynamics*, MacMillan Co., New York, 1960
43. Nestic, S., Postlethwite, J. Olsen, S., An Electrochemical Model for Prediction of Corrosion of Mild Steel in Aqueous Carbon Dioxide Solution, *Corrosion*, 1996, 59: 280-294
44. Nestic, S., Lee, K. L. J., A Mechanistic Model for Carbon Dioxide Corrosion of Mild Steel in the Presence of Protective Iron Carbonate Films - Part 3: Film Growth Model, *Corrosion*, 2003, 59: 616-628

45. Nordsveen, M., Nestic, S., Nyborg, R., A Mechanistic Model for Carbon Dioxide Corrosion of Mild Steel in the Presence of Protective Iron Carbonate Films - Part 1: Theory and verification, *Corrosion*, 2003, 59: 443-456
46. Olsen, S., Dugstad, A., Corrosion under Dewing Conditions, *Corrosion/91*, NACE International, Houston, TX, 1991,, Paper No. 472
47. Pan, L., Hanratty, T. J., Correlation of Entrainment for Annular Flow in Horizontal Pipes, *International Journal of Multiphase Flow*, 2002, 28: 385-408
48. Paras, S. V., Karabelas, A. J., Droplet Entrainment and Deposition in Horizontal Annular Flow, *International Journal of Multiphase Flow*, 1991, 17(4): 455-468
49. Perry, R. H., Green, E. W., *Perry's Chemical Engineers' Handbook*, Mc-Graw Hill, New York, NY, 1997a: 2-363
50. Perry, R. H., Green, E. W., *Perry's Chemical Engineers' Handbook*, Mc-Graw Hill, New York, NY, 1997b: 2-367
51. Perry, R. H., Green, E. W., *Perry's Chemical Engineers' Handbook*, Mc-Graw Hill, New York, NY, 1997c: 2-347
52. Pots, B. F. M., Hendriksen, E. L. J. A., CO<sub>2</sub> Corrosion under Scaling Conditions the Special Case of Top-of-the-Line Corrosion in Wet Gas Pipelines, *Corrosion/2000*, NACE International, Houston, TX, 2000, Paper No. 31
53. Rose, J.W., Glicksman, L.R., Dropwise Condensation: the Distribution of Drop Sizes, *International Journal of Heat Mass Transfer*, 1973, 16: 411-425
54. Rose, J.W., Some Aspects of Condensation Heat Transfer Theory, *International Communication Heat Mass Transfer*, 1988, 15: 449-473

55. Ruschau, G. R., Al-Anezi, M. A., Oil and Gas Exploration and Production, CorrosionCost.com, <http://costofcorrosion.com/pdf/oilgas.pdf>
56. Sapaly G, Singer, M., Zhang Z. Nestic, S., Top of the Line Corrosion Joint Industry Project: Internal Report at Institute for Corrosion and Multiphase Technology, Ohio University, Athens, OH, 2007
57. Singer, M.; Nestic, S.; Gunaltun, Y.M., Top of Line Corrosion in Presence of Acetic Acid and Carbon Dioxide,, CORROSION /2004, NACE International, Houston, TX, 2004, Paper No. 04377
58. Singer, M., Brown, B., Camacho, A., Hinkson, D., Zhang, Z., Mendez, C., Nestic, S., Compilation of Results, TLC JIP, Institute for Corrosion and Multiphase Technology, Ohio University, Athens, OH, 2007
59. Singer, M., Zhang, Z., Hinkson, D., Nestic, S., TLC JIP Advisory Board Meeting Report, Institute for Corrosion and Multiphase Technology, Ohio University, Athens, OH, 2004-2007
60. Slegers, L., Seban, R. A., Laminar Film Condensation of Steam Containing Small Concentration of Air, International Journal of Heat and Mass Transfer, 1970, 13: 1941-1947
61. Steen, D. A., The Transition from Annular Flow to Annular-Mist Concurrent Two-Phase Down Flow, MS thesis, Dartmouth College, 1964
62. Stephan, K., Heat Transfer in Condensation and Boiling, Springer-Verlag, New York, 1992, pp.84

63. Sun, W., Kinetics of Iron Carbonate and Iron Sulfide Scale Formation in CO<sub>2</sub>/H<sub>2</sub>S Corrosion, PhD dissertation, Ohio University, Athens, OH, 2007, pp.37
64. Taitel, Y., Dukler, A. E., A Model for Predicting Flow Regime Transitions in Horizontal and Near Horizontal Gas-Liquid Flow, *AIChE Journal*, 1976, 22(1): 47-55
65. Tanner, D. W., Potter C. J., and West D., Heat Transfer in Dropwise Condensation – Part I: The Effect of Heat Flux, Steam Velocity, and Non-condensable Gas Concentration, *International Journal of Heat Mass Transfer*, 1965, 8: 419-426
66. Utaka, Y., Saito, A., On the Mechanism Determining the Transition Mode from Dropwise to Film Condensation, *International Journal of Heat Mass Transfer*, 1988, 31(5): 1113-1120
67. Vitse, F., Experimental and theoretical study of the Phenomena of Corrosion by Carbon Dioxide under Dewing Conditions at the Top of a Horizontal Pipeline in the Presence of a Non-Condensable Gas, PhD Dissertation, Ohio University, Athens, OH, 2002
68. Vitse, F., Nestic, S., Gunaltun, Y., Mechanistic Model for the Prediction of Top-of-the-Line Corrosion Risk, *Corrosion*, 2003,, 59:1075-1084
69. van Hunnik, E.W. J., Pots, B. F. M., Hendriken, E. L. J., The Formation of Protective FeCO<sub>3</sub> Corrosion Product Layer in CO<sub>2</sub> Corrosion, *CORROSION /96*, NACE International, Houston, TX, 1996, Paper No. 6
70. van Rossum, J. J., Experimental Investigation of Horizontal Liquid Films: Wave Formation, Atomization, Film Thickness, *Chemical Engineering Science*, 1959, 11: 35-52

71. Wang, S.X., and Utaka, Y., Effect of Non-Condensable Gas Mass Fraction on Condensation Heat Transfer For Water-Ethanol Vapor Mixture, JSME International, 2004, 47: 162-167
72. Wang, C. Y., and Tu, C. J., Effects of Non-Condensable Gas on Laminar Film Condensation in a Vertical Tube, International Journal of Heat Mass Transfer, 1988, 31: 2339-2345
73. White, F. M., Fluid Mechanics, 4th Edition, McGraw-Hill International, New York, 1999, pp.460
74. Wilke, C. R., Diffusional Properties of Multicomponent Gases, Chemical Engineering Progress, 1950, 46(2): 95-104
75. Williams, L. R., Entrainment Measurements in a 4-inch Horizontal Pipe, MS, Thesis, The University of Illinois, Urbana, 1986
76. Williams, L. R., Dykhno, L. A., Hanratty, T. J., Droplet Flux Distribution and Entrainment in Gas-Liquid Flow, International Journal of Multiphase flow, 1996, 22: 1-18
77. Wu, W. H., and Maa, J. R., On the Heat Transfer in Dropwise Condensation, The Chemical Engineering Journal, 1976, 12: 225-231
78. Zhivaikin, L. Y., Liquid Film Thickness in Film Type Units, International Chemical Engineering, 2, 337 (a citation from Hewitt, G. F., Hall-Taylor N. S., 1974)
79. Zuber, N., On the Atomization and Entrainment of Liquid Film in Shear Flow, General Electric Co. Report 62 CL 153, 1962 (a citation from Ishii and Grolmes, 1975)

**APPENDIX I: CHEMICAL REACTIONS AND THEIR  
REACTION/EQUILIRIUM CONSTANTS**

Table I-1: Chemical reactions accounted for in the model and their equilibrium constants  
(Adapted from Nordsveen et al., 2003 )

	<b>Reaction</b>	<b>Equilibrium Constant</b>
Dissolution of carbon dioxide	$CO_2(g) \Leftrightarrow CO_2$	$K_{sol} = c_{CO_2} / p_{CO_2}$
Water dissociation	$H_2O \xrightleftharpoons[k_{b,wa}]{k_{f,wa}} H^+ + OH^-$	$K_{wa} = c_{H^+} c_{OH^-}$
Carbon dioxide hydration	$CO_2 + H_2O \xrightleftharpoons[k_{b,hy}]{k_{f,hy}} H_2CO_3$	$K_{hy} = c_{H_2CO_3} / c_{CO_2}$
Carbonic acid dissociation	$H_2CO_3 \xrightleftharpoons[k_{b,ca}]{k_{f,ca}} H^+ + HCO_3^-$	$K_{ca} = c_{H^+} c_{HCO_3^-} / c_{H_2CO_3}$
Biocarbonate anion dissociation	$HCO_3^- \xrightleftharpoons[k_{b,bi}]{k_{f,bi}} H^+ + CO_3^{2-}$	$K_{bi} = c_{H^+} c_{CO_3^{2-}} / c_{HCO_3^-}$
Acetic acid dissociation	$HAc \xrightleftharpoons[k_{b,ac}]{k_{f,ac}} H^+ + Ac^-$	$K_{HAc} = c_{H^+} c_{Ac^-} / c_{HAc}$
Iron carbonate precipitation	$Fe^{2+} + CO_3^{2-} \Rightarrow FeCO_3$	$K_{sp} = c_{Fe^{2+}} c_{CO_3^{2-}}$

Table I-2: Equilibrium ( $K$ ), forward ( $k_f$ ), and backward ( $k_b$ ) reaction rate coefficients(Note:  $K = k_f/k_b$ ) (Adapted from Nordsveen, 2003)

Constant	Source
$K_{sol} = \frac{14.5}{1.00258} \times 10^{-(2.27+5.65 \times 10^{-3} T_f - 8.06 \times 10^{-6} T_f^2 + 0.075 \times I)}$ molar / bar	Oddo and Tomson <sup>38</sup>
$K_{H_2S,sol} = 10^{-0.71742672+0.012145427 \times T_c + 5.6659982 \times 10^{-5} T_c^2 - 8.1902716 \times 10^{-8} T_c^3}$ molar / bar	IUPAC data <sup>39</sup>
$K_{wa} = 10^{-(29.3638-0.0737549 \times T_K + 7.47881 \times 10^{-5} T_K^2)}$ molar <sup>2</sup>	Kharaka, et al. <sup>40</sup>
$k_{b,wa} = 7.85 \times 10^{10} M^{-1} s^{-1}$	Delahay <sup>28</sup>
$K_{hy} = 2.58 \times 10^{-3}$	Palmer and van Eldik <sup>41</sup>
$k_{f,hy} = 10^{\frac{329.85-110.541 \times \log T_K - \frac{17,265.4}{T_K}}{s^{-1}}}$	Palmer and van Eldik <sup>41</sup>
$K_{ca} = 387.6 \times 10^{-(6.41-1.594 \times 10^{-3} T_f + 8.52 \times 10^{-6} T_f^2 - 3.07 \times 10^{-5} p - 0.4772 \times I^{1/2} + 0.1180 \times I)}$ molar	Oddo and Tomson <sup>38</sup>
$k_{f,ca} = 10^{5.71+0.0526 \times T_C - 2.94 \times 10^{-4} \times T_C^2 + 7.91 \times 10^{-7} \times T_C^3}$ s <sup>-1</sup>	Comprehensive Chemical Kinetics <sup>42</sup>
$K_{bi} = 10^{-(10.61-4.97 \times 10^{-3} T_f + 1.331 \times 10^{-5} T_f^2 - 2.624 \times 10^{-5} p - 1.166 \times I^{1/2} + 0.3466 \times I)}$ molar	Oddo and Tomson <sup>38</sup>
$k_{f,bi} = 10^9 s^{-1}$	Estimated
$K_{HAc} = 10^{-(6.66104-0.0134916 \times T_K + 2.37856 \times 10^{-5} T_K^2)}$ molar	Kharaka, et al. <sup>40</sup>
$k_{f,HAc} = 3.2 \times 10^5 s^{-1}$	Vetter <sup>43</sup>

Note: In the table,  $T_f$  is temperature in degrees Fahrenheit,  $T$  is absolute temperature in Kelvin,  $T_C$  is temperature in degrees Celsius,  $I$  is ionic strength in molar, and  $p$  is the pressure in psi.

## APPENDIX II: CALCULATION OF GAS PROPERTIES IN NONIDEAL GAS MIXTURES

In order to calculate the mass transfer coefficient and heat transfer coefficient it is necessary to predict the gas properties including density, viscosity, thermal conductivity, diffusivity, and heat capacity for a gas mixture in non-ideal state.

### 1. Gas density

A generalized equation can be used to calculate the gas density as:

$$\rho = \frac{PM_{mix}}{ZRT} \quad (\text{II-1})$$

where

$P$ : total pressure, Pa

$M_{mix}$ : molecular weight of gas mixture, kg/mol

$Z$ : the compressibility factor, which could be calculated by either Peng-Robison or Redlich-Khong state equation

$R$ : gas constant, 8.314 J/mol K

$T$ : temperature, K

### 2. Gas viscosity (Perry, 1997a)

The viscosity of pure hydrocarbon at low pressure can be calculated by

$$\mu = 4.6 \times 10^{-4} \frac{NM^{1/2}P_c^{2/3}}{T_c^{1/6}} \quad (\text{II-2})$$

where:

$N$ : constant ( $N = 3.4 \times 10^{-4} T_r^{0.94}$  for  $T_r \leq 1.5$ )

or  $N = 1.778 \times 10^{-4} (4.58T_r - 1.67)^{0.625}$  for  $T_r > 1.5$ )

$M$ : molecular weight of a hydrocarbon, kg/mol;

$P_c$ : critical pressure, bar;

$T_c$ : critical temperature, K

$T_r$ : reduced temperature

At the same time the viscosity of pure non-hydrocarbon gases at low pressure can be calculated by

$$\mu = \frac{AT_r}{[1 + 0.36T_r(T_r - 1)]^{1/6}} \quad (\text{II-3})$$

where:

$$A = 1.6104 \times 10^{-10} \frac{M^{1/2}P_c^{2/3}}{T_c^{1/6}}$$

The viscosity of gas mixture at low pressure can be calculated according to a mixture rule:

$$\mu_{mix} = \sum_{\alpha} \frac{x_{\alpha} \mu_{\alpha}}{\sum_{\beta} x_{\beta} \Phi_{\alpha\beta}} \quad (\text{II-4})$$

where:

$$\Phi_{\alpha\beta} = \frac{1}{\sqrt{8}} \left( 1 + \frac{M_{\alpha}}{M_{\beta}} \right)^{-1/2} \left[ 1 + \left( \frac{\mu_{\alpha}}{\mu_{\beta}} \right)^{1/2} \left( \frac{M_{\alpha}}{M_{\beta}} \right)^{1/4} \right]^2$$

The viscosity of gas mixture at high pressure can then be calculated by

$$\mu - \mu_0 = 5.0 \times 10^{-8} \frac{M^{1/2} P_c^{2/3}}{T_c^{1/6}} \left[ \exp(1.439 \rho_r) - \exp(-1.11 \rho_r^{1.858}) \right] \quad (\text{II-5})$$

where:

$\mu_0$ : viscosity of gas mixture at low pressure, m<sup>2</sup>/s

$\rho_r$ : reduced density

### 3. Gas thermal conductivity (Perry, 1997b)

The thermal conductivity of pure gas at low pressure can be calculated by

$$k_G = 10^{-7} (14.52 T_r - 5.14)^{2/3} \left( \frac{C_p}{\lambda} \right) \quad (\text{II-6})$$

where:

$$\lambda = T_c^{1/6} M^{1/2} \left( \frac{101.325}{P_c} \right)^{2/3}$$

$C_p$ : heat capacity, J/kmol K

The thermal conductivity of pure gases at high pressure can be calculated by

$$k_G' = k_G + \frac{A \times 10^{-4} (e^{B\rho_r} + C)}{\frac{M^{1/2} T_c^{1/6}}{P_c^{2/3}} Z_c} \quad (\text{II-7})$$

where:

$$\begin{aligned} \rho_r < 0.5 & \quad A = 2.702 \quad B = 0.535 \quad C = -1.000 \\ 0.5 < \rho_r < 2.0 & \quad A = 2.528 \quad B = 0.67 \quad C = -1.069 \\ \rho_r > 2 & \quad A = 0.574 \quad B = 1.155 \quad C = 2.016 \end{aligned}$$

$k_G$ : thermal conductivity of pure gases at low pressure, W/m K.

There is not a general equation to calculate the thermal conductivity of a gas mixture at high pressure. However, it is reasonable to extend the equation for pure gases to gas mixture at high pressure

#### 4. Gas diffusivity

The gas diffusivity in a binary system can be calculated by (Bird, 2002):

$$\rho D_{AB} = 2.96 \times 10^{-6} \left( \frac{1}{M_A} + \frac{1}{M_B} \right)^{1/2} \frac{(P_{cA} P_{cB})^{1/3}}{(T_{cA} T_{cB})^{1/12}} \quad (\text{II-8})$$

where:

$\rho$ : density of the gas at ideal state, kg/m<sup>3</sup>

The gas diffusivity in a multiple components system can be calculated by (Wilke, 1950):

$$D_{iM} = \frac{[1 - x_i]}{\sum_{j=1}^{N_s} \left[ \frac{x_j}{D_{ij}} \right]} \quad (\text{II--9})$$

where:

$D_{iM}$ : effective diffusivity of species  $i$  in the mixture  $M$ ;  $m^2/s$

$D_{ij}$ : diffusivity of species  $i$  in a binary system with species  $i$  and  $j$ ;  $m^2/s$

$x$ : molar fraction of species

$N_s$ : number of components in the mixture

### 5. Gas heat capacity (Perry, 1997c)

The gas heat capacity can be calculated by an empirical equation

$$C_p = a + bT + cT^2 + dT^3 \quad (\text{II-9})$$

The constants for major components in a typical gas mixture in the laboratory and field are listed in Table I-1:

Table II-1: Constants in the calculation of heat capacity

	$a$	$b \cdot 10^2$	$c \cdot 10^5$	$d \cdot 10^9$
Methane	19.875	5.021	1.268	-11.004
Water vapor	32.218	0.192	1.055	-3.593
Nitrogen	28.883	-0.157	0.808	-2.871
Carbon dioxide	22.243	5.977	-3.499	7.464

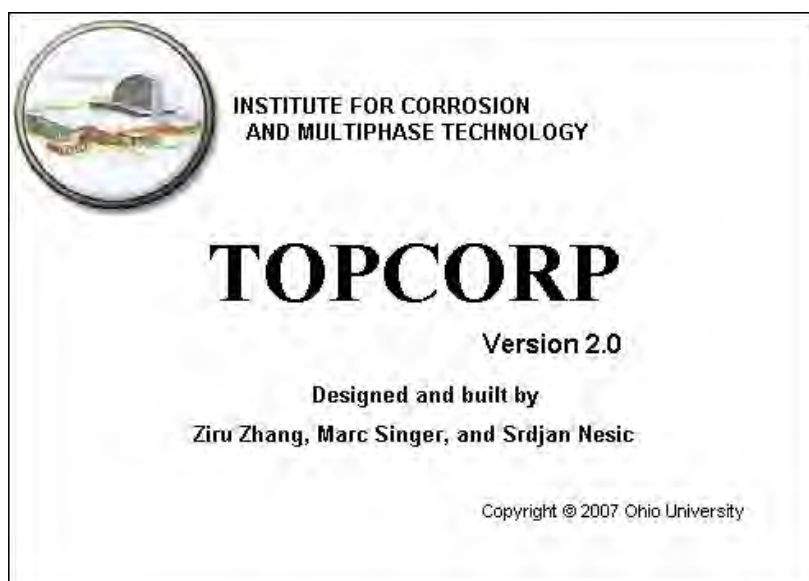
### APPENDIX III: INTERFACE OF TOPCORP

The numerical models developed from this dissertation are incorporated into a software package (TOPCORP) with a user friendly interface. The software provides several different modules for specific task requested by the users, which include:

- Condensation module
- Chemistry module
- General corrosion module
- Localized corrosion module

They also correspond to different models described in this dissertation except the localized corrosion module, which is based on a separate project in our laboratory.

#### III.1 Copyright splash



### III. 2 Main input window

**TOPCORP V2.0 Input Window**

Global input

Gas temperature	<input type="text" value="25"/>	<input type="text" value="C"/>
Total pressure	<input type="text" value="3"/>	<input type="text" value="bar"/>
Internal diameter	<input type="text" value="0.1"/>	<input type="text" value="m"/>
CO2 partial pressure	<input type="text" value="2"/>	<input type="text" value="bar"/>
H2S partial pressure	<input type="text" value="0"/>	<input type="text" value="bar"/>
Gas velocity	<input type="text" value="5"/>	<input type="text" value="m/s"/>
Environmental temperature	<input type="text" value="5"/>	<input type="text" value="C"/>

Modules

<input type="button" value="Condensation"/>	<input type="button" value="Chemistry"/>		
<input type="button" value="Localized corrosion"/>	<input type="button" value="General corrosion"/>	<input type="button" value="Help"/>	<input type="button" value="Cancel"/>

### III. 3 Dropwise condensation module

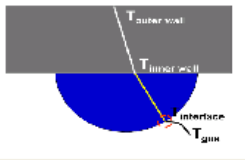
**TOPCORP V2.0 Dropwise Condensation**

**Input**      Output

Global input parameters

Total pressure	3	bar
Gas temperature	25	C
Internal diameter	0.1	m
CO2 partial pressure	2	bar
Gas velocity	5	m/s
Outside temperature	5	C

Pipe configuration



<input checked="" type="checkbox"/> Pipe wall	Conductivity	54	W/m/K
	Thickness	0.006	m
<input type="checkbox"/> Insulation layer	Conductivity	0.1	W/m/K
	Thickness	0.01	m

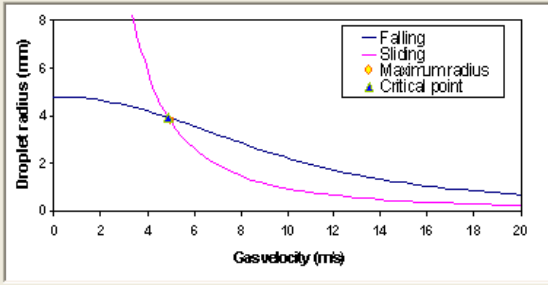
Accept      Calculate      Cancel      Help

**TOPCORP V2.0 Dropwise Condensation**

Input      **Output**

General output

Condensation rate	0.27	ml/m2/s
Maximum radii of droplets	3.77	mm
Critical radii of droplets	4.38	mm
Critical gas velocity	4.64	m/s
Condensation regime	Sliding droplet condensation	



Accept      Calculate      Cancel      Help

### III. 4 Chemistry module

**TOPCORP V2.0 Droplet Chemistry Display**

Input parameters

Total pressure: 3 bar

Gas temperature: 25 C

CO2 partial pressure: 2 bar

HAc concentration

Gas phase: 0.E0 ppm(v)

Water phase at the bottom: 0.E0 ppm(w)

H2S concentration

Gas phase: 0.E0 bar

Water phase at the bottom: 0.E0 ppm(w)

Water speciation in droplets

Name	Concentration	Unit
H+	2.04E-04	M
Ac-	0.00E00	M
OH-	1.09E-11	M
CO32-	3.87E-11	M
HCO3-	2.04E-04	M
H2CO3	2.42E-04	M
HAc	0.00E00	M
H2S	0.00E00	M
HS-	0.00E00	M
S2-	0.00E00	M

Cancel Accept Help

### III.5 Corrosion module

**MULTICORP V4 - Processing Window**

Corrosion rate vs. time

Simulation acceleration factor: 0.01 to 100

Scale porosity vs. distance from the metal surface

Fe++ conc. vs. distance from the metal surface

Global input parameters

T = 70 °C

Ptotal = 3.00 bar

PCO2 = 2.00 bar

PH2S = 0.E0 bar

CHAc = 0.E0 M

WCR = 0.28 ml/m2/s

Vg = 5.0 m/s

Help Interrupt Pause Continue

Output: predicted corrosion rate change vs. time

time = 22.5 hours

CR = 1.38 mm/y